Texto que sistematiza o trabalho científico do candidato para obtenção do título de livre docente

Prof. Guo-Qiang Hai

Departamento de Física e Ciência dos Materiais
Instituto de Física de São Carlos
Universidade de São Paulo

São Carlos, 2002

Agradecimentos

Aproveito este espaço para reconhecer e agradecer o trabalho, esforço, apoio e a amizade das pessoas que contribuíram direta ou indiretamente para a realização deste trabalho.

Aos Profs. Nelson Studart, Gilmar Marques e José Pedro Rino pela amizade, apoio e colaboração durante os 4 anos que estive no DF-UFSCar. Agradeço-lhes também pela oportunidade de poder conhecer e viver em um país encantador.

Aos Profs. François Peeters, Paul Koenraad, Bruce McCombe, Jian-Bai Xia, Slava Sokolov e Euclydes Marega, pela colaboração e amizade.

Aos amigos Marcos Tavares, Alexys Bruno-Alfoso, Ladir Cândido, José Camilo Barbosa, Kahio Tibério Mazon e Victor Lopez pela amizade e colaboração. Ao Haroldo Arakaki e a Isabel Rosani Constantino pelo apoio técnico e pela amizade.

Aos meus pais.

Índice

Capítulo 1

Introdução

Nesse texto procuramos sintetizar, através de uma coletânea de artigos publicados em revistas científicas, nossas atividades principais na área de física de sistemas semicondutores de baixa dimensionalidade. Esses trabalhos foram realizados durante os anos de 1994 a 2001, período que trabalhei no Instituto de Física de São Carlos da USP e no Departamento de Física da UFSCar. Tive também durante este período colaboração com vários grupos de pesquisa.

Nas últimas duas décadas, temos testemunhado um expressivo crescimento na área de física de nanoestruturas semicondutoras. Com as novas tecnologias de crescimento de cristais e litografias modernas, é possível controlar as estruturas cristalinas no nível atômico, bem como produzir linhas litográficas na escala nanométrica, produzindo assim poços e fios quânticos, super-redes e pontos quânticos. Estas estruturas dão origem a novos dispositivos eletrônicos quânticos e também abrem caminho para o estudo de novos efeitos físicos. Nossos trabalhos teóricos estão centrados no estudo dos efeitos de muitos corpos nos espectros ópticos e na mobilidade eletrônica destes sistemas.

No segundo capítulo trataremos as excitações coletivas e os processos de relaxamento de elétrons em fios e poços quânticos acoplados. As excitações coletivas (ou *plasmons*) devido à flutuação de densidade de cargas em um gás de elétrons são excitações dinâmicas fundamentais em cristais, estando relacionadas com as propriedades eletrônicas dos materiais. Nosso estudo sobre os efeitos de tunelamento nas excitações coletivas de fios quânticos paralelos indicou um novo tipo de interação entre as excitações coletivas e de partícula independente (*single-*

particle excitation – SPE). Também estudamos os magnétoplasmons nos fios quânticos acoplados sob campo magnético transversal. Ademais, estendemos a teoria de aproximação GW para sistemas de multisubbandas e estudamos os processos de relaxamento dos elétrons quentes injetados nos fios e poços quânticos acoplados. O tempo de relaxação de elétrons é uma quantidade física crítica para os dispositivos opto-eletrônicos baseados nessas estruturas, como os *"infrared quantum well cascade lasers"* e *"quantum well photodectors"*.

No terceiro capítulo, apresentamos os trabalhos relacionados a propriedades de transporte eletrônico em sistemas quase bidimensionais de multisubbandas, como sistemas com dopagens planares. As estruturas semicondutoras com camadas de impurezas altamente confinadas podem ser construídas nos laboratórios desde a década de 80. As espessuras destas camadas variam desde uma única monocamada até uns poucos parâmetros de rede. Tais perfis de dopagens muito estreitos podem ser descritos matematicamente por uma função delta de Dirac. Semicondutores com estes perfis de dopagens são denominados dopagens planares ou tipo-delta. Estas incorporações de dopantes ionizados em poucas monocamadas levam a um confinamento de cargas espaciais de elétrons em um poço de potencial, onde se observam várias subbandas de energias ocupadas, com o movimento perpendicular às camadas de dopantes quantizado. Elas apresentam um sistema semicondutor quase bidimensional (Q2D), com altas densidades eletrônicas e com novas propriedades ópticas e de transporte. Nossas contribuições sobre este assunto são: (i) pela primeira vez obtemos teoricamente as mobilidades de sistemas quase bidimensionais de multisubbandas, onde destacamos a importância de mecanismos de acoplamento intersubbandas no transporte eletrônico; (ii) em colaboração com um grupo experimental, concluímos que a teoria de RPA pode descrever corretamente a blindagem de gás de elétrons no espalhamento de impureza ionizadas no sistema de multisubbandas; (iii) esclarecemos vários pontos interessantes para experimentalistas, como os efeitos de *"background acceptors"*, mobilidades nos sistemas de duas camadas de dopagem delta, efeitos de confinamento extra e etc.

No capítulo seguinte, apresentamos dois artigos sobre acoplamento entre plasmons e fônons ópticos nos sistemas Q2D de multisubbandas. Apresentamos a teoria de acoplamento plasmon-fônon de sistemas multisubbandas. Também calculamos os espectros de espalhamento inelástico de luz (espectro de Raman) e mostramos os efeitos de espalhamento de impurezas nos espectros de Raman neste sistema.

No capítulo 5, estudamos interação elétron-fônon em poços quânticos. Os trabalhos deste capítulo são uma continuidade do meu trabalho de doutorado motivado pela observação experimental do grupo do Prof. B. D. Macombe na *State University of New York at Buffalo*. Um dos nossos resultados anteriores mostrou que elétrons em poços quânticos de GaAs-AlAs se acoplam fortemente com os modos de fônons interfaciais. Em campos magnéticos fortes, a ressonância polarônica acontece devido a fônons interfaciais neste sistema (*G.Q. Hai, F.M. Peeters, and J.T. Devreese, Phys. Rev. B 47, 13058 (1993)*). Este efeito foi observado em experimentos de ressonância ciclotrônica em múltiplos poços quânticos de GaAs-Al$_{0.3}$Ga$_{0.7}$As em 1996. Em colaboração com o grupo experimental, estendemos nossa teoria para o sistema de GaAs-Al$_{0.3}$Ga$_{0.7}$As e conseguimos um acordo excelente entre os resultados teóricos e experimentais. Além disso, estudamos os harmônicos assistidos por fônons, objeto de estudo por vários anos de nossos colaboradores em Buffalo, Nova York. Nossos cálculos numéricos de espectros de absorção indicaram, quantitativamente, que os harmônicos são muito fracos e dificilmente observados experimentalmente. Entretanto, nossos estudos mostram que os harmônicos assistidos por fônons podem ser observados em sistemas dopados de super-rede de GaAs-Al$_{0.3}$Ga$_{0.7}$As devido aos estados ligados de impurezas rasas.

Capítulo 2

Excitações coletivas e processos de relaxamento de elétrons em sistemas de baixa dimensionalidade

Nossos trabalhos apresentados neste capítulo estão focados nos efeitos de tunelamento nas excitações coletivas e também no processo de relaxamento dos elétrons em sistemas de dois fios e dois poços quânticos acoplados. É oportuno dizer que o primeiro dos artigos listados abaixo (artigo 2.1) poderia resumir todo o capítulo, bem como os artigos subsequentes. Tal artigo é resultado de uma palestra apresentada por mim no "*Workshop on physics of semiconductor nano-systems*" (Beijing, julho 2002).

No artigo 2.2, a relação de dispersão dos modos de excitações coletivas foi obtida, dentro da aproximação de fases aleatórias (RPA), para um sistema de fios quânticos acoplados. De maneira original, mostramos um efeito oriundo da ressonância entre os plasmons acústicos e as excitações de partícula independente. Esta ressonância é assistida pelo tunelamento que pode ocorrer entre os fios quânticos.

O artigo seguinte mostrou o efeito do campo magnético na dispersão de plasmons (magnétoplasmons). A dificuldade no estudo teórico deste problema se deu na convergência da matriz de função dielétrica. Resolvemos este problema através de uma transformação na função de onda dos elétrons e, consequentemente, no potencial de interação elétron-elétron.

Nos últimos dois artigos os espalhamentos inelásticos elétron-elétron foram estudados para os sistemas de fios e poços quânticos acoplados. Analisamos detalhadamente os efeitos do acoplamento intersubbanda na taxa de espalhamento inelástico dos elétrons que são injetados na banda de condução desta estrutura. Tal taxa é inversamente proporcional ao tempo de vida dos elétrons. Dentro deste contexto, verificamos também a importância do tunelamento entre os fios e poços.

2.1. *Collective excitations and fast electron relaxation in coupled low-dimensional electron systems*
G. Q. Hai
Proceedings of the Workshop on "Physics of Semiconductor Nano-systems" (2002).

2.2. *Tunneling-assisted acoustic plasmon-quasiparticle excitation resonances in coupled Q1D electron gases*
G. Q. Hai and M. R. S. Tavares,
Phys. Rev. B 61, 1704-1707 (2000).

2.3. *Collective and single-particle excitation spectra in coupled quantum wires in magnetic fields*
J.-B. Xia and G. Q. Hai,
Phys. Rev. B 65, (24)5326 (2002).

2.4. *Inelastic Coulomb scattering rates due to acoustic and optical plasmon modes in coupled quantum wires*
M. R. S. Tavares and G. Q. Hai
Phys. Rev. B 61, 7564-7570 (2000).

2.5. *Carrier relaxation due to electron-electron interaction in coupled double quantum well structures*
M. R. S. Tavares, G. Q. Hai, and S. Das Sarma,
Phys. Rev. B 64, (04)5325 (2001).

Collective excitations and fast electron relaxation in coupled low-dimensional electron systems

G.-Q. Hai
Instituto de Física de São Carlos, Universidade de São Paulo,
13560-970, São Carlos, SP, Brazil

1. Introduction

Over the past decades it has become possible to fabricate semiconductor nano-structures that exhibit reduced dimensionality. Electrons in such structures subject to an extra confinement. When the confinement in one direction becomes comparable or smaller than the electron Fermi wavelength the motion in that direction becomes quantized, resulting in changes in energy spectrum and physical properties of the system. When only in one dimension the electrons are confined in a space less than Fermi wavelength, a two-dimensional (2D) electron system is reached. If the electrons are confined in two dimensions, we obtain a one-dimensional (1D) electron system or a quantum wire.

The confinement of the electrons can be realized in many ways. In most semiconductor nano-structures, it is due to the compositional confinement arises from the barrier to carrier motion imposed by an abrupt change in chemical composition. The well-known two-dimensional systems are the Si-MOS structure and the GaAs/AlGaAs heterojunction.[1,2] The Si-MOS was one of the first structures used to create a 2D electron system. A positive voltage applied in the gate attracts electrons to the p-Si/SiO$_2$ interface. The electrostatic potential together with the barrier ($\sim$ 3eV) at Si/SiO$_2$ interface creates a potential well to form an inversion electron layer whose effective thickness is typically a few nanometers. The electron density in the inversion layer can be easily varied in the range 10^{11}-10^{12} cm^{-2} by changing the applied gate voltage. The electrostatic potential in GaAs/AlGaAs heterojection is due to modulated doped ionized impurities. By controlled growth technique, one can realize layered semiconductor structures to form the so-called quantum wells and superlattices.[2] In these systems, the low-temperature electron mobility is very high as reflected by the small effective mass (m^*=0.068m_0 in GaAs in contrast to m^*=0.19m_0 in Si-MOS structure) and the modulation doping which separates the electrons from their parent donors. The typical density in GaAs/AlGaAs heterojunctions and quantum wells is of order 10^{11}-10^{12} cm^{-2}. Selective growth combining with the modern lithographic and etching techniques produce confinement potentials in two or three dimensions leading to the one- or even zero-dimensional semiconductor systems.

Another important two-dimensional electron system is realized on the surface of liquid helium.[3] Electrons are subject to their own image force near the surface of liquid helium which acts as a dielectric. The surface of liquid helium presents a barrier of more than 1 eV to electrons. On the other hand, the image potential attracts the electrons

towards the liquid leading to the confinement of the electrons in a 2D plane. In comparison with the 2D system in semiconductors there is no impurity on liquid He so that a very pure 2D system can be realized. Typical electron density in this system is 10^9 cm^{-2}.

A dimensionless parameter r_s to indicate the density of one electron system is defined by the average space occupied by one electron measured by the effective Bohr radius $a_B^* = \hbar^2 \varepsilon_0 / m^* e^2$ with ε_0 being the dielectric constant of the material and m^* the electron effective mass. The parameter r_s decreases as the density n increases given by $r_s = (4\pi n/3)^{-1/3} / a_B^*$ for 3D, $r_s = (\pi n)^{-1/2} / a_B^*$ for 2D, and $r_s = n^{-1} / a_B^*$ for 1D system, where n is the electron density in the respective dimension. If we use the effective Bohr radius and effective Rydberg as the units of length and energy, respectively, the Hamiltonian of an electron system can be written as $H = (1/r_s^2) \left[\sum_i \nabla_i^2 + r_s \sum_{i \neq j} 1/|\vec{r}_i - \vec{r}_j| \right]$. It is clear that r_s is the key parameter to express the ground state energy. We also see that r_s is proportional to the ratio of the potential to kinetic energy of the electrons at low-temperatures. For small r_s the Coulomb potential can be considered as a perturbation to the first term of kinetic energy which represents an ideal electron gas. However, r_s is not necessarily small in actual materials. For instance, in alkali metals, r_s is of order of 2 to 6. In two dimensional semiconductor systems of GaAs heterojunction and quantum wells ($a_B^* = 9.8$ nm), the electron density $n=10^{12}$ cm^{-2} corresponds to $r_s \approx 0.56$. In Si-MOS structure ($a_B^* = 2.1$ nm), the same density gives $r_s \approx 2.7$.

Plasmons are the fundamental dynamical excitations of an electron gas to describe the collective oscillations of the electrons in crystal.[4-6] Considering a uniformly distributed electron gas against an equal density positively charged homogeneous background ionized atoms of crystal, we introduce an additional negative point charge. At the first moment, free electrons are driven away immediately by Coulomb repulsion from the vicinity of the negative point charge leading to a positive charge-cloud around it relative to the average charge density of the electron gas (screening effects). On the other hand, the long-range of the Coulomb potential push initially the electrons too far away. They will flow back. In this process, the collective oscillations appear corresponding to compressive waves of charge density of the electron gas. Plasmons are the quantum mechanical quasi-particles to describe such collective motions of the electron gas just as the phonons for lattice vibrations in crystal. The 3D plasmon is of a constant finite frequency $\omega_p = \sqrt{4\pi n e^2 / m^*}$ at long wavelength limit q $\rightarrow$ 0. It depends only on the electron density n of the system and the effective mass m^* of the electrons. Typical plasmon frequencies of 3D electron gases are several eV up to about 15 eV in metals and less than 1 eV in doped semiconductors.

The 2D electron gas with quantized subband was first confirmed experimentally in the inversion layers in Si-MOS structure by Fowler et al. in 1966.[7] However, the first experiment that directly probed the two-dimensional plasmons was realized in the 2D electron systems on the liquid helium surface in 1976[8]. Later, 2D plasmons were also

observed in Si inversion layer[9] and in GaAs/AlGaAs heterostructures[10] An essential difference of the 2D plasmon mode from its 3D counterpart is that the plasmon frequency approaches to zero at long wavelength limit. The difference stems from the fact that the electron-electron Coulomb electric fields remain 3D character while the induced charge density attends a 2D behavior. Furthermore, the plasmon frequency at low dimension is in general depends on the shape of the confinement potential and the dielectric properties of the host materials. Properties of the collective excitations and their dispersion relations in 3D and 2D systems are well understood based on the Fermi liquid theory, which assumes that the energy states of the electrons near the Fermi surface are not qualitatively altered by Coulomb interactions. The plasmon dispersions obtained within the random-phase approximation (RPA) and its improvement including the exchange-correlation effects are in excellent agreement with the experimental observations.

In a semiconductor quantum wire structure, the electrons confined in two dimensions are allowed free motion only in one dimension. An early motivation behind the proposal of the semiconductor quantum wire structure was that the impurity scattering would be severely reduced and, consequently, the low-temperature electron mobility could be substantially enhanced. However, realization of the quantum wire structure also provides an ideal platform to study the many-body electron effects and the 1D Fermi liquid. In 1D systems, even weak Coulomb interactions cause strong perturbations. It has long been expected that the properties of a 1D electron gas are dramatically different from its 2D and 3D counterparts. Much of the fundamental theoretical understanding of the dynamical properties of the 1D electron systems has been gained from the Luttinger liquid model.[11] The Luttinger mode with a simplified linearized band structure has been claimed to prevail in 1D where exchange-correlation cannot longer be treated perturbatively. Any electron-electron interaction destroys the Fermi surface (i. e., no discontinuity in the momentum distribution function) and consequently, there not exist single-particle excitations in 1D.

However, the theory within the RPA based the Fermi liquid theory agrees remarkably well with the experimental measured plasmon dispersions of semiconductor quantum wires.[12,13] It is argued that the distinct difference at a fundamental theoretical level of the two models are rather irrelevant to the understanding of the collective mode spectra and their experimental realization in semiconductor quantum wire structures. The quantitative agreement between the RPA plasmon dispersion and the Raman scattering experimental results was explained that the RPA and the Luttinger theory for the collective excitations of the 1D electron liquid are equivalent at long wavelengths.[14,15] Theoretical calculations also showed that in the presence of the impurities in semiconductor quantum wire structures, even a slight impurity scattering restores the Fermi surface and the Fermi liquid behavior remains. The actual semiconductor quantum wire structure with slight impurities or defects is probably impure enough to suppress the Luttinger-liquid behavior[16]. Luttinger-liquid behavior has been confirmed in the 1D electron systems in carbon nanotubes[17] and in one-dimensional metallic chains.[18] Experiments on 1D semiconductor quantum wires have also been interpreted by using Luttinger liquid theory[19], but an unequivocal verification of the theoretical predictions has not yet been obtained. Theoretical calculations of the inelastic light scattering spectra

with the Luttinger liquid theory cannot quantitatively explain the experimental data indicating the 1D electron systems in semiconductor quantum wire structures are not in the regime where the Luttinger liquid effects are important.[14] The collective excitations of 1D electron gas are presently described with two competing theoretical models.

In a 1D system, the electron-electron interaction is much stronger than that in higher dimensional ones. For an ideal 1D system with zero thickness, the Fourier transform of the Coulomb potential is divergent. It becomes non-singular at finite q only when the finite thickness of the wire is considered. Another important aspect of the 1D electron gas is that the energy and momentum conservation in 1D restriction opens a gap in the single-particle continuum at low frequency where no Landau damping is possible. This is very different from the 2D and 3D case where there is a continuous Landau damping region in the energy-momentum space.

2. Dielectric function

The simplest and successful theoretical model to obtain the plasmon dispersion is the random-phase approximation[1,20]. Within a one band (or subband for low-dimensional systems) model, the RPA dielectric function can be written as[21]

$$\varepsilon(\omega,q) = 1 - V(q)\,\Pi^0(\omega,q), \qquad (1)$$

Where $V(q)$ is the Fourier transform of the electron Coulomb potential, $\Pi^0(\omega,q)$ is the free particle polarization function, and q is the wavevector in the respective dimensions. $V(q) = 4\pi e^2/\varepsilon_0 q^2$ for 3D; $V(q) = 2\pi e^2/\varepsilon_0 q$ for 2D; and $V(q) = -(2e^2/\varepsilon_0)f_c(qW)$ for 1D with the Coulomb form factor $f_c(qW)$ depending on the confinement potential (W stands for the effective thickness of the wire)[22]. The polarization function is given by

$$\Pi^0(\omega,q) = \frac{2}{\Omega}\sum_{\vec{k}} \frac{f\big(E(\vec{k}+\vec{q})\big) - f\big(E(\vec{k})\big)}{E(\vec{k}+\vec{q}) - E(\vec{k}) + \omega + i\delta}, \qquad (2)$$

where $E(k) = \hbar^2 k^2/2m^*$ is the kinetic energy of the electron with momentum k, $f(E)$ is the Fermi distribution function, and $i\delta$ represents a small imaginary number.

The plasmon dispersions are obtained by the zeros of the dielectric function. At long wavelength limit the plasmon dispersion relations within the RPA are written as $\omega(q) = \omega_p + \alpha(\hbar/m^*)q^2$ for 3D, $\omega(q) = [2\pi ne^2 q/\varepsilon_0 m^*]^{1/2}$ for 2D, and $\omega(q) = [-2\pi ne^2 q^2 \ln(qW)/\varepsilon_0 m^*]^{1/2}$ for 1D, where $\alpha = 3E_F/5\hbar\omega_p$ is a constant describing the leading wavevector dependence of the 3D plasmon mode. The region in the $\omega - q$ plane where $\text{Im}\Pi^0(\omega,q) \neq 0$ defines the single-particle (electron-hole pair) excitation continuum. In the single-particle excitation (SPE) continuum, one electron

below the Fermi surface can be excited above it and leaves a "hole" in the Fermi sea. As a consequence, the plasmon excitations are damped (Landau damping).

The RPA dielectric function which is exact at high electron density limit ($r_s \rightarrow 0$) becomes poor at low density. Most obvious defect is that the RPA leads the pair distribution function $g(r)$ to become negative at small r. The first attempt to improve the RPA was proposed by Hubbard[23] who suggested a dielectric function in the following form

$$\varepsilon(\omega,q) = 1 - \frac{V(q)\,\Pi^0(\omega,q)}{1 + V(q)G(q)\,\Pi^0(\omega,q)}, \tag{3}$$

where $G(q) = q^2/[2(q^2 + k_F^2)]$ is introduced to account for the effects of the exchange interaction. This modification on the dielectric function is called static local field correction. The most important improvement on the RPA is the STLS approximation.[24] The STLS dielectric function is of the same form as the Hubbard dielectric function. However it explicitly incorporates the exchange and correlation effects through a self-consistent function $G(q)$ give by

$$G(q) = -\frac{1}{n}\sum_{\vec{k}} \frac{\vec{q}\cdot\vec{k}}{k^2}[S(|\vec{q}-\vec{k}|) - 1]. \tag{4}$$

Where the static structure factor of the electron gas $S(q)$ can be obtained through dielectric function $\varepsilon(\omega,q)$. In this scheme, the functions $G(q)$, $S(q)$, and $\varepsilon(\omega,q)$ have to be calculated self-consistently. Many different form have been proposed to improve the function $G(q)$. Generally, it may also depends on frequency ω. Here, we will not discuss more. One of them is that, with the Monte Carlo simulation results, the static structure factor $S(q)$ can be obtained directly from the Fourier transform of the pair distribution function.

For low-dimensional electron systems of multisubbands, the dielectric function becomes a tensor due to the quantized subbands. For a 2D system, the electron eigenenergy can be written as $E_n(k) = E_n + \hbar^2 k^2/2m^*$ where E_n (n=1,2,3,...) is the quantized energy levels due to confinement. The corresponding electron wave function (for a confinement in the z-direction and electrons being free in the xy-plane) is given by $\psi_{n,\vec{k}}(\vec{r},z) = (1/\sqrt{A})e^{i\vec{k}\cdot\vec{r}}\psi_n(z)$ where $\vec{r}$ and $\vec{k}$ are position and wavevector in the 2D plane. As a consequence, the dielectric function becomes a tensor with subband indices n, n', m, and m'. Within the RPA it is written as a matrix form[25]

$$\varepsilon_{nn',mm'}(\omega,q) = \delta_{nm}\delta_{n'm'} - V_{nn',mm'}(q)\,\Pi^0_{mm'}(\omega,q), \tag{5}$$

with the matrix element of the Coulomb potential

$$V_{nn',mm'}(q) = \frac{2\pi e^2}{\varepsilon_0 q} \int dz \int dz' \psi_n(z) \psi_{n'}(z) e^{-q|z-z'|} \psi_m(z') \psi_{m'}(z'), \qquad (6)$$

and the polarization function

$$\Pi^0_{mm'}(\omega, \vec{q}) = \frac{2}{A} \sum_{\vec{k}} \frac{f(E_{m'}(\vec{k}+\vec{q})) - f(E_m(\vec{k}))}{E_{m'}(\vec{k}+\vec{q}) - E_m(\vec{k}) + \omega + i\delta}. \qquad (7)$$

In a multisubband 1D system the dielectric function is of the similar form. The plasmon dispersions can be obtained by the determinant equation of the dielectric matrix $\det | \varepsilon_{nn',mm'}(\omega, q) | = 0$.

In a multisubband system, new plasmon modes appear due to interactions of the electrons between different subbands. These intersubband plasmon modes represent oscillations of the electrons in the transverse direction. The frequency of the intersubband plasmons at long wavelength is finite because of the energy spacing between two subbands. But the plasmon frequency does not depend only on the spacing of two subbands. Electron-electron Coulomb interactions lead to two effects on the intersubband plasmon frequency: the depolarization shift[26,27] and the excitonic shift.[28,29] The depolarization shift arises from the resonant screening of the microscopic one-particle dipole excitation by the collective effect of all other electrons. This collective influence is usually calculated within the RPA leading to an increase of the intersubband plasmon frequency. The excitonic shift, due to exchange-correlation effects, results from the energy renormalization when an electron is transferred from one subband to another and leaving a "hole" behind. This effect shifts the intersubband plasma resonance to lower frequency. At low (high) electron density the excitonic (depolarization) shift dominates and the plasmon frequency becomes smaller (larger) than the subband separation.

3. Plasmons in double layer electron systems

Coupled double 2D electron layer system promises to afford interesting new physics. This system is realized in double quantum well structures in which two 2D electron gases are established parallel to each other separated by a potential barrier. In such systems many-body correlations due to Coulomb interaction are the crucial ingredients of the detailed description of their behavior because the interlayer Coulomb interaction can counterbalance the kinetic energy of the electrons leading to many-body effects to dominate. The Coulomb correlation in double quantum wells leads to interesting phenomena such as new states in fractional quantum Hall regime. Coupled double electron and hole layer systems provide a new platform to study the Bose-Einstein condensation in which the carriers of opposite charge in different layers attract each other. They may form excitons and condense into a superfluid. The Coulomb drag effects between two layers of electrons have provided an elegant and sensitive probe to study the electron-electron scattering rate and correlation effects. Plasmons in coupled quantum

wells represent another significant area for the study of many-body effects in low dimensions. Many-body effects and collective excitations have also been studied extensively in multilayer systems in the presence and absence magnetic fields in last two decades. Here we are going to discuss the collective excitations in double electron layers at zero magnetic field.

The RPA was generalized in calculation of the plasmon dispersion in bilayer systems.[30-32] It is shown that, besides the usual plasmon mode of the 2D electron gas, another new lower-lying mode appears whose frequency is of a linear dependence on the wavevector q at long wavelength limit called acoustic mode. The acoustic plasmon mode represents the out-of-phase oscillations of the charge-density waves in different layers of electrons. While the usual 2D plasmon mode, proportional to $\sqrt{q}$ representing the in-phase oscillation of the electrons in different layers, is called optical mode. Raman spectroscopy has been used to probe the plasmon dispersions in GaAs/AlGaAs double quantum well structures.[33-34] Both the optical and acoustic plasmon modes were observed in experiments. Figure 1 shows the plasmon dispersion observed in the Raman scattering spectra from GaAs/Al$_{03}$Ga$_{07}$As double quantum wells of width W$_{QW}$ separated by a barrier of width W$_{b}$.

The acoustic mode is of particular interesting because it is sensitive to the correlation effects. The acoustic behavior is originated from screening of the long-range part of the Coulomb potential by charges in the opposite layer. It is also predicted to enhance the electron-electron inter-layer interaction responsible for the Coulomb drag between electron layers and maybe involve in mechanisms for high temperature superconductivity.
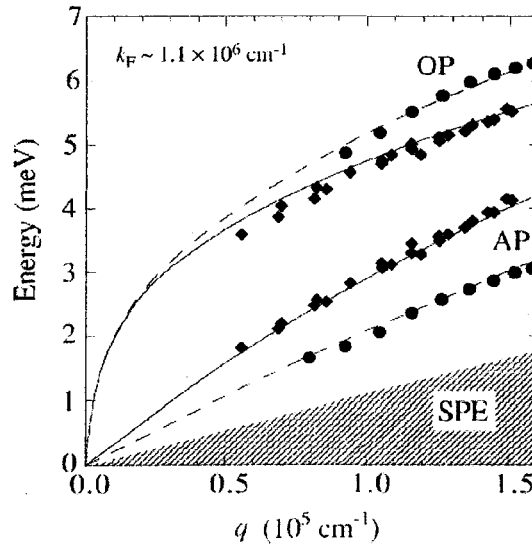

Fig. 1. Dispersion of the optical (OP) and acoustic plasmon (AP) modes in GaAs/Al$_{03}$Ga$_{07}$As double quantum wells. ($\blacklozenge$): W$_{QW}$ =200 Å and W$_{b}$=600 Å; ($\bullet$): W$_{QW}$=180 Å and W$_{b}$=125 Å. The curves are the theoretical fitting (STLS) with the electron density as a parameter. The shaded region indicates the SPE continuum.[34]

The exchange and correlation effects that become even more important in coupled bilayer systems are not considered within the RPA. For instance, the calculations based on the RPA underestimate the transresistance of the interlayer Coulomb drag effects by one order of magnitude. Only the theory including the local field correction due to exchange and correlation effects within the STLS approach gives a reasonable explanation to the experimental data.[35-36] The correlation effects on the plasmon dispersions in coupled 2D electron gases have been studied exhaustedly within the STLS self-consistent scheme. The dispersion of the acoustic mode is strongly affected by correlations. Much work has been focused on the Landau damping effects on the acoustic plasmons. It is expected that this mode is more susceptible to the Landau damping. Although the RPA theory indicates a stable out-of-phase acoustic plasmon mode in couple two identical electron layer system for any distance between them[31], further calculations with correlation effects (STLS with static local field correction) showed that there exists a critical separation between the layers.[37,38] Below this critical distance, correlation pushes the acoustic mode merging entirely with the single-particle excitation continuum and, consequently, being damped out. For two coupled layers with different densities, however, the acoustic mode survives in the single-particle excitation region of the higher density layer where the Landau damping is found very weak.[37] The Landau damping on the acoustic plasmon mode in two coupled charge layers with different effective masses is of similar character.[39] The theory with a frequency-dependent local field function to consider the dynamical correlation effects yields qualitatively similar results as those of the static approximation. Fig. 2 shows the optical and acoustic plasmon dispersion within the RPA, static and dynamical STLS schemes. It is found that both the optical and acoustic plasmon dispersions lie between the RPA and static STLS curves. But it indicates the plasmon modes acquire damping even outside the single-particle excitation region where the RPA and static STLS predict zero damping.[40] Temperature effects on the plasmon modes have also been studied both theoretically and experimentally in bilayer systems. A finite temperature tends to increase the both the acoustic and optical plasmon frequencies in contrast to that the correlations depress the plasmon modes to lower frequencies. Moreover the Landau damping at finite temperature leads to asymmetry in the Raman line-shape of the acoustic plasmons.[33,41] It was also found that the local fields do not change much with temperature for $k_B T < E_F$.

The theoretical study on the plasmon excitations in strongly coupled bilayer systems with the STLS framework was criticized[42,43] based the calculation of the plasmon dispersion relations within the quasilocalized charge approximation (QLCA). The theoretical results with this approach indicate that an energy gap exists in the out-of-phase plasmon mode at long wavelength limit instead a linear (acoustic) dispersion. It is believed that the STLS theory is inappropriate for the analysis of the long wavelength behavior of the plasmon modes in strongly coupled bilayer systems. The discrepancy between the STLS and QLCA may be due to the role played by the third frequency-moment sum rule. On the other hand, Ortner analyzed different theoretical approaches and argued that within the QLCA the neglect of the damping process overestimates the correlations and the correct account of damping yields an acoustic mode without gap. In view of the contradiction of the different theoretical predictions[44], further detail experi-
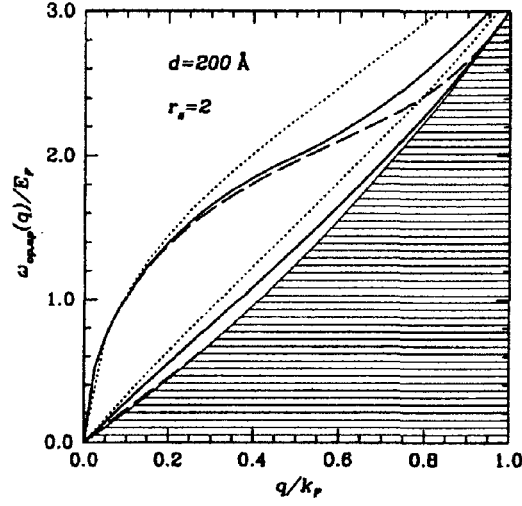
Fig. 2. The plasmon dispersions for a double-layer system of electrons at r_s=2 and d=200 Å: The acoustic (lower curves) and optical (upper curves) plasmons are depicted for the RPA (dotted lines), static STLS (dashed lines), and dynamic STLS (solid lines). The shaded area indicates the single-particle excitation region.[40]

mental study on the collective modes in bilayer system would be interesting, especially the plasmon dispersion at long wavelength limit.

In a real bilayer system, when the two quantum wells are closed enough, tunneling between the two layers occurs. Tunneling introduces qualitatively new physics and new energy scale (i.e. the interlayer tunneling energy) in addition to the Coulomb energy and the interlayer kinetic energy. Effects of tunneling between the two layers on
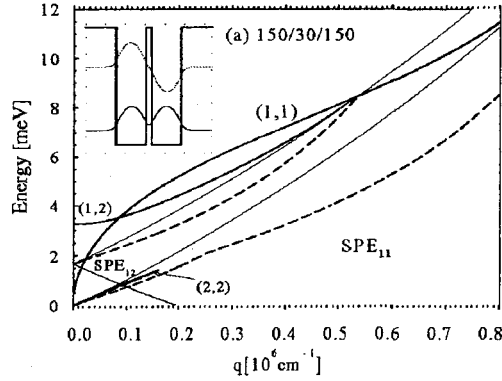

Fig. 3. Plasmon dispersions in two coupled GaAs/Al$_{0.3}$Ga$_{0.7}$As quantum wells of widths W$_1$=W$_2$=150 Å separated by a barrier of width W$_b$=30 Å. The tunneling between the wells is considered. The modes (1,1) and (1,2) correspond to the OP and AP modes when tunneling is absent. The shadow areas present the SPE continua. Total electron density N_e=2×10^{11} cm^{-2}.[46]

the collective excitations are of great interesting. Theoretical calculations within the RPA and Hubbard approximation show the interlayer tunneling introduces an energy gap on the out-of-phase plasmon mode while the in-phase mode is not affected qualitatively. The appearance of the energy gap in the out-of-phase mode is not a surprise in the bilayer system with tunneling. Tunneling results in the bilayers evolving to a 2D systems with two subbands. In this situation, the out-of-phase mode is actually an intersubband-like plasmon mode[46,47] as shown in Fig. 3.

4. Plasmons in quantum wires

The crucial first step in developing the theory of plasmon dispersion in quasi-1D electron gas was taken by Williams and Bloch using the RPA in 1974.[48] Subsequently, a lot of theoretical studies have been carrier out within the RPA and the STLS self-consistent approach. Most experimental work on the semiconductor quantum wires during eighties was involved with the fabrication and characterization of electronic states in wires. A clear signature of the 1D plasmon behavior of an electron gas was observed by resonant Raman spectroscopy in GaAs/AlGaAs quantum wire structures in 1991.[12] The observed plasmon dispersion is of almost a linear q dependence as predicted by the RPA as shown in Fig. 4. Among the important research milestones in semiconductor quantum wires are the observation of the 1D plasmons via inelastic light scattering spectroscopy and the verification of the predicted acoustic linear plasmon dispersion relation[12,49], the observation of pronounced 1D Fermi edge singularity in optical spectra[50], and the quantum wire excitonic laser operation.[51]

Collective excitations and exchange-correlation effects in multisubband quasi-1D electron gases in both isolated quantum wires[12,49,52-60] and multiwire superlattices [61-65] have been extensively studied in the last decade. In contrast to higher dimensional electron gas systems, the SPE are suppressed in 1D electron gas due to the energy–momentum conservation leading to a gap in the SPE continuum at low energies. In a quantum wire with two occupied subbands, the intrasubband plasmon mode due to the second subband lies in the gap between the two intrasubband SPE continua and is undamped. This feature is different from its counterpart in a 2D system where only one intrasubband plasmon mode is undamped. It has also been shown that the higher frequency intrasubband plasmon mode in the Q1D system (due to the lowest subband) is of an energy proportional to $q\sqrt{\ln(qW)}$ at the long wavelength limit, whereas the lower frequency one has a linear q dependence. Furthermore, a large depolarization shift has been found for the intersubband plasmon mode in single wires.

In a similar way to coupled two-dimensional electron gases[33,45,66], optical and acoustic plasmon modes[67-69] were found in two coupled quantum wires. However, the acoustic plasmon mode in coupled quantum wires is of relatively strong spectral weight (comparable to the optical one) because of the non-existence of the low-energy 1D single-particle excitations. These modes were also studied in multiwire superlattices[54,61]. Theoretical work has been done on plasmon dispersions[68,69],
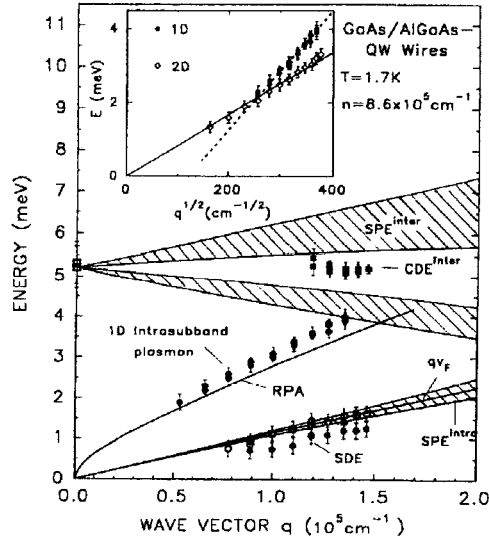
Fig. 4. Collective and SPE spectrum of a 1D electron gas in the quantum limit. Solid dots represent the intrasubband collective charge-density (CDE) and spin-density (SDE) excitations. Open circles display the position of the peak at $\hbar q v_F$ of intrasubband SPEs. Squares correspond to data of Q1D intersubband CDEs measured in VV polarization. The shaded areas indicate SPE regime given by $\mathrm{Im}\Pi(\omega,q) \neq 0$. Inset: comparison of the 1D intrasubband plasmon frequencies with those of a 2D electron gas with $E_F = 3.8$ meV as a function of $q^{1/2}$. (Goñi et al.[12])

electron–electron correlations[70,71], Coulomb drag[72], and tunneling effects in these systems[73,74]. Tunneling effects have provided new devices formed by coupled semiconductor quantum wires[74] and have attracted considerable theoretical interest. A weak resonant tunneling in coupled wires leads to a finite energy value for the acoustic mode at zero wavevector[68,75] as shown in Fig. 5(a). This is similar as that in coupled quantum wells. Furthermore, it was predicted that, in a very weak non-resonance tunneling condition in two coupled asymmetric quantum wires, the acoustic plasmon mode presents two gaps at finite q as indicated in Fig. 5(b).[75] Such acoustic mode splitting indicates a resonant coupling between the acoustic plasmon and the single-particle excitations. Figure 6 shows the calculated Raman spectra due to the plasmon scattering of the corresponding modes in Fig. 5(b) around (a) the lower and (b) the higher energy gap. We see a strong Raman scattering peak at high frequencies due to the optical plasmons. Besides, there are two split peaks due to the acoustic plasmons. With increasing q, the spectral weight transfers from the lower to the higher frequency one. When tunneling between two asymmetric quantum wires is strong in mode mixing occurs among the different intrasubband- and intersubband-like plasmon modes. Calculated Raman spectra indicate such a mixting leading to the intrasubband-like plasmon mode partially Landau damped in the intersubband SPE continua.[47]
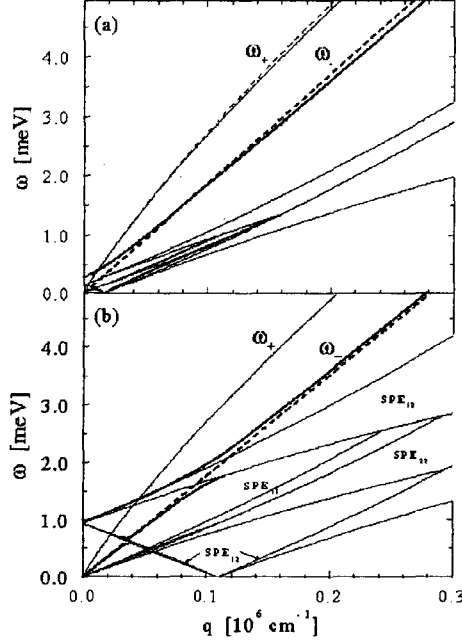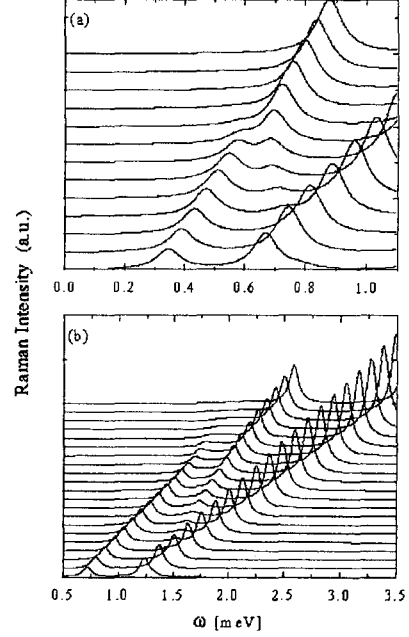
Fig. 5

Fig. 6

Fig. 5. Plasmon dispersions in two coupled GaAs quantum wires of widths (a) $W_1 = W_2 = 150$ Å and (b) $W_1 = 150$ Å and $W_2 = 145$ Å separated by an $Al_{0.3}Ga_{0.7}As$ barrier of width $W_b = 70$ Å. The total electron density $Ne = 10^6$ cm^{-1}. The solid (dash) curves present the plasmon dispersions with (without) tunneling. The thin and thick curves indicate the in-phase (ω_+) and out-of-phase (ω_-) plasmon modes, respectively. The shadow area presents the single-particle excitation regions.[75]

Fig. 6. Raman scattering spectra in the coupled quantum wires corresponding to Fig. 5(b) at different q: (a) from 2 to 5×10^4 cm^{-1} with equivalent difference $\Delta q = 0.25 \times 10^4$ cm^{-1} and (b) from 0.4 to 1.4×10^5 cm^{-1} with $\Delta q = 0.05 \times 10^5$ cm^{-1}. The intensity in (a) is enlarged 4 times as compared to (b). The different curves are offset for clarity.[75]

5. Inelastic Coulomb scattering in coupled quantum wells and wires

Electron-electron interaction induced carrier relaxation is an important inelastic scattering process in low-dimensional semiconductor nanostructures. It is often (particularly in situations where LO phonon emission is energetically prohibited because the excited electrons do not have enough energy) the most dominant relaxation process in semiconductor quantum wells and wires, and is therefore of considerable fundamental and practical importance. Band gap engineering has led to the possibility of fabricating tunable far infrared quantum well cascade lasers (QCL's) and efficient quantum well infrared photodetectors (QWIP's), where inelastic carrier relaxation via electron-electron interaction is a crucial (perhaps even decisive) process in determining device operation and feasibility. For QCL and QWIP operations it is the intersubband inelastic relaxation

that turns out to be the primary rate-limiting scattering process. For other proposed devices, such as the planar hot electron transistors or related 2D high-speed devices, intrasubband relaxation is the important process. A thorough quantitative understanding of intra- and intersubband relaxation due to electron-electron interaction is therefore important for the successful realization of these devices.

With improving materials growth and nanostructure fabrication techniques one expects a wide range of 1D experimental phenomena and projected applications in semiconductor quantum wire systems. Many of the projected applications such as ballistic electron transistors, quantum wire–based infrared photodetectors and lasers, and quantum wire THZ oscillators and modulators will utilize fast carriers (injected or excited) in doped quantum wires as the active device element. Effective control and manipulation of these fast electrons in doped quantum wire systems are therefore essential in projected quantum wire optoelectronic applications.

One of the most crucial physical processes that will limit the quantum well and quantum wire optoelectronic applications is the relaxation of these fast electrons. The main ultrafast mechanism controlling the relaxation process is the electron-electron interaction. In addition to this practical technological motivation arising from the band-gap-engineered quantum nanostructure devices, there is also an obvious fundamental reason for studying inelastic Coulomb scattering in 2D and 1D electronic systems. Inelastic electron-electron scattering determines the quasi-particle spectral width, as determined, for example, in tunneling measurements, through the imaginary part of the electron self-energy function.[76,77]

The central quantity to study the inelastic electron-electron scattering is the imaginary part of the self-energy function. Within the leading-order dynamically screened Coulomb interaction expansion (the so-called GW approximation in the multisubband situation), it is the imaginary part of electronic on-shell self-energy matrix, M, in the quantum well or wire subband index (i, j, etc.). The subband self-energy in the multisubband situation is, in general, off-diagonal, reflecting the breaking of the translational invariance along the confinement direction. The off-diagonal self-energy, $\mathrm{Im}(M_{ij})$, incorporates in an intrinsic many-body manner the possibility of electron-electron-interaction-induced intersubband scattering (both virtual and real) of carriers. In the doped situation of our interest the many-body self-energy approach is also a reasonable technique in calculating the inelastic carrier relaxation rate in spite of the Boltzman equation approach, where the scattering rates are usually calculated using Fermi's golden rule.[78] The dynamical screening inherent in the many-electron system, which affects the calculated inelastic scattering rates in profound and highly nontrivial way, is automatically incorporated in the many-body GW expansion, whereas inclusion of dynamical screening in Fermi's golden rule type formula is done by replacing the bare interaction by a screened interaction in an *ad hoc* manner.

The theory, as mentioned above, is based on the so-called GW self-energy approximation[79-82] where the electron self-energy M is obtained in a leading order expansion of the dynamically screened Coulomb interaction $W \equiv V^s$, where the superscript s denotes dynamical screening of the bare electron-electron interaction matrix V in the multisubband situation. We use the RPA to obtain the dynamically screened
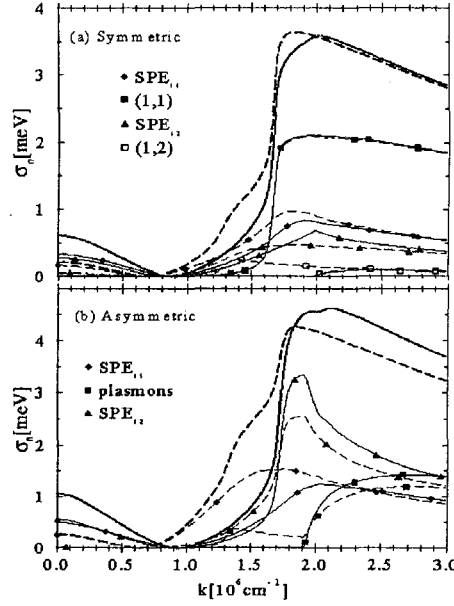
Fig. 7. Total inelastic Coulomb scattering rate of electrons as a function of electron momentum k in coupled two (a) symmetric quantum wells of widths $W_1 = W_2 = 150$ Å and (b) asymmetric wells of $W_1 = 150$ Å and $W_2 = 140$ Å structures separated by a barrier of width $W_b = 30$ Å. (Figure (b) corresponds to figure 3). The thick solid and thick dashed lines denote the total scattering rate $\sigma_n(k)$ for $n=1$ and 2, respectively. The symbols on the thin lines represent each contribution to the total calculated scattering: diamonds standing for the SPE_{11} contribution, the filled squares stand for the intrasubband (1,1) plasmon contribution, triangles stand for the SPE_{12} contribution, and opaque squares stand for the intersubband (1,2) plasmon contribution. Total electron density $N_e = 2 \times 10^{11}$ cm^{-2}.[46]

interaction V^s, i.e., $V^s = \varepsilon^{-1}V$. We also approximate the electron Green's function G by the noninteracting Green's function G^0, making our formal expression for the self-energy matrix to be

$$M = \int G^0 V^s ,$$
(8)

where the integral involves integrating over all internal momentum and energy variables as well as summing over all internal subband indices (and spin). Putting the subband (matrix) indices explicitly in Eq. (8), we get

$$\mathrm{Im}M_{ij} = \mathrm{Im}\sum_{lm} \int G^0_{lm}V^s_{ilmj} .$$
(9)

We note, however, that G^0, being the noninteracting Green's function, is necessarily diagonal in subband indices (i.e., an electron cannot undergo intersubband scattering in the absence of interaction):

$$G^0_{lm} \sim G^0_{ll}\delta_{lm} ,$$
(10)
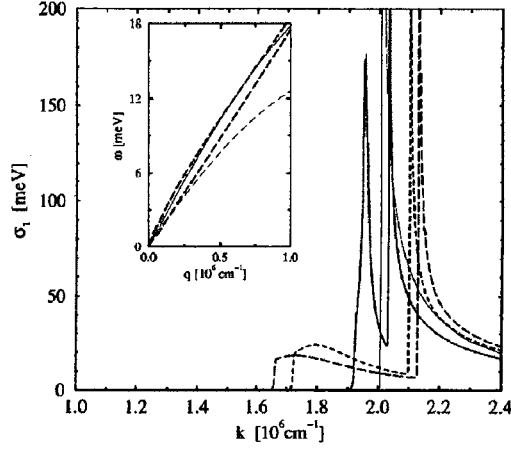
Fig. 8. The inelastic Coulomb scattering rates in two coupled quantum wires of $W_1 = W_2 = 150$ Å separated by a barrier $W_b = 30$ Å (long-dash line), 70 Å (dashed line), 300 Å (dotted line), and ∞ (thin-solid line). No tunneling occurs between the wires and electron density in each wire is $n_e = 0.5 \times 10^6$ cm^{-2}. The inset shows the acoustic and optical modes (thick dashed lines) for $W_b = 30$ Å, and the intrawire energy- vs momentum-loss curves at the onset of the optical (thin solid line) and acoustic (thin dashed line) plasmon scattering.[82]

Then, Eq. (9) becomes

$$\text{Im} M_{ij} = \sum_l \int \text{Im}[G_{ll}^0 V_{illj}^s] , \qquad (11)$$

with $V_{illj}^s = (\varepsilon^{-1} V)_{illj}$. Equations (9) and (10) are the central formal equations to obtain the inelastic relaxation time τ. The scattering rate σ and the relaxation time τ are connected by $\tau = \hbar/(2\sigma)$ where $\sigma = |\text{Im} M|$.

We emphasize that the inelastic relaxation time τ defined above is an energy relaxation time (and not a momentum relaxation time, as, for example, will enter the calculation of the mobility of the system). The inelastic relaxation time defines the lifetime of a single-particle energy eigenstate in the system. Due to Coulomb scattering among the electrons the single-particle stationary states are well-defined only over a limited time scale and our calculated τ is a measure of this lifetime arising from electron-electron interaction.

The total inelastic Coulomb scattering rate $\sigma_1(k)$ (thick solid line) and $\sigma_2(k)$ (thick dashed line) of fast electrons in the subband n=1 and 2 as a function of wavevector k in two symmetric and two asymmetric GaAs/Al$_{0.3}$Ga$_{0.7}$As quantum well structures are shown in Figure 7(a) and 7(b), respectively. The symbols on the thin lines identify the contributions to $\sigma_1(k)$ and $\sigma_2(k)$ coming from the emission of single-particle and collective excitations individually. Single-particle excitations contribute for all values of wavevectors k. However, neither intra- nor intersubband plasmon mode contributes to the

scattering rates close to the subband Fermi wavevectors. (k_{F1}^{sy}=0.88 $\times 10^6$ cm^{-1} and k_{F2}^{sy}=0.69 $\times 10^6$ cm^{-1} for the symmetric case). These collective modes provide excitation channels for inelastic relaxation only above some threshold wavevectors.

The inelastic Coulomb scattering rate $\sigma_1(k)$ in two coupled symmetric quantum wires with no tunneling is shown in Fig. 8. Two sharp peaks are result from the scattering due to the optical and acoustic plasmons, respectively.

6. Summary

We have discussed the collective excitations (plasmons) in low-dimensional electron systems. We describe especially the plasmon dispersion in coupled bilayer electron gases and in coupled quantum wires. In both coupled bilayer and biwire systems, acoustic plasmon mode appears result from the Coulomb interaction between them. This mode is susceptible to electron correlations and is of particular interesting. Effects of electron correations, Landau damping, and tunneling are studied in different systems. We have also studied the electron-electron interaction induced fast electron relaxation. The *GW* approximation is extended to multisubband low-dimensional systems to calculate the inelastic Coulomb scattering rate. The contributions of different scattering channels due to collective and single-particle excitations are analyzed. In comparison to the 2D case, the scattering due to single-particle excitations is suppressed in coupled biwires, but the optical and acoustic plasmons induce two sharp peaks in the scattering rate. Quantitative understanding of such relaxation processes in multisubband low-dimensional systems are meaningful for the successful realization of photoelectronic semiconductor nanodevices.

Acknowledgements

References

1. T. Ando, A. B. Fowler, and F. Stern, Rev. Mod. Phys. 54, 437 (1982).
2. *Physics of low-dimensional semiconductor structures*, Ed. P. Butcher, N.M. March, and M. P. Tosi, Plenum Press, New York (1993).
3. M. W. Cole, Rev. Mod. Phys. 46, 451 (1974).
4. G. D. Mahan, *Many-Particle Physics*, Plenum, New York, (1990).
5. A. Isihara, *Electron Liquids*, Springer-Verlag, Berlin (1998).
6. M.S. Kushwaha, Surf. Sci. Rep. 41, 1 (2001).
7. A. B. Fowler, F. F. Fang, W. E. Howard, and P. J. Stiles, Phys. Rev. Lett. 16, 901 (1966).
8. C. C. Grimes and G. Adams, Phys. Rev. Lett. 36 145 (1976).

9. S. J. Allen, D. C. Tsui, and R. A. Logan, Phys. Rev. Lett. 38, 980 (1977).

10. Olego, A. Pinczuk, A. C. Gossard, and W. Wiegmann, Phys. Rev. B. 25, 7867 (1982).

11. For a review, see, e.g., *One-dimensional Fermi liquids*, J. Voit, Rep. Prog. Phys. 58, 977 (1994).

12. A. R. Goñi, A. Pinczuk, J. S. Weiner, J. M. Calleja, B. S. Dennis, L. N. Pfeiffer, and K. W. West, Phys. Rev. Lett. 67, 3298 (1991); Q. P. Li and S. Das Sarma, Phys. Rev. B 43, 11768 (1991).

13. F. Perez, B. Jusserand, and B. Etienne, Physica E 7, 521 (2000).

14. D. W. Wang, A. J. Millis, and S. Das Sarma, Phys. Rev. Lett, 85, 4570 (2000).

15. S. Das Sarma and E.H. Hwang, Phys. Rev. B 59, 10730 (1999);

16. B.Y.-K. Hu and S. Das Sarma, Phys. Rev. Lett. 68,1750 (1992); Phys. Rev. B 48, 5469 (1993).

17. M. Bockrath, D.H. Cobden, J. Lu, et al. Nature 397, 598, (1999).

18. P. Segovia, D. Purdie, M. Hengsberger, and Y. Baer; Nature 402, 504, 1999).

19. B. Kramer and M. Sassetti, Phys. Rev. 62, 4238 (2000).

20. G. E Brown, *Many-Body Problems,* North-Holland, Amsterdam (1972).

21. F. Stern, p.177 in Ref. [2].

22. G.Q. Hai, P.M. Peeters, J. D. Devreese, and L. Wendler, Phys. Rev. B 48, 12016 (1993).

23. J. J. Hubbard, Proc. R. Soc. London A 243, 336 (1957).

24. K. S. Singwi, M. P. Tosi, R. H. Land, and A. Sjölander, Phys. Rev. 176, 589 (1968).

25. G.Q. Hai, N. Studart, G.E. Marques, Phys. Rev. B 55, 1554 (1997); and the references therein.

26. W. P. Chen, Y. J. Chen, and E. Burstein, Surf. Sci. 58, 263 (1976).

27. S. J. Allen, D. C. Tsui, and B. Vinter, Solid State Commun. 20, 425 (1976).

28. B. Vinter, Phys. Rev. B 13, 4447 (1976).

29. T. Ando, Z. Phys. B 26, 263 (1977).

30. S. Das Sarma and A. Madhukar, Phys. Rev. B 23, 805 (1981).

31. G. E. Santoro and G. Giuliani, Phys. Rev. B 37, 937 (1988); B 37, 8443 (1988).

32. J. K. Jain and S. Das Sarma, Phys. Rev. B 36, 5949 (1987).

33. D. S. Kainth, D. Richards, H. P. Hughes, M. Y. Simmons, and D. A. Ritchie, Phys. Rev. B 57, R2065 (1998)

34. D. S. Kainth et al. Phys. Rev. B 59, 2095 (1999).

35. L. Swierkowski, J. Szymanski, and Z.W. Gortel, Phys. Rev. Lett. 74, 3245 (1995).

36. B. Dong and X. L. Lei, J. Phys.: Condens. Matter 10, 7535 (1998).

37. L. Liu, L. Swierkowski, D. Nielson, and J. Szymanski, Phys. Rev. B 53, 7923 (1996).

38. C. Zhang, Phys. Rev. B 49, 2939 (1994).

39. N. Tzoar and C. Zhang, Phys. Rev. B 34, 1050 (1986).

40. B. Tanatar and B. Davoudi, Phys. Rev. B 63, 165328 (2001); B. Davoudi and B. Tanatar, Solid State Commun. 117, 89 (2001).

41. L. Liu, L. Swierkowski, and D. Nielson, Physica B 251, 937 (1998).

42. G. Kalman and K. I. Golden, Phys. Rev. B 57, 8834 (1998).

43. G. Kalman, V. Valtchinov, and K. I. Golden, Phys. Rev. Lett. 82, 3124 (1999).

44. J. Ortner, Phys. Rev. B 59, 9870 (1999).

45. S. Das Sarma and E. H. Hwang, Phys. Rev. Lett. 81, 4216 (1998).

46. M. R. S. Tavares, G. Q. Hai, and S. Das Sarma, Phys. Rev. B 64, 045325 (2001).

47. M. R. S. Tavares and G. Q. Hai, J. Phys.: Condensed Matter 13, 6421 (2001).

48. P. F. Williams and A. N. Bloch, Phys. Rev. B 10, 1097 (1974).

49. S. Das Sarma and W. Y. Lai, Phys. Rev. B 32, 1401 (1985).

50. J. M. Calleja, B. S. Dennis, A. Pinczuk, S. Schittrink, L. N. Pfeiffer, K. W. West, J. F. Muller, and A. E. Ruckestein, Surf. Sci. 263, 346 (1992).

51. W. Wegscheider, L. N. Pfeiffer, M. M. Dignam, A. Pinczuk, K. W. West, S. L. Mccall, and R. Hull, Phys. Rev. Lett. 71, 4071 (1999).
52. W.I. Friesen and B. Bergersen, J. Phys. C: Solid State Phys. 13, 6627 (1980).
53. A. Gold and A. Ghazali, Phys. Rev. B 41, 7626 (1990).
54. Q. P. Li and S. Das Sarma, Phys. Rev. B 43, 11768 (1991).
55. W.Y. Lai, A. Kobayashi, and S. Das Sarma, Phys. Rev. B 34, 7380 (1986).
56. G. Y. Hu and R. F. O'Connell, Phys. Rev. B 44, 3140 (1991).
57. L. Wang and A. R. Bishop, Phys. Rev. B 51, 7407 (1995).
58. M. Sassetti, F. Napoli and B. Bramer, Phys. Rev. B 59, 7297 (1999); A. Brataas, A. G. Mal'shukov, C. Steinebach, V. Gudmundsson, and K. A. Chao, Phys. Rev. B 55, 13161 (1997).
59. D. Agosti, F. Pederiva, E. Lipparini and K. Takayanagi, Phys. Rev. 57, 14869 (1998).
60. P. C. M. Machado, J. R. Leite, F. A. P. Osório, and A. N. Borges, Phys. Rev. B 56, 4128 (1997).
61. W. Que, Phys. Rev. B 43, 7127 (1991); W. Que and G. Kirczenow, Phys. Rev. 37, 7153 (1988).
62. J. X. Yu and J. B. Xia, Solid State Commun. 98 227 (1996). X. L. Lu, H. L. Cui, and N. J. M. Horing, Solid State Commun. 77, 331 (1996).
63. A. Latgé and J. d'Albuquerque e Castro, Phys. Rev. B 47, 4798 (1993).
64. A. Gold, Z. Phys. B 89, 213 (1992).
65. A. Messica, U. Meirav, H. Shtrikman, V. Umansky, and D. Mahalu, Phys. Rev. B 54 R5247 (1996).
66. J. G. Cordes and A. K. Das, Superlatt. Microstruct. 25, 1954 (1997).
67. T. Demel, D. Heitmann, P. Grambow and K. Ploog K, Phys. Rev. B 38, 12732 (1988); T. Demel, D. Heitmann, P. Grambow, and K. Ploog, Phys. Rev. Lett. 66, 2657 (1991).
68. S. Das Sarma and E. H. Hwang, Phys. Rev. B 59, 10730 (1999).
69. V. Shikin, T. Demel, and D. Heitmann, Phys. Rev. B 46, 3971 (1992).
70. J. S. Thakur and D. Neilson Phys. Rev. B 59, 4671 (1997).
71. N. Mutluay and B. Tanatar, Phys. Rev. B 55, 6697 (1997); A. Gold and L. Calmels, Phys. Rev. B 58, 3497 (1998).
72. B. Tanatar B 1996 Solid State Commun. 99, 1 (1996)
73. T. V. Shahbazyan and S. E. Ulloa, Phys. Rev. B 54 16749 (1996).
74. C. Eugster and J. A. del Alamo, Appl. Phys. Lett. 60 642 (1992); A. Bertoni, et al. Phys. Rev. Lett. 84, 5912 (2000).
75. G. Q. Hai and M. R. S. Tavares, Phys. Rev. B 61, 1704 (2000); J. B. Xia and G. Q. Hai, Phys. Rev. B 65, 245326 (2002).
76. L. Zheng and S. Das Sarma, Phys. Rev. B 54, 2751 (1996); P. Sotirelis, P. von Allmen, and K. Hess, *Phys. Rev. B.* 47, 12744 (1993).
77. Ref. 46 and the references therein.
78. S.-C. Lee and I. Galbraith, Phys. Rev. B 59, 15796 (1999).
79. R. Jalabert and S. Das Sarma, Phys. Rev. B 40, 9723 (1989).
80. L. Hedin, Phys. Rev. 139, A796 (1965); see also G. D. Mahan, *Many-Particle Physics,* Plenum, New York, (1990).
81. M. R. S. Tavares, S. Das Sarma, and G. Q. Hai, Phys. Rev. B. 63, 045324 (2001).
82. M. R. S. Tavares and G. Q. Hai, Phys. Rev. B 61, 7564 (2000).

Tunneling-assisted acoustic-plasmon–quasiparticle excitation resonances in coupled quasi-one-dimensional electron gases

Guo-Qiang Hai and Marcos R. S. Tavares

Instituto de Física de São Carlos, Universidade de São Paulo, 13560-970 São Carlos, SP, Brazil

We show that a weak nonresonant tunneling between two quantum wires leads to splitting of the acoustic plasmon mode at finite wave vector. Two gaps open up in the dipersion of the acoustic plasmon mode when its frequency is close to the frequencies of the quasiparticle excitations. In contrast to the Landau damping of the collective excitations, these gaps are attributed to tunneling-assisted acoustic plasmon–quasiparticle excitation resonances. We predict that such a resonance can be observed in inelastic light scattering spectrum.

The plasmons of coupled low-dimensional electron gas systems provide a valuable platform to study the electronic many-body effects. In coupled double one-dimensional (1D) electron quantum wires, similarly to coupled two-dimensional electron systems,[1] optical and acoustic plasmon modes[2-4] were found. They were interpreted, respectively, as in-phase and out-of-phase oscillations of the electron charge density in the two wires. Theoretical studies[3-10] have been done on the plasmon dispersions, electron-electron correlation, far-infrared absorption, Coulomb drag, and tunneling effects in these systems. Correlation induced instability[8,9] of the collective modes were predicted in coupled low-density quantum wires. Experimentally, far-infrared spectroscopy and Raman scattering were used to detect the collective excitations.[2,11] Very recently, it was shown that a weak resonant tunneling in the coupled two 1D electron gases leads to a plasmon gap in the acoustic mode at zero wave vector.[3]

In this paper, we report a theoretical study of the effects of weak tunneling on the collective excitations in coupled quasi-1D electron gases. Tunneling between quantum wires can modify the collective behavior of the electron systems in several aspects. Interwire charge transfer and intersubband scattering become possible through the tunneling. As a consequence, new plasmon modes and coupling between different modes appear. On the other hand, intersubband interaction leads to intersubband quasiparticle excitations. We expect the tunneling will mainly affect the acoustic plasmon mode because its polarization field is localized in the space between the two wires where the tunneling occurs. Our numerical results of paramount importance show that a weak nonresonant tunneling between the wires produces two gaps in the acoustic plasmon mode at finite wave vector q. These gaps are attributed to the *tunneling-assisted acoustic plasmon–quasiparticle excitation resonances*. It means that, in contrast to the Landau damping of plasmon modes, a resonant scattering occurs between the collective plasmon excitation and the *intersubband quasiparticle excitation* through tunneling. Such a resonance leads to splitting of the acoustic plasmon mode around the quasiparticle excitation region and, consequently, a double-peak structure in the corresponding inelastic light-scattering spectrum.

We consider a two-dimensional system in the xy plane subjected to an additional confinement in the y direction, which forms two quantum wires parallel to each other in the x direction. The confinement potential in the y direction is taken to be of square well type of height V_b and widths W_1 and W_2 representing the first and the second wire, respectively. The potential barrier between the two wires is of width W_b. The subband energies E_n and the wave functions $\phi_n(y)$ are obtained from the numerical solution of the one-dimensional Schrödinger equation in the y direction. We restrict ourselves to the case where $n=1,2$ and define $\omega_0 = E_2 - E_1$ as being the gap between the two subbands. The interpretation of the index n depends on tunneling between the two wires. When there is no tunneling, n is wire index. On the opposite, when the wires are in resonant tunneling condition, n is subband index.

The dispersions of the plasmon modes are obtained by the poles of the density-density correlation function, or equivalently by the zeros of the determinant of the dielectric matrix $\det|\varepsilon(\omega,q)|=0$ within the random-phase approximation (RPA). The RPA has been proved a successful approximation in studying the collective charge excitations of Q1D electron gas by virtue of the vanishing of all vertex corrections to the 1D irreducible polarizability.[3] Figure 1 shows the plasmon dispersions of the coupled GaAs/Al$_{0.3}$Ga$_{0.7}$As ($V_b = 228$ meV) quantum wires in (a) resonant tunneling and (b) nonresonant tunneling. The numerical results, with tunneling effects, of the in-phase (optical) ω_+ and out-of-phase (acoustic) ω_- modes are presented by the thin-solid and thick-solid curves, respectively. For a comparison, the in-phase (out-of-phase) plasmon modes without tunneling are plotted in the thin-dashed (thick-dashed) curves. In Fig. 1(a), we observe that, in resonant tunneling, the out-of-phase mode losses its acoustic characteristic at small q replaced by two intersubband modes. In Fig. 1(b), for the two wires out of resonant tunneling, we find that 99.4% of the electrons in the lowest (second) subband are localized in the wide (narrow) quantum wire. In other words, each quantum wire of the 1D electron gas only has a small edge in the other. However, such an edge affects significantly the acoustic plasmon mode. Two gaps open up around the intersubband quasiparticle excitation region.

The dynamical dielectric function is given by $\varepsilon_{nn',mm'}(\omega,q) = \delta_{nm}\delta_{n'm'} - V_{nn',mm'}(q)\Pi_{nn'}(q,\omega)$, where δ_{nm} is the Kronecker δ function, $V_{nn',mm'}(q)$ the bare electron-electron Coulomb interaction potential, and $\Pi_{nn'}(\omega,q)$ the 1D polarizability.[3,12] Within the RPA, $\Pi_{nn'}(\omega,q)$ is taken as the non-interacting irreducible polar-
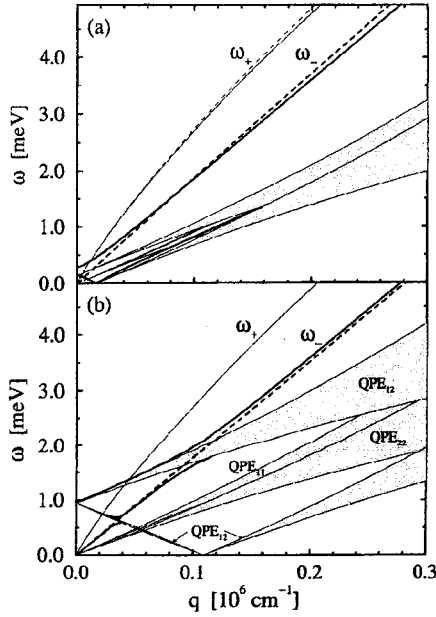
FIG. 1. Plasmon dispersions in two coupled GaAs/Al$_{0.3}$Ga$_{0.7}$As (V_b=228 meV) quantum wires separated by a barrier of width W_b=70 Å of (a) W_1=W_2=150 Å and (b) W_1=150 Å and W_2 =145 Å. The total electron density N_e=10^6 cm^{-1}. The solid (dash) curves present the plasmon dispersions with (without) tunneling. The thin and thick curves indicate the in-phase (ω_+) and out-of-phase (ω_-) plasmon modes, respectively. The shadow area presents the quasiparticle excitation regions QPE$_{nn'}$.

izability function for a clean system free from any impurity scattering. In the presence of impurity scattering, we use Mermin's formula[13] including the effect of level broadening through a phenomenological damping constant γ. The electron-electron interaction potential $V_{nn',mm'}(q)$ describes two-particle scattering events.[12,14] There are different scattering processes in the coupled quantum wires: (i) Intrawire (intrasubband) interactions $V_{11,11}(q)=V_A$,$V_{22,22}(q)=V_B$, and $V_{11,22}(q)=V_{22,11}(q)=V_C$ representing the scattering in which the electrons keep in their original wires (subbands); (ii) Interwire (intersubband) interactions $V_{12,12}(q)$ $=V_{21,21}(q)=V_{12,21}(q)=V_{21,12}(q)=V_D$ representing the scattering in which both electrons change their wire (subband) indices; and (iii) Intra-interwire (subband) interactions $V_{11,12}(q)=V_{11,21}(q)=V_{12,11}(q)=V_{21,11}(q)=V_J$ and $V_{22,12}(q)=V_{22,21}(q)=V_{12,22}(q)=V_{21,22}(q)=V_H$ indicating the scattering in which only one of the electrons suffers the interwire (intersubband) transition. Notice that, when there is no tunneling, $V_D=V_H=V_J=0$. Clearly, they are responsible for tunneling effects on the collective excitations.

When the tunneling is considered, the plasmon dispersions of two coupled quantum wires are determined by the equation,

$$F_1F_2 - [(1-V_A\Pi_{11})V_H^2\Pi_{22}+(1-V_B\Pi_{22})V_J^2\Pi_{11}$$

$$-2V_CV_JV_H\Pi_{11}\Pi_{22}](\Pi_{12}+\Pi_{21})=0, \qquad (1)$$

where $F_1=(1-V_A\Pi_{11})(1-V_B\Pi_{22})-V_C^2\Pi_{11}\Pi_{22}$ and F_2 $=1-V_D(\Pi_{12}+\Pi_{21})$. This equation consists of two terms: F_1F_2 and the rest. We know that tunneling introduces the Coulomb scattering potential V_D,V_J, and V_H. However, for

two symmetric quantum wires in resonant tunneling, V_J and V_H vanish and, consequently, the second term in Eq. (1) is zero. So, the plasmon modes are determined by equations $F_1=0$ and $F_2=0$. The latter carries the information of tunneling effects resulting in two out-of-phase (intersubband) modes as shown in Fig. 1(a). To reveal the relative importance of the different plasmon modes, we performed a numerical calculation of the oscillator strength defined by $\pi\{|\partial(\det|\varepsilon|)/\partial\omega|_{\omega=\omega_\pm}\}^{-1}$. It was found that the higher frequency out-of-phase plasmon mode is of finite oscillator strength at $q=0$. But the lower one has a very small oscillator strength and is unimportant.[14]

When the two wires are out of resonant tunneling, the out-of-phase plasmon mode changes dramatically at small q as shown in Fig. 1(b). It restores the acoustic behavior at q $\rightarrow 0$ but develops two gaps at finite q. The splitting of the acoustic plasmon mode occurs when its frequency is close to the frequencies of the intersubband quasiparticle excitations QPE$_{12}$. In this case, the small overlap between the wave functions of the two subbands leads to V_A,V_B, and V_C $\gg V_D,V_J$ and V_H. It means that the F_1 in Eq. (1) is now responsible for the main features of both the optical and acoustic plasmon modes. A numerical test indicates that the roots of the equation $F_1=0$ can almost recover the optical and acoustic plasmon dispersions of which tunneling is not considered. Whereas, the part F_2 relating to possible intersubband plasmon becomes less important. We also notice that V_D does not appear in the coupling term in Eq. (1). So, the potentials V_J and V_H are responsible for the splitting of the acoustic plasmon mode. These interactions represent the electron-electron scattering during which only one of them experiences intersubband transition. When the momentum and energy transfer between the two electrons occur in the region QPE$_{12}$, only this electron creates an intersubband electron-hole pair. From this point of view, the momentum and energy conservation in the scattering leads to such a transition getting rid of the Landau damping. In other words, the intra-intersubband scattering V_J and V_H produce a resonance between the collective excitation and the quasiparticle excitation. From another point of view, the scattering V_J and V_H result in a net charge transfer between the wires. Thus, they produce a local electric field between the two wires and disturb the polarization field of the acoustic plasmon mode. The energy gaps in the acoustic plasmon mode are dependent
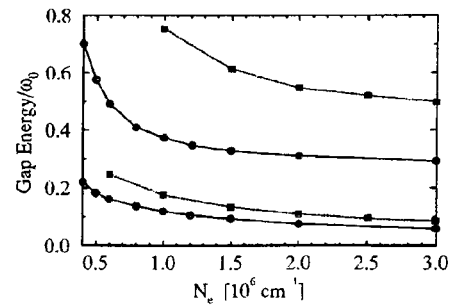

FIG. 2. The normalized gap energies as a function of the total electron density in the coupled GaAs/Al$_{0.3}$Ga$_{0.7}$As quantum wires of (a) W_1=150 Å, W_2=145 Å, and W_b=70 Å (solid circles with ω_0=0.94 meV); and (b) W_1=150 Å, W_2=140 Å, and W_b =50 Å (solid squares with ω_0=2.01 meV).
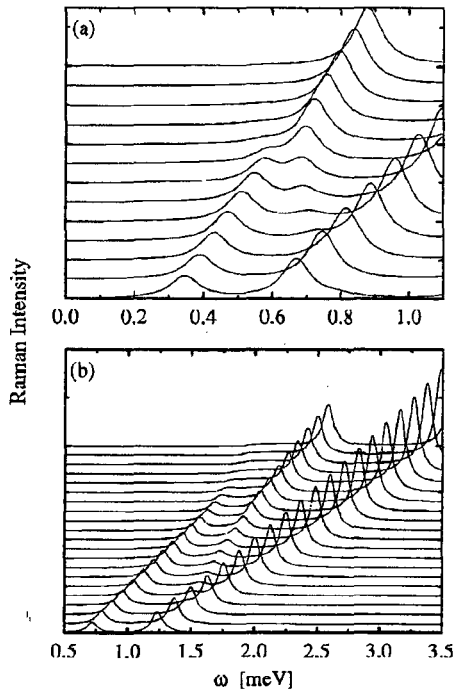
FIG. 3. Raman scattering spectra in the coupled quantum wires with $W_1 = 150$ Å, $W_2 = 145$ Å, and $W_b = 70$ Å at different q: (a) from 2 to 5×10^4 cm^{-1} with equivalent difference $\Delta q = 0.25 \times 10^4$ cm^{-1}, and (b) from 0.4 to 1.4×10^5 cm^{-1} with $\Delta q = 0.05 \times 10^5$ cm^{-1}. $N_e = 10^6$ cm^{-1} and $\gamma = 0.05$ meV. The intensity in (a) is enlarged 4 times as compared to (b). The different curves are offset for clarity.

on the electron density and tunneling strength. We can define the gap as the frequency difference between the lower and upper branch of the split mode at the q where the unperturbed acoustic plasmon frequency is in the center of the quasiparticle excitation region. In Fig. 2, we show the electron density dependence of the two gaps normalized by ω_0 in different structures. The energies of the two gaps decrease with increasing the total electron density. One also sees that, for smaller barrier width, the plasmon gaps become larger.

The plasmon modes in the coupled quantum wires can be observed in the Raman spectroscopy. The intensity of the Raman scattering is proportional to the imaginary part of the screened density-density correlation function with a weight reflecting the coupling between the light and different plasmon modes.[14,15] Figure 3 shows the calculated Raman spectra due to the plasmon scattering of the corresponding modes in Fig. 1(b) around (a) the lower and (b) the higher energy gap. In the calculation, we took the damping constant $\gamma = 0.05$ meV corresponding to a sample with electron mobility in order of 5×10^5 cm^2/Vs. We see a strong Raman scattering peak at high frequencies due to the optical plasmons.
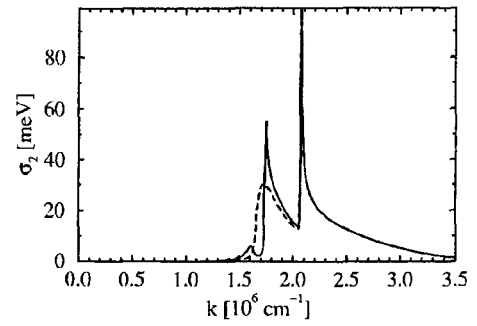
FIG. 4. Inelastic Coulomb scattering rate $\sigma_n(k)$ in the narrower one ($n = 2$) of the coupled quantum wires corresponding to Fig. 1(b). The solid and dashed curves present the results with and without tunneling, respectively.

Besides, there are two split peaks due to the acoustic plasmons. With increasing q, the spectral weight transfers from the lower to the higher frequency one.

Finally, we show the effects of the weak nonresonant tunneling on the inelastic Coulomb scattering rate $\sigma_n(k)$ of an injected electron in the wire n with momentum k. The inelastic Coulomb scattering rate was obtained by the imaginary part of the electron self-energy within the GW approximation.[14,16] In Fig. 4, we plot $\sigma_n(k)$ of an electron in the narrower quantum wire ($n = 2$) of the coupled wire system corresponding to Fig. 1(b). When the tunneling is not included, the lower and higher scattering peaks are resulted from the emission of the acoustic and optical plasmons, respectively. The weak tunneling influences its k-dependent behavior and leads to a splitting of the lower scattering peak in $\sigma_2(k)$, corresponding to the splitting of the acoustic plasmon mode.

In summary, we have studied the effects of weak tunneling on the collective excitations in two coupled quantum wires. We show that a weak nonresonant tunneling between the wires leads to the splitting of the acoustic plasmon mode. Two gaps open up in the dispersion of the acoustic plasmon mode. In contrast to the Landau-damping mechanism of the collective excitations, our result gives an evidence that the resonant coupling between the collective excitations and the quasiparticle excitations occurs in coupled quantum wires through tunneling. Furthermore, we predict that such a resonance can be observed in the inelastic light-scattering spectrum. Besides the optical plasmon scattering, a double peak structure appears around the quasiparticle excitation regime due to the split acoustic plasmon modes. The splitting of the acoustic plasmon mode also influences other electronic properties of the system, for instance, the Coulomb inelastic-scattering rate.

[1] D.S. Kainth, D. Richards, H.P. Hughes, M.Y. Simmons, and D.A. Ritchie, Phys. Rev. B **57**, R2065 (1998); S. Das Sarma and E.H. Hwang, Phys. Rev. Lett. **81**, 4216 (1998), and references therein; D. Grecu, Phys. Rev. B **8**, 1958 (1973).

[2] T. Demel, D. Heitmann, P. Grambow, and K. Ploog, Phys. Rev. B **38**, 12 732 (1988).

[3] S. Das. Sarma and E.H. Hwang, Phys. Rev. B **59**, 10 730 (1999); Q.P. Li and S.Das Sarma, *ibid.* **43**, 11 768 (1991); C. Steine-

bach, D. Heitmann, and V. Gudmundsson, *ibid.* **58**, 13 944 (1998).

[4] V. Shikin, T. Demel, and D. Heitmann, Phys. Rev. B **46**, 3971 (1992); W. Que and G. Kirczcenow, *ibid.* **37**, 7153 (1988).

[5] J.S. Thakur and D. Neilson, Phys. Rev. B **56**, 4671 (1997).

[6] T.V. Shahbazyan and S.E. Ulloa, Phys. Rev. B **54**, 16 749 (1996).

[7] B. Tanatar, Solid State Commun. **99**, 1 (1996).

[8] A. Gold, Philos. Mag. Lett. **66**, 163 (1992).

[9] Z. Wu and P.P. Ruden, J. Appl. Phys. **74**, 6234 (1993); **71**, 1318 (1992).

[10] C. Steinebach, D. Heitmann, and V. Gudmundsson, Phys. Rev. B

56, 6742 (1997).

[11] C. Schüller *et al.*, Phys. Rev. B **54**, R17 304 (1996).

[12] F. Prengel and E. Schöll, Phys. Rev. B **59**, 5806 (1999); G.-Q. Hai, F.M. Peeters, J.T. Devreese, and L. Wendler, *ibid.* **48**, 12 016 (1993).

[13] N.D. Mermin, Phys. Rev. B **1**, 2362 (1970),

[14] Marcos R. S. Tavares and G.-Q. Hai (unpublished).

[15] G.-Q. Hai, N. Studart, and G.E. Marques, Phys. Rev. B **57**, 2276 (1998).

[16] B.Y.-K. Hu and S. Das Sarma, Phys. Rev. B **48**, 5469 (1993); P. Sotirelis, P. von Allmen, and K. Hess, *ibid.* **47**, 12 744 (1993).

Collective and single-particle excitations in coupled quantum wires in magnetic fields

J.-B. Xia

Instituto de Física de São Carlos, Universidade de São Paulo, São Carlos, SP 13560-970, Brazil
and National Laboratory for Superlattices and Microstructures, Institute of Semiconductors, Chinese Academy of Sciences,
Beijing 100083, China

G.-Q. Hai

Instituto de Física de São Carlos, Universidade de São Paulo, São Carlos, SP 13560-970, Brazil

The full spectra of magnetoplasmons and single-particle excitations are obtained of coupled one-dimensional electron gases in parallel semiconductor quantum wires with tunneling. We show the effects of the interwire Coulomb interaction and the tunneling, as well as the magnetic-field-induced localization on the elementary excitations in symmetric and asymmetric coulped quantum wire structures. The interacton and resonance between the plasmon and the intersubband single-particle excitations are found in magnetic fields.

I. INTRODUCTION

In coupled quantum wires, the Coulomb interaction between one-dimensional electron gases leads to the so-called optical and acoustic plasmon modes.[1] Tunneling between the wires modifies these plasmon modes, especially the acoustic one.[2–4] When an asymmetry is introduced between the two wires, a very weak nonresonant tunneling opens up gaps in the acoustic plasmon mode resulting from a resonance between the acoustic plasmon and single-particle excitations. A transverse magnetic field in such systems affects the tunneling strength and also the single-particle and collective excitations.[5,6] In Refs. 5 and 6 the far-infrared absorption spectra due to the intersubband (transverse) magnetoplasmon modes are calculated with and without tunneling between the wires. In such a spectrum, only the plasmon excitations at long wavelength limit ($q \to 0$) contribute to the absorption. To observe the absorption peaks result from the so-called intersubband plasmon modes, a four-subband model was used in their calculations (two subbands originated from each wire). The enhancement due to interwire exchange interaction of the tunneling gap between the symmetric and antisymmetric states was included in the calculation in Ref. 5, and three peaks were found in the absorption spectrum. They were attributed to the intersubband optical and acoustic plasmon modes (from the lowest symmetric state to first excited symmetric and antisymmetric states, respectively). However, no information was given for the intersubband plasmon mode due to tunneling induced two lowest subbands (the lowest symmetric and antisymmetric states). In Ref. 6 the tunneling effect was considered only for the two higher subbands, and the calculation was performed in the small-magnetic-field limit. One intersubband magnetoplasmon absorption peak from the ground state (no tunneling effect) to the higher empty states were found. It was also shown that a small magnetic field could induce a Landau damping of this plasmon mode. However, a clear overall picture of the single-particle and magnetoplasmon excitations in the system of coupled quantum wires has not been obtained so far. A similar situation occurs for these excita-

tions in coupled quantum wells in a parallel magnetic field. Magnetoplasmons were studied in double quantum wells in a parallel magnetic field where the tunneling was included within only the lowest order of perturbation.[7]

The presence of a transverse magnetic field in couple quantum wires leads to the motion of the electrons in the wire direction being coupled to that in the lateral direction. The single-electron wave function in the lateral direction depends on the wave vector k in the wire direction. If we proceed in the standard manner of linear-response theory to derive the dispersion relation of the magnetoplasmons, we would have to solve a secular equation with infinite dimensions according to the wave vector k. This leads to difficulties in the calculations even within the random-phase approximation (RPA). In this work, the magnetoplasmon dispersions are obtained by projecting the electron states of the coupled wires to a basis constructed by the states of corresponding single wires. We show the effects of the tunneling strength and the magnetic-field-induced localization on the plasmon modes in such systems. We find a strong interaction between the collective modes and the single-particle excitations induced by transverse magnetic fields and tunneling.

II. THEORETICAL FORMALISM

We consider two coupled parallel quantum wires in the xy plane subjected a transverse magnetic field **B** in the z-direction. The quantum wires are of zero thickness in the z direction. The confinement potential $V(y)$ in the y direction forms two quantum wires parallel to each other in the x direction. It is taken as square well type of widths W_1 and W_2 and barrier height V_b. The potential barrier between the two wires is of width W_b. The numerical calculation is applied to GaAs/Al$_{0.3}$Ga$_{0.7}$As structures with $V_b = 228$ meV.

The plasmon modes in such a system in the absence of magnetic field were studied in our previous work.[2,3] However, a magnetic field in the z direction strongly affects the

single-particle and collective excitations, as will be shown below. The single-electron Hamiltonian in the present system can be written as

$$H_e = \frac{1}{2m^*}\left[p_x^2 + p_y^2 + \left(\frac{eB}{c}\right)^2\left(y - \frac{c\hbar k}{eB}\right)^2 \right] + V(y), \quad (1)$$

where k is the electron wavevector in the x direction, m^* the electron effective mass, and e the electron charge. The above equation indicates that the effect of an external magnetic field is equivalent to an additional parabolic potential in the y direction, whose origin depends on the wave vector k and the magnetic field B. The eigenenergy and wave function in the y direction are functions of k noted by $E_n(k)$ and $\psi_{n,k}(y)$. We consider symmetric and also asymmetric two coupled wires with tunneling. The asymmetry is introduced by the different wire widths $W_1 \neq W_2$ and the tunneling strength is controlled by the barrier thickness between the wires. For the considered structures the excited states are much higher than the ground states of the two coupled wires. We restrict ourselves to the case of two ground states $n = 1$ and 2. For two symmetric quantum wires, the wave functions $\psi_{n,k}(y)$ at $k = 0$ are symmetric ($n = 1$) and antisymmetric ($n = 2$) functions of y. For nonzero k, the wave function $\psi_{1,k}(y)$ shifts to one wire, while $\psi_{2,k}(y)$ to the other.

The screened Coulomb potential within the RPA is determined by the following self-consistent equation,

$$V^{sc}_{\alpha k, \beta k'}(q,\omega) = V^{C}_{\alpha k, \beta k'}(q) + \sum_{\gamma k''} V^{C}_{\alpha k, \gamma k''}(q)$$

$$\times \Pi^{(0)}_{\gamma k''}(q,\omega) V^{sc}_{\gamma k'', \beta k'}(q,\omega), \quad (2)$$

with the bare Coulomb potential

$$V^{C}_{\alpha k, \beta k'}(q) = \frac{2e^2}{\varepsilon_0} \int dy \int dy' \, \psi_{nk}(y) \psi_{n'k-q}(y)$$

$$\times K_0(q|y - y'|) \psi_{m'k'+q}(y') \psi_{mk'}(y') \quad (3)$$

and

$$\Pi^{(0)}_{\beta k'}(q,\omega) = \frac{f[E_{m'}(k)] - f[E_m(k-q)]}{E_{m'}(k) - E_m(k-q) + \hbar(\omega + i0^-)}, \quad (4)$$

where the indices $\alpha = \{n, n'\}$, $\beta = \{m, m'\}$, and $\gamma = \{l, l'\}$ represent pairs of the quantum numbers, and $f(E)$ is the Fermi distribution function.

In principle, the dispersion relation of the collective excitations can be obtained by the secular equation of the screened Coulomb potential defined by Eq. (2). However, it depends not only on the indices α and β but also on the wave vectors k and k' leading to a dielectric matrix of infinite dimensions which is not "properly" convergent in that a truncated submatrix with a finite dimension. For a system with a parabolic confinement potential, such as a single parabolic quantum well (wire) in a parallel (transverse) magnetic field, this difficulty was overcome by expanding the k-dependent wave function as a series of harmonic function so that the dielectric function is projected in a finite
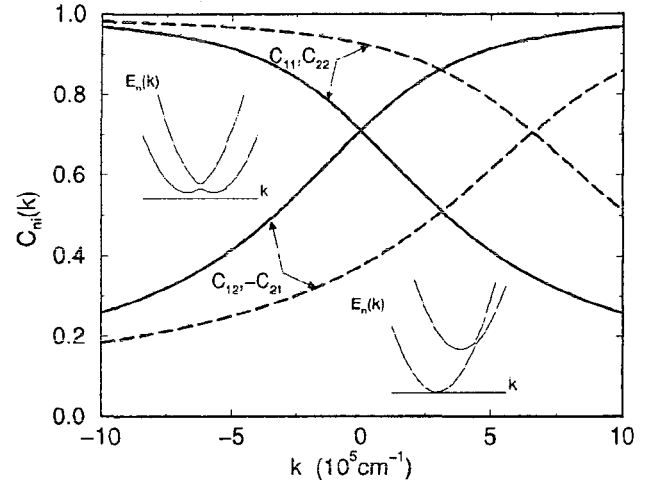

FIG. 1. The coefficients $C_{ni}(k)$ ($n,i = 1$ and 2) at $B = 1$ T for the symmetric (asymmetric) coupled quantum wires of $W_1 = W_2 = 150$ Å ($W_1 = 150$ Å, $W_2 = 140$ Å) and $W_b = 30$ Å are plotted by the solid (dashed) curves. The dispersion relations of a single-electron in the symmetric (asymmetric) structure are indicated in the left (low) inset.

submatrix.[8,9] In this work, however, we choose another basis for our system of the coupled quantum wires. We consider the two quantum wires independently, and find the electron states in the single wires as a basis $\phi_i(y)$. The wave function $\psi_{nk}(y)$ of the coupled wires is expanded in this basis according to the k states. As will be shown below, we find it is enough to include only the ground states of the two single wires,

$$\psi_{nk}(y) = \sum_{i=1,2} C_{ni}(k) \phi_i(y), \quad (5)$$

where $i = 1$ and 2 represent the ground states of the single wires W_1 and W_2, respectively. The coefficients $C_{ni}(k)$ are shown as the solid curves in Fig. 1 for symmetric structures of $W_1 = W_2 = 150$ Å and $W_b = 30$ Å at $B = 1$ T. The dispersion relations of the two subbands are schematically indicated in the inset on the left. At $k = 0$, the expansion coefficients cross and their absolute values are $1/\sqrt{2}$, i.e., the electrons are distributed equally in the two wires. For large $|k|$, their absolute values approach to 1 or 0, indicating a magnetic-field-induced localization. The magnetic field pushes the electrons with $k < 0$ in the $n = 1$ ($n = 2$) subband to the left wire W_1 (the right wire W_2). For those electrons with $k > 0$, the magnetic field has the opposite effect. The expansion coefficients satisfy approximately the equation $\Sigma_{i=1,2} C^2_{ni}(k) = 1$ within a numeric error $< 0.5\%$, indicating that the basis functions $\phi_1(y)$ and $\phi_2(y)$ are orthogonal and almost complete. For the asymmetric structure with $W_1 = 150$ Å, $W_2 = 140$ Å, and $W_b = 30$ Å at $B = 1$ T, the coefficients $C_{ni}(k)$ are given by the dashed curves. They cross at $k = 6.6 \times 10^5$ cm^{-1}, where the anticrossing of the two subbands occurs as indicated by the lower inset in the figure.

With such an expansion, both the Coulomb potential $V^C_{\alpha k,\beta k'}(q)$ and the screened potential $V^{sc}_{\alpha k,\beta k'}(q,\omega)$ can be written in the form

$$V_{\alpha k,\beta k'} = \sum_{\xi,\eta} S_{\alpha k,\xi} S_{\beta k',\eta} v_{\xi,\eta},$$

where $\xi = \{i,i'\}$ and $\eta = \{j,j'\}$ indicate pairs of the quantum numbers in our basis, and $S_{\alpha k,\xi} = C_{ni}(k-q)C_{n'i'}(k)$. As a consequence, Eq. (2) reduces to

$$\sum_{\eta'} \left(\delta_{\xi,\eta'} - \sum_{\xi'} v^C_{\xi,\xi'}(q)\Pi_{\xi',\eta'}(q,\omega) \right) v^{sc}_{\eta',\eta}(q,\omega)$$

$$= v^C_{\xi,\eta}(q).$$

The dispersion relations of the magnetoplasmon excitations can be obtained by the equation

$$\text{Det}\left\{ \delta_{\xi,\eta} - \sum_{\xi'} v^C_{\xi,\xi'}(q)\Pi_{\xi',\eta}(q,\omega) \right\} = 0, \qquad (6)$$

where

$$v^C_{\xi,\eta}(q) = \frac{2e^2}{\varepsilon_0} \int dy \int dy' \, \phi_i(y)\phi_{i'}(y)$$

$$\times K_0(q|y-y'|)\phi_j(y')\phi_{j'}(y') \qquad (7)$$

and

$$\Pi_{\xi,\eta}(q,\omega) = \sum_{mm',k} C_{m'i}(k+q)C_{mi'}(k)$$

$$\times C_{mj}(k)C_{m'j'}(k+q)\Pi^{(0)}_{\beta k}(q,\omega). \qquad (8)$$

III. NUMERICAL RESULTS AND DISCUSSIONS

Figure 2 shows the magnetoplasmon and the single-particle excitation (SPE) spectra of the two coupled symmetric quantum wires of $W_1 = W_2 = 150$ Å with a total electron density $N_e = 10^6$ cm^{-1}. The intrasubband (intersubband) SPE continua are indicated by the dark (light) shadow areas. Figures 2(a), 2(b), and 2(c) show structures of $W_b = 30$ Å with different transverse magnetic fields $B = 0$, 1, and 2 T, respectively. In this structure, the tunneling-induced energy gap between the two subbands at zero magnetic field is $\Delta = 1.7$ meV. Figure 2(d) is for the structure of $W_b = 70$ Å at magnetic field $B = 1$ T. In this case, $\Delta = 0.14$ meV at zero magnetic field indicating a much weaker tunneling.

The plasmon and SPE spectra at zero magnetic field as shown in Fig. 2(a) are similar to those of a single symmetric quantum wire with two occupied subbands. Two intrasubband (solid curves) and two intersubband plasmon modes (dash curves) are found, as discussed in Ref. 3. The symmetry of the system and the parabolicity of the subbands ensure that the intrasubband modes do not couple to the intersubband ones.

The transverse magnetic field pushes the electrons with $k<0$ ($k>0$) in the $n=1$ and 2 ($n=2$ and 1) subbands to the W_1 and W_2 wires, respectively, affecting the tunneling
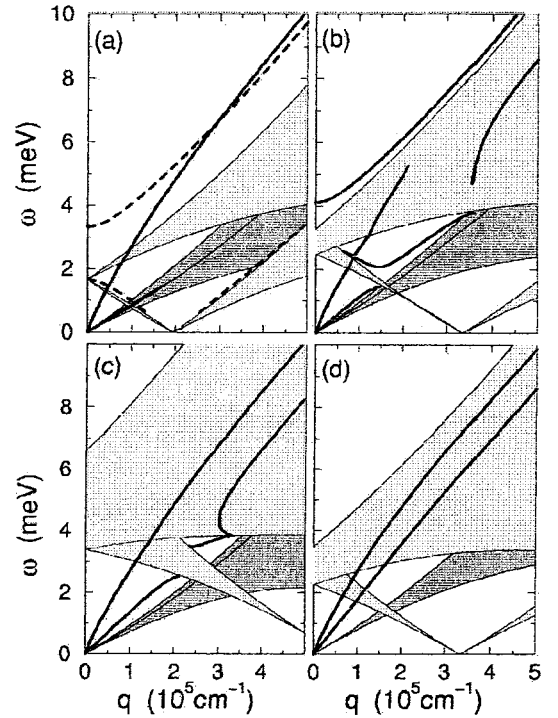

FIG. 2. The plasmon dispersions (thick curves), the intrasubband SPE (dark shadow), and the intersubband SPE (light shadow) continua in the symmetric coupled quantum wire structures of $W_1 = W_2 = 150$ Å and $W_b = 30$ Å at different magnetic fields (a) $B = 0$, (b) $B = 1$ T and (c) $B = 2$ T. The results for the structure of $W_1 = W_2 = 150$ Å and $W_b = 70$ Å at $B = 1$ T are presented in (d). The total electron density $N_e = 10^6$ cm^{-1}.

strength between the wires. In k space, the magnetic field leads to the two original parabolic subbands at $B = 0$ shifting to the opposite directions and the tunneling leads to an anticrossing in the dispersion of the two subbands which is schematically shown in the left inset in Fig. 1. As a consequence, the intersubband SPE region is expanded, developing a band at $q = 0$. The magnetic field and tunneling-induced nonparabolicity in the subband dispersion results in interactions between the single-particle and the collective excitations. Such interactions are represented by the electron-electron scattering events during which only one of the electrons experiences an intersubband transition. When the momentum and energy transfer between the two electrons occurs in the intersubband SPE region, only one of the electrons creates an *intersubband* electron-hole pair, leading to charge tunneling between the wires due to the fact that the transverse magnetic field pushes the electron and the hole to opposite directions. On the other hand, the momentum and energy conservation guarantee the collective excitation due to such transitions, eliminating the so-called "Landau damping." A resonance between the plasmon and the single-particle excitations occurs. Note that the interaction strength depends on the momentum transfer q. Figures 2(b) and 2(c) show the effects of these interactions on the magnetoplasmon modes at $B = 1$ and 2 T, respectively. At $B = 1$ T (corresponding to a cyclotron frequency $\omega_c = 1.65$ meV being close to $\Delta = 1.7$ meV), tunneling is relatively strong, and so is the interaction between
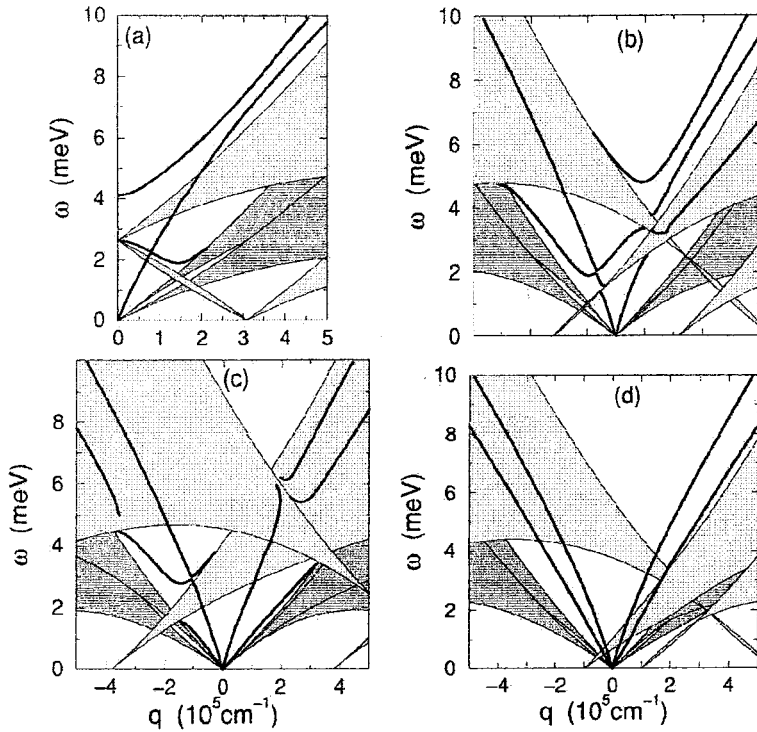
FIG. 3. The same as in Fig. 2, but now for the asymmetric structures with $W_1 = 150$ Å and $W_2 = 140$ Å.

the plasmon modes and the *intersubband* single-particle excitations. Figure 2(b) demonstrates this interaction, leading to (i) the high branch of the plasmon mode (above the intersubband SPE region and originally from the intersubband mode) keeping a distance from the SPE and (ii) a breaking at a certain energy of the plasmon mode in the *intersubband* SPE region. A larger transverse magnetic field leads to a strong localization of the electrons in each wire. The plasmon excitations restore their dispersion relation of two different modes, i.e., the optical and acoustic modes. Such a behavior is clearly seen in Figs. 2(c) and 2(d). In Fig. 2(c) the lower branch plasmon mode, i.e., the acoustic one, is still strongly modified due to its interaction with the intersubband SPE, showing a splitting when it approaches the SPE region at low frequencies. A magnetic field of 1 T for the structure with the larger barrier thickness of 70 Å is strong enough to suppress intersubband transitions completely, as indicated in Fig. 2(d), where the overlap of the electron wavefunctions of different subbands vanishes and so does the strength of the intersubband SPE.

Figure 3 shows the magnetoplasmon modes and the SPE spectra in two coupled asymmetric quantum wires. Comparing to Fig. 2(a), both the intersubband SPE and the plasmons in Fig. 3(a) shift to higher frequencies at small q because the energy gap between the two subbands increases to $E_2 - E_1 = 2.6$ meV by reducing the wire width W_2 to 140 Å. Although, at zero magnetic field, the asymmetry of the electron wave functions in real space leads to an anticrossing of the two high-frequency plasmon modes, as shown in Fig. 3(a), the electron states are symmetric in k space. However, a transverse magnetic field breaks the symmetry of the single-electron states in the k space, as indicated in the lower inset in Fig. 1. The electron gas has different Fermi wave vectors

for $k > 0$ and $k < 0$. Consequently, the plasmon dispersions and the SPE spectra are no longer symmetric functions of q. The asymmetric and nonparabolic subband structures leading to a strong coupling between the intersubband SPE and the plasmon modes are shown in Figs. 3(b) and 3(c). Figure 3(b) shows basically three plasmon modes in a V shape, but the electron-electron interaction results in an anticrossing and an even breaking up of these modes. The two branches with minima at $q = 0.95 \times 10^5$ and -0.97×10^5 cm^{-1}, respectively, are essentially intersubband modes. The one with $\omega = 0$ at $q = 0$ is an intrasubband (optical) plasmon mode. However, for $q > 1 \times 10^5$ cm^{-1}, the plasmon modes are strongly coupled to each other and also strongly interact with the intersubband SPE's. An anticrossing appears between the two higher branches. Moreover, the two lower branches break up at around $q = 1.2 \times 10^5$ cm^{-1}. At a larger magnetic field, the highest intersubband plasmon mode disappears, as shown in Fig. 3(c) but a lower-frequency intrasubband mode appears at small q which will eventually evolve into the so-called acoustic plasmon mode at large magnetic fields. Figure 3(d) shows the plasmon dispersions and the SPE spectra for the two coupled asymmetric quantum wires with $W_b = 70$ Å. In this case, the electrons in two different subbands are completely localized in different wires with a vanishing tunneling strength. An external magnetic field of 1 T almost does not affect the plasmon dispersion, which keeps its symmetry with respect to $q = 0$ as it is at zero magnetic field. Note that the intersubband SPE in this case is of a vanishing strength which has no effects on the plasmon modes.

IV. SUMMARY

In conclusion, the effects of a transverse magnetic field on single-particle and collective excitations are studied in

coupled quantum wires with tunneling. The magnetoplasmon spectra are obtained by an expansion of the electron states in a basis of the corresponding single quantum wires. The magnetic field modifies the electron subband structures and also the localization of the electron states, leading to a strong coupling between the collective and intersubband single-particle excitations. In two asymmetric quantum wires, the magnetic field results in the asymmetry of the plasmon and single-particle spectrum, increasing the flexibility to modulate the SPE and plasmon excitations, which may have some applications in optical or magnetic switches. Our results also show that a larger transverse magnetic field leads to electron localization and completely suppresses the tunneling effects, leading to a recovery of the optical and acoustic plasmon modes.

[1] T. Demel, D. Heitmann, P. Grambow, and K. Ploog, Phys. Rev. B **38**, 12 732 (1988); Phys. Rev. Lett. **66**, 2657 (1991); V. Shikin, T. Demel, and D. Heitmann, Phys. Rev. B **46**, 3971 (1992).

[2] G.Q. Hai and M.R.S. Tavares, Phys. Rev. B **61**, 1704 (2000).

[3] M.R.S. Tavares and G.Q. Hai, J. Phys.: Condens. Matter **13**, 6421 (2001).

[4] S. Das Sarma and E.H. Hwang, Phys. Rev. B **59**, 10 730 (1999).

[5] C. Steinebach, D. Heitmann, and V. Gudmundsson, Phys. Rev. B **56**, 6742 (1997); **58**, 13 944 (1998).

[6] T.V. Shahbazyan and S.E. Ulloa, Phys. Rev. B **54**, 16 749 (1996).

[7] G.R. Aizin and G. Gumbs, Phys. Rev. B **54**, 2049 (1996).

[8] L.H. Wang, Y. Zhu, F.A. Zeng, H.L. Zhao, and S.C. Feng, Phys. Rev. B **47**, 16326 (1993); L.H. Wang, F.A. Zeng, S.C. Feng, and Y. Zhu, *ibid.* **46**, 9804 (1992).

[9] L. Wendler and V.G. Grigoryan, Phys. Rev. B **54**, 8652 (1996); **49**, 13 607 (1994).

Inelastic Coulomb scattering rates due to acoustic and optical plasmon modes in coupled quantum wires

Marcos R. S. Tavares* and Guo-Qiang Hai

Instituto de Física de São Carlos, Universidade de São Paulo, 13560-970 São Carlos, SP, Brazil

(Received 4 June 1999; revised manuscript received 13 October 1999)

We report a theoretical study of the inelastic Coulomb scattering rate of an injected electron in two coupled quantum wires in quasi-one-dimensional doped semiconductors. Two peaks appear in the scattering spectrum due to optical and acoustic plasmon scattering in the system. We find that the scattering rate due to the optical plasmon mode is similar to that in a single wire, but the acoustic plasmon scattering depends crucially on its dispersion relation at small q. Furthermore, the effects of tunneling between the two wires are studied on the inelastic Coulomb scattering rate. We show that a weak tunneling can strongly affect the acoustic plasmon scattering.

I. INTRODUCTION

Recently, single-particle properties of electrons in quasi-one-dimensional (Q1D) electron systems have attracted considerable interest. With theoretical calculations of the single-particle renormalization factor[1] and the momentum distribution function around the Fermi surface, Hu and Das Sarma[2] clarified that a clean 1D electron system shows Luttinger-liquid behavior, but even the slightest amount of impurities restores the Fermi surface and the Fermi-liquid behavior remains. Within a one-subband model, they evaluated the self-energy due to electron-electron Coulomb interaction in unclean Q1D systems by using the leading-order GW dynamical screening approximation.[1,3] Within such an approximation, Hwang and Das Sarma[4] obtained band-gap renormalization in a photoexcited doped-semiconductor quantum wire in the presence of plasmon-phonon coupling. In particular, the inelastic Coulomb scattering rate plays an important role in relaxation processes of an injected electron in the conduction band. The lifetime of the injected electron, determined by this scattering rate, can be measured by femtosecond time-resolved photoemission spectroscopy.[5] The relaxation processes of an injected electron occur through the scattering channels due to different excitations in the system, such as single-particle excitations, plasmons, and phonons.[6,7] Its lifetime provides information on the interactions between the electron and the different excitations. The relaxation mechanism is important because of its technological relevance, as most semiconductor-based devices operate under high-field and hot-electron conditions.[8]

On the other hand, coupling between two parallel quantum wires leads to so-called optical and acoustic plasmon modes in the system.[9] The ground-state properties and the far-infrared absorption in two coupled quantum wires were studied recently.[10] Mode mixing among different plasmon modes is demonstrated due to the asymmetric confinement of the two wires. It is also found that the dynamic depopulation effect in coupled quantum wires results in bistability in electron transport.[11] Tunneling effects have provided devices formed by coupled semiconductor quantum wires,[12] and attracted considerable theoretical interest because of their fundamental applicability.

In this work we present a theoretical study on inelastic Coulomb scattering rates in coupled biwire electron-gas systems. Particular attention will be devoted to the effects of weak resonant tunneling. We find that weak resonant tunneling can introduce a strong intersubband inelastic Coulomb scattering by emitting an acoustic plasmon. The emission of optical plasmon, on the other hand, is provided by intrasubband scattering of injected electrons.

The rest of the paper is organized as follows. In Sec. II, we present the theoretical formalism of inelastic Coulomb scattering rates in a multisubband Q1D system of coupled quantum wires. Section III is devoted to an analysis of the inelastic-scattering rates for a biwire system in the absence of tunneling between the wires. As an extension of such calculations, in Sec. IV we show the numerical results in the presence of weak resonant tunneling. Finally, we summarize our results in Sec. V.

II. THEORETICAL FORMULATION

We consider a two-dimensional system in the xy plane subjected to additional confinement in the y direction, which forms two quantum wires parallel to each other in the x direction. The confinement potential in the y direction is taken to be of square well type, of barrier height V_0, and well widths W_1 and W_2 represent the first and second wires, respectively. The potential barrier between the two wires is of width W_b. The subband energies E_n and the wave functions $\phi_n(y)$ are obtained from a numerical solution of the one-dimensional Schrödinger equation in the y direction. We restrict ourselves to the case where $n = 1$ and 2, and define $\omega_0 = E_2 - E_1$ as being the gap between the two subbands. The interpretation of the index n depends on tunneling between the two wires. When there is no tunneling, the wave function $\phi_n(y)$ of the subband E_n is localized in quantum wire n. Clearly, it is a wire index. For two symmetric quantum wires, i.e., $W_1 = W_2$, one has $E_2 = E_1$ or $\omega_0 = 0$. When tunneling occurs, the wave function of each subband spreads in two quantum wires. In this case, n is interpreted as a subband index. For two symmetric quantum wires with tunneling, the wave functions of the two lowest eigenstates are symmetric and antisymmetric. In this case, the two wires are

in the resonant tunneling condition, and the gap between the two subbands is denoted by $\Delta_{SAS} = \omega_0$.

In a multisubband Q1D system, the inelastic Coulomb scattering rate for an injected electron in subband n with momentum k can be obtained by the imaginary part of the screened exchange self-energy $\Sigma_n[k, \xi_n(k)]$,[1] where, $\xi_n(k) = \hbar^2 k^2 / 2m^* + E_n - E_F$ is the electron energy with respect to the Fermi energy E_F and m^* the electron effective mass. We use the GW approximation to calculate this self-energy. As can be seen in Ref. 10, it is given by

$$\Sigma_n[k, \xi_n(k)] = \frac{i}{(2\pi)^2} \int dq \int d\omega' \sum_{n_1} V^s_{nn_1 n_1 n}(q, \omega')$$
$$\times G^{(0)}_{n_1}(k+q, \xi_n(k) - \omega'), \qquad (1)$$

where $G^{(0)}_{n_1}(k, \omega)$ is the Green's function of noninteracting electrons, and $V^s_{nn_1 n_1 n}(q, \omega)$ is the dynamically screened electron-electron Coulomb potential. The screened Coulomb potential is related to the dielectric function $\varepsilon_{nn'mm'}(q, \omega)$ and the bare electron-electron interaction potential $V_{nn'mm'}(q)$ through the equation

$$\sum_{ll'} \varepsilon_{ll'nn'}(q, \omega) V^s_{ll'mm'}(q, \omega) = V_{nn'mm'}(q). \qquad (2)$$

Similarly to the one-band model,[2] the self-energy in Eq. (1) can be separated into a frequency-independent exchange part and a correlation part, $\Sigma_n[k, \xi_n(k)] = \Sigma^{ex}_n(k) + \Sigma^{cor}_n[k, \xi_n(k)]$. The exchange part is given by

$$\Sigma^{ex}_n(k) = -\frac{1}{2\pi} \int dq \sum_{n_1} V_{nn_1 n_1 n}(q) f_{n_1}[\xi_{n_1}(k+q)], \quad (3)$$

where $f_n(\xi)$ is the Fermi-Dirac distribution function. Notice that $\Sigma^{ex}_n(k)$ is real because the bare electron-electron Coulomb potential $V_{nn_1 n_1 n}(q)$ is totally real. Therefore, one only needs to analyze the imaginary part of $\Sigma^{cor}_n[k, \xi_n(k)]$, since it gives rise to the imaginary part of the self-energy in which we are interested. After some algebra, we find that the Coulomb inelastic-scattering rate for an electron in a subband n with momentum k is given by

$$\sigma_n(k) = -\text{Im}\, \Sigma^{cor}_n[k, \xi_n(k)] = \sum_{n'} \sigma_{n,n'}(k), \qquad (4)$$

with

$$\sigma_{n,n'}(k) = \frac{1}{2\pi} \int dq\, \text{Im}\{V^s_{nn'n'n}[q, \xi_{n'}(k+q) - \xi_n(k)]\}$$
$$\times \{\theta[\xi_n(k) - \xi_{n'}(k+q)] - \theta[-\xi_{n'}(k+q)]\}(5)$$

where $\theta(x)$ is the standard step function. In the above equation, the frequency integration has already been carried out, since the bare Green's function $G^{(0)}_{n_1}$ can be written as a Dirac δ function of ω.[13]

For the present coupled quantum wire systems with two occupied subbands, the multisubband dielectric function within the random-phase approximation is given by

$$\varepsilon_{nn'mm'}(q, \omega) = \delta_{nm}\delta_{n'm'} - \Pi_{nn'}(q, \omega) V_{nn'mm'}(q). \quad (6)$$

The function $\Pi_{nn'}(q, \omega)$ is the 1D noninteracting irreducible polarizability at zero temperature for a system free from any impurity scattering. In the presence of impurity scattering, we use Mermin's formula[14]

$$\Pi^\gamma_{nn'}(q, \omega) = \frac{(\omega + i\gamma)\Pi_{nn'}(q, \omega + i\gamma)}{\omega + i\gamma[\Pi_{nn'}(q, \omega + i\gamma)/\Pi_{nn'}(q, 0)]} \quad (7)$$

to obtain the polarizability, including the effect of level broadening through a phenomenological damping constant γ. The Coulomb potential

$$V_{nn'mm'}(q) = \frac{2e^2}{\epsilon_0} \int dy \int dy'\, \phi_n(y)\phi_{n'}(y)$$
$$\times K_0(q|y - y'|)\phi_m(y')\phi_{m'}(y')$$

is calculated by using the numerical solution of the electron wave function $\phi_n(y)$. Here ϵ_0 is the static lattice dielectric constant, e is the electron charge, and $K_0(q|y - y'|)$ is the zeroth-order modified Bessel function of the second order. The electron-electron Coulomb interaction describes two-particle scattering events. We observe the following characteristics of the electron-electron Coulomb interaction in coupled quantum wires representing different physical scattering processes: $V_{1111}(q) = V_A$, $V_{2222}(q) = V_B$, and $V_{1122}(q) = V_{2211}(q) = V_C$ represent the scattering in which the electrons keep in their original wires or subbands; $V_{1212}(q) = V_{2121}(q) = V_{1221}(q) = V_{2112}(q) = V_D$ represent the scattering in which both electrons change their wire or subband indices; $V_{1112}(q) = V_{1121}(q) = V_{1211}(q) = V_{2111}(q) = V_J$ and $V_{2212}(q) = V_{2221}(q) = V_{1222}(q) = V_{2122}(q) = V_H$ indicate the scattering in which only one of the electrons suffers an interwire or intersubband transition. When there is no tunneling, $V_D = V_H = V_J = 0$. Clearly, these are responsible for tunneling effects. We also note that, for two symmetric quantum wires, V_J and V_H would vanish on account of symmetry along with or without tunneling.

III. BIWIRES WITHOUT TUNNELING

In the following, we will analyze the inelastic Coulomb scattering rate of electrons in two coupled symmetric quantum wires ($W_1 = W_2 = W$) in the absence of tunneling. As we discussed above, when there is no tunneling between two quantum wires, $V_D = V_H = V_J = 0$. Only the Coulomb interactions V_A, V_B, and V_C contribute to the electron-electron interaction. Furthermore, the potentials V_A and V_B are responsible for the intrawire interaction and $V_A = V_B$ due to the symmetry properties of the two wires. The potential V_C is responsible for the interwire Coulomb interaction. If we assume that the two wires have an identical electron density $n_1 = n_2 = n_e$, the total electron density in the system is $N_e = 2n_e$. In this case, the two quantum wires have the same Fermi level E_F, so that $\Pi_{11} = \Pi_{22} = \Pi_0$. Therefore, from Eqs. (2) and (6), we obtain the screened intrawire Coulomb potential $V^s_{1111} = V^s_{2222} = V^s$ given by

$$V^s = \frac{V_A - (V_A + V_C)(V_A - V_C)\Pi_0}{[1 - (V_A + V_C)\Pi_0][1 - (V_A - V_C)\Pi_0]}. \quad (8)$$
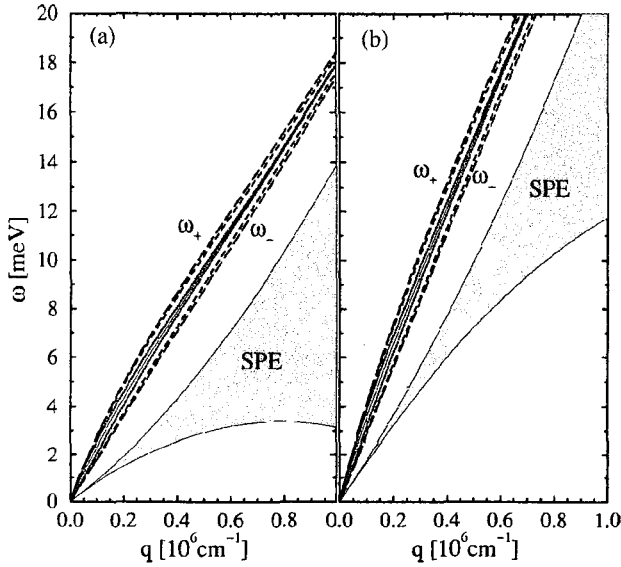
FIG. 1. Dispersions of the collective excitations of two coupled quantum wires of (a) $n_e = 0.5 \times 10^6$ cm^{-1} and (b) $n_e = 10^6$ cm^{-1}, with $W_1 = W_2 = 150$ Å and $W_b = 300$ Å (dotted curves), 70 Å (dashed curves), and 30 Å (long-dashed curves). The plasmon mode of the corresponding single wire ($W_b = \infty$) is presented by the thin solid curves. The shadowed areas indicate the single-particle continua.

The denominator in the above equation is the determinant of the dielectric matrix $\det|\epsilon(q,\omega)|$. The equation $\det|\epsilon(q,\omega)| = 0$ yields the plasmon dispersions of the electron-gas system. The plasmons result in singularities in the screened Coulomb potential which are of the most important contribution to the inelastic Coulomb scattering rate.

According to Eq. (5), the intrawire scattering rate of the symmetric biwires with identical electron density becomes

$$\sigma_{n,n}(k) = \frac{1}{2\pi} \int dq \{ \text{Im}[V^s(q, 2kq + q^2)] \}$$
$$\times \{ \theta(-2kq - q^2) - \theta(E_{Fn} - k^2 - q^2 - 2kq) \} \tag{9}$$

for $n = 1$ and 2, where $E_{Fn} = E_F - E_n$ is the subband Fermi energy. Notice that $E_1 = E_2$ for two symmetric quantum wires. It is obvious that $\sigma_{1,1}(k) = \sigma_{2,2}(k)$. In the absence of tunneling, interwire scattering rates $\sigma_{1,2}(k)$ and $\sigma_{2,1}(k)$ are zero because the transition of an electron from one wire to the other is impossible. Therefore, we have $\sigma_1(k) = \sigma_{1,1}(k) = \sigma_2(k) = \sigma_{2,2}(k)$. But the interwire Coulomb interaction V_C influences the collective excitations in the system, leading to two different plasmon modes, i.e., optical and acoustic modes. Subsequently, it affects the inelastic-scattering rates. We know that the zeros of the two parts $1 - (V_A + V_C)\Pi_0$ and $1 - (V_A - V_C)\Pi_0$ in the denominator in Eq. (8) yield optical and acoustic plasmon mode dispersions, respectively. To understand the scattering mechanism better, in Fig. 1 we show the collective excitation dispersion relations of the two coupled symmetric GaAs quantum wires of width $W = 150$ Å with different barrier widths. In the calculations, we consider the barrier height $V_0 = \infty$, which does not permit tunneling between the wires. The plasmon modes in Fig. 1 correspond
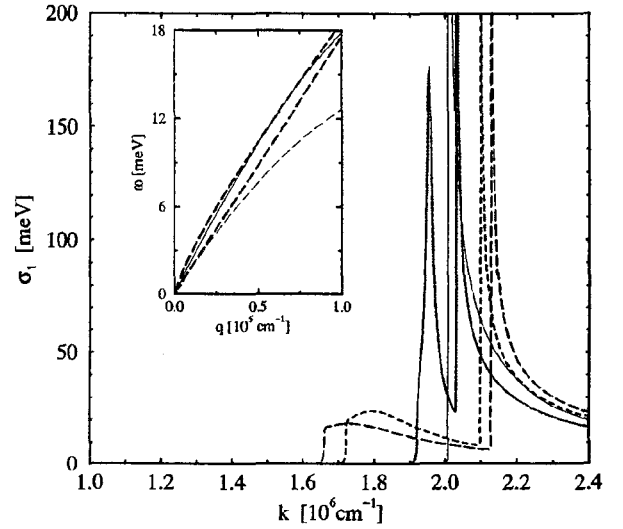
FIG. 2. The inelastic Coulomb scattering rates corresponding to Fig. 1(a) with $n_e = 0.5 \times 10^6$ cm^{-1}. The inset shows the acoustic and optical modes (thick dashed lines) for $W_b = 30$ Å, and the intrawire energy- vs momentum-loss curves at the onset of the optical (thin solid line) and acoustic (thin dashed line) plasmon scattering.

to the different scattering channels through which the injected electron can lose energy. We find a higher- (lower-) frequency plasmon branch which represents the optical (acoustic) plasmon mode ω_+ (ω_-). The intrawire single-particle excitation continuum SPE (shadow region) is also indicated in the figure. The thin solid curve is the plasmon dispersion of a single quantum wire with electron density n_e. It corresponds to the situation in which the distance between the two wires is infinity ($W_b = \infty$) or $V_C = 0$. In this case, the plasmon mode is of dispersion relation $\omega(q) \sim \sqrt{n_e} q |\ln qW|^{1/2}$ at $q \to 0$.[2] As the distance between the wires decreases, the potential V_C increases. A finite V_C leads to a gap between the two plasmon modes. When the two wires are close enough, the acoustic mode develops a linear wave-vector dependence. For $q \to 0$, $\omega_-(q) = vq$ with $v = [v_F + 4V_-(q = 0)/\pi]$, where v_F is the Fermi velocity and $V_-(q) = V_A(q) - V_C(q)$, whereas the optical plasmon still keeps its well-known 1D dispersion relation $\omega_+(q) \sim \sqrt{N_e} q |\ln qW|^{1/2}$.[4,15] Note that the interwire Coulomb interaction V_C, depending on the distance between the two wires, is responsible for the behavior of the wave-vector dependence of the acoustic mode. As we will see, this significantly affects the inelastic Coulomb scattering rate due to the acoustic plasmons.

Figure 2 shows the numerical results of inelastic plasmon scattering rate in the coupled wires corresponding to Fig. 1(a) with a very small broadening constant $\gamma = 10^{-4}$ meV. We observe two scattering peaks. The lower (higher) one is due to the acoustic (optical) plasmon scattering. The abrupt increase of the scattering rate at threshold electron momenta k_c^- and k_c^+ correspond to the onset of scattering of the acoustic and optical plasmon modes, respectively. The higher scattering peak due to the optical plasmon mode is always divergent at the onset $k = k_c^+$ and $\sigma_{1,1}(k) \propto (k - k_c^+)^{-1/2}$, similarly to that in the single wire. But the behavior of the lower scattering peak is dependent on the distance between the two wires, which is directly related to the dispersion relation of
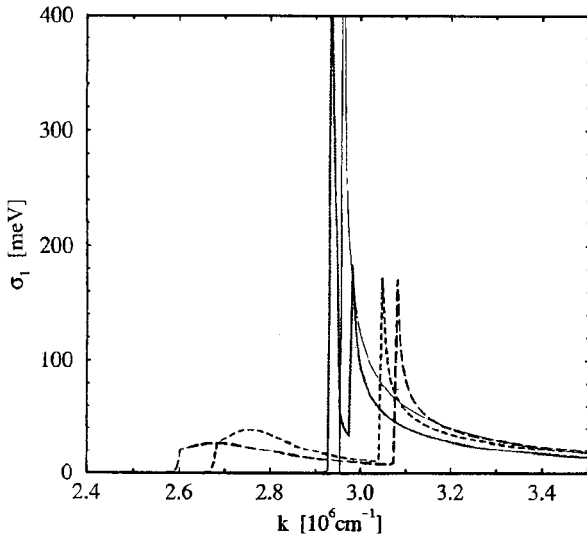
FIG. 3. The same as Fig. 2, but now with $n_e = 10^6$ cm^{-1}.

the acoustic plasmon mode at small q. For small W_b, the acoustic mode is of a linear wave-vector dependence, leading to a finite scattering rate at the onset $k = k_c^-$. With increasing W_b, the acoustic mode loses its linear q dependence, resulting in a divergency at the onset of the scattering. In order to clarify such a behavior, in the inset we show the energy- vs momentum-loss curve

$$\omega_k(q) = 2kq - q^2 \qquad (10)$$

for $k = k_c^+ \simeq 2.13 \times 10^6$ cm^{-1} (thin solid curve) and $k_c^- \simeq 1.65 \times 10^6$ cm^{-1} (thin dashed curve) in the system with $W_b = 30$ Å. Along these curves, momentum and energy conservations are obeyed and electron relaxation is allowed. The dispersions of the optical and acoustic plasmon modes $\omega_+(q)$ and $\omega_-(q)$ are also given by thick long dashed curves in the same figure. At $k = k_c^+$ (k_c^-), the thin solid (thin dashed) curve intersects the optical (acoustic) mode dispersion curve at $q = q_c^+$ (q_c^-). This means that the injected electron with momentum k_c^+ (k_c^-) can emit one optical (acoustic) plasmon of frequency $\omega_+(q_c^+)$ $[\omega_-(q_c^-)]$. Note that the slopes of the curves $\omega_{k_c^+}(q)$ $[\omega_{k_c^-}(q)]$ and $\omega_+(q)$ $[\omega_-(q)]$ are equal at $q = q_c^+$ (q_c^-). For the optical plasmon mode, the intersection always occurs at finite q_c^+ because the optical plasmon goes as $\omega_+(q) \sim q|\ln qW|^{1/2}$ for small q. The divergency due to the optical plasmon scattering is similar to that in the single quantum wire,[2] which results from the coupling of the initial and final states via plasmon emission at $k = k_c^+$. However, for the acoustic plasmon mode with a linear q dependence, $q_c^- = 0$, because $\omega_k(q) \to 2kq$ at $q \to 0$. In this case, one can obtain $k_c^- = v/2$. Due to the fact that the plasmon mode is of vanishing oscillator strength at $q = 0$, the emission of the acoustic plasmon of the wave vector $q = q_c^-$ cannot produce a divergency in the inelastic-scattering rate. As the distance between the two wires is increased, the acoustic plasmon mode loses its linear q dependence and approaches the dispersion of the optical plasmon mode. Consequently, q_c^- becomes finite, and the scattering rate is divergent at the threshold momentum k_c^-. In Fig. 3, we show the scattering rates in the same structures as in Fig. 2, but with a
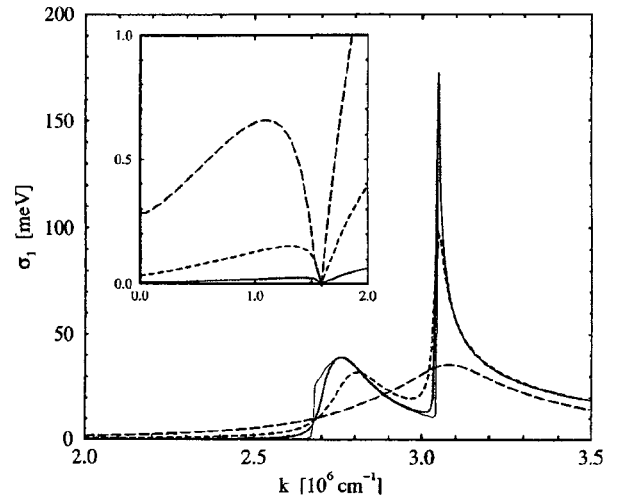

FIG. 4. The inelastic-scattering rate in coupled wires of $n_e = 10^6$ cm^{-1}, $W_1 = W_2 = 150$ Å, and $W_b = 70$ Å for different values of the broadening constant $\gamma = 10^{-4}$ (thin line), 0.01 (dotted line), 0.1 (dashed line), and 1 meV (long dashed line).

higher electron density $n_e = 10^6$ cm^{-1}. We see that, in systems of higher electron density, the scattering threshold shifts to a larger momentum and the scattering is enhanced.

In Figs. 2 and 3, we do not show the inelastic-scattering rate due to virtual emission of single-particle excitations which would occur below the threshold wave vector. It is known that, in a one-subband quantum wire, the contribution of single-particle excitations to the inelastic Coulomb scattering rate is completely suppressed due to the restrictions of the energy and momentum conservations. Consequently, the scattering rate is zero until the onset of the plasmon scattering at a threshold $k_c > k_F$.[2] Single-particle excitations contribute to the inelastic scattering only when the level broadening is introduced. These contributions are negligible when the broadening constant is small. Although, in the present case, we are dealing with two coupled quantum wires, the Coulomb interaction does not influence the single-particle excitations or as their contributions to the inelastic scattering.

At this point we should emphasize the importance of acoustic plasmon scattering in double-wire systems in comparison to double-layer (coupled 2D electron gases) systems. Contrary to their double-wire counterparts, single-particle excitations in double-layer systems contribute essentially at all values of wave vectors in inelastic Coulomb scattering, which is much more important than the plasmon scattering at a small wave vector.[16] The contribution of the acoustic plasmon peaks within a narrow window of wave vectors before the onset optical plasmon scattering, where the single-particle scattering also makes a significant contribution. In double-wire systems, however, inelastic Coulomb scattering is dominated by acoustic plasmon scattering before the onset of optical plasmon scattering due to the surpression of single-particle scattering in the 1D system. So the acoustic plasmon mode in the present system is much more important than that in 2D systems.

As far as the effect of the phenomenological broadening constant γ is concerned, in Fig. 4, we show the dependence of the inelastic-scattering rate for different γ's. Finite broadening values of γ in the system give rise to broken transla-

tional invariance due to the presence of an impurity. This fact is responsible for relaxing the momentum conservation permitting inelastic scattering via single-particle and plasmon excitations for $k < k_c^{\pm}$. We show such a contribution in the inset of Fig. 4. For $k = k_F \simeq 1.6 \times 10^6$ cm^{-1}, conservation of energy and momentum does not permit the opening of any excitation channels. This means that the injected electron has an infinite lifetime at the Fermi surface which has been restored by impurity effects.

IV. WEAK TUNNELING EFFECTS

In this section, we discuss the effect of weak tunneling on inelastic Coulomb scattering rates in two coupled symmetric quantum wires, as shown in Sec. III. When tunneling occurs, an energy gap Δ_{SAS} opens up between the two lowest subbands which have symmetric and antisymmetric wave functions in the y direction about the center of the barrier. In this case, only the subband index is a good quantum number. As we saw in Sec. II, V_J and V_H vanish in two symmetric quantum wires in resonant tunneling. However, V_D is finite and responsible for tunneling effects on the Coulomb scattering. In a weak resonant tunneling condition, one finds $V_A \simeq V_B$ $\simeq V_C \simeq U$. After some algebra, we obtain

$$V_{1111}^s = \frac{1 + U(\Pi_{11} - \Pi_{22})}{1 - U(\Pi_{11} + \Pi_{22})} U, \tag{11}$$

$$V_{2222}^s = \frac{1 - U(\Pi_{11} - \Pi_{22})}{1 - U(\Pi_{11} + \Pi_{22})} U, \tag{12}$$

$$V_{1221}^s = \frac{1 + V_D(\Pi_{12} - \Pi_{21})}{1 - V_D(\Pi_{12} + \Pi_{21})} V_D, \tag{13}$$

and

$$V_{2112}^s = \frac{1 - V_D(\Pi_{12} - \Pi_{21})}{1 - V_D(\Pi_{12} + \Pi_{21})} V_D. \tag{14}$$

From the above equations and Eq. (5), we can obtain the inelastic Coulomb scattering rates in the presence of tunneling. We also note that the zeros of the denominators in Eqs. (11) and (12) yield optical plasmon dispersion, and those in Eqs. (13) and (14) yield acoustic plasmon dispersion. This indicates that the optical plasmons only contribute to the intrasubband scatterings σ_{11} and σ_{22}, and the acoustic plasmons to the intersubband scatterings σ_{12} and σ_{21}.

We consider two coupled GaAs/Al$_{0.3}$Ga$_{0.7}$As ($V_b = 228$ meV) quantum wires of widths $W_1 = W_2 = 150$ Å separated by a barrier of $W_b = 70$ Å . In this case, we find Δ_{SAS} $= 0.14$ meV indicating a very weak resonant tunneling. In Fig. 5(a) we show both intersubband and intrasubband scattering rates. The intrasubband scattering rates σ_{11} and σ_{22}, induced by the emission of optical plasmons, is very similar to that in the absence of tunneling. It is also not difficult to understand that $\sigma_{11} \simeq \sigma_{22}$ because, above the threshold of the optical plasmon emission, the plasmon frequency is much larger than Δ_{SAS} and, consequently, $\Pi_{11} \simeq \Pi_{22}$. On the other hand, tunneling introduces the intersubband scattering rates σ_{12} and σ_{21}, and strongly modifies the mechanism of the acoustic plasmon emission. In order to clarify such results,
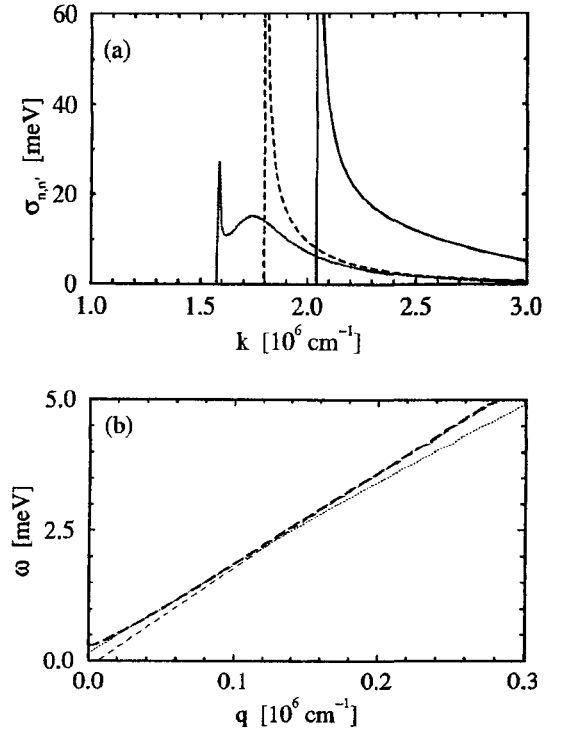

FIG. 5. (a) The intrasubband and intersubband inelastic-sacattering rates in two coupled GaAs/Al$_{0.3}$Ga$_{0.7}$As quantum wires with tunneling. $W_1 = W_2 = 150$ Å, $W_b = 70$ Å, and $N_e = 10^6$ cm^{-1}. The solid curves present $\sigma_{1,1}(k)$ and $\sigma_{2,2}(k)$. The dashed and dotted curves present $\sigma_{1,2}(k)$ and $\sigma_{2,1}(k)$, respectively. (b) The acoustic plasmon dispersion $\omega_-(q)$ (thick dashed curve) in the system. The thin dashed line indicates the $\omega_k^{12}(q)$ curve for $k_c^{12} \simeq 1.79$ $\times 10^6$ cm^{-1}, and the thin dotted line indicates the $\omega_k^{21}(q)$ curve for $k_c^{21} \simeq 1.59 \times 10^6$ cm^{-1}. $n_1 = 0.51 \times 10^6$ cm^{-1} and $n_2 = 0.49$ $\times 10^6$ cm^{-1}.

we plot the corresponding acoustic plasmon dispersion relation by the thick dashed curve in Fig. 5(b). The acoustic mode develops a plasmon gap at zero q due to the tunneling effect.[15] The thin lines indicate the intersubband energy- vs momentum-loss curves at the onset of the acoustic plasmon scattering. They are determined by conservations of energy and momentum, given by

$$\omega_k^{12}(q) = 2qk - q^2 - \Delta_{SAS} \tag{15}$$

for $k = k_c^{12}$ (thin dashed curve), and

$$\omega_k^{21}(q) = 2qk - q^2 + \Delta_{SAS} \tag{16}$$

for $k = k_c^{21}$ (thin dotted curve), where k_c^{12} and k_c^{21} are threshold wave vectors above which the injected electron can be transferred to a different subband by emitting an acoustic plasmon. $\omega_k^{21}(q)$ (thin dotted curve) intersects the acoustic plasmon dispersion at small wave vector $q = q_c^{21} \simeq 0.05$ $\times 10^6$ cm^{-1}. The scattering process is similar to acoustic plasmon scattering in the absence of tunneling, as we discussed in Sec. III. But now, the acoustic plasmon mode is of a finite frequency, with a finite oscillator strength at $q \rightarrow 0$ resulting in a small divergency at k_c^{21} . On the other hand, the intersection between $\omega_k^{12}(q)$ (thin-dashed curve) and the acoustic plasmon dispersion occurs at quite a larger wave
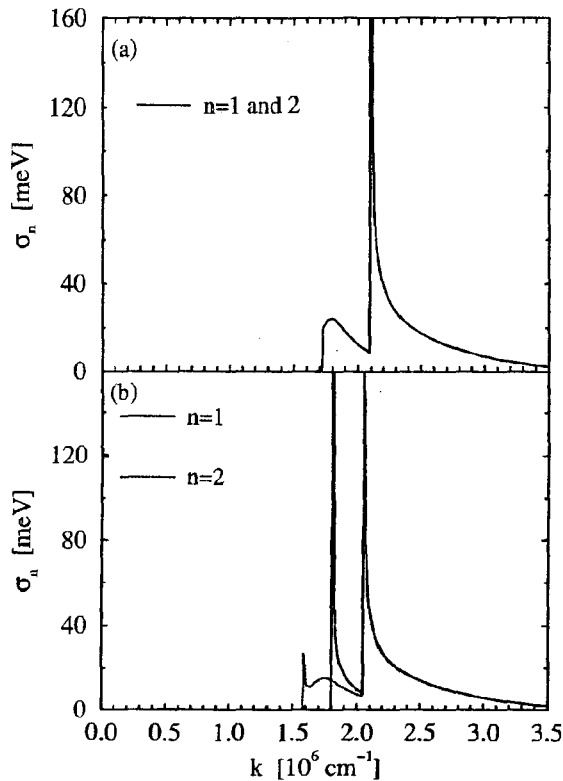
FIG. 6. Total inelastic-scattering rate $\sigma_n(k)$ of the biwire system (a) without ($V_0 = \infty$) and (b) with tunneling ($V_0 = 228$ meV). $W_1 = W_2 = 150$ Å, $W_b = 70$ Å, and $N_e = 10^6$ cm^{-1}.

vector $q = q_c^{12} \approx 0.18 \times 10^6$ cm^{-1} . The scattering, mechanism is more similar to that of the intrasubband scattering and produces a pronounceable divergence at k_c^{12}.

Finally, we would like to show the tunneling effects on the total inelastic Coulomb scattering rates $\sigma_n(k) = \Sigma_{n'} \sigma_{n,n'}(k)$. Figure 6 gives the total scattering rates in (a) the absence and (b) the presence of tunneling between two quantum wires with $W = 150$ Å and $W_b = 70$ Å . We observe that weak resonant tunneling does not influence the optical plasmon scattering very much, but it does strongly affect acoustic plasmon scattering. The acoustic plasmon scattering for the injected electron in the lowest subband is enhanced significantly, and quite a strong scattering peak appears. For

the injected electron in the second subband, tunneling introduces a small divergency in the scattering rate, and shifts the scattering threshold to the lower wave vector.

V. SUMMARY

We have calculated the inelastic Coulomb scattering rates of two coupled Q1D electron-gas systems within the GW approximation. The screened Coulomb potential was obtained within the random-phase approximation. The Coulomb interaction between the two quantum wires leads to optical and acoustic plasmon modes and, consequently, two scattering peaks appear due to the scattering of the two modes. We found that the scattering of the optical plasmons in two coupled quantum wires is very similar to plasmon scattering in a single wire because both plasmon modes have similar dispersion relations at small q. The scattering rate is divergent at the onset of the optical plasmon scattering. However, the acoustic plasmon mode does not produce such a divergency when it is of a linear q dependence at small q. This happens when two wires are close enough. Furthermore, we studied tunneling effects on inelastic scattering. A weak resonant tunneling was introduced between the wires. Such a tunneling lifts the degeneracy of the two subbands that originates from two quantum wires, and also produces a small plasmon gap on the acoustic mode at $q = 0$. Moreover, intersubband scattering appears. We show that, in this case, the optical plasmons are responsible only for intrasubband scattering, and the acoustic plasmons for intersubband scattering. A weak tunneling significantly enhances acoustic plasmon scattering for an injected electron in the lowest subband.

As far as we know, there have been no experimental studies reporting intersubband scattering of Q1D electrons in two coupled quantum wires. For two-dimensional systems, however, theoretical calculations on the intersubband relaxation times[17] motivated tunneling spectroscopy experiments to measure electron lifetimes[18] in a strong-coupling situation. We believe that our work can be useful to understand scattering mechanisms which could be observed in double-wire tunneling spectroscopy.

ACKNOWLEDGMENTS

*Present address: Department of Physics, University of Maryland, College Park, Maryland 20742-4111.

[1] For a review, see G. D. Mahan, *Many-Particle Physics*, 2nd ed. (Plenum, New York, 1981).

[2] B. Y.-K. Hu and S. Das Sarma, Phys. Rev. B **48**, 5469 (1993).

[3] J. J. Quinn and R. A. Ferrel, Phys. Rev. **112**, 812 (1958).

[4] E. H. Hwang and S. Das Sarma, Phys. Rev. B **58**, R1738 (1998).

[5] S. Xu, J. Cao, C. C. Miller, D. A. Mantell, R. J. D. Miller, and Y. Gao, Phys. Rev. Lett. **76**, 483 (1996).

[6] L. Zheng and S. Das Sarma, Phys. Rev. B **54**, 2751 (1996).

[7] C. R. Bennett and B. Tanatar, Phys. Rev. **55**, 7165 (1997).

[8] S. Q. Murphy, J. P. Eisenstein, L. N. Pfeiffer, and K. W. West,

Phys. Rev. B **52**, 14 825 (1995), and references therein.

[9] T. Demel, D. Heitmann, P. Granbow, and K. Ploog, Phys. Rev. B **38**, 12 732 (1988); R. Wang and P. P. Ruden, *ibid.* **52**, 7826 (1995).

[10] C. Steinebach, D. Heitmann, and V. Gudmundsson, Phys. Rev. B **56**, 6742 (1997); **58**, 13 944 (1998).

[11] A. Messica, U. Meirav, H. Shtrikman, V. Umansky, and D. Mahalu, Phys. Rev. B **54**, R5247 (1996).

[12] V. Shikin, T. Demel, and D. Heitmann, Phys. Rev. B **46**, 3971 (1992), and references therein; C. Eugster and J. A. del Alamo, Appl. Phys. Lett. **60**, 642 (1992).

[13] B. Vinter, Phys. Rev. B **15**, 3947 (1977).

[14] N. D. Mermin, Phys. Rev. B **1**, 2362 (1970).

[15] M. R. S. Tavares and G.-Q. Hai (unpublished).

[16] L. Zheng and S. Das Sarma, Phys. Rev. B **54**, 13 908 (1996); S. Das Sarma and E.H. Hwang, Phys. Rev. Lett. **81**, 4216 (1998).

[17] P. Sotirelis, P. Von Allmen, and K. Hess, Phys. Rev. B **47**, 12 744 (1993); G. F. Giuliani and J. J. Quinn, *ibid.* **26**, 4421 (1982); H. Fukuyama and E. Abrahams, *ibid.* **27**, 5976 (1983).

[18] S. Q. Murphy, J. P. Eisenstein, L. N. Pfeiffer, and K. W. West, Phys. Rev. B **52**, 14 825 (1995).

Carrier relaxation due to electron-electron interaction in coupled double quantum well structures

Marcos R. S. Tavares,[1,2] G.-Q Hai,[2] and S. Das Sarma[1]

[1]*Department of Physics, University of Maryland, College Park, Maryland 20742-4111*
[2]*Instituto de Física de São Carlos, Universidade de São Paulo, São Carlos, SP 13560-970, Brazil*

We calculate the electron-electron interaction induced energy-dependent inelastic carrier relaxation rate in doped semiconductor coupled double quantum well nanostructures within the two-subband approximation at zero temperature. In particular, we calculate, using many-body theory, the imaginary part of the full self-energy matrix by expanding in the dynamically random-phase approximation screened Coulomb interaction, obtaining the intrasubband and intersubband electron relaxation rates in the ground and excited subbands as a function of electron energy. We separate out the single-particle and the collective excitation contributions, and comment on the effects of structural asymmetry in the quantum well on the relaxation rate. Effects of dynamical screening and Fermi statistics are automatically included in our many-body formalism rather than being incorporated in an *ad hoc* manner as one must do in the Boltzmann theory.

I. INTRODUCTION

Electron-electron interaction induced carrier relaxation is an important inelastic scattering process in low-dimensional semiconductor nanostructures. It is often (particularly in situations where LO phonon emission is energetically prohibited because the excited electrons do not have enough energy) the most dominant relaxation process in semiconductor quantum wells and wires, and is therefore of considerable fundamental and practical importance. Band gap engineering has led to the possibility of fabricating tunable far infrared quantum well cascade lasers (QCL's) and efficient quantum well infrared photodetectors (QWIP's), where inelastic carrier relaxation via electron-electron interaction is a crucial (perhaps even decisive) process in determining device operation and feasibility.[1] For QCL and QWIP operations it is the intersubband inelastic relaxation that turns out to be the primary rate-limiting scattering process. For other proposed devices, such as the planar hot electron transistors or related two-dimensional (2D) high-speed devices, intrasubband relaxation is the important process. A thorough quantitative understanding of intra- and intersubband relaxation due to electron-electron interaction is therefore important for the successful realization of these devices. In addition to this practical technological motivation arising from QCL, QWIP, and other proposed band-gap-engineered quantum well devices, there is also an obvious fundamental reason for studying inelastic Coulomb scattering in 2D quantum well systems. Inelastic electron-electron scattering determines the 2D quasiparticle spectral width, as determined, for example, in tunneling measurements, through the imaginary part of the electron self-energy function.[2]

In this article we use a many-body approach in calculating the inelastic relaxation rate of 2D electrons confined in GaAs-Al$_x$Ga$_{1-x}$As semiconductor quantum well structures. Our work is a multisubband generalization of the earlier work[3] by Jalabert and Das Sarma, who considered only intrasubband relaxation within a single subband model. We consider both intra- and intersubband relaxation in the two lowest subbands, and consider both single-well and coupled double-well structures. An additional important issue addressed in our work is the effect of structural asymmetry in the quantum well on the relaxation rate. This is in fact a potentially significant factor in the fabrication of QCL and QWIP structures since asymmetry could lead to the opening of new electron-electron interaction channels in the inelastic intersubband relaxation as we discuss below in this article.

The central quantity we calculate in this work, within the leading-order dynamically screened Coulomb interaction expansion (the so-called GW approximation in the multisubband situation), is the imaginary part of electronic on-shell self-energy matrix, M, in the quantum well subband index (i,j, etc.). The subband self-energy in the multisubband situation is, in general, off-diagonal, reflecting the breaking of the translational invariance along the growth (z) direction (we take the x-y plane to be the 2D plane with all wave vectors in this paper being 2D wave vectors in the x-y plane). The off-diagonal self-energy, Im(M_{ij}), incorporates in an intrinsic many-body manner the possibility of electron-electron-interaction-induced intersubband scattering (both virtual and real) of carriers. We believe that in the doped situation of our interest, where the quantum well subbands are occupied by many electrons, the many-body self-energy approach is also a reasonable technique in calculating the inelastic carrier relaxation rate in spite of the Boltzman equation approach, where the scattering rates are usually calculated using Fermi's golden rule. The dynamical screening inherent in the many-electron system, which affects the calculated inelastic scattering rates in profound and highly nontrivial way, is automatically incorporated in our many-body GW expansion, whereas inclusion of dynamical screening in Fermi's golden rule type formula is done by replacing the bare interaction by a screened interaction in an *ad hoc* manner.

Our theory, as mentioned above, is based on the so-called GW self-energy approximation[3,4] where the electron self-energy M is obtained in a leading order expansion of the dynamically screened Coulomb interaction $W \equiv V^s$, where the superscript s denotes dynamical screening of the bare electron-electron interaction matrix V in the multisubband

situation. We use the RPA to obtain the dynamical screened interaction V^s, i.e., $V^s \equiv \varepsilon^{-1} V$, with $\varepsilon \equiv 1 - V\Pi$, where Π is the leading-order (i.e., noninteracting) electron polarizability matrix. We also approximate the electron Green's function G by the noninteracting Green's function G^0, making our formal expression for the self-energy matrix to be

$$M \sim \int G^0 V^s, \qquad (1)$$

where the integral involves integrating over all internal momentum and energy variables as well as summing over all internal subband indices (and spin). Putting the subband (matrix) indices explicitly in Eq. (1), we get

$$\text{Im } M_{ij} = \text{Im } \sum_{lm} \int G^0_{lm} V^s_{ilmj}. \qquad (2)$$

We note, however, that G^0, being the noninteracting Green's function, is necessarily diagonal in subband indices (i.e., an electron cannot undergo intersubband scattering in the absence of interaction):

$$G^0_{lm} \sim G^0_{ll} \delta_{lm}. \qquad (3)$$

Then, Eq. (2) becomes

$$\text{Im } M_{ij} = \sum_l \int \text{Im } [G^0_{ll} V^s_{illj}], \qquad (4)$$

with

$$V^s_{illj} = (\varepsilon^{-1} V)_{illj}. \qquad (5)$$

Equations (4) and (5) are the central formal equations we use in our theory to obtain the inelastic relaxation time τ, remembering that the scattering rate Γ and the relaxation time τ are connected by

$$\tau = \frac{\hbar}{2\Gamma}, \qquad (6)$$

where

$$\Gamma = |\text{Im } M|. \qquad (7)$$

We emphasize that the inelastic relaxation time τ defined by Eq. (6) and calculated in this paper is an energy relaxation time (and not a momentum relaxation time, as, for example, will enter the calculation of the mobility of the system). The inelastic relaxation time calculated in this paper defines the lifetime of a single-particle energy eigenstate in the system. Due to Coulomb scattering among the electrons the single-particle stationary states are well-defined only over a limited time scale and our calculated τ is a measure of this lifetime arising from electron-electron interaction.

In Eqs. (6) and (7), $\Gamma = |\text{Im } M|$ is calculated on-shell, i.e., the quasiparticle self-energy defines Γ. To demonstrate how Eq. (4) may, in principle, differ from the Fermi golden rule approach we consider the specific two-subband model of interest to us in this paper. Then $i, j, l = 1, 2$ with only subband 1, the ground subband, and the subband 2, the first excited

subband being considered in the theory assuming all other subbands to be substantially higher in energy, making negligible contributions to the self-energies of the lowest two subbands. We also assume the square well structure to be symmetric, so that parity is a good quantum number in the problem which makes all "off-diagonal" interaction matrix elements vanish[5] by virtue of parity conservation with the only nonzero elements of V^s being $V^s_{1111}, V^s_{2222}, V^s_{1212}$, and V^s_{1122} (note that $V^s_{1221} = V^s_{2112}$ and $V^s_{1122} = V^s_{2211}$ by symmetry). In this situation Eq. (4) implies that

$$\text{Im } M_{12} = \text{Im } M_{21} = 0 \qquad (8)$$

and

$$\text{Im } M_{22} \sim \int \text{Im } [G^0_{11} V^s_{2112} + G^0_{22} V^s_{2222}]. \qquad (9)$$

We note that the dynamically screened interaction matrix element V^s_{1122} is not explicitly present in Eq. (9). On the other hand, a Fermi golden rule approach[6] will explicitly include such a V^s_{1122} term, because it seems to arise from the direct Coulomb interaction V_{1122} between an electron in subband 1 and an electron in subband 2 without any intersubband scattering. We mention, however, that dynamical screening of V_{2222} produces an effective V_{2211} term in our theory since dynamical screening proceeds through virtual creation of electron-hole pairs.

We have calculated the energy-dependent inelastic relaxation rate at $T = 0$ for a two-subband (1 and 2) GaAs-Al$_x$Ga$_{1-x}$As quantum well system with a total electron density $N_e = 2 \times 10^{11}$ cm^{-2} for the following five distinct situations. (i) Two coupled symmetric quantum wells of width 150 Å each with interwell tunneling induced by a tunneling barrier of height 228 meV and width 30 Å. Here the lowest two subbands are the so-called symmetric (bonding) and antisymmetric (antibonding) levels with energies $E_1 = 15.35$ meV and $E_2 = 17.03$ meV, respectively. The third level $E_3 = 60.53$ meV is sufficiently high to be ignored ($E_{F1} = E_F - E_1 = 4.28$ meV; $E_{F2} = E_F - E_2 = 2.61$ meV), with both subbands 1 and 2 occupied by carriers. These results are presented in Sec. III A below. (ii) Two coupled asymmetric quantum wells with interwell tunneling [the same as in (i) above], with one well of width 150 Å and the other of width 140 Å, leading to $E_1 = 15.93$ meV and $E_2 = 18.55$ meV ($E_{F1} = E_F - E_1 = 4.75$ meV; $E_{F2} = E_F - E_2 = 2.13$ meV). Again, the next excited subband $E_3 = 62.86$ meV is high enough to be ignored. These results are presented in Sec. III A below. (iii) Two coupled identical symmetric quantum wells of width 150 Å each with no interwell tunneling (i.e., the interwell barrier is taken to be infinity) and with a barrier width of 30 Å. Here, $E_1 = E_2 = 23.87$ meV (this degeneracy arises because the two wells are identical and there is no tunneling), $E_{F1} = E_{F2} = E_F - E_1 = E_F - E_2 = 3.44$ meV, and the next subband $E_3 = 96$ meV is sufficiently high in energy to be neglected. These results are presented in Sec. III B below. (iv) The same as in the last case with no interwell tunneling but an asymmetric situation with the two wells being different. One has a width of 150 Å and the other a width of 142.4 Å so that the subband Fermi

energies $E_{F1} = E_F - E_1 = 4.75$ meV and $E_{F2} = E_F - E_2 = 2.13$ meV, which are the same as in (ii) above. In this situation $E_1 = 23.87$ meV, $E_2 = 26.49$ meV (again E_3 can be neglected). Furthermore, to keep the average distance between the two electron layers the same as in (ii), we choose a barrier of width 28.8 Å. These results are presented in Sec. III B below in comparison with those in (ii). (v) A single symmetric quantum well of width 300 Å and a barrier height 228 meV, which leads to the lowest two subbands at $E_1 = 4.88$ meV, $E_2 = 19.51$ meV, and the Fermi energy $E_{F1} = E_F - E_1 = 6.88$ meV (with $E_F < E_2$, so that the second subband is empty). In this situation, the next excited subband, $E_3 = 43.74$ meV, is high enough in energy to be neglected. These results are present in Sec. III C below. Our reason for studying the five different classes of systems described above is that we are interested in understanding the effects of interwell tunneling and structural asymmetry on the electron relaxation rate. In particular, asymmetry breaks parity conservation, making the off-diagonal matrix elements of Coulomb interaction (e.g., $V_{1112}, V_{1121}, V_{1211}, V_{2111}, V_{2221}, V_{2212}, V_{2122}, V_{1222}$ all of which are zero in the symmetric situation) nonzero, leading to new inelastic relaxation channels not present in symmetric structures. For the sake of brevity we present results for a single representative carrier density and well parameters in each of the five cases. Our theory could be easily generalized to obtain finite temperature relaxation rates. Note that our goal here is to provide a qualitative understanding of how various physical parameters affect Coulomb scattering rates in 2D quantum wells.

The plan of this article is the following. In Sec. II we present a brief theory with working formulas; in Sec. III we provide our numerical results and discussions; we conclude in Sec. IV with a summary.

II. THEORY

Our basic theory is outlined in the Introduction, where the formal expression for the self-energies to be calculated were given. Our central GW random-phase approximation (RPA) expression[7] for the self-energy can be explicitly written out by using the noninteracting subband Green's function

$$G_{ij}^0(\omega,k) = \delta_{ij}[\omega - E_i(k) + E_F]^{-1}, \quad (10)$$

where ω is a complex frequency ($\hbar = 1$), and $E_i(k) = E_i + k^2/2m^*$ is the noninteracting subband one-electron energy dispersion. Using Eq. (10) in Eqs. (4) and (5), and carrying out the internal frequency integration, and taking the imaginary part after the on-shell analytic continuation, we get

$$\text{Im } M_{ij}(k) = \frac{1}{(2\pi)^2} \sum_l \int d^2q$$
$$\times \text{Im}[V_{illj}^s(\mathbf{q},\xi_l(\mathbf{k+q}) - \xi_i(\mathbf{k})]$$
$$\times \{\theta(\xi_i(\mathbf{k}) - \xi_l(\mathbf{k+q}))$$
$$- \theta(-\xi_l(\mathbf{k+q}))\}, \quad (11)$$

where the on-shell subband energy $\xi_i(\mathbf{k})$ is given by

$$\xi_i(\mathbf{k}) = E_i(\mathbf{k}) - E_F, \quad (12)$$

and $\theta(x) = 0(1)$, for $x < 0 (>0)$, is the Heaviside step function. The dynamically screened Coulomb interaction is given by [see Eq. (5)]

$$V_{ijlm}^s = (\varepsilon^{-1} V)_{ijlm}, \quad (13)$$

with the multisubband RPA approximation[7] defined by the dielectric matrix

$$\varepsilon_{ijlm} = (1 - V_{ijlm} \Pi_{lm}^0), \quad (14)$$

where V_{ijlm} is the bare Coulomb interaction matrix element in the subband representation, and Π_{ij}^0, the noninteracting polarizability, is given by

$$\Pi_{ij}^0(\mathbf{k},\omega) = -2 \int \frac{d^2q}{(2\pi)^2} \frac{f_i(\mathbf{k+q}) - f_i(\mathbf{k})}{\omega - E_i(\mathbf{k+q}) + E_j(\mathbf{k})}, \quad (15)$$

where $f_i(\mathbf{k})$ is the Fermi distribution function in the ith subband. In this paper, we take the impurity-scattering-induced background broadening γ as being a small phenomenological damping parameter which equivalent to be working in the clean limit. We are therefore restricting ourselves to high mobility quantum wells with small impurity-scattering-induced level broadening.

Using Eqs. (11)–(15) it is straightforward to calculate the imaginary part of the on-shell self-energy. For the sake of completeness, we show below the detailed expressions for Im M_{ij} in the GW approximation for the two-subband model:

$$\text{Im } M_{11}(k) = \sigma_{1111}(k) + \sigma_{1221}(k), \quad (16)$$

$$\text{Im } M_{12}(k) = \sigma_{1112}(k) + \sigma_{1222}(k), \quad (17)$$

$$\text{Im } M_{21}(k) = \sigma_{2111}(k) + \sigma_{2221}(k) \quad (18)$$

and

$$\text{Im } M_{22}(k) = \sigma_{2112}(k) + \sigma_{2222}(k). \quad (19)$$

Here,

$$\sigma_{1111}(k) = \frac{1}{(2\pi)^2} \int d^2q \{ \text{Im}[V_{1111}^s(\mathbf{q},A)]$$
$$\times [\theta(-A) - \theta(-\xi_1(\mathbf{k+q}))]\}, \quad (20)$$

$$\sigma_{1221}(k) = \frac{1}{(2\pi)^2} \int d^2q \{ \text{Im}[V_{1221}^s(\mathbf{q},A+\omega_0)]$$
$$\times [\theta(-A-\omega_0) - \theta(-\xi_2(\mathbf{k+q}))]\}, \quad (21)$$

$$\sigma_{1112}(k) = \frac{1}{(2\pi)^2} \int d^2q \{ \text{Im}[V_{1112}^s(\mathbf{q},A)]$$
$$\times [\theta(-A) - \theta(-\xi_1(\mathbf{k+q}))]\}, \quad (22)$$

$$\sigma_{1222}(k) = \frac{1}{(2\pi)^2} \int d^2\mathbf{q}\{\mathrm{Im}\,[V^s_{1222}(\mathbf{q},A+\omega_0)]$$
$$\times [\theta(-A-\omega_0) - \theta(-\xi_2(\mathbf{k}+\mathbf{q}))]\}, \quad (23)$$

$$\sigma_{2111}(k) = \frac{1}{(2\pi)^2} \int d^2\mathbf{q}\{\mathrm{Im}\,[V^s_{2111}(\mathbf{q},A-\omega_0)]$$
$$\times [\theta(-A+\omega_0) - \theta(-\xi_1(\mathbf{k}+\mathbf{q}))]\}, \quad (24)$$

$$\sigma_{2221}(k) = \frac{1}{(2\pi)^2} \int d^2\mathbf{q}\{\mathrm{Im}\,[V^s_{2221}(\mathbf{q},A)]$$
$$\times [\theta(-A) - \theta(-\xi_2(\mathbf{k}+\mathbf{q}))]\}, \quad (25)$$

$$\sigma_{2112}(k) = \frac{1}{(2\pi)^2} \int d^2\mathbf{q}\{\mathrm{Im}\,[V^s_{2112}(\mathbf{q},A-\omega_0)]$$
$$\times [\theta(-A+\omega_0) - \theta(-\xi_1(\mathbf{k}+\mathbf{q}))]\}, \quad (26)$$

and

$$\sigma_{2222}(k) = \frac{1}{(2\pi)^2} \int d^2\mathbf{q}\{\mathrm{Im}\,[V^s_{2222}(\mathbf{q},A)]$$
$$\times [\theta(-A) - \theta(-\xi_2(\mathbf{k}+\mathbf{q}))]\}, \quad (27)$$

where $\omega_0 = E_2 - E_1$ is the subband energy difference, $A \equiv A(\mathbf{q},\mathbf{k}) = (2kq\cos\eta + q^2)/2m^*$ with η being the angle between $\mathbf{k}$ and $\mathbf{q}$; and $m^* = 0.07m_e$ being the GaAs conduction band electron effective mass. Now, we define the *total* inelastic Coulomb scattering rate for an electron with wave vector k (i.e., an energy of $k^2/2m^*$ with respect to the subband bottom) in the subband 1 and 2 as

$$\sigma_1(k) = \mathrm{Im}\,M_{11}(k) + \mathrm{Im}\,M_{12}(k) \quad (28)$$

and

$$\sigma_2(k) = \mathrm{Im}\,M_{21}(k) + \mathrm{Im}\,M_{22}(k). \quad (29)$$

It is important to realize that the screened potentials V^s_{ijlm} for $j \neq l$ do not appear in Eqs. (20)–(27) and, consequently, do not explicitly contribute to scattering rate. They are implicitly induced in the theory through dynamical screening[8] as discussed before. Furthermore, all screened interactions V^s_{ijlm} involved in Eqs. (20)–(27) are obtained from the relation between the bare electron-electron potential[7]

$$V_{ijlm}(q) = \frac{2\pi e^2}{q\varepsilon_0} \int dz \int dz' \phi_i(z)\phi_j(z)$$
$$\times e^{-q|z-z'|}\phi_l(z')\phi_m(z')$$

and the inverse matrix of the dynamical dielectric function $\varepsilon_{ijlm}(q,\omega)$ [see Eqs. (13) and (14), where the indices $i,j,l, m = 1,2$]. These bare Coulomb potentials $V_{ijlm}(q)$ are calculated here by using both the one-electron wave function $\phi_i(z)$ and the subband energy E_i obtained through the numerical solution of the Schrödinger equation in the z direc-

tion for the specific quantum well confinement potential. Furthermore, the potential $V_{ijlm}(q)$ can be separated into intra- and intersubband terms, and understood as follows: (i) intralayer (intrasubband) interactions $V_{1111}(q) = V_A$, $V_{2222}(q) = V_B$, and $V_{1122}(q) = V_{2211}(q) = V_C$ represent those scattering events which the electrons remain in their original well (subband); (ii) interlayer (intersubband) interactions $V_{1212}(q) = V_{2121}(q) = V_{1221}(q) = V_{2112}(q) = V_D$ represent scattering in which both electrons change their well (subband) indices; and (iii) intrawell-interwell (subband) interactions $V_{1112}(q) = V_{1121}(q) = V_{1211}(q) = V_{2111}(q) = V_J$ and $V_{2212}(q) = V_{2221}(q) = V_{1222}(q) = V_{2122}(q) = V_H$ indicate the scattering in which only one of the electrons suffers the interwell (intersubband) transition.

For each wave vector k, the two-dimensional $\mathbf{q}$ integrals in Eqs. (20)–(27) are performed within the planes determined through the variables $\mathbf{q}$ and A in the screened interactions V^s_{ijlm}. The integration domains of q and η (in A) variables are restricted by the two θ functions appearing in the integrals in Eqs. (20)–(27). The integrals involving V^s_{1111} and V^s_{1112} are performed within the planes formed by those regions in the q space where

$$\theta(-A) - \theta(-\xi_1(\mathbf{k}+\mathbf{q})) \neq 0, \quad (30)$$

while the integrals involving V^s_{1221} and V^s_{1222} are calculated within the planes defined by

$$\theta(-A-\omega_0) - \theta(-\xi_2(\mathbf{k}+\mathbf{q})) \neq 0. \quad (31)$$

In the same way, the integrals involving V^s_{2222} and V^s_{2221} are performed within the planes defined by

$$\theta(-A) - \theta(-\xi_2(\mathbf{k}+\mathbf{q})) \neq 0, \quad (32)$$

and, finally, for V^s_{2112} and V^s_{2111} the integrating plane is defined by

$$\theta(-A+\omega_0) - \theta(-\xi_1(\mathbf{k}+\mathbf{q})) \neq 0. \quad (33)$$

The inelastic scattering rates in Eqs. (20)–(27) vanish outside each corresponding integrating plane, which means that the momentum and energy conservation cannot be simultaneously obeyed for such values of $(\mathbf{k},\mathbf{k}+\mathbf{q})$, and therefore no Coulomb scattering is allowed there. It is easy to see that these integrals are nonvanishing only if the corresponding integrating plane contains either some part of the single-particle excitation continuum or some branch representing the collective excitations (plasmons) in the 2D q plane. This is of course expected since a finite scattering rate must involve real excitations, which in this case are single-particle and collective plasmon excitations.

III. NUMERICAL RESULTS AND DISCUSSIONS

A. Coulomb coupled bilayers with interwell tunneling

We consider first two coupled symmetric identical quantum wells of same width $W_1 = W_2 = 150$ Å with an interwell tunneling induced by a barrier of height 228 meV and width 30 Å. The total electron density $N_e = n_1 + n_2 = 2 \times 10^{11}$ cm^{-2} in all structures studied in this paper, with

n_1 and n_2 being the density in the subband 1 and 2, respectively. For these sample parameters, the Fermi wave vectors in the first and second subband are $k_{F1}^{sy} \approx 0.88 \times 10^6$ cm^{-1} and $k_{F2}^{sy} \approx 0.69 \times 10^6$ cm^{-1}, respectively (the superscript sy stands for symmetric). Here, both subbands 1 and 2 (symmetric and antisymmetric, respectively) are occupied by carriers with $n_1 \approx 1.23 \times 10^{11}$ cm^{-2} and $n_2 \approx 0.77 \times 10^{11}$ cm^{-2}.

The plasmon dispersion relation is determined by the roots of the determinantal equation $\det|\varepsilon_{ijlm}(q,\omega)| = 0$, which, after some algebra, can be rewritten as

$$\varepsilon_{intra}\varepsilon_{inter} - [(1 - V_A\Pi_{11}^0)V_H^2\Pi_{22}^0 + (1 - V_B\Pi_{22}^0)V_J^2\Pi_{11}^0$$
$$-2V_CV_JV_H\Pi_{11}^0\Pi_{22}^0(\Pi_{12}^0 + \Pi_{21}^0)] = 0, \qquad (34)$$

where

$$\varepsilon_{intra} = (1 - V_A\Pi_{11}^0)(1 - V_B\Pi_{22}^0) - V_C^2\Pi_{11}^0\Pi_{22}^0 \qquad (35)$$

and

$$\varepsilon_{inter} = 1 - V_D(\Pi_{12}^0 + \Pi_{21}^0). \qquad (36)$$

For notational simplicity, we do not explicitly write the energy and wave vector dependence in Eqs. (34)–(36). For the present symmetric situation, the unscreened Coulomb potential $V_J = V_H = 0$ by virtue of parity symmetry, because the wave functions $\phi_1(z)$ and $\phi_2(z)$ are symmetric and antisymmetric functions of z, respectively. According to Eq. (34), therefore, the plasmons dispersion relation in our symmetric bilayer structure is determined by the roots of the equation $\varepsilon_{intra}\varepsilon_{inter} = 0$, i.e., either $\varepsilon_{intra} = 0$ corresponding to the 2D intrasubband plasmons, or $\varepsilon_{inter} = 0$ corresponding to the intersubband plasmons.

There are four roots of $\varepsilon_{intra} = 0$. Two of them are shown in Fig. 1(a) by the solid lines indicating the intrasubband plasmon modes (1,1) and (2,2). Notice that, for each solid line, there is a corresponding dashed line that is also the root of the same equation always lying in the corresponding single-particle excitation continuum. It is well known that the plasmon modes indicated by the dashed lines inside the single-particle continua are strongly Landau damped by single-particle excitations and will be ignored in the following discussion. Furthermore, the intersubband plasmon mode (1,2) comes from the roots of $\varepsilon_{inter} = 0$. The wave functions $\phi_1(z)$ and $\phi_2(z)$ are schematically shown in the inset by the solid and dot lines, respectively. Notice that, one is always able to separate the intra and inter-subband plasmon modes in structures that are invariant under space inversion. In addition, the intrasubband plasmons are not Landau damped by intersubband single-particle excitations (SPE's) and vice versa in symmetric bilayer systems. The single-particle continua SPE$_{11}$ (intrasubband SPE) and SPE$_{12}$ (intersubband SPE) in Fig. 1(a) are those regions where $\text{Im}\{\Pi_{11}^0(q,\omega)\} \neq 0$ and $\text{Im}\{\Pi_{12}^0(q,\omega)\} \neq 0$, respectively. For the sake of simplicity, we will not indicate the continuum SPE$_{22}$ in this paper because it lies totally inside the continuum SPE$_{11}$. Moreover, we claim that the plasmon mode (2,2) should be strongly damped by single-particle excitations in the SPE$_{11}$ continuum and will also be ignored in the following qualita-
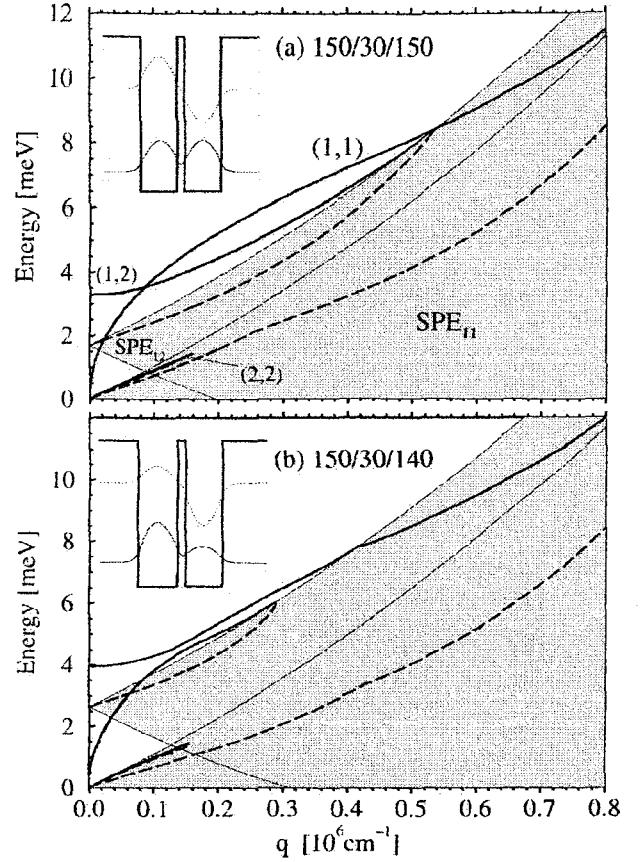

FIG. 1. Plasmon dispersions in two coupled GaAs/Al$_{0.3}$Ga$_{0.7}$As quantum wells of widths (a) $W_1 = W_2 = 150$ Å (symmetric) and (b) $W_1 = 150$ Å and $W_2 = 140$ Å (asymmetric); and separated by a barrier of width 30 Å. For the symmetric (asymmetric) situation the energy separation between the two subbands is $\omega_0 = 1.68$ meV ($\omega_0 = 2.62$ meV). The shadow areas present the single-particle excitation regions SPE$_{nn'}$, where $\text{Im}\{\Pi_{nn'}^0(q,\omega)\} \neq 0$. Each structure is shown in the inset where $\phi_1(z)$ and $\phi_2(z)$ are schematically shown by the solid and dot lines, respectively.

tive scattering rate discussion. Our numerical results of course include all contributions as obtained by evaluating the 2D integrals in Eqs. (20)–(27).

Figure 1(b) shows the same plasmon dispersion relation as in Fig. 1(a) but now in two coupled *asymmetric* quantum wells with interwell tunneling. Here, one well is of width 150 Å and the other is of width 140 Å. For these parameters, the Fermi wave vector in the subband 1 and 2 are $k_{F1}^a \approx 0.93 \times 10^6$ cm^{-1} and $k_{F2}^a \approx 0.62 \times 10^6$ cm^{-1}, respectively (the superscript a stands for asymmetric). Both subbands are occupied with $n_1 \approx 1.37 \times 10^{11}$ cm^{-2} and $n_2 \approx 0.63 \times 10^{11}$ cm^{-2}. In this asymmetric situation, the plasmon modes are obtained directly from the roots of Eq. (34). We show in Fig. 1(b) all these roots. We mention that it does not make sense naming the solid lines as pure intra- or intersubband plasmon modes because the structural asymmetry leads to a strong coupling (or mixing) between them, and this intrasubband-intersubband mode coupling eliminates the simplicity of Fig. 1(a). The solid line that is of finite frequency as $q \rightarrow 0$ in Fig. 1(b) is the intersubbandlike plasmon

mode (1,2). This mode enters the continuum SPE_{12} at q $\cong 0.42 \times 10^6$ cm^{-1} and should be, in principle, Landau damped. For small values of q, we find the same number of roots as in the symmetric situation. The interactions V_J and V_H are finite in the asymmetric case and are responsible for the strong mixing between the intrasubbandlike plasmon mode (1,1) and the intersubbandlike mode (1,2) around q $\cong 0.18 \times 10^6$ cm^{-1}. Moreover, when the asymmetry is introduced, the depolarization shift (i.e., the shift of the intersubband plasmon from the subband energy separation E_{21}) in the intersubbandlike plasmon (1,2) at $q = 0$ decreases. We point out that these roots of Eq. (34) do not provide a complete description of the plasmon modes in asymmetric bilayer structures. A detailed theoretical calculation of the dynamical structure factor giving the plasmon spectral weight provides a complete picture of the collective mode spectra and can be obtained using our multisubband theory.

Having studied the plasmon dispersion relations we now investigate in Fig. 2(a) the corresponding total inelastic Coulomb scattering rate $\sigma_1(k)$ (thick solid line) and $\sigma_2(k)$ (thick dashed line) of fast electrons in the subband 1 and 2, respectively, as a function of wave vector k in our symmetric bilayer structure. The symbols on the thin lines identify the contributions to $\sigma_1(k)$ and $\sigma_2(k)$ coming from the emission of single-particle and collective excitations individually. The dynamically screened Coulomb interaction components entering in Eqs. (20)–(27) can be calculated from Eqs. (13) and (14). After some algebra, we get

$$V^s_{1111} = \frac{V_A(1 - V_B\Pi^0_{22}) + V^2_C\Pi^0_{22}}{\varepsilon_{\mathrm{intra}}}, \qquad (37)$$

$$V^s_{2222} = \frac{V_B(1 - V_A\Pi^0_{11}) + V^2_C\Pi^0_{11}}{\varepsilon_{\mathrm{intra}}}, \qquad (38)$$

and

$$V^s_{1221} = V^s_{2112} = \frac{V_D}{\varepsilon_{\mathrm{inter}}}. \qquad (39)$$

For the symmetric well case the off-diagonal components of the Coulomb potential all vanish by parity: $V^s_{1112} = V^s_{1121}$ $= V^s_{1211} = V^s_{2111} = V^s_{2221} = V^s_{2212} = V^s_{2122} = V^s_{1222} = 0$ because V_J $= V_H = 0$ for symmetric systems. Therefore, according to Eqs. (20)–(29), the total inelastic scattering rates in the subband 1 and 2 are

$$\sigma_1(k) = \sigma_{1111} + \sigma_{1221} \qquad (40)$$

and

$$\sigma_2(k) = \sigma_{2222} + \sigma_{2112}, \qquad (41)$$

respectively. The terms σ_{1111}, σ_{1221}, σ_{2222}, and σ_{2112} involve integrations of the interactions V^s_{1111}, V^s_{1221}, V^s_{2222} and V^s_{2112}, respectively, in Eqs. (20), (21), (27), and (26). The self-energy components in Eqs. (22)–(25) are zero in the symmetric case. *Intrasubband* contributions to the scattering rates arise from the terms σ_{1111} and σ_{2222}, while *intersubband* contributions are due to the terms σ_{1221} and σ_{2112}. The
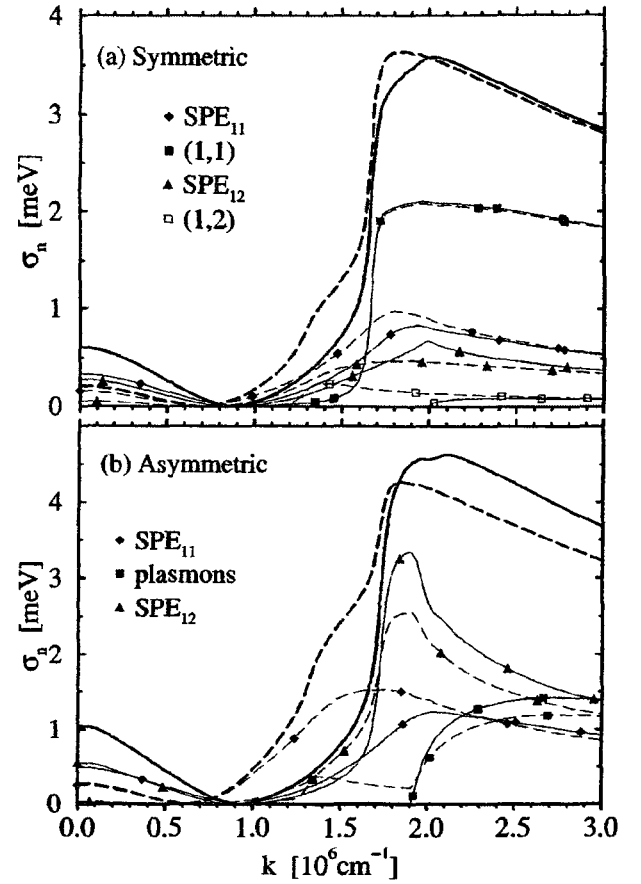

FIG. 2. Total inelastic Coulomb scattering rate of electrons in our coupled bilayer (a) symmetric and (b) asymmetric structures. The thick solid and thick dashed lines denote the total scattering rate $\sigma_n(k)$ for $n = 1$ and 2, respectively. The symbols on the thin lines represent each contribution to the total calculated scattering: diamonds standing for the SPE_{11} contribution, the filled squares stand for the intrasubband (1,1) plasmon contribution, triangles stand for the SPE_{12} contribution, and opaque squares stand for the intersubband (1,2) plasmon contribution.

contributions coming from the plasmon modes (filled-square lines) are obtained separately by excluding the continua SPE_{11} and SPE_{12} from the numerical integrations, whereas contributions coming only from the single-particle continua are obtained by numerically evaluating Eqs. (21) and (26) only for the region representing each continuum. Single-particle excitations contribute for all values of wave vectors k. However, neither intra- nor intersubband plasmon mode contributes to the scattering rates close to k^{sy}_{F1} or k^{sy}_{F2}. These collective modes provide excitation channels for inelastic relaxation only above some threshold wave vectors. The intrasubband plasmon mode (1,1) begins to contribute to either $\sigma_1(k)$ or $\sigma_2(k)$ when the wave vector is larger than the same threshold $k^{sy}_{11} \cong 1.65 \times 10^6$ cm^{-1}. On the other hand, the contribution coming from the plasmon mode (1,2) has a different threshold for each scattering rate. This mode begins contributing to $\sigma_1(k)$ and $\sigma_2(k)$ when the wave vector is larger than the thresholds $k^{sy}_{12} \cong 1.25 \times 10^6$ cm^{-1} and $k^{sy}_{12'}$ $\cong 2.0 \times 10^6$ cm^{-1}, respectively (notice that $k^{sy}_{F2} < k^{sy}_{F1} < k^{sy}_{12}$

$<k_{11}^{sy}<k_{12'}^{sy})$. Obviously, these thresholds depend on the particular choice of sample parameters. In the present paper, they are smooth (instead of being a very sharp threshold) because we are considering the impurity-induced constant $\gamma=0.2$ meV in our numerical evaluation. These thresholds become much sharper for smaller values of γ without any other substantive changes in our numerical results.

Figure 2(b) shows the same results as in Fig. 2(a) but for the asymmetric bilayer system of Fig. 1(b). In contrast to the symmetric case, where we were able to separately obtain the inter- and intrasubband plasmon modes through the roots of $\varepsilon_{inter}=0$ and $\varepsilon_{intra}=0$, respectively; the coupled plasmon dispersion in the asymmetric system is obtained directly from the numerical roots of Eq. (34) in which the bare off-diagonal Coulomb interactions V_J and V_H are now nonvanishing. The terms in Eq. (34) involving V_J and V_H are responsible for the mixing between the inter- and intrasubband plasmon modes and for not allowing the contributions coming from the intra- and intersubbandlike plasmon modes (1,1) and (1,2) to be picked up completely separated from each other in the scattering rate. Notice that the dynamically screened Coulomb potential V_{ijlm}^s is a full 16×16 matrix (for the two-subband model—in general, it is an $n^4 \times n^4$ matrix for an n-subband problem) in the present situation and is obtained from Eq. (13), which involves the dielectric matrix $\varepsilon_{ijlm}(q,\omega)$ and the bare Coulomb interactions V_A, V_B, V_C, V_D, V_J, and V_H (all of which are finite in this strongly coupled asymmetric bilayer structure).[9] Therefore, both inelastic scattering rates $\sigma_1(k)$ and $\sigma_2(k)$ in the asymmetric case contain all terms shown in Eqs. (20)–(27), which are finite in this situation. For the sake of clarity and to understand Fig. 2(b) in the same way as done for Fig. 2(a), we choose to show three contributions to the inelastic scattering rates $\sigma_1(k)$ and $\sigma_2(k)$ in Fig. 2(b) separately: the single-particle excitations in the continua (i) SPE_{12} (up triangles) and (ii) SPE_{11} (diamonds); and (iii) the plasmon mode segment outside these continua (filled squares). The filled squares in Fig. 2(b) represent contributions coming from those segments of the plasmon modes that lie outside any single-particle excitation continua [see Fig. 1(b)]. Contributions coming from the plasmon segments lying inside each continuum have been kept in our numerical work along with the single-particle excitation contributions because it is essentially numerically impossible to separate the two in this regime. We should mention that, due to the fact that one is not able to eliminate the contributions coming from the overdamped plasmon modes lying inside the Landau continua, the thin lines in Fig. 2(b) only serve as a qualitative illustration.[10]

B. Coulomb coupled bilayers with no interwell tunneling

Now we investigate the two Coulomb coupled identical symmetric quantum wells of width $W_1=W_2=150$ Å each with no interwell tunneling (i.e., the interwell barrier is taken to be infinity) and with a barrier width of 30 Å. Here, the Fermi wave vectors in the two wells are of the same value, i.e., $k_{F0}=k_{F1}=k_{F2}=0.79 \times 10^6$ cm^{-1} (or, equivalently, $n_1 = n_2 = 10^{11}$ cm^{-2}). Notice that the indices 1 and 2 should
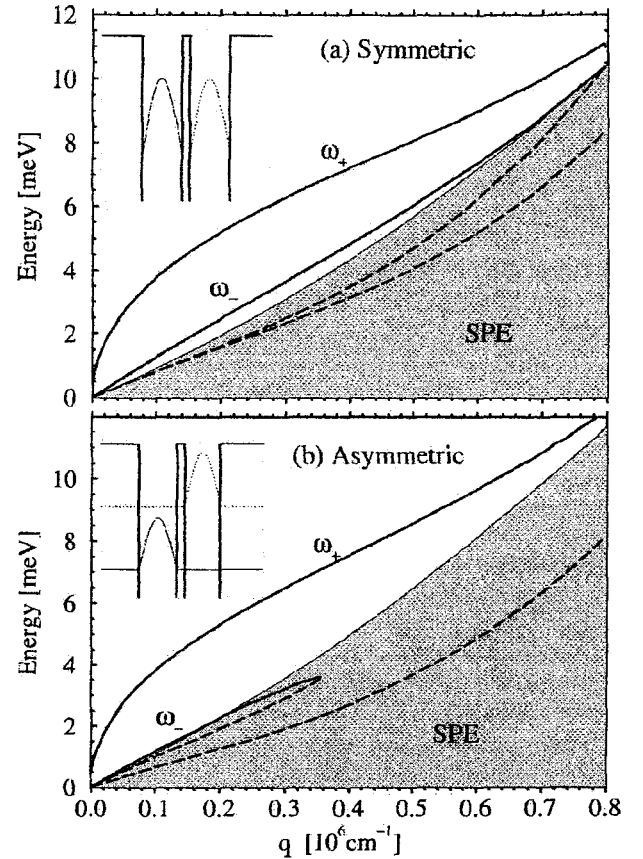

FIG. 3. Plasmon dispersions in two coupled with no interwell tunneling GaAs/Al$_{0.3}$Ga$_{0.7}$As quantum wells of widths (a) $W_1 = W_2 = 150$ Å and (b) $W_1 = 150$ Å (symmetric) and $W_2 = 142.4$ (asymmetric) Å, and separated by an infinity barrier of width 28.87 Å. The shadow areas present the single-particle excitation regions SPE_{11}, where $Im\{\Pi_{11}^0(q,\omega)\} \neq 0$. Each structure is shown in the inset where $\phi_1(z)$ and $\phi_2(z)$ are schematically shown by the solid and dotted lines, respectively.

now be treated as well indices since there is no tunneling-induced bonding-antibonding states. As we mentioned in the Introduction, an energy degeneracy arises in this case, i.e., $E_1=E_2$ because the two wells are identical with no interwell tunneling. If there is no tunneling, the bare Coulomb potential components $V_J=V_H=V_D=0$ and the polarizability $\Pi_{12}^0 = \Pi_{21}^0 = 0$ independent of whether the bilayer structure is symmetric or not. Besides, for this symmetric no-tunneling bilayer structure, the bare Coulomb potential $V_A=V_B$ by symmetry and the polarizability $\Pi_{11}^0 = \Pi_{22}^0 = \Pi_0$ due to the fact that the densities in each well are identical.

According to Eqs. (34)–(36), therefore, the plasmon dispersion relation should be obtained only from the roots of

$$\varepsilon_{nt}^{sy} = (1 - V_A\Pi_0)^2 - V_C^2\Pi_0^2 = 0. \qquad (42)$$

Here, the subscript (superscript) nt (sy) stands for no tunneling (symmetric). As shown in Fig. 3(a), we find four roots of Eq. (42). The solid curves correspond to the in-phase optical, $\omega_+(q)$, and the out-of-phase acoustic, $\omega_-(q)$, plasmon

modes in the bilayer structure.[11] These $\omega_\pm(q)$ modes have been observed[12] in multilayer semiconductor systems via inelastic light scattering spectroscopic experiments. They represent in-phase and out-of-phase interlayer density fluctuation modes: the out-of-phase acoustic mode, $\omega_-(q\to 0) \sim O(q)$ represents densities in the two layers fluctuating out of phase with a linear wave vector dispersion and the in-phase optical mode, $\omega_+(q\to 0) \sim \sqrt{N_e q}$, represents densities in the two layers fluctuating in phase with the usual 2D plasma dispersion. The dashed lines represent the collective modes that should be strongly Landau damped by the single-particle excitation continuum SPE, i.e., the region where $\mathrm{Im}\{\Pi_0(q,\omega)\} \neq 0$.

Figure 3(b) shows the same quantities as in Fig. 3(a) but for an asymmetric no-tunneling situation with the two wells being different, one with a width of $W_1 = 150$ Å and the other a width of $W_2 = 142.4$ Å. In this case, our no-tunneling bilayer structure is no longer invariant under space inversion and, consequently, the energy level degeneracy is broken, leading to the energy $E_1 < E_2$. Besides, the bare Coulomb potential V_A is now different from V_B. As we discussed before, the two wells now have different charge densities but we consider the whole system still being in equilibrium. Furthermore, the Fermi wave vector in the first and second subbands is the same as indicated before, i.e., k_{F1}^a and k_{F2}^a, respectively. Because of the densities in the two wells being different from each other, the polarizability $\Pi_{22}^0 \neq \Pi_{11}^0$. The shadow area in Fig. 3(b) is the single-particle excitation continuum in the wider quantum well, i.e., the region where $\mathrm{Im}\{\Pi_{11}^0(q,\omega)\} \neq 0$. The plasma dispersion relation is now given by the roots of the Eq. (35). Note that all plasma modes in the zero tunneling system are by definition intrasubband plasmons in our model where higher subbands are neglected.

As shown in Fig. 3(b), we again find four roots of such an equation and consider that the dashed lines should be strongly Landau damped modes since they are inside the single-particle continua. Furthermore, it does not make sense, in principle, to define the solid lines in Fig. 3(b) as pure acoustic or optical plasmon modes because the asymmetry leads to a difference between the electron densities in each layer. Now, the wider well has 30% more electrons than the narrower one, and, consequently, the densities in the two layers are not fluctuating exactly either in phase or out of phase. The solid lines in Fig. 3(b) are the approximate acoustic- and optical-like plasmon modes with the strict distinction meaningful only in the long-wavelength limit. Due to the structural asymmetry the acousticlike plasmon mode enters the SPE continuum at a smaller wave vector, leading to significant Landau damping of the acoustic plasmon mode by single-particle excitations in the asymmetric bilayer system. In the single-particle continuum of the layer 2 (the narrower well) the acousticlike plasmon mode is completely suppressed and we find no acousticlike mode in the $\mathrm{Im}\{\Pi_{22}^0(q,\omega)\} \neq 0$ regime. In general the acousticlike plasmon mode is found to be much more sensitive to small asymmetry effects than the optical-like plasmon mode.[13]

This is physically reasonable and should be experimentally tested via inelastic light scattering experiments.

Now we concentrate on the investigation of the scattering rates $\sigma_1(k)$ and $\sigma_2(k)$ in the symmetric bilayer structure with no tunneling. As the bare Coulomb potential $V_J = V_H = V_D = 0$, it is straightforward to see that only V_{1111}^s and V_{2222}^s are finite in the screened Coulomb interaction matrix V^s for a bilayer structure without any tunneling. Therefore the scattering rates in Eqs. (21)–(26) all vanish by symmetry in this case. The only nonvanishing terms to be calculated are σ_{1111} and σ_{2222} in Eqs. (20) and (27), respectively. Furthermore, as we discussed before, we have the polarizability $\Pi_{11}^0 = \Pi_{22}^0 = \Pi_0$ and the bare potential $V_A = V_B$ for identical (i.e., symmetric case) quantum wells. According to Eqs. (37) and (38), therefore, the screened Coulomb potential is given by

$$V_{1111}^s = V_{2222}^s = \frac{V_A(1 - V_A \Pi^0) + V_C^2 \Pi^0}{\varepsilon_{nt}^{sy}} \qquad (43)$$

in the present situation of a symmetric bilayer system with no interwell tunneling. In fact, the total inelastic Coulomb scattering $\sigma_1(k)$ and $\sigma_2(k)$ are identical because the two wells are identical with the same density. The thick line shown in Fig. 4(a) represents the total inelastic scattering rate, which is equal $[\sigma_1(k) = \sigma_{1111} = \sigma_2(k) = \sigma_{2222}]$ in both subbands, as a function of the wave vector k. To show separately the contributions coming from the emission of plasmons (squares) and single-particle excitations (diamonds), we again exclude the region where $\mathrm{Im}[\Pi_0(q,\omega)] \neq 0$ from the numerical calculations to obtain the plasmon contribution. Single-particle excitations again contribute at all values of the wave vector, whereas the plasmons begin contributing to the scattering rate for wave vectors k larger than the Fermi wave vector k_{F0}. There are clearly two thresholds wave vectors in the plasmon contribution (squares), one at $k = k_{ac}^{sy} \simeq 1.25 \times 10^6$ cm^{-1} and other at $k = k_{op}^{sy} \simeq 1.65 \times 10^6$ cm^{-1}. These are the thresholds for the emission of the acoustic and the optical plasmon, respectively. The substantial difference between Figs. 4(a) and 2(a) demonstrates the strong effect of tunneling on the inelastic scattering rates in bilayer structures. This is one of the important qualitative results in our paper.

Figure 4(b) shows the same results as in Fig. 4(a) but for the asymmetric bilayer structure without tunneling. As we discussed before, the asymmetry leads to $\Pi_{22}^0 \neq \Pi_{11}^0$. Furthermore, the bare Coulomb potential $V_A \neq V_B$ and, therefore according to Eqs. (37) and (38), the screened Coulomb potential $V_{1111}^s \neq V_{2222}^s$ in the asymmetric case. In this situation, $\sigma_1(k) = \sigma_{1111}$ (thick solid line) and $\sigma_2(k) = \sigma_{2222}$ (thick dashed line) represent the total inelastic Coulomb scattering rates in the wider and narrower layer, respectively. They are different from each other because the two wells have different widths and densities in the asymmetric situation. Again, we separate the different contributions (by plasmons and by SPE) by excluding the single-particle excitation continuum SPE from the numerical calculations to obtain the plasmon contribution. It is important to point out again that the
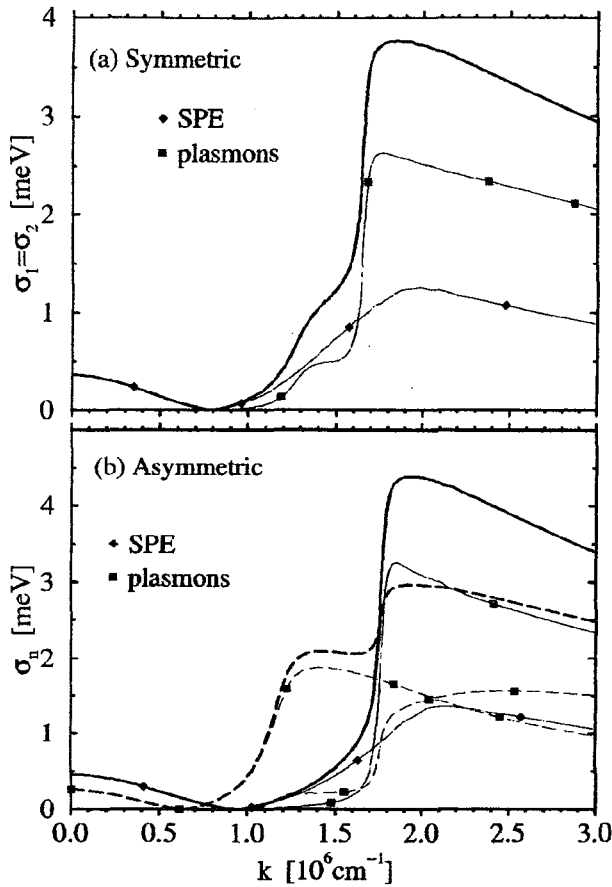
FIG. 4. Total inelastic Coulomb scattering rate of electrons in our coupled bilayer (a) symmetric and (b) asymmetric structures with no tunneling. In (b), the thick solid and thick dashed lines denote the total scattering rate $\sigma_n(k)$ for $n=1$ and 2, respectively. The symbols on the thin lines represent each contribution to the total scattering: diamonds stand for the SPE contributions, and the filled squares stand for the plasmon contributions.

squares in Fig. 4(b) represent contributions coming from the emission of undamped plasmon modes whose frequency $\omega(q)$ lies outside the continuum SPE [see Fig. 3(b)]. There is only one threshold wave vector $k\approx1.71\times10^6$ cm^{-1} in the thin solid line (squares) corresponding the plasmon contribution to $\sigma_1(k)$. This threshold is due to the emission of the optical-like plasmon mode shown in Fig. 3(b). We also find that the thin solid line (diamonds) corresponding to the SPE contribution to $\sigma_1(k)$ does not contain any contribution coming from the acousticlike plasmon mode. As a matter of fact, there is no contribution to $\sigma_1(k)$ in Fig. 4(b) coming from the emission of the acousticlike plasmon mode at all because the integral in $\sigma_1(k)$ does not contain any segment representing the acousticlike plasmon mode which is heavily Landau damped in the asymmetric situation under consideration. On the other hand, the thin dashed line (squares), corresponding to the plasmon contribution to $\sigma_2(k)$, clearly has two threshold wave vectors $k\approx1.15\times10^6$ cm^{-1} and k $\approx1.76\times10^6$ cm^{-1}, which characterizes the emission of the acoustic- and optical-like plasmon mode, respectively. Thus, in the asymmetric case, the acoustic-like plasmon modes

contribute to carrier scattering $\sigma_2(k)$ in the narrower well but not to $\sigma_1(k)$ in the wider well by virtue of strong Landau damping. The difference between Figs. 2(b) and 4(b) represents the strong effect of tunneling on the second component of the inelastic scattering rates $\sigma_2(k)$ in bilayer asymmetric structures.

C. Single symmetric quantum well

We now consider (for the sake of comparison) a single symmetric GaAs-Al$_x$Ga$_{1-x}$As quantum well of width 300 Å, barrier height 228 meV, and with the same total electron density $N_e=2\times10^{11}$ cm^{-2} as used before. These sample parameters lead to the Fermi wave vector in the first subband $k_{F1}^{single}\approx1.13\times10^6$ cm^{-1} with only one subband occupancy. Here, the second subband is empty, which leads to $\Pi_{22}^0=0$. As we discussed before, only the bare Coulomb potential V_A, V_B, V_C, and V_D are finite because $V_J=V_H=0$ in symmetric structure. According to Eqs. (35) and (36), therefore, the intra- and intersubband plasmon modes are obtained from the roots of the equations

$$\varepsilon_{intra}^{single}=(1-V_A\Pi_{11}^0)=0$$

and

$$\varepsilon_{inter}^{single}=1-V_D(\Pi_{12}^0+\Pi_{21}^0)=0.$$

Taking $\Pi_{22}^0=0$ (unoccupied excited subband) in Eqs. (37), (38), and (39) we get

$$V_{1111}^s=\frac{V_A}{\varepsilon_{intra}^{single}}, \tag{44}$$

$$V_{2222}^s=\frac{V_B(1-V_A\Pi_{11}^0)+V_C^2\Pi_{11}^0}{\varepsilon_{intra}^{single}}, \tag{45}$$

and

$$V_{1221}^s=V_{2112}^s=\frac{V_D}{\varepsilon_{inter}^{single}}. \tag{46}$$

Again in this case, the screened Coulomb potential V_{1112}^s $=V_{1121}^s=V_{1211}^s=V_{2111}^s=V_{2221}^s=V_{2212}^s=V_{2122}^s=V_{1222}^s=0$ by symmetry because $V_J=V_H=0$. Therefore, as we discussed in the Sec. III A, the total inelastic scattering rates in the first and the second subband are given by Eqs. (40) and (41), respectively. In the same way as done for the bilayer structures, we present the scattering rates $\sigma_1(k)$ and $\sigma_2(k)$ in Fig. 5 in the thick solid and thick-dashed lines, respectively. The symmetric nature of the single-well system enables us to separate out the different contributions to the scattering rates as discussed before. We find that contributions to $\sigma_1(k)$ come mainly from the emission of both the intrasubband plasmons (1,1) and the intrasubband single-particle excitations SPE$_{11}$. The emission of intersubband excitations turn out to make negligible contributions to the scattering because of the sufficiently large energy gap between the two subbands ($\omega_0=E_{21}=14.63$ meV). For this particular choice of
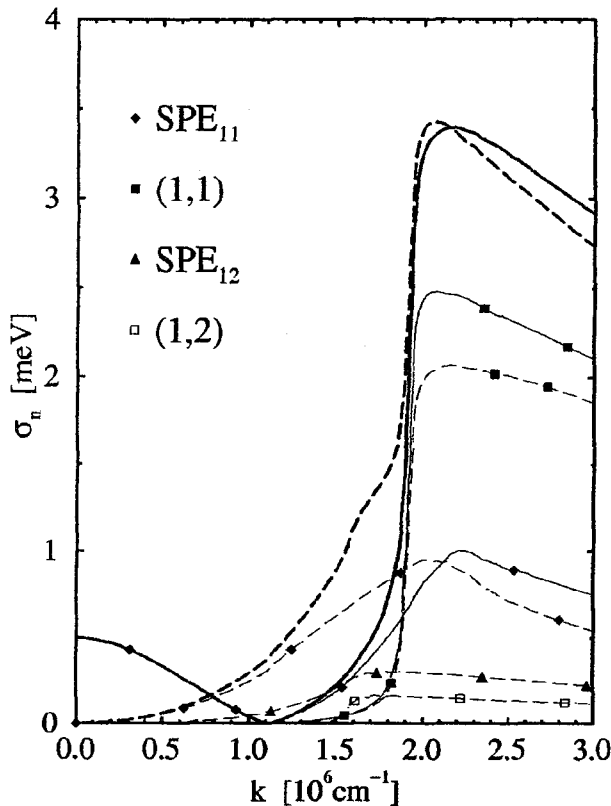
FIG. 5. Total inelastic Coulomb scattering rate of electrons in a single quantum well. The thick solid and thick dashed lines denote the total scattering rate $\sigma_n(k)$ for $n=1$ and 2, respectively. The symbols on the thin lines stand for the same as indicated in Fig. 2(a).

the sample parameters, σ_{1111} turns out to be much larger than σ_{1221}, implying that the carrier relaxation process in the ground subband is almost entirely via intrasubband scattering. Another important point in Fig. 5 is that inter- and intrasubband plasmon modes as well as intra- and intersubband single-particle excitations contribute to the total inelastic

scattering rate $\sigma_2(k)$ in the second subband. Notice that, in contrast to the behavior of $\sigma_1(k)$, the total inelastic scattering rate in the second subband $\sigma_2(k)$ does not vanish for any wave vectors k. This is due the fact that there is no Fermi surface in the second subband. This should lead to qualitatively different effects in the measured carrier injected in the second subband compared with that in the ground subband.[14] This lifetime, which is inversely proportional to the total inelastic scattering rate $\sigma_2(k)$, should be finite for all finite wave vectors in the excited empty subband.

IV. CONCLUSIONS

We have developed a theory for calculating the inelastic relaxation rate for Coulomb scattering in coupled bilayer structures in semiconductor double quantum well systems. We use a many-body theory based on a multisubband generalized GW approximation with the inelastic scattering rate defined by the magnitude of the imaginary part of the on-shell electron self-energy. Effects of dynamical screening, mode coupling, and Fermi statistics are naturally included in our many-body theory. We demonstrate the usefulness of our theory by obtaining results for general representative two-subband model systems: Coulomb coupled bilayer GaAs-Al$_x$Ga$_{1-x}$As double quantum well structures both with and without interwell tunneling and also with and without interwell asymmetry in the system. Our theory naturally allows for distinguishing various physical mechanisms contributing to the inelastic scattering rate: intra- and intersubband contributions. We provide a critical qualitative discussion of these various contributions to scattering and comment on the effect of interwell tunneling and structural asymmetry in bilayer quantum wells.

[1] See, for example, the Proceedings of the 5th International Conference on Intersubband Transition in Quantum Wells (ITQW) [Physica E 7 (1/2) (2000)] for the latest status of the field.

[2] L. Zheng and S. Das Sarma, Phys. Rev. B **54**, 2751 (1996); P. Sotirelis, Paul von Allmen, and Karl Hess, ibid. **47**, 12 744 (1993).

[3] R. Jalabert and S. Das Sarma, Phys. Rev. B **40**, 9723 (1989).

[4] L. Hedin, Phys. Rev. **139**, A796 (1965); see also G. D. Mahan, *Many-Particle Physics* 2nd ed. (Plenum, New York, 1981).

[5] J. K. Jain and S. Das Sarma, Phys. Rev. B **36**, 5949 (1987); S. Das Sarma, ibid. **29**, 2324 (1984).

[6] S.-C. Lee and I. Galbraith, Phys. Rev. B **59**, 15 796 (1999).

[7] S. Das Sarma et al., Phys. Rev. B **19**, 6397 (1979); B. Y. K. Hu and S. Das Sarma, ibid. **48**, 5469 (1993); M. R. S. Tavares, S. Das Sarma, and G. Q. Hai, ibid. **63**, 045324 (2001).

[8] G. Q. Hai, N. Studart, F. M. Peeters, P. M. Koenraad, and J. H. Wolter, J. Appl. Phys. **80**, 5809 (1996).

[9] We do not present here the full $16\times16 V^s_{ijlm}$ or ε_{ijlm} matrix in the asymmetric situation because it is not particularly illuminating. In fact, it is much more convenient to evaluate everything numerically using the matrix inversion shown in Eqs. (13) and (14).

[10] Notice that, it is extremely difficult, by numerical means, to exclude contributions from those segments of the damped plasmon modes lying inside each single-particle continua when we are calculating the single-particle excitation contributions to the scattering rate.

[11] S. Das Sarma and A. Madhukar, Phys. Rev. B **23**, 805 (1981); D. Olego, A. Pinczuk, A. C. Gossard, and W. Wiegmann, ibid. **25**, 7867 (1982); D. S. Kainth, D. Richards, H. P. Hughes, M. Y.

Simmons, and D. A. Ritchie, *ibid.* **57**, R2065 (1998).

[12] A. Pinczuk, M. G. Lamont, and A. C. Gossard, Phys. Rev. Lett. **56**, 2092 (1986); G. Fasol, N. Mestres, H. P. Hughes, A. Fischer, and K. Ploog, *ibid.* **56**, 2517 (1986); S. Das Sarma and E. H. Hwang, *ibid.* **81**, 4216 (1998).

[13] G. Q. Hai and Marcos R. S. Tavares, Phys. Rev. B **61**, 1704 (2000); Marcos R. S. Tavares and G. Q. Hai, *ibid.* **61**, 7564 (2000).

[14] S. Q. Murphy, J. P. Eisenstein, L. N. Pfeiffer, and K. W. West, Phys. Rev. B **52**, 14 825 (1995).

Capítulo 3

Propriedades de transporte e espalhamento de impurezas ionizadas em estruturas semicondutoras com dopagem do tipo-delta

Um grande número de investigações experimentais foi realizado com respeito às propriedades de transporte e propriedades ópticas destas estruturas. Estes sistemas são interessantes para estudo dos mecanismos físicos fundamentais envolvidos em sistemas com **altas densidades de portadores** e com estruturas eletrônicas com um caráter de **multisubbandas** (várias subbandas ocupadas). Estas altas doses de dopagem com impurezas constituem ainda um novo sistema onde é possível estudar os mecanismos de espalhamento. Além do mais, novos dispositivos semicondutores estão sendo fabricados a partir destas estruturas tipo-delta.

Em sistemas semicondutores Q2D com alta dopagem, tais como semicondutores com dopagem planar, a distância média entre as impurezas é menor que o raio de Bohr efetivo. Geralmente, acredita-se que as correlações espaciais entre as impurezas tornam-se muito importantes para as propriedades de transporte. Por outro lado, o efeito de blindagem do gás de elétrons Q2D nos potenciais de espalhamento de impurezas ionizadas é o fator mais importante que modifica o potencial de espalhamento de impurezas ionizadas. Várias aproximações

de blindagens do gás de elétrons são usadas em sistemas Q2D. Os mecanismos de blindagem não foram ainda bem entendidos.

Em um dos nossos projetos, que começou em 1993, tratamos das propriedades de transporte eletrônico neste sistema em colaboração com o grupo experimental de *Eindhoven University of Technology*. Estudamos o transporte de elétrons e as mobilidades das subbandas em estruturas semicondutoras Q2D a baixas temperaturas. Os nossos cálculos descrevem de maneira correta e quantitativa os resultados experimentais para as mobilidades quânticas. No nosso trabalho, os mecanismos de espalhamento por impurezas ionizadas e os efeitos de blindagem foram estudados. Conseguimos os seguinte resultados principais:

1) Mostramos os acoplamentos intersubbandas tem um papel crucial nos espalhamentos por impurezas ionizadas e no transporte deste sistema de várias subbandas. As mobilidades das subbandas de maior energia são dominadas por tal acoplamento. Embora existam altas concentrações de impurezas nas estruturas tipo-delta, o espalhamento por impurezas ionizadas ainda pode ser descrito pelo potencial de Coulomb com blindagem. As correlações entre as impurezas podem ser introduzidas pelo fator de estrutura das distribuições de impurezas, que não deve levar a um aumento significativo da mobilidade no GaAs com estruturas planares dopadas com Si.

2) A aproximação de Thomas-Fermi e a aproximação onde são considerados apenas os elementos diagonais da matriz dielétrica de RPA (que são freqüentemente usados para sistemas Q2D e Q1D), não são capazes de descrever os efeitos de blindagens nestes sistemas com multisubbandas. Entretanto, a RPA com a completa dependência no vetor de onda q fornece uma razoável descrição dos resultados experimentais.

3) Mostramos também que as concentrações de aceitadores de fundo (*background*) modificam fortemente as mobilidades das subbandas mais altas e a mobilidade média de arrasto em GaAs com estruturas planares dopadas com Si. Tal efeito reflete a característica específica dos sistemas com dopagem tipo-delta onde o confinamento de elétrons é determinado simplesmente pelo potencial auto-consistente. Mostramos também os efeitos de acoplamento entre duas camadas de dopantes na mobilidade, bem como os efeitos do confinamento extra devido ao poço quântico (QW). Estes efeitos têm grande interesse experimental.

Multisubband electron transport in δ-doped semiconductor systems

Guo-Qiang Hai and Nelson Studart

Departamento de Física, Universidade Federal de São Carlos, 13565-905 São Carlos, São Paulo, Brazil

François M. Peeters

Department of Physics, University of Antwerp (UIA), B-2610 Antwerpen, Belgium

(Received 1 February 1995; revised manuscript received 11 May 1995)

The electron transport properties in δ-doped semiconductor systems are studied. The subband electronic structure of the δ-doped system is obtained by solving the coupled Schrödinger and Poisson equations. The screening of the quasi-two-dimensional electron gas is taken into account for the ionized impurity scattering through the matrix dielectric function within the random-phase approximation. The quantum and transport mobilities are calculated numerically as a function of the total electron density and the width of the doped layer at zero temperature. The intersubband scattering and the effect of empty subbands above the Fermi level on the electron mobilities are investigated. The calculated mobilities are in reasonable agreement with the available experimental results.

I. INTRODUCTION

In recent years, there has been increasing interest in the study of the electron transport properties in δ-doped semiconductor systems. The δ-doped systems are, in general, characterized by a rather high electron concentration, which makes them different from the other quasi-two-dimensional (Q2D) systems, such as heterojunctions and quantum wells. Typically, several subbands are occupied in a δ-doped system and the effects resulting from the occupation of several subbands are very important. An advantage of the actual system is that no interfaces are present to confine the electrons and ionized impurity scattering is by far the most important scattering mechanism.

A large number of experimental investigations[1-13] have been carried out on the electron transport properties in δ layers. However, the theoretical studies on the electron transport properties of δ-doped systems are limited in some way. Gillman *et al.*[2] reported the calculation results of temperature dependence of the average electron drift mobility in δ-doped GaAs and they found the same trends as found experimentally for the Hall mobility. But they did not give details about the calculation and the electron subband mobility at low temperature was not obtained. However, in δ-doped systems, the electrons in different subbands have very different mobilities. Gold *et al.*[14] studied theoretically the electron transport in structures with low doping concentration such that only the lowest subband is populated. They included the influence of the disorder in the doping layer on the density of states and screening effects. The mobility was calculated by using a multiple-scattering theory. Mezrin and Shik[15] calculated the electron mobility in heavily doped δ layers using screened Coulomb potential within the Thomas-Fermi approximation (TFA). Very recently, González, Krupski, and Szwacka[16] calculated the elec-

tron subband transport mobilities due to the ionized impurity scattering. The screening on the Coulomb scattering potential was taken into account within the random-phase approximation (RPA). In Refs. 15 and 16, the calculations for electron mobility were based on the electronic subband structure obtained within the semiclassical Thomas-Fermi approximation,[17,15] which yields analytical expressions for the effective confinement potential and subband wave functions. In doing so, they had assumed the impurity layer with zero thickness. Furthermore, the condition of a vanishing background acceptor concentration was used in Ref. 15. In order to introduce a finite background acceptor concentration, a variational approach was employed and the electron subband wave function and the transport mobilities were obtained up to three subbands in Ref. 16.

In this work, we study the electron subband mobilities in heavily doped δ layers. To describe the system more realistically in such a way that the results obtained can reflect the experimental situation, we calculate the electronic structure of the δ layer by solving self-consistently the coupled Schrödinger and Poisson equations. Although the calculation of the electron transport properties becomes more laborious using the numerical self-consistent results for the subband energies and wave functions, the distribution of the donors and acceptors and the exchange-correlation contribution of the 2D electron gas can be easily introduced. As a result, the influences of the doping concentration and the thickness of the doped layer on the electron subband mobility can be studied in contrast with previous works. In our calculation, the screening effects of the 2D electron gas on the scattering potential of the ionized impurity are included and the effect of the empty subbands above the Fermi level on the electron mobility is also investigated through the dielectric matrix within the RPA. The theory is applied to Si δ-doped GaAs structures.

52   8363

The paper is organized as follows. The electronic structure of the system is presented in Sec. II. In Sec. III, the scattering potential and screening effects on it are described. The transport mobility obtained from the Boltzmann transport equations within the relaxation time approximation and the quantum mobility coming from the linear response theory are exhibited in Sec. IV. The numerical results for the electron mobilities and the comparison with experiments are discussed in Sec. V. We present our concluding remarks in Sec. VI.

II. ELECTRONIC STRUCTURE OF THE SYSTEM

We consider the following impurity distribution for a Si δ-doped GaAs structure,

$$n_D(z) = \begin{cases} N_D/W_D, & |z| < W_D/2 \\ 0, & |z| > W_D/2, \end{cases} \qquad (1)$$

where N_D is the areal impurity concentration, W_D is the width of the doped layer, which is taken in the xy plane. For typical experimental conditions, we have $N_D \gtrsim 10^{12}/\text{cm}^2$ and $W_D \lesssim 100$ Å. At such a high doping level, the average distance between impurities is smaller than the effective Bohr radius $a_B = \hbar^2\epsilon_0/m^*e^2$ ($a_B \approx 100$ Å for GaAs) and the electron wave function of the individual Si donors overlaps strongly with each other. As a consequence, the donors no longer act as isolated trapping centers and an impurity band is formed just below the conduction band of GaAs. The electrons are free to move in the doping plane and they do not freeze out on the donors at low temperature. Due to the interaction between the ionized impurities and the delocalized electrons, an effective attractive potential is formed in the z direction, which confines the electrons close to the δ layer. The electron energy in this direction is quantized into discrete levels and a Q2D electron system is formed. In GaAs, a critical n-type doping concentration is about 0.3×10^{12} cm^{-2}.[13] In the low doping concentration regime below this critical Mott density, the electron wave functions of the individual donors do not have an important overlap with each other. No impurity band is formed and the conduction takes place by electrons that hop from one donor site to another. In this case, the electric conductivity vanishes at zero temperature. In the present work, we are interested in the electron transport in the δ-doped systems in the high doping concentration regime.

The conventional way to determine the electronic structure of the δ-doped system is to employ the so-called self-consistent calculation within the Hartree-Fock approximation.[18-20,11] It amounts to replace the exact many-particle potential by an average one. Each electron is assumed to move in a self-consistent potential $V_{sc}(z)$ and the coupled one-dimensional Poisson and Schrödinger equations have to be solved self-consistently. In such a calculation, the impurity distribution, the exchange-correlation potential of the 2D electron gas, and the nonparabolicity of the conduction band can be

included. In another way, the electron subband energy and wave functions of the δ-doped system can be obtained within the semiclassical TFA. It has been proven that for a system with zero-thickness doping layer and vanishing background acceptor concentration, such an approximation yields the results that are equivalent to those obtained from the self-consistent approximation.[17] The advantage of the TFA is that it gives an analytical expression for the effective confinement potential and subband wave functions. However, it is difficult to take into account the thickness of the doped layer and the acceptor background.

In this work, the subband wave functions are obtained from a self-consistent solution of the one-dimensional Schrödinger and Poisson equations. The total electron energy and wave function can be written as

$$E_n(\vec{k}_\parallel) = E_n + \varepsilon(\vec{k}_\parallel) \qquad (2)$$

and

$$\Psi_{n,\vec{k}_\parallel}(x,y,z) = \psi_n(z)\frac{1}{\sqrt{A}}\exp(i\vec{k}_\parallel \cdot \vec{r}_\parallel), \qquad (3)$$

where $n = 1, 2, ...,$ is the subband index, $\vec{r}_\parallel$ ($\vec{k}_\parallel$) is the electron position (wave vector) in the xy plane, E_n is the subband energy, $\psi_n(z)$ is the electron wave function in the z direction, $\varepsilon(\vec{k}_\parallel) = \hbar^2 k_\parallel^2/2m^*$ is the electron kinetic energy, m^* the electron effective mass, and A is the area of the sample.

The Schrödinger equation in the z direction is given by

$$-\frac{\hbar^2}{2m^*}\frac{d^2\psi_n(z)}{dz^2} + V_{sc}(z)\psi_n(z) = E_n\psi_n(z), \qquad (4)$$

where $V_{sc}(z) = V_H(z)+V_{xc}(z)$ is the effective confinement potential, which is composed as a sum of the Hartree potential $V_H(z)$ and exchange-correlation potential $V_{xc}(z)$. The Hartree potential, due to the electrostatic interaction of the electrons with themselves and with ionized impurities, is determined by the following Poisson equation:

$$\frac{d^2V_H}{dz^2} = \frac{4\pi e^2}{\epsilon_0}[n_e(z) - n_D(z) + n_A], \qquad (5)$$

where $n_e(z)$ is the electron concentration distribution and n_A is the ionized background acceptor concentration. In Eq. (5), we assumed that all the donors in the doping layer are ionized. At zero temperature, the electron distribution is obtained by

$$n_e(z) = \sum_{n=1}^{N} |\psi_n(z)|^2 \int_{E_n}^{E_F} \rho(E)dE, \qquad (6)$$

where N is the number of the occupied subbands, $\rho(E)$ is the electron density of states of the system, and E_F is the Fermi energy. For a parabolic conduction band, $\rho(E) = m^*/\pi\hbar^2$ is a constant for the 2D system. The effect of the nonparabolicity of the conduction band on the electronic subband structures can be included through

electron density of states (or the effective mass m^*). In the numerical calculations, we found that using the usual formalism for Q2D systems,[21] the nonparabolicity modifies the self-consistent solution slightly. So, we will not give the details here. The total electron density $N_e = \int_{-\infty}^{\infty} n_e(z)dz$ is determined by the difference between N_D and N_A, where N_A is the areal ionized acceptor concentration and can be estimated from the thickness of the depletion layer. For $n_A = 10^{14}/\mathrm{cm}^3$, $N_A \simeq 10^{11}/\mathrm{cm}^2$.

The exchange-correlation potential $V_{xc}(z)$ is a function of electron density and can be evaluated within the local-density approximation[22]

$$V_{xc}(z) = -\frac{e^2}{8\pi\epsilon_0 a_B}\frac{2}{\alpha\pi r_s}\left[1 + 0.0545\ln\left(1 + \frac{11.4}{r_s}\right)\right],$$
(7)

where $\alpha = (4/9\pi)^{1/3}$ and $r_s = [4\pi n_e(z)/3]^{-1/3}/a_B$.

We performed a self-consistent calculation for the subband electronic structures of a Si δ-doped GaAs system.
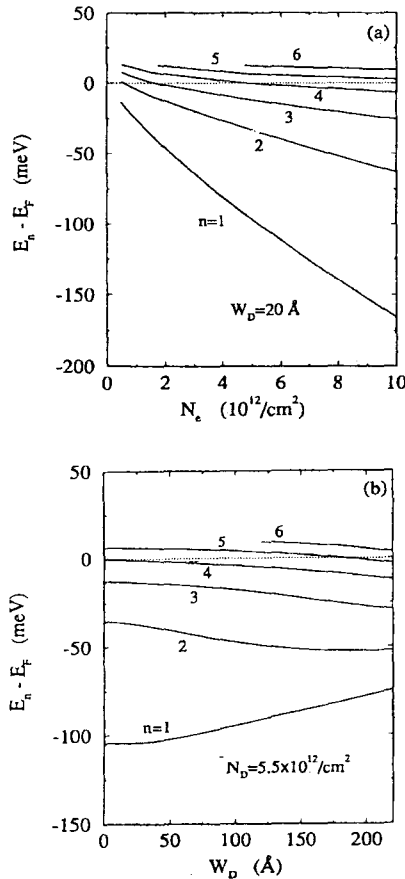
FIG. 1. The subband energy as a function of (a) total electron density for $W_D = 20$ Å and (b) the width of the doping layer for $N_D = 5.5 \times 10^{12}/\mathrm{cm}^2$. The dotted line indicates the Fermi level.

In the calculation, we took the parameters $m^* = 0.07m_0$, $\epsilon_0 = 13.18$, and $n_A = 10^{14}/\mathrm{cm}^3$. The electron exchange-correlation energy and the band nonparabolicity were included. We input the donor concentration N_D and the width of the doped layer W_D. The effective confining potential profile $V_{sc}(z)$, the subband energy E_n, the wave function $\psi_n(z)$, the Fermi energy E_F, and the subband electron population were obtained. We confirmed that the subband electron population density from our calculation is in good agreement with the electron densities obtained from Shubnikov–de Haas (SdH) experiments.[11,13]

Figure 1 shows the subband energy E_n as a function of (a) the total electron density N_e for $W_D = 20$ Å and (b) the thickness of the doped layer W_D for $N_D = 5.5 \times 10^{12}/\mathrm{cm}^2$. In the figure, the energy level E_n is measured from the Fermi energy E_F, which is indicated by the dotted line. In Fig. 1(a) for $W_D = 20$ Å, only the lowest subband is populated at low electron density (low doping concentration). With increasing N_e (or N_D), the effective confinement potential becomes narrow and deep. The distance between two levels increases and more subbands are populated. The $n=2$, 3, and 4 subbands begin to be occupied at $N_e = 0.58$, 1.62, and $4.76 \times 10^{12}/\mathrm{cm}^2$, respectively. With increasing W_D, we also find that more subbands are populated as shown in Fig. 1(b). In this case, however, the total electron density is fixed. Wide doped layers lead to a broad and shallow confinement potential.

III. SCATTERING POTENTIAL AND SCREENING

In the following, we will consider only the ionized donor scattering because it is the most important scattering mechanism for the considered system. The ionized impurities scattering potential is given by

$$V(\vec{r}) = -\sum_i \frac{e^2}{\epsilon_0}\frac{1}{|\vec{r} - \vec{R}_i|},$$
(8)

where $\vec{R}_i$ is the position of the impurity, the sum runs over all the impurities in the system which are distributed randomly in the doped layer. The two-dimensional Fourier transform of the scattering potential is given by

$$v(q_\parallel, z) = -\frac{2\pi e^2}{\epsilon_0 q_\parallel}\sum_i e^{-q_\parallel|z-z_i|}e^{i\vec{q}_\parallel\cdot\vec{R}_{\parallel i}},$$
(9)

where $\vec{R}_i = (\vec{R}_{\parallel i}, z_i)$.

In the calculation of the electron transport properties, we assume a parabolic conduction band. Using the Fermi golden rule, the electron transition probability from state $|n, \vec{k}_\parallel\rangle$ to $|n', \vec{k}_\parallel'\rangle$ for electron-impurity scattering is given by

$$W_{n,n'}(\vec{k}_\parallel, \vec{k}_\parallel') = \frac{2\pi}{\hbar}|u_{n,n'}(\vec{q}_\parallel)|^2\delta_{\vec{k}_\parallel'-\vec{k}_\parallel,\vec{q}_\parallel}$$
$$\times\delta[E_{n'}(k_\parallel') - E_n(k_\parallel)],$$
(10)

where $u_{n,n'}(\vec{q}_\parallel)$ is the transition matrix element due to the scattering.

The present system has a rather high electron density and consequently the screening of the scattering potential due to the electron gas will be significant. The screened ionized impurity potential can be obtained in terms of the static dielectric response function within RPA. Because of the occupation of several subbands, the dielectric function has a tensor character given by $\epsilon_{\alpha,\beta}(\vec{q}_\parallel) = \epsilon_{nn',mm'}(\vec{q}_\parallel)$, where $\alpha = (n,n')$, $\beta = (m,m')$. If we assume that the impurities are uniformly distributed in the doped layer and are uncorrelated, the square of the transition matrix element due to the screened Coulomb scattering potential is given by

$$|u_{n,n'}(\vec{q}_\parallel)|^2 = \left(\frac{2\pi e^2}{\epsilon_0 q_\parallel}\right)^2 \frac{N_D}{W_D} \int_{-W_D/2}^{W_D/2}$$

$$\times dz_i \left[\sum_\beta \epsilon_{\alpha,\beta}^{-1}(\vec{q}_\parallel) G_\beta(q_\parallel, z_i)\right]^2 \quad (11a)$$

and

$$G_\beta(q_\parallel, z_i) = \int_0^\infty dz \psi_m(z) \psi_{m'}(z)[e^{-q_\parallel|z-z_i|}$$

$$+ (-1)^{m+m'} e^{-q_\parallel|z+z_i|}], \quad (11b)$$

with the change in electron momentum due to scattering

$$q_\parallel = \left[(E_n - E_{n'})\frac{2m^*}{\hbar^2}\right.$$

$$\left. + 2k_\parallel^2 - 2k_\parallel \cos\theta \sqrt{(E_n - E_{n'})\frac{2m^*}{\hbar^2} + k_\parallel^2}\right]^{1/2} \quad (11c)$$

and θ is the angle between $\vec{k}_\parallel$ and $\vec{k}'_\parallel$.

In the above equations, $\epsilon_{\alpha,\beta}^{-1}(\vec{q}_\parallel)$ is the element of the inverse matrix of the dielectric response function, and the sum $\beta = (m,m')$ runs over all the subbands of the system. In actual calculations, however, we have to limit the β sum. In most previous works, only the matrix elements of the dielectric function associated with the occupied subbands were considered. Consequently for a system of N occupied subbands, the dielectric function $\epsilon_{\alpha,\beta}(\vec{q}_\parallel)$ is approximated by a $N^2 \times N^2$ matrix. Following this approach, the subband mobilities in heterojunctions with two occupied subbands were studied in Refs. 23–25. And those in a δ-doped system with three occupied subbands were calculated in Ref. 16.

The dielectric function within the RPA is given by

$$\epsilon_{\alpha,\beta}(q_\parallel) = \delta_{\alpha,\beta} + \frac{2}{a_B q_\parallel} F_{\alpha,\beta}(q_\parallel) \chi_\beta^0(q_\parallel), \quad (12a)$$

where

$$F_{\alpha,\beta}(q_\parallel) = \int_{-\infty}^\infty dz \psi_n(z) \psi_{n'}(z)$$

$$\times \int_{-\infty}^\infty dz' \psi_m(z') \psi_{m'}(z') e^{-q_\parallel|z-z'|} \quad (12b)$$

is the Coulomb form factor and $\chi_\beta^0(\vec{q}_\parallel)$ is the static electron density-density correlation function[23,24,26–28] without the electron-electron interaction. Notice that $\chi_{mm'}^0(\vec{q}_\parallel) = 0$ only when both the subbands m and m' are empty, and $\chi_{mm'}^0(\vec{q}_\parallel) \neq 0$ as long as one of the them is populated. It means that the unoccupied subbands have contributions to the intersubband interaction of the Q2D electron gases.[28] They could also influence the intrasubband interaction of the occupied subbands through the mode coupling between the intrasubband and intersubband excitations. Such an effect in the collective excitations of the Q1D electron system with a three-band model (one of them was empty), was investigated in Ref. 30.

IV. TRANSPORT EQUATIONS

Considering only the ionized impurity scattering, we calculate the electron subband quantum and transport mobilities. These are determined from the different scattering times connected to the average time between the scattering events. The quantum lifetime or the single particle relaxation time is the averaged elastic scattering time. On the other hand, in the transport lifetime or the momentum relaxation time, every scattering event is averaged over its projection of the outgoing wave vector on the incident direction.[13] The Boltzmann equation of the δ-doped system for steady-state transport can be written as

$$-\frac{e}{m^*} \hbar \vec{k}_\parallel \cdot \vec{E}_\parallel \frac{\partial f_n(\vec{k}_\parallel)}{\partial \varepsilon(\vec{k}_\parallel)} = \sum_{n',\vec{k}_\parallel'} W_{n,n'}(\vec{k}_\parallel, \vec{k}_\parallel')$$

$$\times [f_{n'}(\vec{k}_\parallel') - f_n(\vec{k}_\parallel)], \quad (13)$$

where $W_{n,n'}(\vec{k}_\parallel, \vec{k}_\parallel')$ is given by Eq. (10), and $f_n(\vec{k}_\parallel)$ is the electron distribution function. Notice that $W_{n',n}(\vec{k}_\parallel', \vec{k}_\parallel) = W_{n,n'}(\vec{k}_\parallel, \vec{k}_\parallel')$.

Within the relaxation time approximation, the distribution function can be written as[29,19]

$$f_n(\vec{k}_\parallel) = f_n^{(0)}(\vec{k}_\parallel) + \frac{e}{m^*} \hbar \vec{k}_\parallel \cdot \vec{E}_\parallel \frac{\partial f_n^{(0)}(\vec{k}_\parallel)}{\partial \varepsilon(\vec{k}_\parallel)} \tau_n^t(\varepsilon),$$

where $f_n^{(0)}$ is the Fermi-Dirac distribution function and $\tau_n^t(\varepsilon)$ is the so-called subband transport lifetime (momentum relaxation time). The Boltzmann equation can be reduced to a coupled linear equation about $\tau_n^t(\varepsilon)$.[29] At $T = 0$, only the electrons on the Fermi surface contribute to electric transport and we have $\tau_n^t = \tau_n^t(E_{Fn})$, where $E_{Fn} = E_F - E_n$. For a system of N subbands populated, the electron subband transport lifetime is determined by the equations

$$\sum_{n'=1}^N K_{n,n'} \tau_n^t = 1 \quad \text{for } n = 1, 2, ..., N \quad (14a)$$

with

$$K_{n,n} = \frac{m^*}{\pi\hbar^3}\left\{\int_0^\pi d\theta |u_{n,n}(q'_\parallel)|^2(1-\cos\theta)\right.$$

$$\left. + \sum_{n'\neq n}^{N}\int_0^\pi d\theta |u_{n,n'}(q'_\parallel)|^2\right\}, \qquad (14b)$$

and, for $n' \neq n$,

$$K_{n,n'} = \frac{m^*}{\pi\hbar^3}\sqrt{\frac{E_{Fn'}}{E_{Fn}}}\int_0^\pi d\theta |u_{n,n'}(q'_\parallel)|^2\cos\theta, \qquad (14c)$$

where

$$q'_\parallel = \frac{2m^*}{\hbar^2}\left[E_{Fn}+E_{Fn'}-2\sqrt{E_{Fn}E_{Fn'}}\cos\theta\right]^{1/2}. \qquad (14d)$$

The quantum mobility or the single-particle mobility τ_n^q is determined by the average scattering time. Within the linear response theory, the subband quantum lifetime is given by[24]

$$\frac{1}{\tau_n^q} = \frac{m^*}{\pi\hbar^3}\sum_{n'=1}^{N}\int_0^\pi d\theta |u_{n,n'}(q'_\parallel)|^2. \qquad (15)$$

From the transport and quantum lifetime, the electron subband transport mobility and quantum mobility can be obtained easily,

$$\mu_n^t = \frac{e}{m^*}\tau_n^t, \qquad \mu_n^q = \frac{e}{m^*}\tau_n^q. \qquad (16)$$

Notice that the empty subbands $n > N$ do not appear in the transport equations (14) and (15) which determine the electron mobilities. They are not involved in the scattering processes directly. However, the empty subbands influence the impurity scattering potential through screening effects, which is taken into account by the dielectric function.

V. NUMERICAL RESULTS AND DISCUSSION

Using the previous results for the transport properties, we calculated the electron transport mobility and the quantum mobility in the δ layer. In Fig. 2, the electron subband (a) quantum mobility and (b) transport mobility for the Si δ-doped GaAs structures of $W_D = 20$ Å are plotted as a function of the total electron density. The solid curves indicate the results considering only the N occupied subbands in the dielectric function, which is approximated by a $N^2 \times N^2$ matrix. The dashed and dotted curves present the results including one and two empty subbands, respectively, in the dielectric function, which is given by a $(N+1)^2 \times (N+1)^2$ and a $(N+2)^2 \times (N+2)^2$ matrix. It is seen that the empty subbands above the Fermi level indeed influence the electron mobility through the effect of the screening on the Coulomb scattering in the present multisubband system. Such an influence on the mobility of the electrons in the higher subband is stronger than in the lower ones. Both the quantum and transport mobilities coming from the
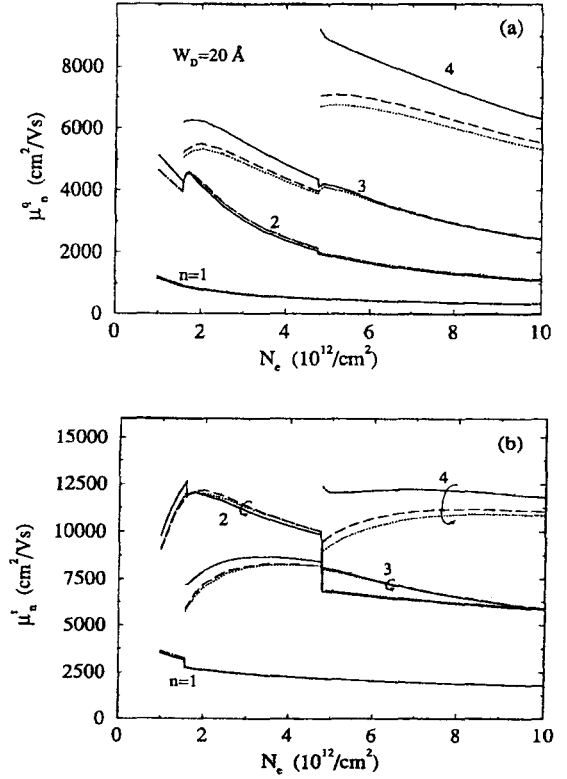
FIG. 2. The subband (a) quantum mobility and (b) transport mobility as a function of the total electron density for $W_D = 20$ Å. The solid, dashed, and dotted curves present the results including 0, 1, and 2 empty subbands in the dielectric matrix, respectively.

highest occupied subband are depressed due to the effects related to the empty subbands. However, such an influence on the mobilities from the lower subbands is not pronounced.

We found that the quantum mobility, as shown in Fig 2(a), increases with increasing subband index and decreases with increasing total electron density (or donor concentration). At the onset of occupation of a new subband, the theoretical subband mobility exhibits an abrupt jump. Such a discontinuity is due to the intersubband scattering and has been discussed in Refs. 16, 23, and 24 for the multisubband transport in Q2D systems. However, for the transport mobility, as shown in Fig. 2(b), $\mu_2^t > \mu_3^t$ when only three subbands are populated, which is qualitatively in agreement with the results in Ref. 16. This is mainly due to the fact that the wave function $\psi_2(z)$ is antisymmetric and has a node at $z = 0$. For a narrow doped layer, electrons in this subband have a smaller overlap with the impurities than those in the third subband and, consequently, the scattering is weaker. After the onset of occupation of the $n = 4$ subband, μ_2^t becomes smaller than μ_3^t. This is because $\psi_2(z)$ and $\psi_4(z)$ have the same parity, and the intersubband
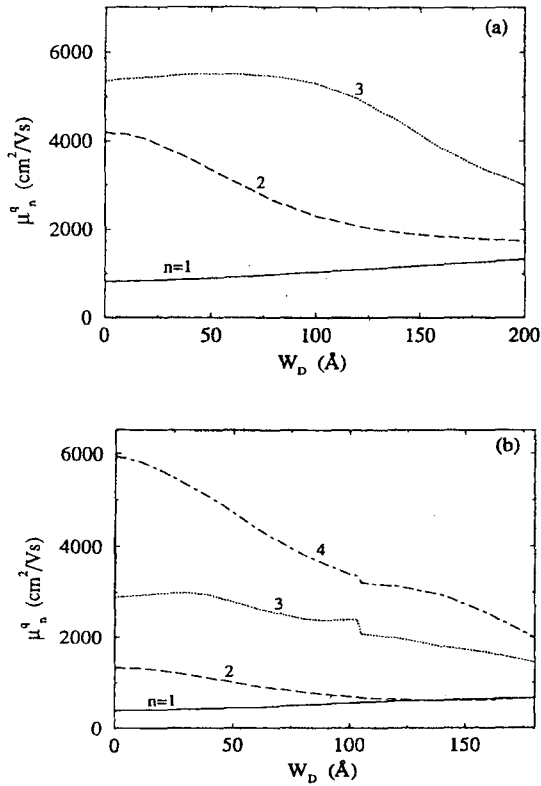
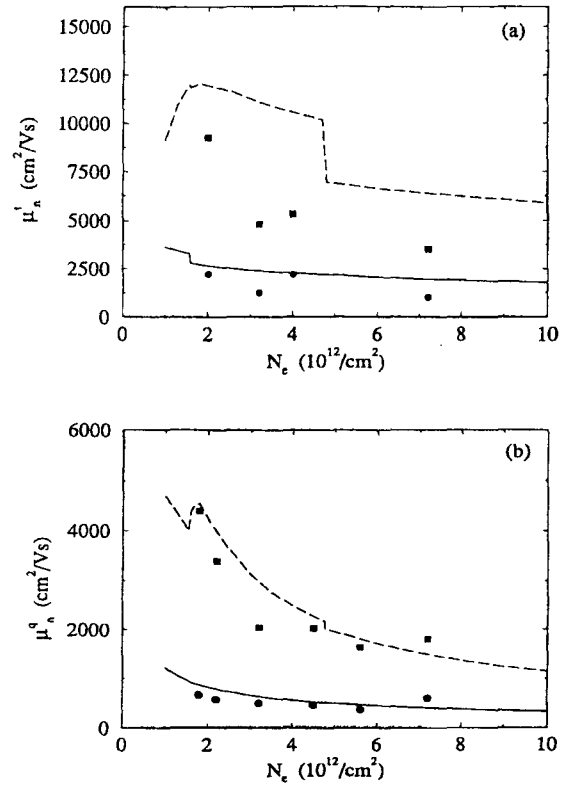FIG. 4. The same as Fig. 3 but now for the quantum mobility.

FIG. 5. The electron density dependence of (a) the transport mobility and (b) the quantum mobility in Si δ-doped GaAs. The solid and dashed curves present the calculated mobilities of the $n = 1$ and 2 subbands, respectively, for $W_D = 20$ Å. The experimental results are indicated by the solid circles ($n = 1$) and squares ($n = 2$). The experimental results are from Refs. 5 and 11, but the results at $N_e = 7.2 \times 10^{12}/cm^2$ are from Ref. 4 and the results of transport mobilities at $N_e = 4.0 \times 10^{12}/cm^2$ are from Ref. 7.

5(a) and 5(b), respectively. In this figure, the calculated mobilities of the first two subbands for $W_D = 20$ Å are given by the solid ($n = 1$) and dashed ($n = 2$) curves. The experimental results of a Si δ-doped GaAs are indicated by solid circles ($n = 1$) and squares ($n = 2$). For the transport mobility in Fig. 5(a), our calculation shows the correct qualitative behavior as found experimentally. Quantitatively, the calculated transport mobility of $n = 1$ subband has a better agreement with experimental measurements than that of $n = 2$ subband, which is about a factor of 2 larger than observed experimentally for $N_e > 3.0 \times 10^{12}/cm^2$. At the onset of the population of a new subband, the theoretical subband mobility exhibits an abrupt decrease, which is not seen experimentally. This is probably due to the fact that in real systems there exist thickness fluctuations in the doped layer, which lead to fluctuations in E_n. However, in Fig. 5(b), the calculated quantum mobility shows a quite good agreement with the experimental results.

In Fig. 6, the quantum mobility is given as a function of the width of doped layer W_D for Si δ-doped GaAs of $N_D = 5.5 \times 10^{12}/cm^2$. The theoretical (experimental) quantum mobilities are presented by solid curve (circles) for $n = 1$, dashed curve (squares) for $n = 2$, and dotted curve (triangles) for $n = 3$. We found that for the first two subbands, the calculated mobility is in good agreement with the experimental results. By increasing W_D, μ_1^q increases slowly and μ_2^q tends to μ_1^q at $W_D > 120$

FIG. 6. The dependence of quantum mobility on the width of the layer for Si δ-doped GaAs with $N_D = 5.5 \times 10^{12}/cm^2$. The solid, dashed, and dotted curves present the calculated results of the $n = 1$, 2 and 3, respectively. The experimental results are indicated by the solid circles ($n = 1$), squares ($n = 2$), and triangles ($n = 3$) (Refs. 11 and 13).

Å. For the higher subband $n = 3$, the calculated mobility shows qualitatively similar W_D dependence as found experimentally.

We also found that the ratio of the transport mobility to the quantum mobility from our calculation increases with increasing the doping concentration. But it is almost not influenced by the thickness of the doped layer. In the range of the doping concentration considered, it increases from three to six for the lowest two subbands and from one to three for the third one. Experimentally, this ratio was found to be in the range $1.3 - 2.9$ for the δ-layer structure[11,13] and it is about two for the δ-doped quantum wells.[9] The ratio of the transport to the quantum mobility reflects the nature of the scattering mechanism, i.e., long-range versus short-range scattering. It is seen that the present calculation yields a higher transport mobility than the experimental result. It seems that the model of the screened Coulomb scattering potential with static RPA describes the short-range scattering more exactly than the long-range scattering.

In the present calculation, only the scattering of ionized donors is considered. Even though ionized impurity scattering dominates the electron mobility in δ-doped systems, there are several unknown factors, which can modify the electron transport properties. For instance, from an experimental point of view, the profile of the impurity layer and the effective thickness of the doping layer are not always exactly known. In heavily doped semiconductor systems, the random distribution of the impurities induces a band tail and creates localized states. Then the density of states of the δ-doped system is no longer a steplike function. Because of the localized states and the deep level centers, the electron density becomes much lower than the intended doping concentration at high doping level. For the present system, this is expected to be relevant for $N_D > 6 \times 10^{12}$ cm^{-2}. Other scattering mechanisms will also influence the electron mobility slightly, such as scattering with ionized acceptors, neutral impurities, and the electron-electron interaction. Deep level centers and the presence of possible impurity clusters may also play a role. Because of the high impurity concentration, the correlation among the impurities becomes important and should be considered. Besides, the screening is an important factor that influences the electron-impurity scattering. In the theoretical study of the electron transport properties in Q2D systems, the static RPA screening is often used. In principle, all the energy states in the system, including the screening effects, and the full energy spectrum should be considered in the dielectric function within RPA for a multisubband system. In the present calculation, we included all the occupied subbands and two empty subbands above E_F in the dielectric function. In such a case, the numerical calculation was already very difficult for four or five populated subbands.

In our calculation, we assumed a steplike electron density of states for each subband of the Q2D systems. This is justified when the subbands are well separated in energy and are much larger than the band tail of localization states. This is the case for the first few subbands. When there is a band tail at the onset of subband occu-

pation, the Fermi level will cross the mobility edge of the subband leading to a different scattering rate.

VI. CONCLUSIONS

In summary, the electron transport properties in δ-doped semiconductor systems have been studied. Our mobility calculations were based on the self-consistent solution of the subband electronic structure and wave functions. The influences of the doping concentration and the thickness of the doped layer on the electron subband transport and quantum mobilities were investigated. The ionized donor scattering was considered and the screening was included within the static RPA for the multisubband 2D system. To the best of our knowledge, this is the first work where the self-consistent electronic structure of δ-layers has been used to investigate the subband quantum and transport mobilities. The effects due to the thickness of the doped layer on the subband mobility and due to use of empty subbands in the screening of 2D electron gas were also studied.

Our calculation shows that the electrons in the lowest subband have a low mobility, which is not much influenced by the doping concentration and the thickness of the doped layer. The mobilities due to the occupation of higher subbands are much bigger than those of the lowest one for small W_D, and they are strongly dependent on the different parameters. We demonstrated that intersubband scattering is also important, as we have seen at the onset of the occupation of a new subband. Although the empty subbands are not involved in the solution of the Boltzmann transport equation at zero temperature, they affect the electron mobility through screening effects on the scattering potential. The result of our calculation shows that the empty subbands modify the subband mobility, especially for the highest occupied subband. So, in this way our calculation includes the important effect of the mode coupling between the intrasubband and intersubband excitations that has been shown to be relevant in multisubband models of plasmon excitations. We also observed that is very important to obtain an accurate electronic structure for the mobility calculations. For instance, the position of the onset of the population of a new subband determines where a new scattering channel is introduced, which leads to the discontinuity in mobility.

Our calculated quantum mobilities of the lowest two subbands, both for N_e dependence and W_D dependence, are in quite good agreement with experimental results from Shubnikov–de Haas measurements.[11,13] The transport mobilities and the quantum mobilities of higher subbands have the same behavior as observed experimentally but, quantitatively, they are larger than experimental results.

[1] A. Zrenner, F. Koch, J. Leotin, M. Goiran, and K. Ploog, Semicond. Sci. Technol. **3**, 1132 (1988).

[2] G. Gillman, B. Vinter, E. Barbier, and A. Tardella, Appl. Phys. Lett. **52**, 972 (1988).

[3] E. F. Schubert, J. E. Cunningham, and W. T. Tsang, Solid State Commun. **63**, 591 (1987).

[4] E. Skuras, R. Kumar, R. L. Williams, R. A. Stradling, J. E. Dmochowski, E. A. Johnson, A. Mackinnon, J. J. Harris, R. B. Beall, C. Skierbeszewski, J. Singleton, P. J. van der Wel, and P. Wisnieski, Semicond. Sci. Technol. **6**, 535 (1991).

[5] P. M. Koenraad, F. A. P. Blom, C. J. G. M. Langerak, M. R. Leys, J. A. A. J. Perenboom, J. Singleton, S. J. R. M. Spermon, W. C. van der Vleuten, A. P. J. Voncken, and J. H. Wolter, Semicond. Sci. Technol. **5**, 861 (1990).

[6] P. M. Koenraad, B. F. A. van Hest, F. A. P. Blom, R. van Dalen, M. Leys, J. A. A. J. Perenboom, and J. H. Wolter, Physica B **177**, 485 (1992).

[7] G. M. Gusev, Z. D. Kvon, D. I. Lubyshev, V. P. Migal, and A. G. Pogosov, Fiz. Tekh. Poluprovodn. **25**, 601 (1991) [Sov. Phys. Semicond. **25**, 364 (1991)].

[8] I. A. Panaev, S. A. Studenikin, D. I. Lubyshev, and V. A. Migal, Semicond. Sci. Technol. **8**, 1822 (1993).

[9] J. J. Harris, R. Murray, and C. T. Foxon, Semicond. Sci. Technol. **8**, 31 (1993).

[10] X. Zheng, T. K. Carns, K. L. Wang, and B. Wu, Appl. Phys. Lett. **62**, 504 (1993).

[11] P. M. Koenraad, A. C. L. Heessels, F. A. P. Blom, J. A. A. J. Perenboom, and J. H. Wolter, Physica B **184**, 221 (1993).

[12] P. Sobkowicz, Z. Wilamowski, and J. Kossut, Semicond. Sci. Technol. **7**, 1155 (1992).

[13] P. M. Koenraad, in *Delta Doping of Semiconductors*, edited by E. F. Schubert (Cambridge University Press, Cambridge, 1995).

[14] A. Gold, A. Ghazali, and J. Serre, Semicond. Sci. Technol. **7**, 972 (1992).

[15] O. Mezrin and A. Shik, Superlatt. Microstruct. **10**, 107 (1991).

[16] L. R. González, J. Krupski, and T. Szwacka, Phys. Rev. B **49**, 11 111 (1994).

[17] L. Ioriatti, Phys. Rev. B **41**, 8340 (1990).

[18] A. Zrenner, F. Koch, and K. Ploog, Surf. Sci. **196**, 671 (1988).

[19] G. Bastard, *Wave Mechanics Applied to Semiconductor Heterostructures* (Halsted Press, New York, 1988), p. 193.

[20] M. H. Degani, Phys. Rev. B **44**, 5580 (1991).

[21] U. Ekenberg, Phys. Rev. B **36**, 6152 (1987); **40**, 7714 (1989).

[22] L. Hedin and B. I. Lundqvist, J. Phys. C **4**, 2064 (1971).

[23] S. Mori and T. Ando, Phys. Rev. B **19**, 6433 (1979).

[24] R. Fletcher, E. Zaremba, M. D'Iorio, C. T. Foxon, and J. J. Harris, Phys. Rev. B **41**, 10 649 (1990).

[25] W. Xu, F. M. Peeters, and J. T. Devreese, Phys. Rev. B **48**, 1562 (1993).

[26] F. Stern, Phys. Rev. Lett. **18**, 542 (1967).

[27] J. K. Jain and S. Das Sarma, Phys. Rev. B **36**, 5949 (1987).

[28] W. H. Backes, F. M. Peeters, F. Brosens, and J. T. Devreese, Phys. Rev. B **45**, 8437 (1992).

[29] E. D. Siggia and P. C. Kwok, Phys. Rev. B **2**, 1024 (1970).

[30] Q. Li and S. Das Sarma, Phys. Rev. B **40**, 5860 (1989); **43**, 11 768 (1991).

[31] W. A. Beck and J. R. Anderson, J. Appl. Phys. **62**, 541 (1992).

HAI, G.-Q.; STUDART, N.; PEETERS, F. M.; KOENRAAD, P.M.; WOLTER, J.H. Intersubband-coupling and screening effects on the electron transport in a quasi-two-dimensional δ-doped semiconductor system. **Journal of Applied Physics**, New York, v.80, n.10, p.5809-5814, 1996.

Dependence of the electron mobility on the acceptor concentration in Si δ-doped GaAs

G. Q. Hai and Nelson Studart

Departamento de Física, Universidade Federal de São Carlos, 13565-905, São Carlos, São Paulo, Brazil

(Received 10 February 1995; revised manuscript received 4 April 1995)

The effect of the background acceptor concentration on the electron mobility in Si δ-doped GaAs has been investigated. The subband electronic structure of the δ-doped system was obtained by solving self-consistently the coupled Schrödinger and Poisson equations. The screened ionized impurity potential is considered by taking the dielectric matrix of the multisubband system within the random-phase approximation. We found that the background acceptor concentration in the present system strongly modifies both the mobilities of electrons in higher subbands and the average drift mobility. Our results may provide useful information for the interpretation of experimental mobility data in δ-doped semiconductors and related devices.

The quasi-two-dimensional (Q2D) electron gas system in a δ-doped semiconductor structure is realized by producing a very thin doping layer with high impurity concentration. Typically, the thickness of the doping layer $W_D < 100$ Å and the areal concentration $N_D \gtrsim 10^{12}/\text{cm}^2$. In contrast with other Q2D semiconductor systems, such as heterojunctions and quantum wells, no interface is present in a δ-doped structure. The confinement potential is simply formed by the interaction between the ionized impurities in the doping layer and the delocalized electrons around it. Usually, several subbands are populated in δ-doped systems because of high electron density, and the ionized impurity scattering is by far the most important scattering mechanism at low temperature.

In recent years, an appreciable amount of experimental work has been carried out on the electron transport properties in δ layers.[1] The effects of the doping concentration, thickness of the doping layer and temperature, on the electron mobility have been studied.[1-4] However, the influence of the background acceptors is not considered. In general, such an effect is not well pronounced on the electronic properties of a Q2D system. However, in δ-doped structures, the quantum confinement is a result of the self-consistent bound potential. The electronic subband structure of the system is mainly determined by the doping concentration, the profile of the doped impurities, and also the background acceptor concentration. In this paper, we will show that the background acceptor concentration in a Si δ-doped GaAs strongly influences the mobilities of electrons in the higher subbands and the average drift mobility.

In the system here considered, the impurity layer is placed in the xy plane with thickness $W_D = 20$ Å and areal donor concentration N_D. The background acceptors are distributed uniformly in the sample. The electronic structure of the system is determined by employing the so-called self-consistent calculation within the local density approximation.[4-6] In such a calculation, impurity distribution, the exchange-correlation potential of the 2D electron gas, and the nonparabolicity of the conduction band can be included. The subband energy $\bar{E}_n$ and wave function $\psi_n(z)$ are then obtained from the numerical self-consistent solution of the one-dimensional Poisson and Schrödinger equations. The total electron energy is given by $E_n(\vec{k}_\parallel) = E_n + \varepsilon(\vec{k}_\parallel)$, where

$n = 1, 2, \ldots$ is the subband index, $\varepsilon(\vec{k}_\parallel) = \hbar^2 k_\parallel^2 / 2m^*$ is the electron kinetic energy, and $\vec{k}_\parallel$ is the electron wave vector in the xy plane. The effective confinement potential $V_{sc}(z) = V_H(z) + V_{xc}(z)$ is composed as a sum of the Hartree potential $V_H(z)$ and exchange-correlation potential $V_{xc}(z)$. The Hartree potential is determined by the Poisson equation. In the calculation, we assumed that all the donors in the doping layer are ionized. The subband nonparabolicity is included through the electron density of states.[7] The ionized acceptor distribution can be written as

$$n_a(z) = n_A \Theta(W_A - |z|), \tag{1}$$

where n_A is the background acceptor concentration which is about 10^{14}–$10^{15}/\text{cm}^3$ in the experimental situation, $\Theta(x)$ is the step function. W_A is determined by $E_F = E_v + E_a$ for $|z| \geq W_A$, where E_a is the binding energy of the acceptors measured from the top of the valence band E_v. Then, we have $V_{sc}(W_A) = E_F + E_g - E_a$, because in the depletion layer n_A is much larger than the electron concentration. The thickness of the depletion layer can be estimated by $W_{dep} = \sqrt{\epsilon_0(E_g - E_a)/2\pi e^2 n_A}$, where $E_g = 1.52$ eV is the energy gap of GaAs and we took $E_a = 30$ meV which is a typical binding energy for shallow acceptors in GaAs. W_A is determined self-consistently from the requirements of charge neutrality and Fermi energy lineup by using the initial value of W_{dep}. The total areal electron density is given by $N_e = N_D - 2n_A W_A$.

The exchange-correlation potential as a function of electron density $n_e(z)$ is given by[6]

$$V_{xc}(z) = -\frac{e^2}{8\pi\epsilon_0 a_B} \frac{2}{\pi\alpha r_s}\left[1 + 0.0545 \ln\left(1 + \frac{11.4}{r_s}\right)\right], \tag{2}$$

where $\alpha = (4/9\pi)^{1/3}$, $r_s = [4\pi n_e(z)/3]^{-1/3}/a_B$, and a_B is the effective Bohr radius.

In Fig. 1, we give the self-consistent solutions of the confinement potential profile $V_{sc}(z)$, the first five quantized levels E_n, and the electron distributions for two different acceptor concentrations $n_A = 10^{14}$ and $10^{15}/\text{cm}^3$ of Si δ-doped GaAs with $N_D = 8 \times 10^{12}/\text{cm}^2$. The shadow indicates the doping layer. We found that $W_A = 4.674$ and 1.478 μm for $n_A = 10^{14}$ and $10^{15}/\text{cm}^3$, respectively. In the figure, the en-
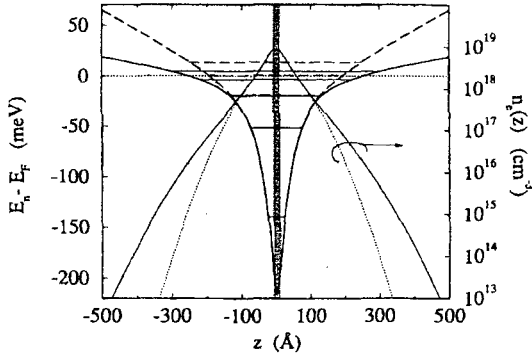
FIG. 1. The effective confinement potential profile $V_{sc}(z)$ and the electron density distribution $n_e(z)$ in Si δ-doped GaAs of $W_D = 20$ Å and $N_D = 8 \times 10^{12}/\text{cm}^2$. The thick solid and thick dashed curves indicate $V_{sc}(z)$ for $n_A = 10^{14}$ and $10^{15}/\text{cm}^3$, respectively. The corresponding $n_e(z)$ is presented by the thin solid and thin dotted curves. The shadow indicates the doping layer and E_n are given by the thin solid and thin dashed lines.

ergy is measured from the Fermi energy E_F which is indicated by the dotted line. Figure 2 shows the influence of the n_A on the subband energy E_n in the structure of $N_D = 8 \times 10^{12}/\text{cm}^2$. It is seen that, at $n_A = 10^{14}/\text{cm}^3$, $E_n < E_F$ for the first four subbands ($n \leq 4$) which are populated. With increasing n_A, E_1 almost does not change, and the other levels shift to higher energy. The distance between the different levels also increases. E_4 crosses the Fermi energy at $n_A = 9 \times 10^{14}/\text{cm}^3$ and becomes depopulated for higher acceptor concentrations. We also found that the fractional electron density of the lowest subband increases with increasing n_A, while those of the higher subbands decrease.

When we calculated the electron subband mobility, only the ionized donor scattering was considered because it is the most important scattering mechanism in the δ-doped systems. The ionized donor scattering potential is given by
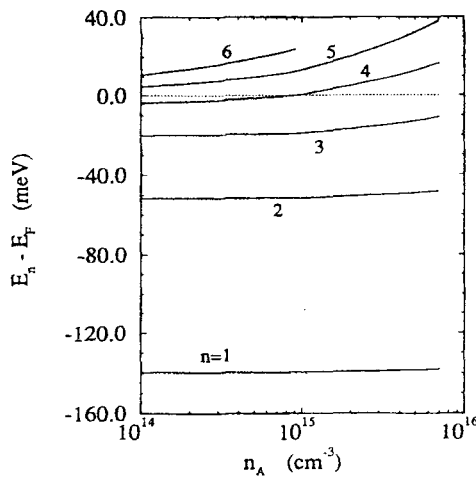
FIG. 2. Subband energy as a function of background acceptor concentration for Si δ-doped GaAs of $W_D = 20$ Å and $N_D = 8 \times 10^{12}/\text{cm}^2$.

$$V(\vec{r}) = -\sum_i \frac{e^2}{\epsilon_0} \frac{1}{|\vec{r} - \vec{R}_i|}, \qquad (3)$$

where $\vec{R}_i$ is the position of the impurity and the sum runs over all the impurities which are distributed randomly in the doping layer. In the calculation of the electron transport properties, we assumed a parabolic conduction band. Using the Fermi golden rule, the electron transition probability from state $|n, \vec{k}_\parallel\rangle$ to $|n', \vec{k}'_\parallel\rangle$ for electron-impurity scattering is given by

$$W_{n,n'}(\vec{k}_\parallel, \vec{k}'_\parallel) = \frac{2\pi}{\hbar} |u_{n,n'}(\vec{q}_\parallel)|^2 \delta_{\vec{k}'_\parallel - \vec{k}_\parallel, \vec{q}_\parallel} \delta(E_{n'}(k'_\parallel) - E_n(k_\parallel)), \qquad (4)$$

where $u_{n,n'}(\vec{q}_\parallel)$ is the transition matrix element. If we ignore the correlation between impurities, the square of the transition matrix element due to the screened ionized donor scattering is given by

$$|u_{n,n'}(\vec{q}_\parallel)|^2 = \left(\frac{2\pi e^2}{\epsilon_0 q_\parallel}\right)^2 \frac{N_D}{W_D} \int_{-W_D/2}^{W_D/2} dz_i [G_{n,n'}(q_\parallel, z_i)]^2, \qquad (5)$$

where

$$G_{nn'}(q_\parallel, z_i) = \sum_{mm'} \epsilon^{-1}_{nn',mm'}(\vec{q}_\parallel) \int_0^\infty dz \psi_m(z) \psi_{m'}(z)$$
$$\times [e^{-q_\parallel|z - z_i|} + (-1)^{m+m'} e^{-q_\parallel|z + z_i|}], \qquad (6)$$

with the change in electron momentum due to scattering written as

$$q_\parallel = \left[(E_n - E_{n'}) \frac{2m^*}{\hbar^2} + 2k_\parallel^2 \right.$$
$$\left. - 2k_\parallel \cos\theta \sqrt{(E_n - E_{n'}) \frac{2m^*}{\hbar^2} + k_\parallel^2} \right]^{1/2}. \qquad (7)$$

In Eq. (7), θ is the angle between $\vec{k}_\parallel$ and $\vec{k}'_\parallel$. $\epsilon^{-1}_{nn',mm'}(\vec{q}_\parallel)$ is the element of the inverse matrix of the dielectric response function, and the sum (m, m') runs over all the subbands of the system. In this work, the dielectric function is calculated within random-phase approximation.[8,9] In practical calculations, we have to limit the (m, m') sum. In most previous works, only the matrix elements of the dielectric function associated with the occupied subbands were considered. Consequently for a system of N occupied subbands the dielectric function $\epsilon_{nn',mm'}(\vec{q}_\parallel)$ is approximated by an $N^2 \times N^2$ matrix.[3,10,11] In our calculation, we included all the occupied subbands and two empty subbands above E_F in the dielectric response function which is approximated by an $(N+2)^2 \times (N+2)^2$ matrix.[4]

The electron mobility has been calculated by solving the Boltzmann equation within relaxation time approximation for the multisubband system at zero temperature.[10,11,4] The transport mobility is shown as a function of the total electron density in Fig. 3 for $n_A = 10^{14}/\text{cm}^3$. It is seen that the transport mobilities of the $n=2$ and $n=3$ subbands are close to each other and much higher than that of the lowest subband. The abrupt decrease of the mobility at $N_e = 4.76 \times 10^{12}/\text{cm}^2$
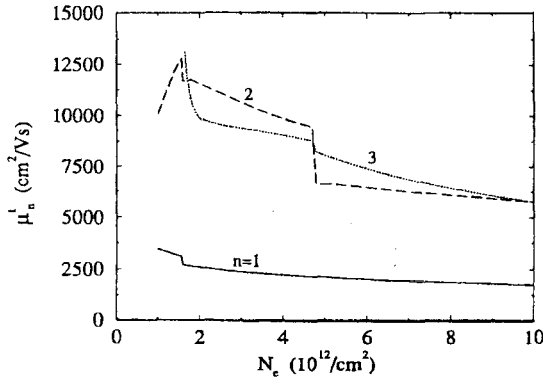
FIG. 3. The transport mobilities of the lowest three subbands as a function of the total electron density for $W_D = 20$ Å and $n_A = 10^{14}/cm^3$. The solid, dashed, and dotted curves show the results of $n = 1$, 2, and 3 subbands, respectively.

is due to the onset of the occupation of the $n = 4$ subband, where the intersubband scattering related to the fourth subband starts to be included in the scattering processes.

Now, we proceed to a discussion on the main contribution of our paper, i.e., the influence of the background acceptor concentration on the subband electron mobilities. In Fig. 4, the transport mobility is plotted as a function of the acceptor concentration for Si δ-doped GaAs with (a) $N_D = 2 \times 10^{12}/$
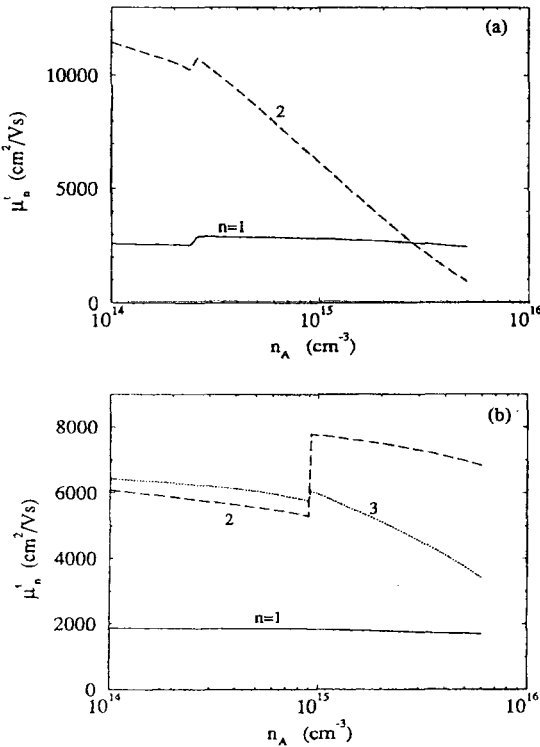
FIG. 4. The transport mobility as a function of the acceptor concentration for (a) $N_D = 2 \times 10^{12}/cm^2$ and (b) $N_D = 8 \times 10^{12}/cm^2$. $W_D = 20$ Å.
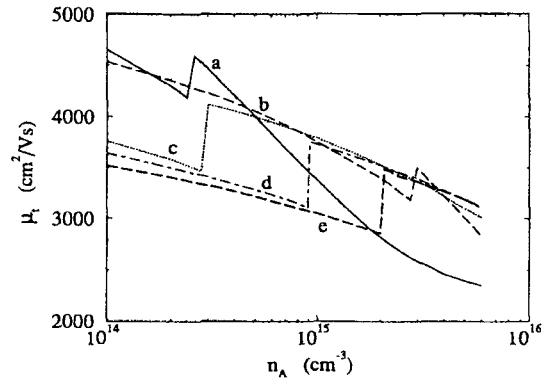
FIG. 5. The average drift mobility as a function of the acceptor concentration for δ layers of $W_D = 20$ Å and different N_D: a, $2 \times 10^{12}/cm^2$; b, $4 \times 10^{12}/cm^2$; c, $6 \times 10^{12}/cm^2$; d, $8 \times 10^{12}/cm^2$; and e, $1 \times 10^{13}/cm^2$.

cm^2 and (b) $N_D = 8 \times 10^{12}/cm^2$. It is seen that, when n_A varies from 10^{14} to $5 \times 10^{15}/cm^3$, the mobility of electrons in the lowest subband does not change in an appreciable way. However, the mobilities of higher subbands change significantly. The abrupt increase of the mobility at $n_A = 2.5 \times 10^{14}/cm^3$ in Fig. 4(a) and at $n_A = 9 \times 10^{14}/cm^3$ in Fig. 4(b) is due to the depopulation of the $n = 3$ and $n = 4$ subbands, respectively. Except for this increasing jump, the mobility decreases with increasing n_A. Figure 4(a) shows that μ_2^t is about four times larger than μ_1^t at $n_A = 10^{14}/cm^3$. But, when $n_A > 2.7 \times 10^{15}/cm^3$, μ_2^t becomes smaller than μ_1^t. For a higher doping concentration N_D, the influence of n_A on the mobility becomes weaker but still significant as shown in Fig. 4(b). Notice that we did not take into account the ionized acceptor scattering in the calculation because it is much smaller than the ionized donor scattering. The effect of the background acceptor concentration on the subband mobility can be understood as follows. By increasing n_A, the thickness of the depletion layer decreases and the profile of the effective confinement potential becomes narrower and deeper. On one hand, this leads to a strong interaction between the conduction electrons and the ionized donors because they become closer. As a consequence the impurity scattering increases. If the acceptor scattering is included, such an increase of the impurity scattering on the electrons will be enhanced slightly. On the other hand, the separation between the subbands increases and more electrons are transferred to the lowest subband from the higher ones. At some n_A, the highest occupied subband becomes depopulated and the intersubband scattering related to this subband disappears.

The average drift mobility μ_t of the electrons is obtained from the subband mobility and electron population as $\mu_t = \Sigma_{n=1}^{N} \mu_n^t N_n^e / N_e$. Figure 5 shows the dependence of the electron drift mobility on the acceptor concentration. The solid, dashed, dotted, dotted-dashed, and thick-dashed curves present the results for (a) $N_D = 2 \times 10^{12}$, (b) $N_D = 4 \times 10^{12}$, (c) $N_D = 6 \times 10^2$, (d) $N_D = 8 \times 10^{12}$, and (e) $N_D = 10^{13}/cm^2$. It is seen that the electron drift mobility is also strongly influenced by the background acceptor concentration. For instance, for the donor concentration of $N_D = 2 \times 10^{12}/cm^2$, the mobility $\mu_t = 4654$ cm^2/V s at

$n_A = 1 \times 10^{14}/\text{cm}^3$ and decreases to 2397 $\text{cm}^2/\text{V s}$ at $n_A = 5 \times 10^{15}/\text{cm}^3$. The abrupt change of the mobility in curves a and b is due to the depopulation of $n=3$ subband, and that in curves c, d, and e is induced by the depopulation of $n=4$ subband. We observe that, in Si δ-doped GaAs of $N_D = 10^{12}-10^{13}/\text{cm}^2$ and $n_A = 10^{14}-5 \times 10^{15}/\text{cm}^3$, which is the usual experimental situation, there are two up to four populated subbands. The onset of the occupation of the fourth subband depresses strongly the drift mobility.

In the present calculation, only the scattering of ionized donors was considered. Although several other scattering mechanisms, such as ionized acceptors, neutral impurities, deep level centers, and electron-electron interaction, can modify the electron transport properties, the main feature of the effect of the background acceptors on the electron mobilities in this work will not change. If including ionized acceptor scattering, this effect will be enhanced slightly.

In a δ-doped system, high donor concentration leads to an impurity band just below the conduction band. The disorder of the impurity distribution could create localization states and a band tail. The thickness fluctuations in the doping layer may also broaden the energy level E_n. When there is a band tail at the onset of subband occupation, the Fermi level will cross the mobility edge of the subband leading to a different scattering rate. In experiments, the change of the mobility at the onset (or depopulation) of a higher subband will not be abrupt. In the calculation, we assumed a steplike electron density of states for each subband of the Q2D systems. This is justified when the separation between subbands is much larger than the band tail of localization states. This is the case for the first few subbands.

In conclusion, we have studied theoretically the electron mobility in Si δ-doped GaAs. We found that the background acceptor concentration strongly influences the mobilities of electrons in high subbands and the average drift mobility. Such an effect reflects the specific characteristics of Q2D system in a δ layer which is simply determined by the self-consistent potential. We hope our calculation can provide useful information for experimentalists to optimize the samples and the related devices.

[1] P.M. Koenraad, in *Delta Doping of Semiconductors*, edited by E.F. Schubert (Springer, New York, 1994), and references therein.

[2] A. Zrenner, F. Koch, J. Leotin, M. Goiran, and K. Ploog, Semicond. Sci. Technol. 3, 1132 (1988).

[3] L.R. González, J. Krupski, and T. Szwacka, Phys. Rev. B 49, 11 111 (1994).

[4] G.Q. Hai, N. Studart, and F.M. Peeters (unpublished).

[5] G. Bastard, *Wave Mechanics Applied to Semiconductor Heterostructures* (Halsted Press, New York, 1988), p. 193; M.H. Dega-

ni, Phys. Rev. B 44, 5580 (1991).

[6] L. Hedin and B.I. Lundqvist, J. Phys. C 4, 2064 (1971).

[7] U. Ekenberg, Phys. Rev. B 36, 6152 (1987); 40, 7714 (1989).

[8] J.K. Jain and S. Das Sarma, Phys. Rev. B 36, 5949 (1987).

[9] W.H. Backes, F.M. Peeters, F. Brosens, and J.T. Devreese, Phys. Rev. B 45, 8437 (1992).

[10] S. Mori and T. Ando, Phys. Rev. B 19, 6433 (1979).

[11] R. Fletcher, E. Zaremba, M. D'Iorio, C.T. Foxon, and J.J. Harris, Phys. Rev. B 41, 10 649 (1990).

Electron mobility in two coupled δ layers

Guo-Qiang Hai and Nelson Studart

Departamento de Física, Universidade Federal de São Carlos, 13565-905 São Carlos, São Paulo, Brazil

François M. Peeters

Department of Physics, University of Antwerp (UIA), B-2610, Antwerpen, Belgium

The low-temperature transport properties are studied for electrons confined in δ-doped semiconductor structures with two sheets in parallel. The subband quantum mobility and transport mobility are calculated numerically for the Si δ-doped GaAs systems. The effect of coupling of the two δ layers on the electron transport is investigated. Our calculations are in good agreement with experimental results.

I. INTRODUCTION

In recent years, an appreciable amount of work has been devoted to the electron transport properties in δ-doped semiconductor systems.[1-13] The quasi-two-dimensional electron system in δ-doped semiconductors is realized, typically, by a very thin doped layer ($W_D \lesssim 20$ Å) of high doping concentration ($N_D \gtrsim 10^{12}$ cm^{-2}). On one hand, a high concentration of impurities leads to a high electron density in the system and several subbands are populated. On the other hand, as a consequence, this results in a very strong scattering on the electrons and, consequently, a low electron mobility. In order to fabricate high-mobility δ-doped devices, some works are focused in improving doping and material growth techniques.[2,4,5] An alternative way to improve the electron mobility in the δ-doped semiconductors, which has been proposed recently, is to make a structure with double δ layers.[10-13] It is expected that the coupling between the two layers leads to an increase of the average distance of the electrons from the doped layers. The impurity scattering is then reduced and the electron mobility is enhanced. It was shown that the electron mobility is increased by two to five times over that of a single δ-doped case.[10]

In previous works,[7,8] we studied theoretically the electron transport properties in single δ-layer systems. The effects of the doping concentration, thickness of the doped layer, as well as the background acceptor concentration on the electron subband mobility were investigated. The screening of the electron gas on the impurity scattering potential was included within the static random-phase approximation (RPA). In this paper, we report a theoretical study of the electron transport properties in double δ layer systems. We calculate the elec-

tron subband mobility for two interacting Si δ-doped layers in GaAs based on the self-consistent calculation of the electronic structure and wave functions in such a system. The electron subband quantum and transport mobilities are determined from the different scattering times connected to the average time between the scattering events. The quantum lifetime or the single particle relaxation time is the averaged elastic scattering time. On the other hand, in order to obtain the transport lifetime or the momentum relaxation time, every scattering event is averaged over its projection of the outgoing wave vector on the incident direction.[2] For a discussion from a theoretical point of view, see Ref. 14. Experimentally, the quantum mobility is obtained by Shubnikov–de Haas (SdH) measurements and the transport mobility is determined by the so-called mobility spectrum technique or by Hall measurements combined with the subband electron density obtained from SdH measurements.[2,11] We show the effect of the coupling between the two δ layers on the quantum and transport mobility of electrons in different subbands. In Sec. II, the self-consistent electronic structure of the coupled δ wells is determined and in Sec. III, the electron mobilities are numerically calculated and the theoretical results are compared with the available experimental ones.

II. SELF-CONSISTENT ELECTRONIC STRUCTURE

We consider the Si δ-doped GaAs structure with doubly doped layers in parallel. We assume that the two doped layers are symmetric, i.e., they have the same thickness and doping concentration. If we take the doped layers in the xy plane, the donor impurity distribution can be written as

$$n_D(z) = \begin{cases} N_D/W_D, & (W_S - W_D)/2 < |z| < (W_S + W_D)/2 \\ 0, & \text{otherwise}, \end{cases} \tag{1}$$

where N_D is the donor areal concentration of each layer, W_D the thickness of the doped layer, and W_S the separation between the two layers. In Eq. (1), we have assumed $W_S > W_D$. For $W_S \leq W_D$, the two doped layers become overlapped. In this case, we deal with the system as single doped layer.[7] The electron energy and wave function in the system can be written as $E_n(\vec{k}_\|) = E_n + \varepsilon(\vec{k}_\|)$, where $n = 1, 2, 3, ...$ is the subband index, $\varepsilon(\vec{k}_\|) = \hbar^2 k_\|^2 / 2m^*$ is the electron kinetic energy, and $\vec{k}_\|$ the electron wave vector in the plane. The subband energies E_n and wave functions $\psi_n(z)$ are obtained from the self-consistent solution of the coupled one-dimensional Schrödinger and Poisson equations. In the calculation, we assume that all the impurities in the doping layers are ionized and the conduction band is parabolic. We took the parameters $m^* = 0.067m_e$, $\epsilon_0 = 13.18$, and the energy gap of GaAs $E_g = 1.52$ eV. The exchange-correlation potential of the electron gas was included within the local-density approximation.[15,7,8] In Fig. 1, the effective confinement potential $V_{sc}(z)$, the subband energies, and the probability distributions of the electrons in different subbands are depicted in the case of a structure with $W_S = 160$ Å, $W_D = 10$ Å, $N_D = 2.5 \times 10^{12}/\text{cm}^2$, and background acceptor concentration $n_A = 10^{15}/\text{cm}^3$. The shadow indicates the impurity sheets. In this figure $V_{sc}(z)$ is given by the thick curve and the thin curves indicate the subband electron distributions. It is seen that the lowest two levels are closed to each other and their respective electron distributions, which strongly overlap with the impurity layers, are very similar. Furthermore, the electron wave functions in the higher levels spread out in a much wider region as compared with those of the lowest subbands. Notice that the wave functions of the lowest two subbands have different parity. One $(n = 1)$ is symmetric and the other one $(n = 2)$ is antisymmetric. In the case of $E_1 = E_2$, the two levels become degenerate and the wave function can

FIG. 2. The subband energy as a function of the separation between the two doped layers with $N_D = 2.5 \times 10^{12}/\text{cm}^2$ and $W_D = 10$ Å for each layer. The dash curve indicates the barrier at $z = 0$ between the two coupled quantum wells. $n_A = 10^{15}/\text{cm}^3$.

also be expressed as $\psi_\pm(z) = [\psi_1(z) \pm \psi_2(z)]/\sqrt{2}$, where $\psi_+(z)$ and $\psi_-(z)$ present the electron states in the right and the left quantum well, respectively. In Fig. 2, the subband energy E_n is depicted as a function of the separation of the two sheets W_S for $N_D = 2.5 \times 10^{12}/\text{cm}^2$, $W_D = 10$ Å, and $n_A = 10^{15}/\text{cm}^3$. The dashed curve presents the barrier (at $z = 0$) between the two quantum wells. For small W_S, where the barrier $V_{sc}(0)$ is much smaller than the lowest subband energy, the system is similar to the single δ layer. When $W_S \leq W_D$, the system becomes a single doped layer with doping concentration $2N_D$. With increasing W_S, the barrier $V_{sc}(0)$ increases rapidly. We find that $E_1 = V_{sc}(0)$ at $W_S = 89.4$ Å, and $E_2 = V_{sc}(0)$ at $W_S = 132.5$ Å. For $W_S = 200$ Å, the first two subbands become almost degenerate. At small W_S, the lowest three subbands are populated by electrons. The $n = 4$ and 5 subbands become populated for $W_S \geq 46$ Å and 196 Å, respectively. When $W_S \to \infty$, the system behaves like two independent single δ layers and the energy level E_3 corresponds to the second level of the independent δ layer.

III. ELECTRON MOBILITIES

Based on the above self-consistent solution of the electronic structure and the wave functions, we study the electron transport properties of the system. In the calculation, only the scattering by ionized donors in the doped layers are considered, because it is the most important scattering mechanism at low temperature. We consider the Coulomb scattering potential due to ionized impurities, distributed randomly in the doped layer at positions $\vec{R}_i$, whose two-dimensional Fourier transform is given by

$$v(q_\|, z) = -\frac{2\pi e^2}{\epsilon_0 q_\|} \sum_i e^{-q_\||z - z_i|} e^{i\vec{q}_\| \cdot \vec{R}_{\|i}}. \tag{2}$$
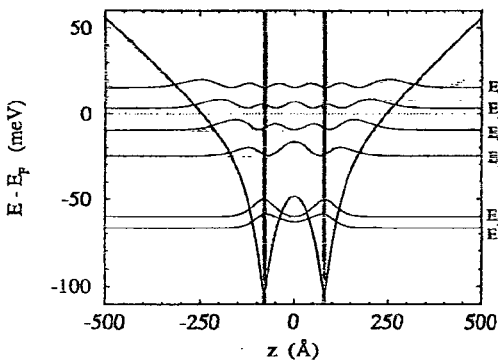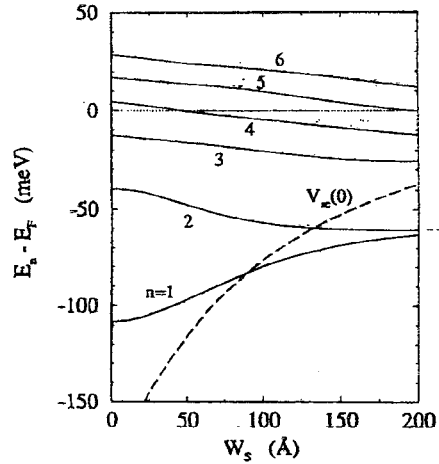

FIG. 1. The results of the self-consistent calculation of the effective confinement potential (thick-solid curve), the energy levels E_n, and the electron probability distribution (thin-solid curves) for a double δ layer structure of $W_S = 160$ Å, $W_D = 10$ Å, $N_D = 2.5 \times 10^{12}/\text{cm}^2$ for each layer, and $n_A = 10^{15}/\text{cm}^3$. The energy is measured from the Fermi energy (thin-dotted line), and the shadow indicates the Si δ-doped layers.

Using the Fermi golden rule, the electron transition probability from state $|n, \vec{k}_\parallel\rangle$ to $|n', \vec{k}'_\parallel\rangle$ for the electron-impurity scattering is given by

$$W_{n,n'}(\vec{k}_\parallel, \vec{k}'_\parallel) = \frac{2\pi}{\hbar}|u_{n,n'}(\vec{q}_\parallel)|^2 \delta_{\vec{k}'_\parallel - \vec{k}_\parallel, \vec{q}_\parallel} \delta[E_{n'}(k'_\parallel) - E_n(k_\parallel)], \quad (3)$$

where $u_{n,n'}(\vec{q}_\parallel)$ is the transition matrix element. Because of the high electron density in the present system, the screening effects of the electron gas on the scattering potential has to be taken into account properly. The screened ionized impurity potential can be obtained in terms of the static dielectric response function within the RPA.[7,16–19] The dielectric function in the present multisubband system has a tensor character given by $\epsilon_{nn',mm'}(\vec{q}_\parallel)$. For the present double δ layer system, the transition matrix elements, due to the screened scattering potential, is written as

$$|u_{n,n'}(\vec{q}_\parallel)|^2 = \left(\frac{2\pi e^2}{\epsilon_0 q_\parallel}\right)^2 \frac{N_D}{W_D} \int_{(W_S-W_D)/2}^{(W_S+W_D)/2} \\ \times dz_i \{|G^+_{nn'}(q_\parallel, z_i)|^2 + |G^-_{nn'}(q_\parallel, z_i)|^2\}, \quad (4a)$$

where

$$G^\pm_{n,n'}(q_\parallel, z_i) = \sum_{mm'}(\pm 1)^{m+m'}\epsilon^{-1}_{nn',mm'}(\vec{q}_\parallel)G^{(0)}_{mm'}(q_\parallel, z_i), \quad (4b)$$

where the overlapping function $G^{(0)}_{n,n'}(q_\parallel, z_i)$ is written as

$$G^{(0)}_{n,n'}(q_\parallel, z_i) = \int_{-\infty}^{\infty} dz \psi_n(z)\psi_{n'}(z)e^{-q_\parallel|z-z_i|}, \quad (4c)$$

with the change in electron momentum, due to scattering given by

$$q_\parallel = \left[(E_n - E_{n'})\frac{2m^*}{\hbar^2} + 2k_\parallel^2 \right. \\ \left. -2k_\parallel \cos\theta \sqrt{(E_n - E_{n'})\frac{2m^*}{\hbar^2} + k_\parallel^2}\right]^{1/2}, \quad (5)$$

and θ is the angle between $\vec{k}_\parallel$ and $\vec{k}'_\parallel$.

We have performed the numerical calculation for the electron subband transport and quantum mobility, using the self-consistent subband wave function to evaluate the transition matrix elements. In practical calculations, we have to limit the sum over (m, m') in Eq. (4b). For a system with N populated subbands, we include $N+2$ subbands in the matrix of the dielectric function, i.e., we consider all the occupied subbands and two empty ones. Within such an approximation, the dielectric function $\epsilon_{nn',mm'}(\vec{q}_\parallel)$ is approximated by an $(N+2)^2 \times (N+2)^2$ matrix. The thick curves in Fig. 3 show the quantum mobility, as a function of W_S for $N_D = 2.5 \times 10^{12}/\text{cm}^2$, $W_D = 10$ Å, and $n_A = 10^{15}/\text{cm}^3$. We found that the quantum mobility of the lowest subband μ_1^q increases

slightly with increasing W_S until $W_S = 130$ Å and then turns out to be a decreasing function. The μ_2^q decreases monotonously as a function of W_S. For small W_S, $\mu_2^q \gg \mu_1^q$. When $W_S > 82$ Å, μ_2^q becomes smaller than μ_1^q and they are very close to each other. The mobility μ_3^q is about a factor of 3 larger than μ_1^q. μ_4^q is close to μ_3^q and it increases slowly with increasing W_S. At $W_S = 46$ and 196 Å, due to the onset of the occupation of the subbands $n = 4$ and 5, the calculated subband mobility exhibits an abrupt jump as a consequence of the intersubband interaction. We also notice that, at the onset of the occupation of $n = 4$ subband, μ_1^q and μ_2^q have small decreasing jumps, due to the contribution of the intersubband scattering related to the $n = 4$ subband. However, μ_3^q increases abruptly. Such a result reflects the screening effect in the intersubband interaction. At the onset of the occupation of $n = 5$ subband, the changes of the quantum mobilities of the lower subbands are not pronounced. The experimental results of the quantum mobility[11] are presented by the different symbols in Fig. 3: circles ($n = 1$), squares ($n = 2$), triangles ($n = 3$), and diamonds ($n = 4$). Our calculation is in quite good agreement with the experimental results for the four subbands. The thick curves in Fig. 4 give the transport mobility as a function of W_S. It is seen that the subband transport mobility has a similar behavior as the quantum mobilities. But the transport mobilities of the lowest two subbands are about a factor 4 larger than the corresponding quantum mobilities. Such a factor is about 2–3 for the $n = 3$ and 4 subbands. Besides, the transport mobility is different from the quantum mobility in the following ways. (i) $\mu_1^t \simeq \mu_2^t$ for $W_S > 80$ Å, $\mu_2^t > \mu_3^t$ for $W_S < 18$ Å, and $\mu_3^t \sim \mu_4^t$ for $W_S > 150$ Å. (ii) At the onset of the occupation of the $n = 4$ subband, μ_4^t is about a factor of 2 smaller than μ_3^t, but it increases rapidly and approaches to μ_3^t at larger W_S. (iii)
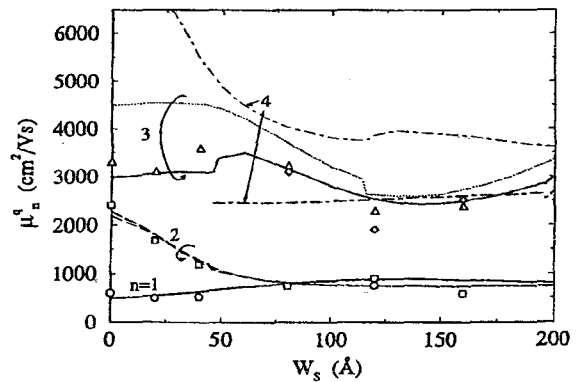

FIG. 3. The subband quantum mobility as a function of the separation of the two δ layers for $N_D = 2.5 \times 10^{12}/\text{cm}^2$ and $W_D = 10$ Å in Si δ-doped GaAs. The thick and thin curves indicate the calculation results of $n_A = 10^{15}$ and 10^{14} cm^{-3}, respectively. The solid, dashed, dotted, and dotted-dashed curves present the results of the $n = 1, 2, 3,$ and 4 subbands, respectively. The experimental results are indicated by the circles, squares, triangles, and diamonds, which correspond to $n = 1, 2, 3,$ and 4, respectively (see Ref. 11).
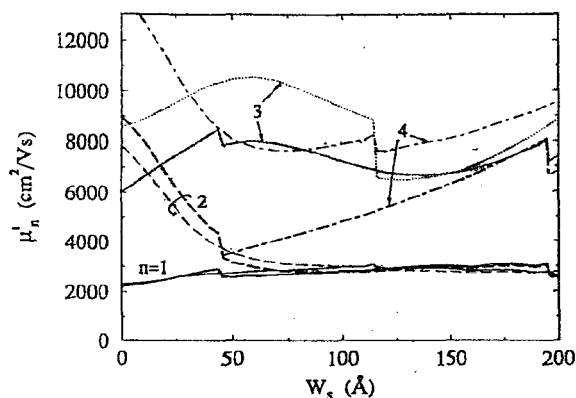
FIG. 4. The same as Fig. 3, but for the subband transport mobilities.

At the onset of the occupation of a higher subband, the transport mobilities of all the lower subbands exhibit an abrupt decrease. (iv) Intersubband scattering is stronger for the transport mobility. Unfortunately, as far as we know, there are no available low-temperature measurements of the transport mobility for our structure, except the experimental results for the Hall mobility for $T \geq 77$ K.[10]

We also examined the influence of the background acceptor concentration on the electron transport properties. The calculated quantum mobility and the transport mobility with $10^{14}/cm^3$ ($N_D = 2.5 \times 10^{12}/cm^2$ and $W_D = 10$ Å) are given in thin curves in Fig. 3 and Fig. 4, respectively. It is seen that n_A strongly influences the mobility of the electrons in the higher subbands in such a system. The mobilities of the $n = 3$ and 4 subbands are enhanced pronouncedly, due to the reduction of the background acceptor concentration. This is a rather indirect effect: the background acceptor concentration influences the band bending (e.g., higher concentration leads to a narrower confinement potential), which influences the distribution of electrons in real space and between the subbands (e.g., the conduction electrons become closer to the doped layers), and this in turn affects the mobility. We demonstrated explicitly this effect in the case of a single δ layer.[8]

In conclusion, we have presented a theoretical study of the electron subband mobility in double δ layer structures. The electron subband quantum and transport mobilities are calculated for the Si δ-doped GaAs systems. We found that, for $W_S \geq 50$ Å, the mobilities of the lowest two subbands are very close to each other and much smaller than those of the higher subbands. For $W_S \geq 120$ Å, the influence of the separation of the two doping layers on the subband quantum mobilities is not pronounced. Furthermore, the transport mobilities of the $n = 3$ and 4 subbands increase with increasing W_S. We also found that the background acceptor concentration modify the electron mobility of the higher subbands. Such an influence is very pronounced in the transport mobility. Our calculation of the electron quantum mobility is in good agreement with the experimental results of Refs. 11 and 2.

[1] A. Zrenner, F. Koch, J. Leotin, M. Goiran, and K. Ploog, Semicond. Sci. Technol. **3**, 1132 (1988).

[2] P.M. Koenraad, in *Delta Doping of Semiconductors*, edited by E.F. Schubert (Cambridge University Press, Cambridge, England, 1995).

[3] G.Q. Hai, N. Studart, F.M. Peeters, J.T. Devreese, P.M. Koenraad, A.F.W. van de Stadt, and J.H. Wolter, *Proceedings of the 22nd International Conference on the Physics of Semiconductors*, edited by J. Lockwood (World Scientific, Singapore, 1995).

[4] E.F. Schubert, J.E. Cunningham, and W.T. Tsang, Solid State Commun. **63**, 591 (1987); E.F. Schubert, J. Vac. Sci. Technol. A **87**, 2980 (1990).

[5] G. Gillman, B. Vinter, E. Barbier, and A. Tardella, Appl. Phys. Lett. **52**, 972 (1988).

[6] E. Skuras, R. Kumar, R.L. Williams, R.A. Stradling, J.E. Dmochowski, E.A. Johnson, A. Mackinnon, J.J. Harris, R.B. Beall, C. Skierbeszewski, J. Singleton, P.J. van der Wel, and P. Wisnieski, Semicond. Sci. Technol. **6**, 535 (1991).

[7] G.Q. Hai, N. Studart, and F.M. Peeters, Phys. Rev. B (to be published).

[8] G.Q. Hai and N. Studart, Phys. Rev. B **52**, R2245 (1995).

[9] R. Enderlein, L.M.R. Scolfaro, and J. R. Leite, Phys. Rev. B **50**, 18 312 (1994).

[10] X. Zheng, T.K. Carns, K.L. Wang, and B. Wu, Appl. Phys. Lett. **62**, 504 (1993).

[11] P.M. Koenraad, A.C.L. Heessels, F.A.P. Blom, J.A.A.J. Perenboom, and J.H. Wolter, Physica B **184**, 221 (1993).

[12] T.K. Carns, X. Zheng, and K.L. Wang, Appl. Phys. Lett. **62**, 3455 (1993).

[13] H.H. Radamson, M.R. Sardela, Jr., O. Nur, M. Willander, B.E. Sernelius, W.-X. Ni, and G.V. Hansson, Appl. Phys. Lett. **64**, 1842 (1994).

[14] S. Das Sarma and F. Stern, Phys. Rev. B **32**, 8442 (1985).

[15] L. Hedin and B.I. Lundqvist, J. Phys. C **4**, 2064 (1971).

[16] S. Mori and T. Ando, Phys. Rev. B **19**, 6433 (1979).

[17] J.K. Jain and S. Das Sarma, Phys. Rev. B **36**, 5949 (1987).

[18] R. Fletcher, E. Zaremba, M. D'Iorio, C.T. Foxon, and J.J. Harris, Phys. Rev. B **41**, 10 649 (1990).

[19] W. Xu, F.M. Peeters, and J. T. Devreese, Phys. Rev. B **48**, 1562 (1993).

Capítulo 4

Acoplamento plasmon-fônon em sistemas quase bidimensionais de multisubbandas

Em sistemas de gás de elétrons, as excitações coletivas e de partícula independente são freqüentemente observadas. Nos semicondutores polares, as excitações coletivas podem ser fortemente modificadas devido ao acoplamento com fônons LO. Assim, o espalhamento de luz fornece importantes informações sobre estes fenômenos.

Estudamos teoricamente o espectro de excitações coletivas e o espalhamento inelástico de luz (Raman) devidos aos modos acoplados de plasmon-fônons em estruturas planares com multisubbandas ocupadas. Nossos cálculos mostraram um forte acoplamento entre os modos de plasmons intra e intersubbandas com os fônons LO e suas ressonâncias. Devido ao alargamento das subbandas induzido pelo espalhamento por impurezas, somente uns poucos picos principais são mantidos nos espectros de Raman. Mas a influência do amortecimento não é tão importante para aqueles picos com modos do tipo fônon, e que estão próximos da freqüência dos fônons TO do sistema. Nossos cálculos permitem uma clara explicação para alguns resultados experimentais publicados.

4.2. *Level broadening effects on inelastic light scattering due to coupled plasmon-phonon modes in δ-doped Semiconductors*

G. Q. Hai, N. Studart, and G. E. Marques,

Plasmon-phonon coupling in δ-doped polar semiconductors

Guo-Qiang Hai, Nelson Studart, and Gilmar E. Marques

Departamento de Física, Universidade Federal de São Carlos, 13565-905 São Carlos, São Paulo, Brazil

(Received 28 May 1996; revised manuscript received 3 September 1996)

The collective excitations and their coupling to optical phonons have been studied for a two-dimensional electron gas in δ-doped polar semiconductors within the random-phase approximation. Our calculation shows that, due to the high electron density in these systems in which several subbands are occupied, both intrasubband and intersubband plasmon modes are strongly coupled to the optical-phonon modes. [S0163-1829(97)06204-8]

I. INTRODUCTION

The quasi-two-dimensional (Q2D) electron gas system in δ-doped semiconductor structure is realized by producing a very thin doping layer with high impurity concentration. Because the dopants are confined to a single or few monolayers of the semiconductor lattice, the doping profile can be mathematically described by Dirac's δ function. Semiconductors with such dopant distributions are referred to as δ-doped semiconductors.[1] The incorporation of dopants within a few monolayers leads to electron confinement in the space-charge potential well and thus to a set of subbands where the electron motion perpendicular to the doping layer is quantized. It presents an important Q2D semiconductor system in which high electron densities are attained and several subbands are occupied leading to a new multisubband system. The electron confinement in δ-doped semiconductors is simply realized by a space-charge potential well. So, the subband energy E_n and the wave function $\psi_n(z)$ are obtained from the numerical solution of the coupled one-dimensional Poisson and Schrödinger equations. If we take the doping layer in the xy plane located at $z=0$, the confinement potential of the system is symmetric about the $z=0$ plane. The total electron energy and wave function are given by

$$E_n(\vec{k}) = E_n + \varepsilon(\vec{k}) \tag{1}$$

and

$$\Psi_{n,\vec{k}}(\vec{r},z) = \psi_n(z) \frac{1}{\sqrt{A}} \exp(i\vec{k}\cdot\vec{r}), \tag{2}$$

where $n=1, 2, \ldots$ is the subband index, $\vec{r}$ ($\vec{k}$) the electron position (wave vector) in the xy plane, $\varepsilon(\vec{k}) = \hbar^2 k^2/2m^*$ the electron kinetic energy, m^* the electron effective mass, and A the area of sample.

Since the pioneering experimental work by Bass,[2] Wood et al.,[3] and Schubert et al.,[4] highly spatially confined impurity doping layers have been achieved in semiconductors by the molecular-beam epitaxy technique. A large number of experimental investigations[1,5-11] have been carried out on the electron transport and optical properties in δ-doped semiconductors. Furthermore, novel and improved semiconductor devices have been fabricated from δ-doped structures, such as δ-doped doping-superlattice light-emitting diodes,[12]

lasers,[13] and modulators,[14] high-transconductance selectively δ-doped heterostructure transistors,[15] planar-doped barrier diodes,[16] negative differential conductance oscillators,[17] etc.

Plasma excitations in low-dimensional electron systems have been studied extensively.[18] As proposed by Burnstein et al.,[19] resonant inelastic light scattering is a sensitive method for the investigation of the elementary excitations in 2D electron systems. It yields separate spectra of single-particle and collective excitations, which leads to the determination of the energy states and collective electron-electron interaction. This yields substantial information on different 2D semiconductor systems. Plasmons in semiconductor superlattices have also attracted much attention.[20-26] Novel collective modes have been found in artificially structured superlattices. Das Sarma[27] presented a generalized many-body dielectric theory to study the spectrum of collective excitations in Q2D electron systems realized in semiconductor heterostructures. The intersubband plasmon modes and their coupling to the intrasubband plasmon modes also were investigated.[27-29] It was shown that the resonant mode coupling of intersubband and intrasubband plasmons takes place in an asymmetric quantum well at high electron densities and small energy separation between the subbands. Backes et al.[30] investigated the effects of confinement on the plasmon modes in the Q2D system. By including all the energy levels in an infinite quantum well, they recovered the results of the ideal 2D and 3D electron systems by varying the width of the quantum well from zero to infinity.

Collective excitations and their coupling to the longitudinal-optical (LO) phonons in doped polar semiconductor structures are the basic physical phenomena which affect the different aspects of the electronic and optical properties of the systems.[18] Wu, Peeters, and Devreese[31] studied the plasmon-phonon coupling of 2D electron electron gas in GaAs/Al$_x$Ga$_{1-x}$As heterojunctions. They showed that the intrasubband plasmon mode in GaAs heterostructures is strongly coupled to the LO phonon modes at high electron densities. When the unperturbed plasmon frequency is close to the LO-phonon frequency, a resonant coupling takes place and there is a splitting of the plasmon frequency. Wendler and Pechstedt[32] investigated interface effects on the phonon modes and the plasmon-phonon coupling in a semiconductor quantum well. They found that the Landau damping of the intersubband plasmon modes depends strongly on the width of the quantum well and the electron density. The δ-doped

polar semiconductors, e.g., Si δ-doped GaAs, have also several advantages to study the collective excitations and their coupling to LO phonons. The electron density in δ-doped semiconductors is much higher than the other Q2D systems, such as heterojunctions and quantum wells, in which electron-electron interactions play a substantial role. It could be a good system to investigate the electron-electron interaction for a deeper understanding of the many-body effects. Typically, several subbands are occupied in δ-doped semiconductors, so the intersubband interaction is strong. Furthermore, the separation between the different subbands is close to the optical phonon energy in such a way that the electron LO-phonon coupling is strong and easier to be detected experimentally. On the other hand, the host semiconductor is uniform in such a way that there is no material interface present. The phonon modes in δ-doped systems have, therefore, a three-dimensional character. The electron-phonon interaction can be described by the Fröhlich Hamiltonian. This is different from other Q2D systems, such as GaAs/Al$_x$Ga$_{1-x}$As heterostructures, where the interface modifies the phonon modes, and consequently, the electron-phonon interaction. In this case, the Fröhlich Hamiltonian is only a good approximation to describe the electron-phonon interaction when the interface effects are not pronounced.[33]

In our previous works,[34-36] we studied the electron transport properties in δ-doped semiconductors. The effects due to intersubband coupling and screening of the Q2D electron gas on the ionized impurity scattering were investigated theoretically. The subband transport and quantum mobilities coming from ionized impurity scattering were analyzed. We found that not only the intersubband scattering by itself, but also the intersubband coupling through the screening of the Q2D electron gas plays an essential role in the electron transport in this multisubband system.

In this paper, we study the spectrum of collective excitations of a Q2D electron gas in δ-doped polar semiconductors. Our model consists of a multisubband 2D electron gas system coupled to 3D bulk optical phonons at zero temperature. The intrasubband and intersubband plasmon modes and their coupling to the optical phonons are investigated. Our calculation is based on the dielectric function in the random-phase approximation (RPA) and is applied to Si δ-doped GaAs structure of an impurity layer in the xy plane with thickness $W_D = 10$ Å. The electronic structure is determined by employing a self-consistent method within the local density approximation.[35] We assumed that all the donors in the doping layer are ionized and the background acceptor concentration, which is supposed to be uniformly distributed in the sample, is $n_A = 10^{15}$ cm^{-3}. We found that in the present system the $n = 2$, 3, and 4 subbands begin to be occupied at the total electron density $N_e = 0.93$, 2.67, and 8.33×10^{-12} cm^{-2}, respectively.

Experimentally, Mlayah et al.[9] investigated the intersubband plasmon-phonon coupling in Si δ-doped GaAs. The signature of the coupled modes was pointed out by means of Raman scattering measurements. They found that the phononlike mode, due to the coupling of the intersubband plasmon of the lowest two subbands to the LO phonons, is located between LO and TO phonon frequencies. Influences of the doping concentration and thickness of the doping layer on these phononlike modes were discussed.

According to the experimental accessible electron densities, we consider a realistic four-subband model, and in order to make our discussion clearer, we analyze first the case where one subband is occupied and the other three are empty. Second, we discuss the results when electrons occupy two subbands and the other ones are empty, and finally the case where three subbands are occupied. Our calculation shows that both the intersubband plasmon modes and their coupling to the LO phonons are much more pronounced in δ-doped polar semiconductors than those in other Q2D semiconductor systems. In a wide range of electron densities (donor concentrations), the frequencies of the phononlike branches of the intersubband plasmon-phonon modes due to the first four subbands are in the reststrahlen region of GaAs.

We do not consider impurity scattering effects on the plasmon excitation spectrum. Such scattering should be strong in the δ-doped system and soften the plasmon spectrum. It may also lead to a mixture of different plasmon modes when they are close to each other. But the main features shown in this work will not be modified essentially. As far as we know, this is the first theoretical work studying the collective excitations and their coupling to LO phonons in δ-doped semiconductors.

II. PLASMON-PHONON COUPLING

For an electron gas embedded in a polar semiconductor, the optical phonons interact with the electrons. Since the host material of the 2D electron gas in the δ-doped system is homogeneous, which is different from the other 2D systems such as heterojunctions and quantum wells where interfaces between different materials are present, the electron-phonon interaction can be described by the well-known Fröhlich Hamiltonian. The electrons interact among themselves through the Coulomb interaction and through the virtual LO phonons via the Fröhlich interaction. In this way, both the electron-electron interaction and the electron-phonon interaction play significant roles and affect substantially the electron and the phonon systems.[37] Especially, the electron-phonon coupling may be strong because the intersubband plasmon frequencies in Si δ-doped GaAs are close to the optical phonon frequency.

In a Q2D system, the screened interaction potential $V^{sc}_{nn',mm'}(\vec{q},\omega)$ within the RPA is determined by the Dyson equation[37]

$$V^{sc}_{nn',mm'}(\vec{q},\omega) = V_{nn',mm'}(\vec{q},\omega)$$

$$+ \sum_{ll'} V_{nn',ll'}(\vec{q},\omega)$$

$$\times \Pi^0_{ll'}(\vec{q},\omega) V^{sc}_{ll',mm'}(\vec{q},\omega), \qquad (3)$$

where $V_{nn',mm'}(\vec{q},\omega) = v^c_{nn',mm'}(\vec{q}) + v^{ph}_{nn',mm'}(\vec{q},\omega)$ is the bare interaction potential which is composed by the electron-electron Coulomb potential and the electron-phonon interaction determined by the Fröhlich Hamiltonian, and $\Pi^0_{mm'}(\vec{q},\omega)$ is the polarizability function of the noninteracting 2D electron gas. The well-known bare electron-electron potential is[38]

$$v^c_{nn',mm'}(\vec{q}) = \frac{2\pi e^2}{\epsilon_\infty q} F_{nn',mm'}(q), \qquad (4)$$

with the Coulomb form factor

$$F_{nn',mm'}(q) = \int_{-\infty}^{\infty} dz\, \psi_n(z)\psi_{n'}(z)$$

$$\times \int_{-\infty}^{\infty} dz'\, \psi_m(z')\psi_{m'}(z')e^{-q|z-z'|}. \qquad (5)$$

Due to the spatial symmetry of the potential about the $z=0$ plane, which is a characteristic of the δ-doped system, we have

$$F_{nn',mm'}(q) = F_{n'n,mm'}(q) = F_{nn',m'm}(q) = F_{n'n,m'm}(q).$$

Furthermore, the Coulomb form factor $F_{nn',mm'}(q)$ vanishes if $n+n'+m+m'$ is an odd number. Notice that $F_{nn',mm'}(0) = 1$ for $n=n'$ and $m=m'$, and $F_{nn',mm'}(0) = 0$ otherwise.

The bare electron-phonon interaction coming from the Fröhlich Hamiltonian is given by

$$v^{ph}_{nn',mm'}(\vec{q},\omega) = \frac{2\omega_{LO}}{\hbar(\omega^2 - \omega_{LO}^2)} \sum_{q_z} M_{nn'}(\vec{q},q_z)$$

$$\times M^*_{mm'}(-\vec{q},q_z), \qquad (6)$$

where $M_{nn'}(\vec{q},q_z)$ is the matrix element representing the interaction between the 2D electron gas and 3D phonons, which is defined by

$$M_{nn'}(\vec{q},q_z) = \int_{\infty}^{\infty} dz\, \psi_n(z) V_{\vec{q},q_z} e^{iq_z z} \psi_{n'}(z), \qquad (7)$$

where $V_{\vec{q},q_z}$ is the coefficient of the Fourier transform of the Fröhlich Hamiltonian,

$$V_{\vec{q},q_z} = -i\hbar\omega_{LO}\left(\frac{\hbar}{2m^*\omega_{LO}}\right)^{1/4}\sqrt{\frac{4\pi\alpha}{\Omega(q^2+q_z^2)}}, \qquad (8)$$

α is the Fröhlich coupling constant, and Ω is the volume of the sample. After some algebra, we obtain

$$v^{ph}_{nn',mm'}(\vec{q},\omega) = \frac{2\pi e^2}{\epsilon_\infty q}\left(\frac{\omega_{LO}^2 - \omega_{TO}^2}{\omega^2 - \omega_{LO}^2}\right)F_{nn',mm'}(q). \qquad (9)$$

The free polarizability function of the Q2D electron gas in the multisubband system, at zero temperature, is given by

$$\Pi^0_{mm'}(\vec{q},\omega) = 2\sum_{\vec{k}} \frac{f_{m'}[E_{m'}(\vec{k}+\vec{q})] - f_m[E_m(\vec{k})]}{E_{m'}(\vec{k}+\vec{q}) - E_m(\vec{k}) + \hbar(\omega+i\gamma)}, \qquad (10)$$

where $f(E)$ is the Fermi-Dirac distribution function, and γ is broadening of the energy level related to impurity scattering. When $\gamma \to 0$, we obtain[26,28,32]

$$\mathrm{Re}\Pi^0_{mm'}(\vec{q},\omega) = \frac{m^*}{\pi\hbar^2}\left\{\left[\frac{\nu^-_{mm'}}{2\varepsilon_q} - \frac{1}{\sqrt{\varepsilon_q}}\mathrm{sgn}(\nu^-_{mm'})\right.\right.$$

$$\left. \times \mathrm{Re}(\varepsilon^-_{mm'} - E_{Fm})^{1/2}\right]\Theta(E_{Fm})$$

$$- \left[\frac{\nu^+_{mm'}}{2\varepsilon_q} - \frac{1}{\sqrt{\varepsilon_q}}\mathrm{sgn}(\nu^+_{mm'})\right.$$

$$\left.\left. \times \mathrm{Re}(\varepsilon^+_{mm'} - E_{Fm'})^{1/2}\right]\Theta(E_{Fm'})\right\}$$

$$(11)$$

and

$$\mathrm{Im}\Pi^0_{mm'}(\vec{q},\omega) = -\frac{m^*}{\pi\hbar^2}\{\mathrm{Re}[4E_{Fm}/\varepsilon_q - (\nu^-_{mm'}/\varepsilon_q)^2]^{1/2}$$

$$- \mathrm{Re}[4E_{Fm'}/\varepsilon_q - (\nu^+_{mm'}/\varepsilon_q)^2]^{1/2}\}, \qquad (12)$$

where $\varepsilon_q = \hbar^2 q^2/2m^*$, $\nu^\pm_{mm'} = \hbar\omega + E_{m'} - E_m \pm \varepsilon_q$, $\varepsilon^\pm_{mm'} = (\nu^\pm_{mm'})^2/4\varepsilon_q$, $E_{Fm} = E_F - E_m$, and $\Theta(E)$ is the step function.

The dielectric function $\epsilon_{nn',ll'}(\vec{q},\omega)$ is defined through the equation $v^c_{nn',mm'}(\vec{q}) = \sum_{ll'}\epsilon_{nn',ll'}(\vec{q},\omega)V^{sc}_{ll',mm'}(\vec{q},\omega)$. When both the electron-electron and the electron-phonon interactions are included in the dielectric function, we obtain within RPA (Ref. 37)

$$\epsilon_{nn',mm'}(q,\omega) = \epsilon_b(\omega)\delta_{nm}\delta_{n'm'} - v^c_{nn',mm'}(q)\Pi^0_{mm'}(q,\omega), \qquad (13)$$

with

$$\epsilon_b(\omega) = (\omega^2 - \omega_{LO}^2)/(\omega^2 - \omega_{TO}^2). \qquad (14)$$

Note that the dielectric function of a 2D electron gas without taking the electron-phonon interaction into account is easily recovered by substituting 1 for $\epsilon_b(\omega)$ in Eq. (13).

The spectrum of collective excitations of the system is given by the zeros of the generalized dielectric function

$$\det|\epsilon_{nn',mm'}(q,\omega)| = 0. \qquad (15)$$

In principle, all the subbands in the system should be considered in the above equation. If we keep N subbands for numerical calculations, Eq. (15) will be reduced to an $N^2 \times N^2$ determinantal equation. In the region where the dielectric function has an imaginary part, i.e., $\mathrm{Im}\,\Pi^0_{mm'} = 0$, the plasmon modes are Landau damped. We found that, in the ω-q plane, it corresponds to $\omega^+_{nn'} > \omega > \omega^-_{nn'}$, with $\omega^\pm_{nn'}(q) = (\hbar^2/2m^*)[(q\pm k_{Fn})^2 - k_{Fn'}^2]$, where $k_{Fn} = \sqrt{2m^*E_{Fn}}/\hbar$ is the Fermi wave vector of each subband. Notice that the intrasubband plasmon is not damped inside the regime of intersubband single-particle excitations because a charge-density wave parallel to the xy plane cannot excite particles across the subbands.[28]

III. NUMERICAL RESULTS AND DISCUSSIONS

We restrict ourselves to a four-subband model by considering the cases where one, two, or three subbands are occupied by the electrons and we neglect the effect of higher empty subbands.

To begin with, we consider the situation in which only one subband is occupied by the electrons and the other three are empty. There exist plasmon modes denoted by $(1,n')$, where $(1,1)$ is the single intrasubband plasmon mode and those with $n' \geq 2$ represent the intersubband plasmon modes. Within the four-subband model, the intrasubband mode $(1,1)$ and the intersubband mode $(1,3)$ are coupled. The modes are determined by the following dispersion equation (see the Appendix for details):

$$[\epsilon_b(\omega) - v^c_{11,11}(q)\chi^0_{11}(q,\omega)][\epsilon_b(\omega) - v^c_{13,13}(q)\chi^0_{13}(q,\omega)]$$
$$- v^{c\,2}_{11,13}(q)\chi^0_{11}(q,\omega)\chi^0_{13}(q,\omega) = 0, \qquad (16)$$

where $\chi^0_{mm}(q,\omega) = \Pi^0_{mm}(q,\omega)$ and $\chi^0_{mm'}(q,\omega)$ $= \Pi^0_{mm'}(q,\omega) + \Pi^0_{m'm}(q,\omega)$ for $m \neq m'$. On the other hand, the intersubband modes $(1,2)$ and $(1,4)$ are coupled to each other and are given by the solution of

$$[\epsilon_b(\omega) - v^c_{12,12}(q)\chi^0_{12}(q,\omega)][\epsilon_b(\omega) - v^c_{14,14}(q)\chi^0_{14}(q,\omega)]$$
$$- v^{c\,2}_{12,14}(q)\chi^0_{12}(q,\omega)\chi^0_{14}(q,\omega) = 0. \qquad (17)$$

The dispersion relations of the coupled plasmon-phonon modes in a Si δ-doped GaAs system with electron density $N_e = 0.7 \times 10^{12}$ cm^{-2} are depicted in Fig. 1. In the calculation, we took $\omega_{LO} = 36.25$ meV and $\omega_{TO} = 33.29$ meV. For this density, only the lowest subband is occupied by electrons. The subband Fermi energy $E_{F1} = 22.45$ meV and the subband Fermi wave vector $k_{F1} = 2.03 \times 10^6$ cm^{-1}. The dispersion relations of the unperturbed plasmon modes without electron-phonon interaction are given by the dashed curves in the figure. Figure 1(a) shows the dispersions of the intrasubband mode $(1,1)$ and the intersubband modes $(1,3)$. The spectrum of the other two modes $(1,2)$ and $(1,4)$ is given in Fig. 1(b). The shadow area corresponds to the single-particle continuum region where Im $\Pi^0_{nn'} \neq 0$. The results of Fig. 1(a) indicate that the dispersion of the unperturbed intrasubband plasmon mode $(1,1)$ develops a loop in the ω-q plane and has an acoustical-like behavior, since ω approaches zero when $q \rightarrow 0$. The maximum frequency appears at $(\omega,q) = (35.57, 1.23)$ on the edge of the region where Im $\Pi^0_{1,1} = 0$. Hereafter, ω is in energy units meV and q is in units of 10^6 cm^{-1}. In between, there are two frequencies for a given q. The upper branch is located in the region with Im $\Pi_{1,1} = 0$ whereas the lower one is in the region where Im $\Pi_{1,1} \neq 0$ and the collective excitations are strongly Landau damped and are not significant. The above results in the region where the dielectric function has an imaginary part do not exactly correspond to the frequency of the plasmon, which should be determined from the position of the peak in the electron energy-loss function defined as the imaginary part of the inverse of the dielectric function. Nevertheless, it was shown in Ref. 31 that for the plasmon-phonon modes in 2D electron systems, the zeros of the dielectric function correspond to peaks in the energy-loss spectrum. It is seen that
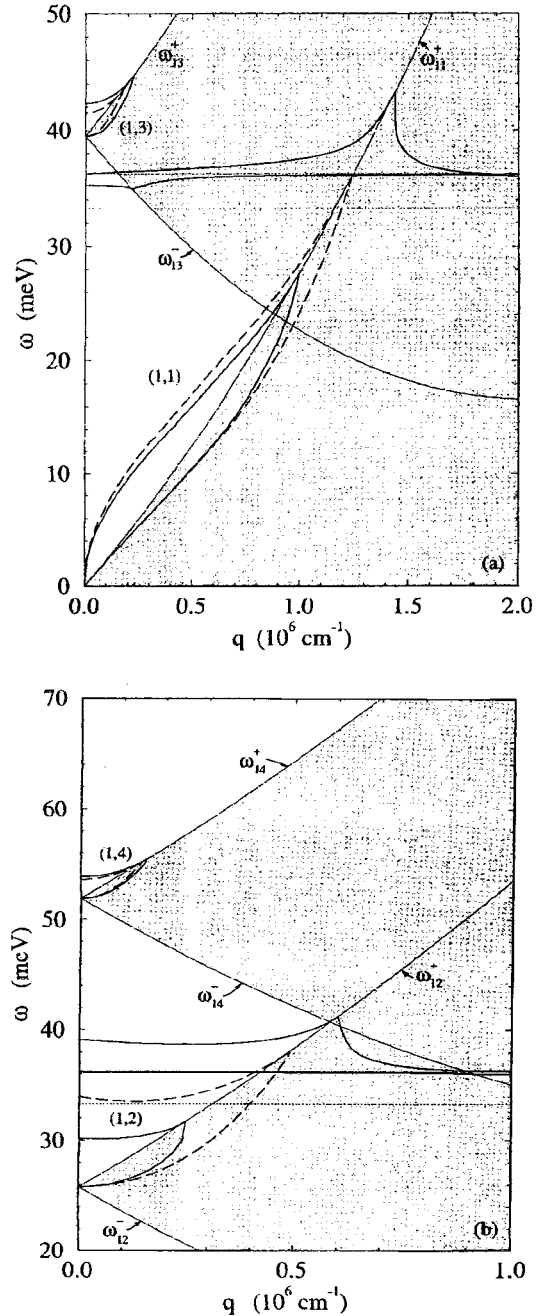

FIG. 1. Dispersions of the collective (a) intrasubband mode $(1,1)$ and the intersubband mode $(1,3)$ and (b) the intersubband modes $(1,2)$ and $(1,4)$ for Si δ-doped GaAs of $N_e = 0.7 \times 10^{12}$ cm^{-2}. The dispersions of the coupled plasmon-phonon modes and the unperturbed plasmon modes are shown by the thick-solid and the thick-dashed curves, respectively. The thin-solid curves $(\omega^\pm_{nn'})$ are the boundaries of the 2D single-particle excitation continuum. The shadow indicates the region where Im$\Pi^0_{nn'} \neq 0$. The dotted lines indicate the optical-phonon frequencies ω_{LO} and ω_{TO}.

the plasmon-phonon coupling is strong for both the intrasubband and the intersubband modes and this shows up at wave vectors far from the resonance where the unperturbed plasmon frequency is close to the LO phonon frequency ω_{LO}.

We observe in Fig. 1(a) that the frequency of the unper-

turbed intrasubband plasmon mode (1,1) is smaller than ω_{LO} for all q. When the electron-phonon interaction is considered, the coupled intrasubband plasmon-phonon modes show two branches in the region where Im $\Pi_{11}^0 = 0$. The lower branch is shrunk in comparison with the unperturbed plasmon mode, which penetrates into the continuum at $(\omega, q) = (27.20, 0.99)$. The upper one is above the LO-phonon frequency. It is very close to ω_{LO} at $q = 0$. By considering the intersubband mode (1,3), we see that the energy difference E_{13} between the two subbands is 39.48 meV, which is greater than ω_{LO}. However, the unperturbed intersubband plasmon frequency is 41.46 meV at $q = 0$, which is larger than E_{13} due to the depolarization shift coming from many-body effects. The electron-phonon coupling shifts this intersubband mode to higher frequency. In addition, a phononlike mode appears in the reststrahlen region of GaAs. Figure 1(b) shows the dispersion relations of the intersubband modes (1,2) and (1,4) in the four-subband model when only one subband is occupied. It is seen now that the unperturbed plasmon mode (1,2) crosses the LO-phonon frequency. We observe that the electron-phonon interaction leads to a large splitting of this mode.

Now, we analyze the case where $N_e = 2.0 \times 10^{12}$ cm^{-2} and two subbands of the four-subband model are occupied. The dispersion equations are given by Eqs. (A6) and (A7) in the Appendix. In Fig. 2, we plot the dispersion relations of the coupled plasmon-phonon modes. The subband Fermi energies are $E_{F1} = 50.41$ meV and $E_{F2} = 11.24$ meV, respectively. Consequently, $k_{F1} = 3.04 \times 10^6$ cm^{-1} and $k_{F2} = 1.42 \times 10^6$ cm^{-1}. Figure 2(a) shows the dispersion of the coupled modes (1,1), (2,2), (1,3), and (2,4). The dashed curves in the figure indicate the dispersion relations of the plasmon modes without the electron-phonon interaction. By comparing with the results shown in Fig. 1(a), we observe that two extra plasmon modes (2,2) and (2,4) arise due to the occupation of the $n = 2$ subband. Furthermore, the increase of the total electron density (doping concentration) leads to higher subband electron density and larger separation in energy between two subbands. Due to the higher electron density (larger Fermi wave vector) in the lowest subband, the unperturbed intrasubband plasmon mode (1,1) crosses over the LO-phonon frequency, and the electron-phonon interaction leads to the splitting of this mode. We see that the intrasubband mode (2,2) is not so pronounced and it is located within the single-particle continuum of the lowest subband. The intersubband mode (2,4) is close to, but smaller than, the phonon frequency ω_{LO}. The shrink of this mode is pronounced due to the electron-phonon coupling. Contrary to the situation shown in Fig. 1(a), the effect of the electron-phonon coupling on the intersubband mode (1,3) is not significant since its frequency is much larger than ω_{LO} in the present case. In Fig. 2(b) the most significant effect of the electron-phonon interaction is shown on the intersubband plasmon mode (1,2). The electron-phonon coupling leads to a shift of this mode to higher frequency and another phononlike mode appears in the reststrahlen region. This phononlike mode is almost flat.

Finally, we analyze the case where the electron density $N_e = 5.0 \times 10^{12}$ cm^{-2} which corresponds to three occupied subbands. Here, the subband Fermi energies (Fermi wave vectors) are $E_{F1} = 100.89$ meV ($k_{F1} = 4.31 \times 10^6$ cm^{-1}),
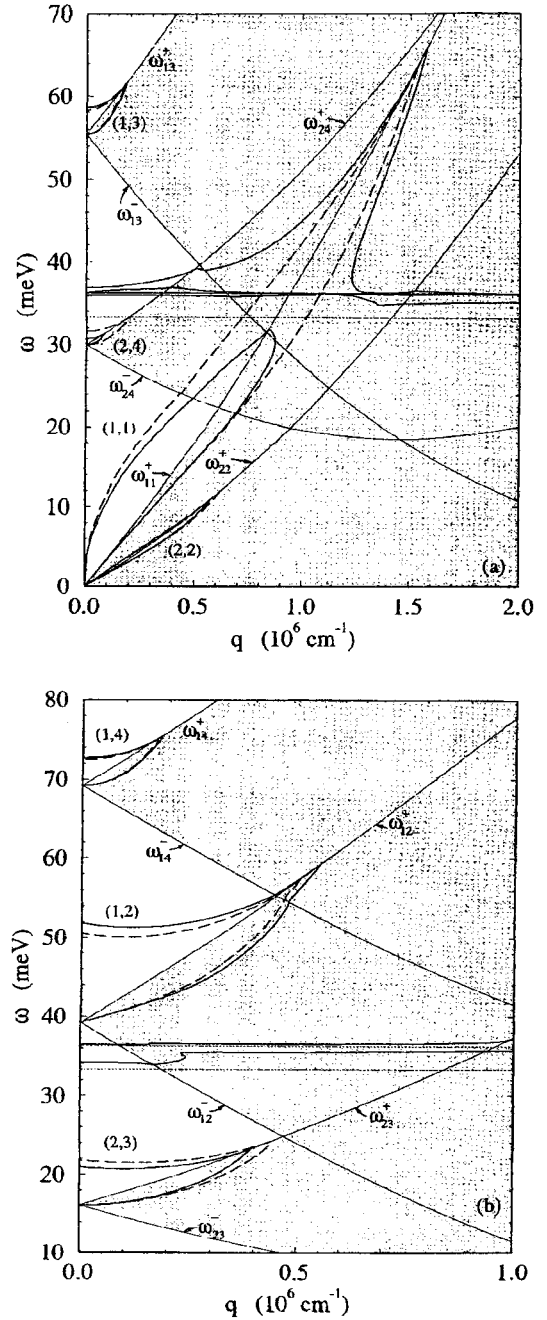

FIG. 2. The same as Fig. 1 but now for $N_e = 2 \times 10^{12}$ cm^{-2}. Four plasmon modes (1,1), (2,2), (1,3), and (2,4) appear in (a) and three plasmon modes (1,2), (2,3), and (1,4) in (b).

$E_{F2} = 33.23$ meV ($k_{F2} = 2.47 \times 10^6$ cm^{-1}), and $E_{F3} = 8.82$ meV ($k_{F3} = 1.27 \times 10^6$ cm^{-1}), respectively. Figure 3 shows the dispersion relations of the coupled plasmon-phonon modes. Two additional plasmon modes are found: the intrasubband mode (3,3) shown in Fig. 3(a) and the intersubband mode (3,4) in Fig. 3(b). The intrasubband mode (1,1) in Fig. 3(a) is strongly coupled to the LO-phonon modes. The coupling of the intersubband mode (2,4) to the LO-phonon leads to a phononlike mode in the reststrahlen region starting from $\omega = 35.11$ meV at $q = 0$. In Fig. 3(b), the electron-phonon

FIG. 4. The unperturbed intersubband plasmon frequencies at $q=10^4$ cm^{-1} as a function of the total electron density in Si δ-doped GaAs. The dotted curves indicate the energy differences between the subbands.
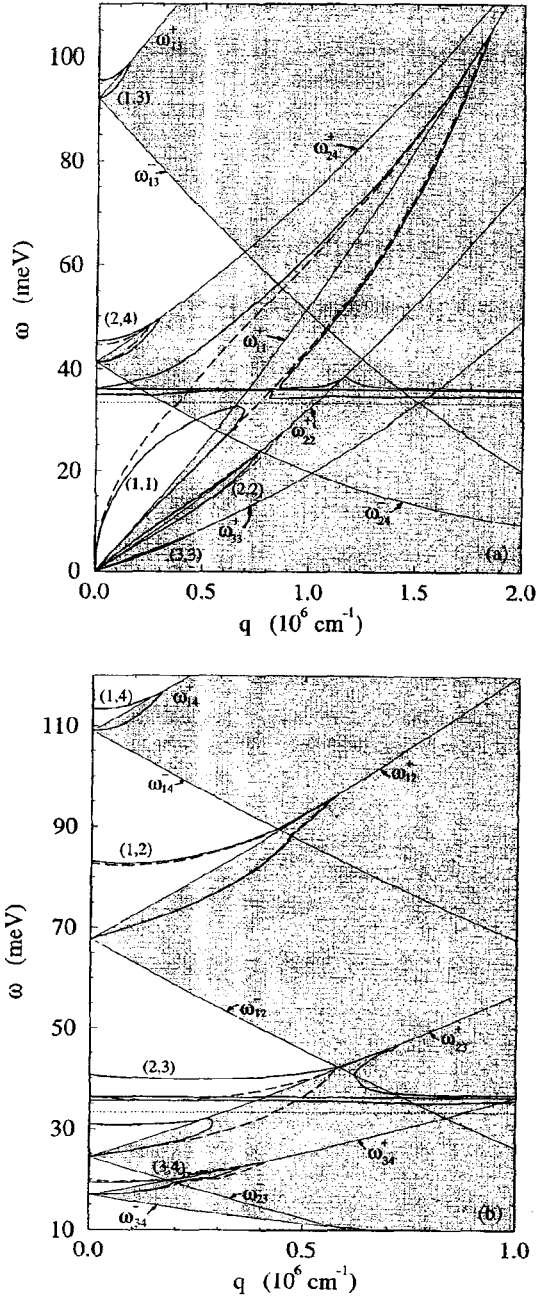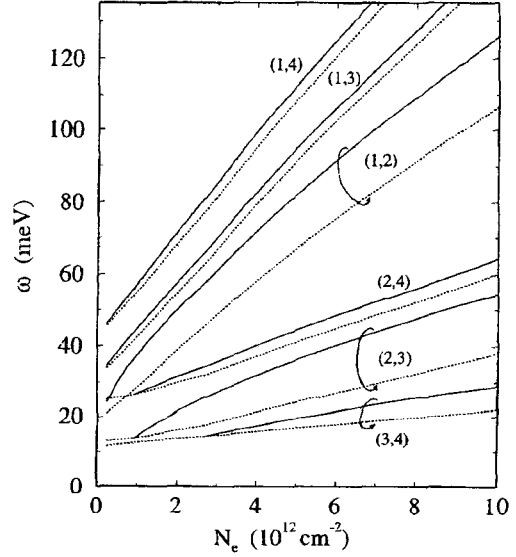
FIG. 3. The same as Fig. 1 but now for $N_e = 5 \times 10^{12}$ cm^{-2}. Five plasmon modes (1,1), (2,2), (3,3), (1,3), and (2,4) appear in (a) and four plasmon modes (1,2), (1,4), (2,3), and (3,4) in (b).

coupling results in a pronounced splitting of the intersubband mode (2,3).

In Fig. 4, the unperturbed intersubband plasmon frequencies at $q = 1 \times 10^4$ cm^{-1} are plotted as a function of the total electron density in the δ-doped system. The dotted curves represent the energy difference $E_{n'} - E_n$ between the two subbands. We see that, at the onset of the occupation of a subband, the intersubband plasmon frequency is equal to the energy difference. By increasing the total electron density, and the subband electron density, the intersubband plasmon frequency becomes larger than the energy difference. This

results in a depolarization shift due to many-body effects. The shift is more pronounced for adjacent subbands, i.e., the intersubband modes (1,2) and (2,3). When the electron-phonon interaction is included, the intersubband plasmon frequency splits around the LO-phonon frequency. The frequencies of the coupled plasmon-phonon modes at $q = 1 \times 10^4$ cm^{-1}, as a function of the total electron density, are depicted in Fig. 5(a) for the (1,2) and (1,3) intersubband modes and in Fig. 5(b) for the (2,3) and (2,4) modes. The thin curves represent the corresponding intersubband plasmon frequencies without the electron-phonon interaction. We see that the intersubband plasmon modes are strongly coupled to the optical-phonon modes. When the unperturbed intersubband frequency is equal to ω_{LO}, the splitting is 9.29 meV for the (1,2) mode and 9.73 meV and 5.45 meV for (2,3) and (2,4) modes, respectively. At low electron densities, the lower branch is close to the unperturbed plasmon frequency and it is much smaller than ω_{LO}, while the frequencies of the upper branch are close to ω_{LO}. However, the lower branch approaches the ω_{LO} at high densities whereas the upper one becomes close to the unperturbed plasmon frequency. For a wide range of electron densities, the frequencies of the lower branch of the intersubband plasmon-phonon modes (1,3), (1,2), and (2,4) lie in the reststrahlen region of GaAs.

The coupled plasmon-phonon mode in the reststrahlen region was observed experimentally for the Si δ-doped GaAs system by Mlayah et al.[9] They found in the Raman spectrum that the phononlike mode appears at $\omega = 34.97$ meV (282 cm^{-1}) for the sample with donor concentration $N_D = 2.7 \times 10^{12}$ cm^{-2} and $W_D = 20$ Å. By fitting the Raman spectrum, they obtained the depolarization shift about 26.67 meV (215 cm^{-1}) for the unperturbed intersubband mode (1,2). From our calculation with the same donor concentration, we obtained for the intersubband mode (1,2) ($E_{12} = 42.09$ meV), the unperturbed plasmon frequency
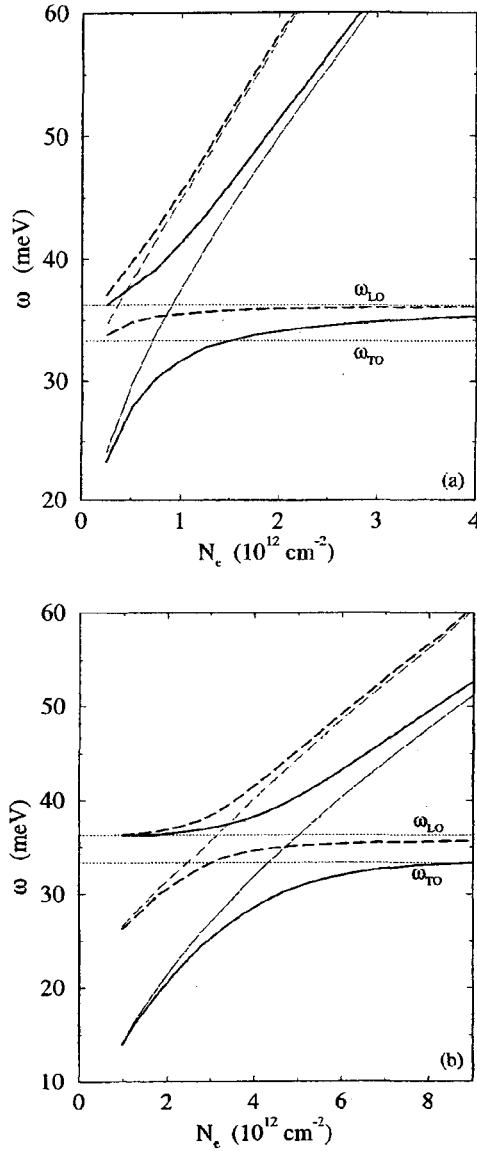
FIG. 5. The frequencies of the coupled intersubband plasmon-phonon modes (a) (1,2) (solid curves) and (1,3) (dashed curves) and (b) (2,3) (solid curves) and (2,4) (dashed curves) at $q = 10^4$ cm^{-1} as a function of electron density. The thin curves indicate the unperturbed plasmon frequency.

equals to 54.21 meV, a depolarization shift of 34.08 meV, and frequencies of the coupled plasmon-phonon modes with values 34.28 meV and 55.54 meV. So, our results are in reasonable agreement with the experimental results of Ref. 9. However, we also observed that, for higher electron densities, there are two or more intersubband plasmon-phonon modes in the reststrahlen region such as (1,2), (1,3), and (2,4) modes. At $N_e > 8 \times 10^{12}$ cm^{-2}, the intersubband mode (2,3) would play an important role in this region.

IV. CONCLUSIONS

We have calculated the spectrum of the coupled plasmon-phonon modes for a multisubband electron system realized in Si δ-doped GaAs. The numerical results show that the electron-phonon interaction alters the unperturbed plasmon-excitation spectrum considerably. Due to its high electron density, the plasmon-phonon coupling is substantially stronger than that in other 2D systems, such as semiconductor quantum wells and heterojunctions. Since several subbands are occupied by the electrons, the intersubband plasmon modes have be shown to be essential to the physical description of the system.

Our results show that the high electron density leads to a large depolarization shift of the intersubband plasmon frequencies between adjacent subbands. Furthermore, both intrasubband plasmon and intersubband plasmon modes are strongly coupled to the optical-phonon modes. The frequencies of the coupled intrasubband plasmon-phonon modes do not enter in the reststrahlen region of GaAs. However, the frequencies of the coupled intersubband plasmon-phonon modes split around the LO-phonon frequency ω_{LO}. In a wide range of electron density (donor concentration), the frequencies of the phononlike branch of the intersubband plasmon-phonon modes (1,2), (1,3), (2,3), and (2,4) are in the reststrahlen region of GaAs.

APPENDIX

In this appendix, we show in detail how the determinantal equation for the dielectric matrix, Eq. (15), was solved numerically. Due to the symmetry of the confinement potential in the δ-doped system which results in the vanishing of the form factor $F_{nn',mm'}(q)$, given by Eq. (5), when $n + n' + m + m'$ is an odd number, and the corresponding matrix elements of the dielectric function, given by Eq. (13), we find that there are two groups of plasmon modes. One of them includes all the intrasubband modes as well as the intersubband modes whose wave functions have the same parity. All plasmon modes in this group are coupled to each other. The other group is formed by the intersubband modes of two subbands with different parities and the plasmon modes in this group are also coupled to each other but they do not interact with the modes of the former one.

In the four-subband model, the 16×16 determinantal equation is reduced to the following two groups of equations:

$$\begin{vmatrix} \kappa_{11,11} & \kappa_{11,22} & \kappa_{11,33} & \kappa_{11,44} & \kappa_{11,13} & \kappa_{11,24} \\ \kappa_{22,11} & \kappa_{22,22} & \kappa_{22,33} & \kappa_{22,44} & \kappa_{22,13} & \kappa_{22,24} \\ \kappa_{33,11} & \kappa_{33,22} & \kappa_{33,33} & \kappa_{33,44} & \kappa_{33,13} & \kappa_{33,24} \\ \kappa_{44,11} & \kappa_{44,22} & \kappa_{44,33} & \kappa_{44,44} & \kappa_{44,13} & \kappa_{44,24} \\ \kappa_{13,11} & \kappa_{13,22} & \kappa_{13,33} & \kappa_{13,44} & \kappa_{13,13} & \kappa_{13,24} \\ \kappa_{24,11} & \kappa_{24,22} & \kappa_{24,33} & \kappa_{24,44} & \kappa_{24,13} & \kappa_{24,24} \end{vmatrix} = 0$$

(A1)

and

$$
\begin{vmatrix}
\kappa_{12,12} & \kappa_{12,14} & \kappa_{12,23} & \kappa_{12,34} \\
\kappa_{14,12} & \kappa_{14,14} & \kappa_{14,23} & \kappa_{14,34} \\
\kappa_{23,12} & \kappa_{23,14} & \kappa_{23,23} & \kappa_{23,34} \\
\kappa_{34,12} & \kappa_{34,14} & \kappa_{34,23} & \kappa_{34,34}
\end{vmatrix} = 0, \qquad \text{(A2)}
$$

where

$$
\kappa_{nn',mm'}(q,\omega) = \epsilon_b(\omega)\,\delta_{nm}\delta_{n'm'} - v^c_{nn',mm'}(q)\chi^0_{mm'}(q,\omega),
$$
$$\text{(A3)}$$

with $\chi^0_{mm}(q,\omega) = \Pi^0_{mm}(q,\omega)$ and $\chi^0_{mm'}(q,\omega) = \Pi^0_{mm'}(q,\omega) + \Pi^0_{m'm}(q,\omega)$ for $m \neq m'$.

In the case of only one occupied subband, Eqs. (A1) and (A2) reduce to

$$
\begin{vmatrix}
\kappa_{11,11} & \kappa_{11,13} \\
\kappa_{13,11} & \kappa_{13,13}
\end{vmatrix} = 0 \qquad \text{(A4)}
$$

and

$$
\begin{vmatrix}
\kappa_{12,12} & \kappa_{12,14} \\
\kappa_{14,12} & \kappa_{14,14}
\end{vmatrix} = 0. \qquad \text{(A5)}
$$

It is seen that the intrasubband mode (1,1) couples to the intersubband mode (1,3) determined by Eq. (A4). The other two intersubband modes (1,2) and (1,4) are coupled to each other.

In the case of two occupied subbands within the four-subband model, the determinantal equations, given by Eqs. (A1) and (A2), are now written in terms of 4×4 and 3×3

determinants. There are two intrasubband modes (1,1) and (2,2). These two modes are coupled to each other and also coupled to the intersubband modes (1,3) and (2,4). They are determined by the dispersion equation

$$
\begin{vmatrix}
\kappa_{11,11} & \kappa_{11,22} & \kappa_{11,13} & \kappa_{11,24} \\
\kappa_{22,11} & \kappa_{22,22} & \kappa_{22,13} & \kappa_{22,24} \\
\kappa_{13,11} & \kappa_{13,22} & \kappa_{13,13} & \kappa_{13,24} \\
\kappa_{24,11} & \kappa_{24,22} & \kappa_{24,13} & \kappa_{24,24}
\end{vmatrix} = 0. \qquad \text{(A6)}
$$

The remaining coupled intersubband modes (1,2), (2,3), and (1,4) can be calculated from

$$
\begin{vmatrix}
\kappa_{12,12} & \kappa_{12,14} & \kappa_{12,23} \\
\kappa_{14,12} & \kappa_{14,14} & \kappa_{14,23} \\
\kappa_{23,12} & \kappa_{23,14} & \kappa_{23,23}
\end{vmatrix} = 0. \qquad \text{(A7)}
$$

In the case of three occupied subbands, Eq. (A1) reduces to

$$
\begin{vmatrix}
\kappa_{11,11} & \kappa_{11,22} & \kappa_{11,33} & \kappa_{11,13} & \kappa_{11,24} \\
\kappa_{22,11} & \kappa_{22,22} & \kappa_{22,33} & \kappa_{22,13} & \kappa_{22,24} \\
\kappa_{33,11} & \kappa_{33,22} & \kappa_{33,33} & \kappa_{33,13} & \kappa_{33,24} \\
\kappa_{13,11} & \kappa_{13,22} & \kappa_{13,33} & \kappa_{13,13} & \kappa_{13,24} \\
\kappa_{24,11} & \kappa_{24,22} & \kappa_{24,33} & \kappa_{24,13} & \kappa_{24,24}
\end{vmatrix} = 0, \qquad \text{(A8)}
$$

while Eq. (A2) keeps the same form.

[1] E. F. Schubert, in *Semiconductors and Semimetals*, edited by A. C. Gossard (Academic Press, New York, 1994), Vol. 40, p. 1.

[2] S. J. Bass, J. Cryst. Growth 47, 613 (1979).

[3] C. E. C. Wood, G. M. Metze, J. D. Berry, and L. F. Eastman, J. Appl. Phys. 51, 383 (1980).

[4] E. F. Schubert, J. B. Stark, B. Ullrich, and J. E. Cunningham, Appl. Phys. Lett. 52, 1508 (1988).

[5] P.M. Koenraad, in *Delta Doping of Semiconductors*, edited by E.F. Schubert (Cambridge Univ. Press, London, 1995), p. 304.

[6] A. Zrenner, F. Koch, J. Leotin, M. Goiran, and K. Ploog, Semicond. Sci. Technol. 3, 1132 (1988).

[7] E. Skuras, R. Kumar, R. L. Williams, R. A. Stradling, J. E. Dmochowski, E. A. Johnson, A. Mackinnon, J. J. Harris, R. B. Beall, C. Skierbeszewski, J. Singleton, P. J. van der Wel, and P. Wisnieski, Semicond. Sci. Technol. 6, 535 (1991).

[8] J. J. Harris, R. Murray, and C. T. Foxon, Semicond. Sci. Technol. 8, 31 (1993).

[9] A. Mlayah, R. Carles, E. Bedel, and A. Muñoz-Yagüe, Appl. Phys. Lett. 62, 2848 (1993); J. Appl. Phys. 74, 1072 (1993).

[10] C. Lohe, A. Leuther, A. Förster, and H. Lüth, Phys. Rev. B 47, 3819 (1993).

[11] Yu. A. Pusep, M. T. O. Silva, J. C. Galzerani, S. W. da Silva, L. M. R. Scolfaro, R. Enderlein, A. A. Quivy, A. P. Lima, and J. R. Leite, Phys. Rev. B 54, (to be published).

[12] G. Hasnain, G. H. Döhler, J. R. Whimery, J. N. Miller, and A. Dienes, Appl. Phys. Lett. 49, 1357 (1986).

[13] E. F. Schubert, J. P. van der Ziel, J. E. Cunningham, and T. D.

Harris, Appl. Phys. Lett. 55, 757 (1989).

[14] E. F. Schubert and J. E. Cunningham, Electron. Lett. 24, 980 (1988).

[15] E. F. Schubert, J. E. Cunningham, W. T. Tsang, and G. L. Timp, Appl. Phys. Lett. 51, 1170 (1987).

[16] R. J. Malik, T. R. AuCoin, R. L. Ross, K. Board, C. E. C. Wood, and L. F. Eastman, Electron. Lett. 16, 836 (1980).

[17] J. N. Bailargeon, K. Y. Cheng, J. Lasker, and J. Kolodzey, Appl Phys. Lett. 55, 663 (1989).

[18] G. Abstreiter, M. Cardona, and A. Pinczuk, in *Light Scattering in Solids IV*, edited by M. Cardona and G. Güntherodt (Springer-Verlag, Berlin, 1984), p. 36.

[19] E. Burnstein, A. Pinczuk, and S. Bucher, in *Physics of Semiconductors*, edited by B. L. H. Wilson (The Institute of Physics, London, 1979), p. 1231; E. Burstein, A. Pinczuk, and D. L. Mills, Surf. Sci. 98, 451 (1980).

[20] D. Olego, A. Pinczuk, A. C. Gossard, and W. Wiegmann, Phys. Rev. B 25, 7867 (1982); R. Sooryakumar, A. Pinczuk, A. C. Gossard, and W. Wiegmann, *ibid.* 29, 3318 (1984).

[21] A. Pinczuk, M. G. Lamont, and A. C. Gossard, Phys. Rev. Lett. 56, 2092 (1986).

[22] G. Fasol, N. Mestres, H. P. Hughes, A. Fischer, and K. Ploog, Phys. Rev. Lett. 56, 2517 (1986).

[23] J. W. Wu, P. Hawrylak, and J. J. Quinn, Phys. Rev. Lett. 55, 879 (1985).

[24] J. K. Jain and P. B. Allen, Phys. Rev. Lett. 54, 947 (1984); 55, 997 (1985).

[25] S. Das Sarma, A. Kobayashi, and R. E. Prange, Phys. Rev. Lett. 56, 1280 (1986); Phys. Rev. B 34, 5309 (1986).

[26] X. Wu and S. E. Ulloa, Phys. Rev. B 48, 14 407 (1993).

[27] S. Das Sarma, Phys. Rev. B 29, 2334 (1984).

[28] J. K. Jain and S. Das Sarma, Phys. Rev. B 36, 5949 (1987).

[29] Q. Li and S. Das Sarma, Phys. Rev. B 40, 5860 (1989); 43, 11 768 (1991).

[30] W. H. Backes, F. M. Peeters, F. Brosens, and J. T. Devreese, Phys. Rev. B 45, 8437 (1992).

[31] X.-G. Wu, F. M. Peeters, and J. T. Devreese, Phys. Rev. B 32, 6982 (1985).

[32] L. Wendler and R. Pechstedt, Phys. Status Solidi B 138, 197 (1986); 141, 129 (1987).

[33] G.-Q. Hai, F. M. Peeters, and J. T Devreese, Phys. Rev. B 42, 11 063 (1990); 47, 10 358 (1993).

[34] G.-Q. Hai and N. Studart, Phys. Rev. B 52, R2245 (1995).

[35] G.-Q. Hai, N. Studart, and F. M. Peeters, Phys. Rev. B 52, 8363 (1995).

[36] G.-Q. Hai, N. Studart, F.M. Peeters, P. M. Koenraad, and J. H. Wolter, J. Appl. Phys. (to be published).

[37] G. D. Mahan, *Many-Particle Physics* (Plenum Press, New York, 1981).

[38] M. Jonson, J. Phys. C 9, 3055 (1976); P. J. Price, Phys. Rev. B 30, 2234 (1984); U. de Freitas and N. Studart, *ibid.* 36, 6677 (1987).

Level-broadening effects on the inelastic light-scattering spectrum due to coupled plasmon-phonon modes in δ-doped semiconductors

Guo-Qiang Hai, Nelson Studart, and Gilmar E. Marques

Departamento de Física, Universidade Federal de São Carlos, 13565-905 São Carlos, São Paulo, Brazil

(Received 6 January 1997; revised manuscript received 7 July 1997)

The Raman scattering intensity of δ-doped semiconductors is evaluated. The dynamical response of the multisubband two-dimensional electron system which is coupled to optical phonons is calculated within the random-phase approximation. Our calculation shows that both intrasubband and intersubband plasmon modes are strongly coupled to optical-phonon modes. Level broadening due to high impurity concentration modifies the inelastic light scattering spectrum significantly. However, a few scattering peaks corresponding to phonon-like modes can be observed even at large broadening. [S0163-1829(98)04304-5]

I. INTRODUCTION

Inelastic light (Raman) scattering has been used extensively to investigate novel aspects of the electronic structure and collective excitations in low-dimensional semiconductor systems.[1-5] In semiconductors with simple band extrema, collective excitations due to charge-density fluctuations and single-particle excitations related to spin density fluctuations have been observed.[8] In polar semiconductors, the collective excitations due to charge-density fluctuations of the electron gas can be modified by their coupling to longitudinal-optical (LO) phonons as shown in light scattering experiments.[1,6-8]

In δ-doped polar semiconductors, such as Si δ-doped GaAs, the plasmon-phonon coupling is quite pronounced and essentially important because the electron density is high and also because the energy separation between different subbands is close to the optical-phonon energy.[9] The quasi-two-dimensional electron gas (Q2DEG) in a δ-doped semiconductor is formed by a highly doped impurity layer. Since the electrons share the same spatial region with the ionized donors, they are strongly scattered by the impurities. Consequently, the scattering reduces not only the electron mobility[10] but also broadens the optical spectrum. The present work is intended to describe theoretically the light scattering spectrum due to coupled plasmon-phonon modes in the Si δ-doped GaAs system based on a self-consistent calculation of the subband structure and the dielectric many-body theory within the random-phase approximation (RPA). This paper stresses the broadening effects on the light spectrum and predicts the scattering peaks which can be detected experimentally. In Sec. II, we develop the dielectric formalism that is used to evaluate the plasmon-phonon spectrum and the inelastic light-scattering intensity. Section III is devoted to a discussion of the calculation results and in Sec. IV we summarize our main conclusions.

II. THEORETICAL FORMALISM

We have derived the inelastic light scattering cross section due to coupled plasmon-phonon modes in a *multisubband* Q2DEG embedded into a polar semiconductor. The inelastic light scattering intensity is related to the dynamical structure factor and can be written as

$$I(k_z,q,\omega) = \int dz \int dz' e^{-ik_z(z-z')}$$
$$\times [-\text{Im}\{\epsilon_b(\omega)\chi(q,\omega,z,z')\}], \quad (1)$$

where k_z is the z component of wave vector of the incident light and q is the electron wave vector transfer in the xy plane. In Eq. (1), the polarization of the background polar semiconductor is modeled by a frequency-dependent dielectric function $\epsilon_b(\omega)$ determined by the longitudinal (ω_{LO}) and transversal (ω_{TO}) optical-phonon frequencies, with the following simplified form:

$$\epsilon_b(\omega) = 1 + \frac{\omega_{TO}^2 - \omega_{LO}^2}{\omega^2 - \omega_{TO}^2 + i\omega\eta}, \quad (2)$$

where we have introduced a phenomenological parameter η, to incorporate the phonon damping associated to possible defects in the crystalline structure.

The density-density correlation $\chi(q,\omega,z,z')$ of the Q2DEG is calculated as an expansion in single-particle wave functions $\psi_n(z)$, as

$$\chi(q,\omega,z,z') = \sum_{nn',mm'} \chi_{nn',mm'}(q,\omega)\psi_n(z)$$
$$\times \psi_{n'}(z)\psi_m(z')\psi_{m'}(z'), \quad (3)$$

where $n,m = 1,2,3,\ldots$, are the subband indices. The density-density correlation function $\chi_{nn',mm'}(q,\omega)$ is related to the dielectric function $\epsilon_{nn',mm'}(q,\omega)$ through the equation

$$\sum_{ll'} \epsilon_{ll',nn'}(q,\omega)\chi_{ll',mm'}(q,\omega) = \Pi_{nn'}(q,\omega)\delta_{nm}\delta_{n'm'}, \quad (4)$$

with the polarizability of the noninteracting electron gas given by

$$\Pi_{nn'}(q,\omega) = 2\sum_k \frac{f_{n'}[E_{n'}(\vec{k}+\vec{q})] - f_n[E_n(\vec{k})]}{E_{n'}(\vec{k}+\vec{q}) - E_n(\vec{k}) + \hbar(\omega+i\gamma)}. \quad (5)$$

Here $f_n(E)$ is the Fermi-Dirac function, the electron energy is given by $E_n(k) = E_n + \hbar^2 k^2/2m^*$, m^* being the electron

effective mass, and γ is a phenomenological damping constant which takes into account the level broadening mainly induced by scattering of electrons by impurity centers. In the case $\gamma = 0$, Stern[11] was the first to give an analytical expression for $\Pi_{nn'}(q,\omega)$. In general, the damping constant η for the phonon system is much smaller that the damping constant of electrons and, due to the high impurity concentration in the δ-doped system, we can safely take η as a positive infinitesimal in reliable calculations.

It is well known that the polarizabilities from both electron and phonon systems are additive in the RPA so that when both the electron-electron and the electron-phonon interactions are included we can write the total dielectric function as

$$\epsilon_{nn',mm'}(q,\omega) = \epsilon_b(\omega)\delta_{nm}\delta_{n'm'}$$
$$- v_q F_{nn',mm'}(q)\Pi_{mm'}(q,\omega), \qquad (6)$$

where $v_q = 2\pi e^2/\epsilon_\infty q$ is the 2D Fourier transform of the bare electron-electron interaction, with ϵ_∞ being the high-frequency dielectric constant of the background. Finally $F_{nn',mm'}(q)$ is the Coulomb form factor which results from the spreading of the electron wave in the z direction and is given by[10]

$$F_{nn',mm'}(q) = \int_{-\infty}^{\infty} dz\,\psi_n(z)\psi_{n'}(z)$$
$$\times \int_{-\infty}^{\infty} dz'\,\psi_m(z')\psi_{m'}(z')e^{-q|z-z'|}.$$

Note that by setting $\epsilon_b(\omega) = 1$ in Eq. (6), the dielectric function of the Q2DEG in the RPA, without considering the electron-phonon interaction, is easily recovered.

Equations (1)–(6) describe the inelastic light scattering by charge density fluctuations of the coupled plasmon LO-phonon modes in a multisubband system. It is worth noticing that the light scattering intensity, given by Eq. (1), is proportional to the product of $\chi(q,\omega,z,z')$ and $\epsilon_b(\omega)$. As a consequence, one important feature is that the scattering intensity is zero at $\omega = \omega_{LO}$. This is a signature of a charge-density fluctuation mechanism because, at $\omega = \omega_{LO}$, there are no free-electron density fluctuations in the coupled plasmon LO-phonon system.

III. NUMERICAL RESULTS AND DISCUSSION

As in our previous works,[9,10] we consider a Si δ-doped GaAs structure with a doping layer in the xy plane with thickness $W_D = 10$ Å. The background acceptor concentration in the sample is taken to be $n_A = 10^{15}$ cm^{-3}. In Fig. 1, the inelastic light intensity is indicated by solid curves, for different q's, ranging from 10^4 to 1.4×10^6 cm^{-1}, in the system where the electron density $N_e = 2 \times 10^{12}$ cm^{-2} and $\gamma = 0.5$ meV. In this situation, two subbands whose subband Fermi energies are $E_{F1} = 50.41$ meV and $E_{F2} = 11.24$ meV are occupied. The energy separations between subband pairs $(E_{nn'} = E_{n'} - E_n)$ are $E_{12} = 39.17$ meV, $E_{13} = 55.38$ meV, and $E_{23} = 16.19$ meV. In the calculation, we have included a third unoccupied subband. The thin solid curves show the scattering intensity due to plasmon modes of the Q2DEG,
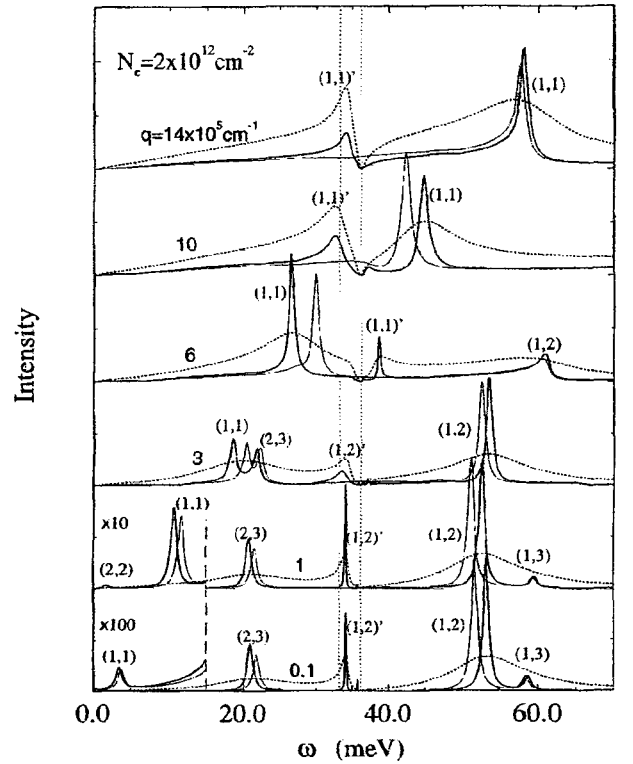

FIG. 1. The inelastic light scattering intensity due to plasmon (thin solid curves) and coupled plasmon-phonon modes at $q = 0.1$, 1, 3, 6, 10, and 14×10^5 cm^{-1} in Si δ-doped GaAs with $N_e = 2 \times 10^{12}$ cm^{-2}. The thick solid and dotted curves indicate the results with $\gamma = 0.5$ and 6 meV, respectively. The scattering peaks due to different plasmon modes are labeled by (n,m). Note the change in spectra scales: the intensity for $\gamma = 6$ meV is enlarged 3 times.

without phonons, and the thick solid curves are the results with the inclusion of the plasmon-phonon coupling. The vertical dotted lines indicate the frequencies of TO and LO phonons, $\hbar\omega_{LO} = 36.25$ meV and $\hbar\omega_{TO} = 33.29$ meV, respectively.

The Raman spectrum in the absence of plasmon-phonon coupling exhibits a rich peak structure corresponding to excitation modes which are denoted by (n,m) . We can observe in the thin curves of Fig. 1, the peaks at small wave vectors related to the intrasubband modes (2,2) and (1,1), with very weak intensity, and the intersubband modes (2,3), (1,2), and (1,3). With increasing q, the peaks of the modes (2,2) and (1,3) disappear, while the peak corresponding to the (1,1) mode becomes pronounced and survives at large q. When the plasmon-phonon coupling is considered, a comparison of the two scattering spectra shows that the resonance frequencies below ω_{LO} are redshifted while those above ω_{LO} are blueshifted. More essentially, new coupled modes, which are denoted by $(n,m)'$, arise around ω_{LO} due to the plasmon-phonon coupling. At small q, we can see clearly a phononlike mode in the reststrahlen region of GaAs which comes from the phonon-coupling of the intersubband mode (1,2). At large q, the intrasubband mode (1,1) is strongly coupled to the phonons.

Now, we investigate the effect of the impurity scattering on the light spectrum, which is described by the broadening
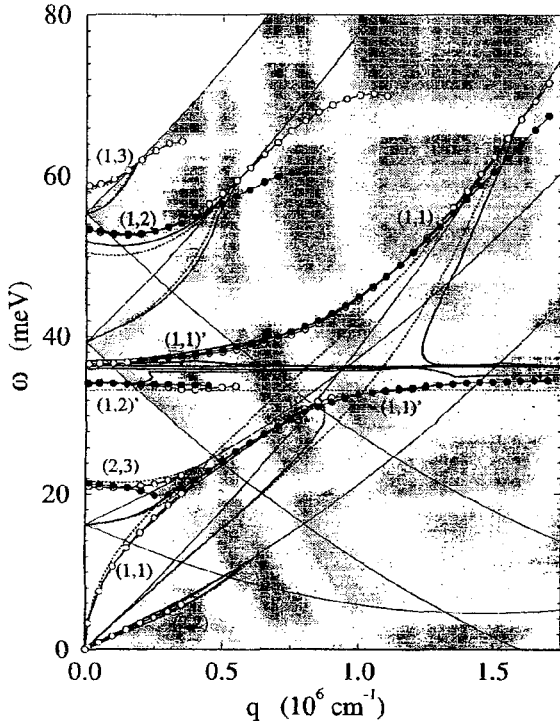
FIG. 2. The dispersion relations of the plasmon (thick dotted curves) and coupled plasmon-phonon (thick-solid curves) modes with $\gamma=0$ in the system of $N_e=2\times10^{12}$ cm^{-2}. The open and solid circles indicate the peak positions in the scattering spectrum due to coupled plasmon-phonon modes with $\gamma=0.5$ and 6 meV, respectively. The shaded area corresponds to the pair-excitation region (Landau damping).

width γ related to the electron subband quantum lifetime or the single-particle relaxation time. From our previous works,[10] the subband quantum mobility varies from about 500 cm^2/Vs (the lowest subband with energy of 24 meV) to 4000 cm^2/Vs (the third subband with energy of 3 meV). The dotted curves in Fig. 1 represent the scattering intensity with $\gamma=6$ meV. As expected, some of the peaks are merged. The scattering peak of the intrasubband mode $(1,1)'$ cannot be observed at small q. Also, those peaks corresponding to the intrasubband mode $(2,2)$ and to the intersubband $(1,3)$ disappear. However, the broadening does not affect considerably the phononlike modes, e.g., the peak $(1,2)'$ located at a little higher than ω_{TO}.

In order to clarify the scattering spectra, we have calculated the dispersion relations of the plasmon and coupled plasmon-phonon modes. For $\gamma=0$, the dispersion relation of the collective excitations can be obtained from[9]

$$\det|\epsilon_{nn',mm'}(q,\omega)|=0. \tag{7}$$

Figure 2 shows the plasmon dispersion (thick-dotted curves) and coupled plasmon-phonon modes (thick-solid curves) within the three-band model. The shaded area shows the single-particle spin-density excitation regime where $\text{Im}\,\Pi_{nn'}\neq0$. It can be seen that the dispersion of the unperturbed plasmon modes $(1,1)$ and $(2,2)$ develops a loop in the $\omega-q$ plane. There are two frequencies, for a given q, but the lower branch is in the region where $\text{Im}\Pi_{n,n}\neq0$ and the corresponding modes are strongly Landau damped. Due to the
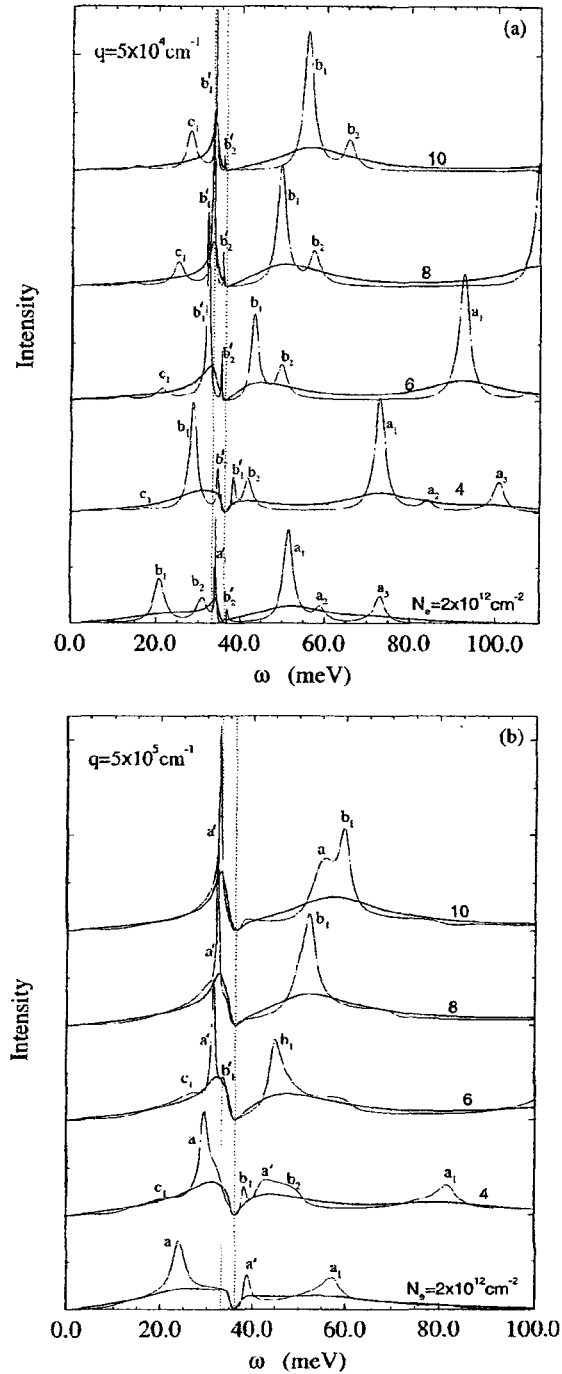

FIG. 3. The scattering spectra with $\gamma=1.5$ meV (thin curves) and $\gamma=10$ meV (thick curves) at (a) $q=5\times10^4$ cm^{-1} and (b) $q=5\times10^5$ cm^{-1} for the systems of different electron densities $N_e=2,4,6,8$, and 10×10^{12} cm^{-2}. The scattering peaks due to different plasmon-phonon modes are labeled by a and a' (1,1); a_1 and a_1': (1,2); a_2: (1,2); a_3: (1,4); b_1 and b_1': (2,3); b_2 and b_2': (2,4); c_1: (3,4).

high electron density in the lowest subband, the unperturbed plasmon mode $(1,1)$ crosses over the LO-phonon frequency and the electron-phonon interaction leads to a splitting of this mode. The electron-phonon coupling also alters the intersubband mode $(1,2)$ by inducing a shift to higher frequency and another phononlike mode $(1,2)'$ arises between ω_{TO} and

ω_{LO}. The results obtained from the peak positions of the scattering spectrum with $\gamma=0.5$ and 6 meV are indicated by open and solid circles in Fig. 2, respectively. From the spectrum with $\gamma=0.5$ meV, we observe all the plasmon-phonon modes in the region where $\mathrm{Im}\Pi_{n,m}=0$. From the above results, we conclude that (i) each mode (n,m) is Landau damped only in the region where $\mathrm{Im}\,\Pi_{n,m}\neq0$, (ii) the scattering peak coming from the intrasubband or intersubband mode vanishes slowly when it enters into its own single-particle continuum region, and (iii) the scattering intensity of the intrasubband modes is almost zero at small q and it increases with increasing q. Conversely, the intersubband modes exhibit the most intensity at small q, and it decreases with increasing q. For larger broadening, $\gamma=6$ meV, only three peaks can be observed at small q. These are related to the plasmonlike mode (2,3) and the coupled plasmon-phonon modes (1,2) and (1.2)$'$. At large q, these peaks disappear, but the intrasubband plasmon-phonon mode (1,1) becomes relevant. When we further increase γ, the calculated scattering spectrum remains similar to the structure for $\gamma=6$ meV.

Finally we discuss the electron density dependence of the light scattering spectrum for two wave vectors and two level-broadening widths. Figure 3 shows the Raman intensities at (a) $q=5\times10^4$ cm^{-1} and (b) $q=5\times10^5$ cm^{-1} for N_e $=2,4,6,8$, and 10×10^{12} cm^{-2}. The thin and thick curves are the results for $\gamma=1.5$ and $\gamma=10$ meV, respectively. With increasing electron density, the $n=2$, 3, and 4 subbands begin to be occupied at $N_e=0.93$, 2.67, and 8.33×10^{12} cm^{-2}, respectively. For $N_e=10^{13}$ cm^{-2}, four subbands are occupied. Then the contribution from the $n=4$ subband becomes prominent. In the calculation, we now have to consider a four-subband model. In Fig. 3(a), we see that the intrasubband scattering is very weak. For $\gamma=1.5$ meV, we can observe the scattering peaks due to the coupled intersubband plasmon-phonon modes labeled by a_1: (1,2); a_1': (1,2)$'$; a_2: (1,3); a_3: (1,4); b_1: (2,3); b_1': (2,3)$'$; b_2: (2,4); b_2': (2,4)$'$; and c_1: (3,4). The scattering due to intersubband modes from two adjacent subbands, such as (1,2) and (2,3), is significant. For high electron density $N_e=10^{13}$ cm^{-2}, the intersubband mode (3,4) also becomes pronounced. When γ $=10$ meV, most scattering peaks merge together and the scattering spectrum assumes a simple structure with a few broad peaks. However, the scattering peaks due to the phononlike modes, which are close to ω_{LO}, are not strongly affected. For $q=5\times10^5$ cm^{-1}, the peak from the intrasub-

band mode (1,1) becomes the most important one, as is shown in Fig. 3(b). For the lower electron density $N_e=$ 2×10^{12} cm^{-2}, we can see two peaks a and a' corresponding to the coupled intrasubband plasmon-phonon mode (1,1). For intermediate densities, the peak a from the (1,1) mode mixes with the peak b_1 from the (2,3) mode which dominates the scattering around this frequency. Also, the (2,3) and (3,4) modes merge into the lower peak (1,1). For the higher electron density, the peak below ω_{LO} is mainly due to the (1,1) mode, while the other one above ω_{LO} comes from the (2,3) mode.

IV. CONCLUSIONS

We have investigated the inelastic light scattering due to *coupled plasmon-phonon* modes in a *multisubband* Q2DEG realized in δ-doped semiconductors. Our study stressed the broadening effects (induced by impurity scattering) on the Raman spectrum and we have calculated the overall features of the spectrum which could be observed in realistic experimental situations. For small broadening, we have found a very rich structure in the light scattering spectrum. All the peaks due to different intra- and intersubband modes can be observed. At small q, the intersubband modes have the largest scattering strength. But the scattering due to the intrasubband modes of the lowest subband becomes very pronounced for large q. For large broadening widths, which corresponds closely to the experimental situation, most of the modes are strongly damped. Only a few scattering peaks clearly observable with a large full width at half maximum. However, the influence of the damping is not very pronounced for the phononlike modes which are close to the LO-phonon frequency. For $N_e=2\times10^{12}$ cm^{-2}, the phononlike mode from the intersubband (1,2) can be seen clearly at small q. For large q, only the intrasubband mode (1,1) is relevant. For high electron density systems, the phonon-like mode from intersubband (2,3) becomes important at small q. We hope our results will provide useful information and stimulate further experimental study.[8]

ACKNOWLEDGMENTS

[1] G. Abstreiter, M. Cardona, and A. Pinczuk, in *Light Scattering in Solids IV*, edited by M. Cardona and G. Güntherodt (Springer-Verlag, Berlin, 1984), p. 36.

[2] J. K. Jain and S. Das Sarma, Phys. Rev. B **36**, 5949 (1987).

[3] X. Wu and S. E. Ulloa, Phys. Rev. B **48**, 14 407 (1993).

[4] L. Ioriatti, Phys. Rev. B **43**, 14 742 (1991); L. A. O. Nunes, L. Ioriatti, L. T. Florez, and J. P. Harbison, *ibid.* **47**, 13 011 (1993).

[5] V. Anjos, L. Ioriatti, and L. A. O. Nunes, Phys. Rev. B **49**, 7805 (1994).

[6] G. D. Mahan, *Many-Particle Physics* (Plenum, New York, 1981).

[7] E. H. Hwang and S. Das Sarma, Phys. Rev. B **52**, R8668 (1995).

[8] A. Mlayah, R. Carles, E. Bedel, and A. Muñoz-Yagüe, Appl. Phys. Lett. **62**, 2848 (1993); J. Appl. Phys. **74**, 1072 (1993).

[9] G.-Q. Hai, N. Studart, and G. E. Marques, Phys. Rev. B **55**, 1554 (1997).

[10] G.-Q. Hai, N. Studart, and F. M. Peeters, Phys. Rev. B **52**, 8363 (1995); G.-Q. Hai and N. Studart, *ibid.* **R2245**, (1995).

[11] F. Stern, Phys. Rev. Lett. **18**, 546 (1967).

Capítulo 5

Interação elétron-fônon em poços quânticos semicondutores sob campos magnéticos

Desde a década de 80, a interação elétron-fônon e os efeitos de interface em heteroestruturas semicondutoras têm sido bastante estudados. Estudos teóricos mostraram que, considerando apenas o confinamento de elétrons e tratando os fônons como 3D ou ``bulk-like'', as propriedades polarônicas no sistema eletrônico 2D são qualitativamente semelhantes ao caso 3D. Ainda que um grande número de trabalhos tenham se dedicado ao acoplamento elétron-fônon devido aos efeitos interfaciais nas estruturas 2D, não existia evidência experimental que confirmasse ou desmistificasse esta aproximação até recentemente. Nos trabalhos anteriores, investigamos os efeitos de acoplamento devidos ao fônons-LO interfaciais, fônons-LO confinados numa camada e fônons-LO com modos para o semi-espaço, em estruturas GaAs-AlGaAs.

Um dos nossos resultados mostrou que os elétrons em poços quânticos de GaAs-AlAs, acoplam-se muito fortemente com os modos de fônons interfaciais. Em campos magnéticos fortes, a ressonância polarônica acontece muito próximo das freqüências de fônons interfaciais de GaAs e de AlAs. Este efeito foi observado em experimentos de ressonância ciclotrônica em múltiplos poços quânticos de GaAs-$Al_{0.3}Ga_{0.7}As$ com dimensões, 120Å/240Å e 240Å/240Å, pelo grupo do Prof. B. D. McCombe (*State University of New York at Buffallo*) indicando que mesmo nos poços quânticos muito largos (~200Å) os modos de fônons do material das barreiras ainda interagiam com elétrons dentro do poço quântico através dos efeitos de interface. Parte do trabalho mostrado em seguida foi motivado por esta observação.

Nos primeiro dois artigos neste capítulo, estudamos os efeitos no espectro ciclotrônico devido aos fônons interfaciais de poços quânticos de GaAs- $Al_{0.3}Ga_{0.7}As$. Estendemos nossa teoria do sistema GaAs-AsAl para o GaAs-AlGaAs. Neste contexto, o espectro de absorção magneto-óptico foi determinado, e foram ainda investigados detalhadamente os harmônicos assistidos por fônons. Confirmamos os resultados experimentais que relatam os efeitos devido aos *magneto-polarons* ressonantes. Em colaboração com os autores de tais experimentos, mostramos a importância dos efeitos de interface nos *magneto-polarons* sujeitos a campos magnéticos intensos. Como uma extensão deste trabalho teórico, estudamos quantitativamente os espectros de absorção dos harmônicos assistidos por fônons. Ao contrario de algumas previsões anteriores concluímos que os harmônicos são dificilmente observados experimentalmente.

No artigo 5.3, estudamos os estados de alta energia das impurezas rasas em super-redes GaAs-AlGaAs em campo magnético. Obtemos as energias de transições, os espectros de absorção, e os efeitos de *magneto-polarons*. Confirmamos as observações experimentais dos harmônicos assistidos por fônons dos estados ligados de impurezas rasas no super-redes de GaAs-AlGaAs.

No último artigo mostramos que as ressonâncias magneto-fônon, que são bastante estudadas em experimentos de transporte, também podem ser detectadas opticamente (*optically detected magnet-phonon resonances*) em semicondutores polares volumétricos.

5.1. Interface effects on magnetopolarons in GaAs/AlxGa1-xAs quantum wells at high magnetic fields
G. Q. Hai, F. M. Peeters, N. Studart, Y. J. Wang, and B. D. McCombe,
Phys. Rev. B 58, 7822-7828 (1998).

5.2 Resonant magnetopolaron effects due to interface phonons in GaAs/AlGaAs multiple quantum wells
Y. J. Wang, H. A. Nickel, B. D. McCombe, F. M. Peeters, J. M. Shi,
G. Q. Hai, X.-G. Wu, T. J. Eustis, and W. Schaff,
Phys. Rev. Lett. 79, 3226-3229 (1997).

5.2. High energy transitions of shallow magneto-donors in a GaAs/AlGaAs multiple quantum well
A. Bruno-Alfonso, G. Q. Hai, F. M. Peeters, T. Yeo, S. R. Ryu,
and B. D. McCombe,
J. Phys.: Condensed Matter 13, 9761-9772 (2001).

5.4. Optically detected magnetophonon resonances in GaAs
G. Q. Hai and F. M. Peeters,
Phys. Rev. B 60, 16513-16518 (1999).

Interface effects on magnetopolarons in GaAs/Al$_x$Ga$_{1-x}$As quantum wells at high magnetic fields

G. Q. Hai

Instituto de Física de São Carlos, Universidade de São Paulo, 13560-970, São Carlos, SP, Brazil

F. M. Peeters

Department of Physics, University of Antwerp (UIA), B-2610, Antwerp, Belgium

N. Studart

Departamento de Física, Universidade Federal de São Carlos, 13565-905, São Carlos, SP, Brazil

Y. J. Wang

National High Magnetic Field Laboratory at Florida State University, Tallahassee, Florida 32306

B. D. McCombe

Department of Physics, State University of New York at Buffalo, Buffalo, New York 14260

Effects due to interface optical-phonon modes on the cyclotron resonance in high magnetic field are investigated for GaAs/Al$_x$Ga$_{1-x}$As quantum wells with the inclusion of band nonparabolicity. The polaron cyclotron resonant frequencies are obtained from the magneto-optical absorption spectrum which exhibits magnetopolaron resonances near the GaAs and AlAs-like phonon frequencies. Our theoretical results are in good agreement with recent cyclotron resonance experiments. Furthermore, we present calculations of interface-phonon-assisted harmonics at high frequency whose positions are determined by the resonant phonon frequencies. [S0163-1829(98)04936-4]

I. INTRODUCTION

The effects of interface phonons on magnetopolarons in quasi-two-dimensional (Q2D) systems of semiconductor heterostructures have received considerable attention in the last decade. In quantum wells (QW's), the electron motion is confined in one direction, which leads to an increased localization of the electron wave function. This results in an increase of single polaron effects. A second effect of the confinement is the modification of the phonon modes. The confinement is a result of the sandwiching of the electron between different dielectric materials, which will also modify the phonons resulting in confined slab phonons, interface phonons, and barrier bulk phonons.[1-3]

For zero magnetic field, there exists a sum rule[3] indicating that the polarization due to different modes is practically the same as for bulk phonon modes. This makes it difficult to discriminate the relative importance of the interaction of the various phonon modes from the result one would obtain from a calculation using only bulk-phonon modes. But increasing the magnetic field allows one to bring the cyclotron frequency into resonance with the different confined phonon modes, resulting in magnetopolaron effects which are markedly different from those found using only the bulk phonons. Such a study provides information on the frequency of the confined phonons and on the strength of their interaction with the electrons.

Although a large amount of theoretical work has been done[1,2,4] concerning the effects of interface phonons on the position of the cyclotron resonance (CR) peak, only recently has the magnetopolaron resonance due to interface phonon modes been observed experimentally.[5] In Ref. 5, a detailed experimental and theoretical study of the polaron cyclotron resonance in modulation-doped GaAs/Al$_{0.3}$Ga$_{0.7}$As multiple quantum wells was carried out in magnetic fields up to 30 T. Resonant magnetopolaron effects due to the interaction between the electrons and the interface optical phonon modes were observed for the first time. Splitting of the polaron CR frequency was found in the region of the AlAs-like optical-phonon modes. Our calculation confirmed that this resonance resulted from the AlAs-like interface optical phonons in the quantum wells.

In this paper, we present a detailed theoretical calculation of the magnetopolaron CR spectrum with interface effects in GaAs/Al$_x$Ga$_{1-x}$As quantum wells based on our previous work of polaron cyclotron resonance in GaAs/AlAs systems.[1] The calculation is improved by taking into account the nonparabolicity of the conduction band, and we extend our theory to GaAs/Al$_x$Ga$_{1-x}$As structures for $x \neq 1$, where the GaAs- and AlAs-like phonon modes appear in the barrier material. The QW width dependence of the resonance magnetopolaron effect due to interface phonons is studied in detail and compared to experimental results. The oscillator strength of the different peaks in the CR spectrum are investigated as a function of the magnetic field. Furthermore, we investigate the interface and slab-phonon-assisted harmonics which occur above the optical-phonon frequencies. Such phonon-assisted harmonics have been studied in three-dimensional (3D) systems[6] and were observed in InSb (Ref. 7) and Hg$_x$Cd$_{1-x}$Te.[8] Here we generalized this to lower dimensional systems.

II. MAGNETOPOLARON RESONANCE

In the presence of a magnetic field **B** applied in the z direction perpendicular to the interface, the energy levels of an electron are given by

$$E_{n,l}^0 = E_l^z + \hbar \omega_c (n + 1/2), \tag{1}$$

where E_l^z is the level $(l = 1, 2, ...)$ due to the QW confinement corresponding to the motion in the z direction, $\omega_c = eB/m_\parallel$ is the unperturbed cyclotron frequency, n is the Landau-level index, and $m_\parallel$ is the electron band mass in the xy plane given by

$$m_\parallel = \frac{m_e^* m_{eb}^*}{P_w m_{eb}^* + P_b m_e^*}, \tag{2}$$

where P_w (P_b) is the probability to find the electron inside (outside) the quantum well, and m_e^* and m_{eb}^* are the electron effective mass in the well and in the barrier, respectively. Equation (2) includes the penetration of the electron wave function into the barrier resulting in a renormalization of the effective electron mass. This leads to an increase of the electron mass because $m_{eb}^* > m_e^*$, which is appreciable for narrow quantum wells. Here we are interested in the Landau levels $E_{n,1}^0 = E_1^z + \hbar \omega_c (n + 1/2)$ associated with the lowest electric subband E_1^z.

To compare theoretical results for the cyclotron resonant frequency with the experimental results, it is necessary to include the band nonparabolicity of the conduction band in the calculation. The electronic structure of III-V compound semiconductors in the presence of external magnetic fields can be described very well within the framework of $\mathbf{k} \cdot \mathbf{p}$ theory.[9-11] Ruf and Cardona[9] studied the electronic structure of GaAs by the technique of resonant Raman scattering in magnetic fields. They showed that the nonparabolicity of the bulk GaAs conduction band can accurately be described by the expression

$$E_n = -\frac{E_g^*}{2} + \left[\left(\frac{E_g^*}{2} \right)^2 + \left(1 - \frac{m_e^*}{m_0} - \frac{m_e^*}{m_0} C^* \right) E_g^* E_n^0 \right]^{1/2} + \frac{m_e^*}{m_0} (1 + C^*) E_n^0, \tag{3}$$

with the fitting parameter $C^* = -2.3$, and $E_g^* = E_g + \Delta_0/3$, $E_g = 1520$ meV, $E_g + \Delta_0/3 = 1631$ meV, $E_n^0 = \hbar \omega_c (n + 1/2)$, and $m_e^* = 0.0665 m_0$. Here we generalized this expression to the quasi-two-dimensional case by (1) replacing the bulk mass m_e^* by the effective electron mass in the 2D plane $m_\parallel$, and (2) by including the confinement energy in the band gap energy $E_g^* = E_g + \Delta_0/3 + E_1^z$. The CR frequency including the correction due to band nonparabolicity is now obtained from

$$\omega_c^{np} = (E_1 - E_0)/\hbar. \tag{4}$$

The present calculation of the magneto-optical absorption spectrum is similar to the one described in Ref. 1 for GaAs/AlAs quantum wells, except that we additionally include band nonparabolicity and consider the different effective phonon modes of the GaAs/Al$_x$Ga$_{1-x}$As system. Within the linear-response theory, the polaron magneto-optical absorption is proportional to[1,12]

$$\frac{-\mathrm{Im}\, \Sigma(\omega)}{[\omega - \omega_c^{np} - \mathrm{Re}\, \Sigma(\omega)]^2 + [\mathrm{Im}\, \Sigma(\omega)]^2}, \tag{5}$$

where $\Sigma(\omega)$ is the so-called memory function and ω_c^{np} is the unperturbed CR frequency. In the absence of Landau-level broadening we have $\mathrm{Im}\Sigma(\omega) = 0$, and the position of the CR peak is determined by the equation $\omega - \omega_c^{np} - \mathrm{Re}\Sigma(\omega) = 0$. When we calculated the CR frequency of the polarons in the GaAs/AlAs quantum well,[1] the memory function could be decomposed into

$$\Sigma(\omega) = \Sigma^{slab}(\omega) + \Sigma^{S+}(\omega) + \Sigma^{S-}(\omega), \tag{6}$$

which is a sum of the contribution from the slab phonon modes, the $S+$ interface mode (supported by the AlAs phonons), and the $S-$ interface mode (supported by the GaAs phonons).

In GaAs/Al$_x$Ga$_{1-x}$As quantum-well structures, the barrier material is the Al$_x$Ga$_{1-x}$As alloy which has two LO- and two TO-phonon modes. They are the GaAs- and AlAs-like modes, respectively. In the small-magnetic-field regime, it is possible to replace, in an approximate way, the two TO- and LO-phonon modes by single effective TO and LO modes as introduced in Ref. 13 and used, e.g., in Ref. 2, in the study of the electron-phonon renormalization of the electron energy and mass. However, for magnetopolaron effects in high magnetic fields, this approximation is no longer valid because resonant polaron effects occur and the electron energy can be comparable to the energy of the different TO- and LO-phonon modes. In principle, we should consider all the TO- and LO-phonon modes in the different materials in order to obtain the "exact" interface phonon modes.

For the GaAs/Al$_x$Ga$_{1-x}$As structures, frequencies of the AlAs-like phonon modes in the Al$_x$Ga$_{1-x}$As alloy are given by $\Omega_{LO}^{AlAs} = 360 + 70.8x - 26.8x^2$ cm^{-1} and $\Omega_{TO}^{AlAs} = 360 + 4.4x - 2.4x^2$ cm^{-1}. Those of the GaAs-like phonon modes are $\Omega_{LO}^{GaAs} = 296 - 52.8x + 14.4x^2$ cm^{-1} and $\Omega_{TO}^{GaAs} = 270 - 5.2x - 9.4x^2$ cm^{-1}. Typically, one uses $x = 0.3$, and we have $\Omega_{LO}^{AlAs} = 379$ cm^{-1}, $\Omega_{TO}^{AlAs} = 361$ cm^{-1}, $\Omega_{LO}^{GaAs} = 281$ cm^{-1}, and $\Omega_{TO}^{GaAs} = 268$ cm^{-1}. In this work, we are interested in the magnetopolaron resonance close to the GaAs phonon frequencies and the AlAs-like phonon frequencies. Notice that the frequencies of the GaAs-like phonons are close to those of bulk GaAs, which are $\omega_{LO}(GaAs) = 296$ cm^{-1} and $\omega_{TO}(GaAs) = 270$ cm^{-1}. In a full theory one should calculate the interface phonon modes of the GaAs/Al$_x$Ga$_{1-x}$As interface which for $x \neq 0$ leads to six different modes of which two are AlAs like and the four others GaAs like. Two of these four GaAs-like interface modes are supported by the GaAs in the quantum well (corresponding to the $S-$ modes) and the two others are from the GaAs-like modes (with weight $1 - x$) in the barrier material whose frequencies are between the TO and LO GaAs-like phonon frequencies. In order to avoid this extra complication, it is physically more transparent to weight the different interface phonon modes of the GaAs/AlAs system by the concentration of Al or Ga in the Al$_x$Ga$_{1-x}$As alloy. Therefore, as in

Ref. 1, in the present paper we approximate the memory function of the $S+$ interface phonon mode as

$$\Sigma^{S+}(\omega) \rightarrow x\Sigma^{S+}(\omega) + (1-x)\Sigma^{S-}(\omega). \quad (7)$$

Then Eq. (6) becomes

$$\Sigma(\omega) = \Sigma^{slab}(\omega) + x\Sigma^{S+}(\omega) + (2-x)\Sigma^{S-}(\omega). \quad (8)$$

We see that Eq. (8) reduces to Eq. (6) for $x=1$. On the other hand, for $x \rightarrow 0$ we also have the correct limit because $\Sigma^{S+}(\omega)$ and $\Sigma^{S-}(\omega)$ approach each other and vanish. The approximation in Eq. (7) indicates that we have separated the contribution of the barrier material $Al_xGa_{1-x}As$ to the interfcace polaron effect into two parts. The first part is from the AlAs-like phonons and is weighted by x, and the second part is from the GaAs-like phonons and is weighted by $1-x$. Furthermore, the momery function of the second part is approximated by that of the $S-$ mode.

In the calculation of the magneto-optical-absorption spectrum in $GaAs/Al_{0.3}Ga_{0.7}As$ quantum wells, we take $\alpha = 0.068$, $\epsilon_0 = 12.85$, and $\epsilon_\infty = 11.00$ in GaAs; and $\epsilon_0 = 11.91$ and $\epsilon_\infty = 10.18$ in $Al_{0.3}Ga_{0.7}As$ in Eqs. (59) and (60) of Ref. 1. The CR frequency is determined by the position of the peaks in the magneto-optical-absorption spectrum. Figure 1 shows the polaron CR frequency as a function of magnetic field in $GaAs/Al_{0.3}Ga_{0.7}As$ quantum wells of widths (a) 120 Å and (b) 240 Å. The thin-dashed lines are the CR frequencies within the parabolic band approximation in the absence of electron-phonon interaction. The thin-solid lines are the results including band nonparabolicity which decreases the CR frequency, in particular at high magnetic fields. The CR frequencies of the polarons using the 3D GaAs phonon modes and band nonparabolicity are indicated by the dot-dashed curves, and exhibit only one magnetopolaron resonance around the GaAs phonon frequency. The thick-solid curves are the CR frequencies including band nonparabolicity and the electron-phonon interaction with interface and slab phonons. The experimental results are indicated by the dots. Away from the resonant magnetopolaron region around the AlAs phonons, the theory based on only bulk GaAs phonons describes the experimental results quite well, and coincides with our theory which includes interface and slab phonons. Therefore, earlier claims[4] that interface phonons are needed to describe the resonant magnetopolaron effect near the GaAs phonons, i.e., $\omega < 340$ cm^{-1}, are questionable. Those claims are often based on crude approximations which, e.g., did not include band nonparabolicity and/or the finite height of the quantum well and/or the electron mass difference between the well and barrier region which result in important corrections to the CR peak position. The present calculation with interface and slab phonons is in agreement with the experimental results not only near the GaAs phonon region but also near the AlAs phonon region. Deviations from the experimental results near the AlAs resonant region can be attributed to (i) many-electron effects which are not included here, (ii) fluctuation of the frequncies of the AlAs-like phonons of the $Al_xGa_{1-x}As$ alloy barrier from sample to sample, and (iii) the larger error bar in the experimental data. From the experimental results, we also could not observe a decrease of the resonant frequency near an AlAs-like phonon frequency with an increasing width of
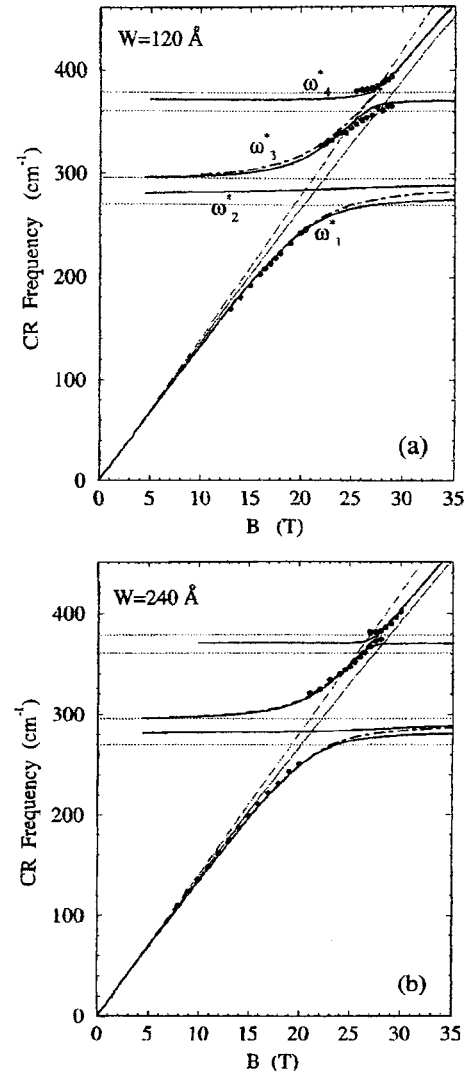

FIG. 1. The polaron CR frequency due to interface and slab phonons (thick solid curves), and due to 3D LO phonons (dotted-dashed curves) as a function of magnetic field in (a) 120-Å, and (b) 240-Å-wide $GaAs/Al_{0.3}Ga_{0.7}As$ quantum wells with the inclusion of band nonparabolicity. The thin-dashed and thin-solid lines are the unperturbed CR frequencies for parabolic and nonparabolic bands without inclusion of polaron effects, respectively. The dots indicate the experimental results. The horizontal dotted lines indicate the LO- and TO-phonon frequencies of GaAs and AlAs-like modes. The four branches of the CR frqencies in (a) are indicated by ω_1^*, ω_2^*, ω_3^*, and ω_4^* in increasing order of frequency.

the quantum well, which is expected from our theoretical calculations. We notice that only three of the four branches of the calculated magnetopolaron CR frequency are observed in the experiment. In order to see the relative importance of the different branches in the CR spectrum, we calculate the oscillator strength of the different absorption peaks in the magneto-optical spectrum which, for $Im\Sigma(\omega) = 0$, is given by $[1 - \partial Re\Sigma(\omega)/\partial\omega]^{-1}$. The results are shown in Fig. 2 for a 120-Å QW. This figure shows the following: (1) There are only experimental results available in certain magnetic-field regions for the different branches; e.g., for the lowest CR frequency branch, i.e., ω_1^*, the oscillator strength re-
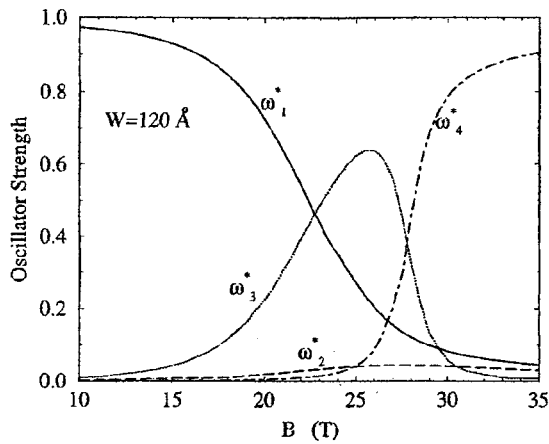
FIG. 2. The oscillator strength of the first four peaks in the magneto-optical-absorption spectrum as a function of the magnetic field in a 120-Å-wide GaAs/Al$_{0.3}$Ga$_{0.7}$As QW. They are indicated by ω_1^*, ω_2^*, ω_3^*, and ω_4^* in increasing order of frequency.

duces with increasing magnetic field, and near B = 22 T a large part of its oscillator strength is transfered to the ω_3^* peak which becomes now experimentally observable, while the ω_1^* peak becomes too weak to be seen experimentally. (2) The second CR frequency, i.e., ω_2^*, exhibits on oscillator strength which is typically one order of magnitude smaller than the main CR peak. Notice that the ω_2^* peak is in the reststrahlen region, which is a second reason why it is not observed experimentally.

A direct measure for the strength of the electron-phonon interaction is the splitting of the avoided-level-crossing resonance near the GaAs- and AlAs-like phonon modes. For simplicity, we define the splitting near the AlAs-like phonons as the frequency difference between ω_4^* and ω_3^* at the magnetic field, where ω_c^{np} equals ω_∞^{S+} (the frequency of the interface phonon mode $S+$ at wave number $q \to \infty$), and that near the GaAs-like phonon is the difference between ω_3^* and ω_1^* at $\omega_c^{np} = \omega_{LO}$ of GaAs. These splittings are shown in Fig. 3 as a function of the well width of the GaAs/Al$_{0.3}$Ga$_{0.7}$As system. The solid (dashed) curve indicates the resonance in the region of the AlAs (GaAs)-like optical-phonon frequencies.
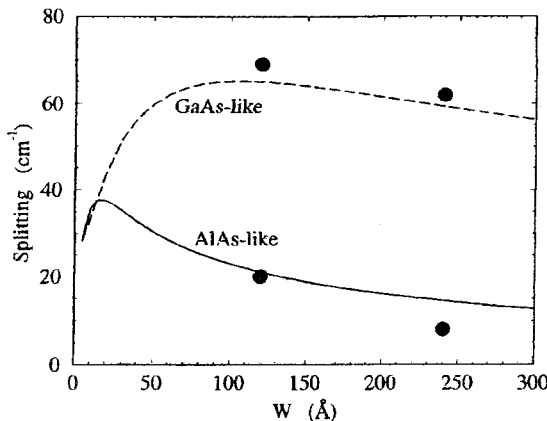

FIG. 3. The splitting of the magnetopolaron resonance around the GaAs-like (dashed curve) and AlAs-like phonon frequencies (solid curve). The dots are the experimental results.

The solid dots are the experimental results. The present theoretical results predict that the largest splitting as due to the AlAs-like interface phonons (solid curve in Fig. 3) occurs in a GaAs/Al$_{0.3}$Ga$_{0.7}$As quantum well of width $W = 18$ Å. The largest splitting near the GaAs phonon frequency occurs for a much larger well width of about $W = 100$ Å. The decrease of the resonant splitting for a large well width near the AlAs-like optical phonon is mainly a consequence of the reduced overlap between the electron wave function and the interface phonon polarization which falls off like e^{-kz} from the interface. The polaron splitting near the GaAs optical-phonon modes is largely due to the interaction with GaAs slab modes, and consequently the reduction for large widths is due to the smaller confinement of the electrons and is similar to the decrease of the polaron effects when one goes from a 2D system to a 3D system. The reduction of the splitting for $W < 18$ Å is a consequence of the finite height of the quantum well, which results in a large penetration of the electron wave function into the Al$_x$Ga$_{1-x}$As barrier and consequently a reduced probability of finding the electron in the QW or near the interface. The reduction of the splitting near the GaAs phonon for $W < 100$ Å is a consequence of the reduced number of slab modes with decreasing W.

In Fig. 4 we plot the absorption spectra of the magnetopolarons around (a) the GaAs and (b) AlAs-like phonon frequencies at different magnetic fields for a QW of width $W = 120$ Å. The results are obtained for a Landau-level broadening $\Gamma = 1$ meV. Figure 4(a) shows the magnetopolaron resonance due to GaAs-like interface and slab phonons. Notice that only two absorption peaks are observed, and that the peak corresponding to the second branch in Fig. 1(a), situated between the TO- and LO-phonon frequencies of GaAs, is absent. This is a consequence of its small oscillator strength, which makes it disappear in the tail of the other Landau-level broadened peaks. It is seen that, at $B = 20.5$ T, most of the absorption strength is in the lower peak at $\omega = 244$ cm^{-1}. When the magnetic field is increased, this peak is pinned "around" the ω_{TO} of GaAs, and its absorption strength is transfered to the higher peak located above the ω_{LO} of GaAs. Figure 4(b) demonstrates the magnetopolaron resonance due to AlAs-like interface phonons. It is seen that, at lower magnetic fields ($B < 26.5$ T), the absorption peak at higher frequency is in the reststrahlen region of the AlAs-like phonons. With increasing magnetic field, the peak at lower frequency enters this reststrahlen region. It becomes very broad, and it loses most of its oscillator strength to the higher-frequency peak.

III. PHONON-ASSISTED HARMONICS

Figure 5 shows the magneto-optical-absorption spectrum for a polaron interacting with interface and slab phonon modes in the frequency region above the AlAs optical phonon in GaAs/Al$_{0.3}$Ga$_{0.7}$As quantum wells of widths (a) 20 Å and (b) 120 Å for two different values of Landau-level broadening: $\Gamma = 0.5$ meV (solid curves) and $\Gamma = 1$ meV (dotted curves). The scale of these figures is multiplied with a factor of 300 as compared to the one of Fig. 4(a). We clearly observe optical-phonon-assisted harmonics[6,12] for the slab and interface phonons (namely, three series can clearly be discriminated), as indicated by $S-$, slab, and $S+$, respec-
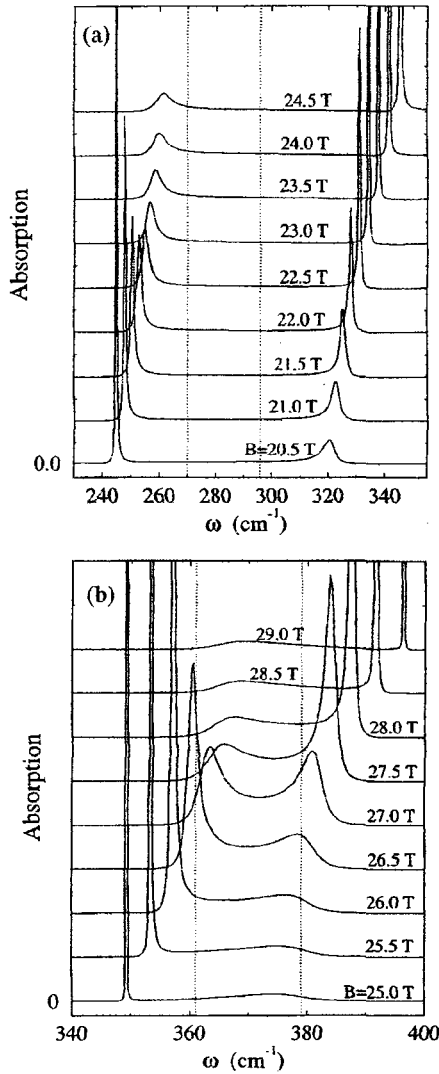
FIG. 4. The magnetopolaron absorption spectrum around (a) the GaAs-like and (b) the AlAs-like phonon frequencies at different magnetic fields in a GaAs/Al$_{0.3}$Ga$_{0.7}$As QW of width $W = 120$ Å. The two vertical dotted lines in (a) indicate the TO- and LO-phonon frequencies of GaAs, and those in (b) indicate the frequencies of the AlAs-like phonons. The Landau-level broadening is $\Gamma = 1$ meV. The intensity in (b) is enlarged by a factor of 2 as compared to (a). The different curves are offset for clarity.

FIG. 5. The phonon-assisted harmonics in the polaron magneto-optical-absorption spectrum in (a) 20-Å and (b) 120-Å-wide GaAs/Al$_{0.3}$Ga$_{0.7}$As quantum wells for three different magnetic fields and two values of the Landau-level broadening $\Gamma = 0.5$ meV (solid curves) and $\Gamma = 1$ meV (dotted curves). The intensity is enlarged 300 times as compared to Fig. 4(a).

tively. In Fig. 5(a) for $W = 20$ Å, we notice that the absorption strength of the interface-phonon-assisted harmonics $S-$ and $S+$ is larger than the one due to the slab phonons. These three peaks are repeated periodically with period ω_c, but their strength decreases with increasing frequency. For a 120-Å QW, as shown in Fig. 5(b), the slab-phonon-assisted harmonics become much stronger than those of the interface phonons, indicating the decreased (increased) interaction of the electron with the interface (slab) phonons with increasing QW width.

The position of the first ten absorption peaks in a QW of width 120 Å are plotted in Fig. 6. We found that the position of the phonon-assisted harmonics depends only on the resonant optical-phonon frequencies ω_j^r, and is given by $\omega_{n,j} = \omega_j^r + n\omega_c^{np}$ with $n = 1,2,\ldots$. For the slab phonons we have

$\omega_{slab}^r = \omega_{LO}$ because the slab modes were taken dispersionless. On the other hand, the interface phonons have dispersion, and consequently the resonant frequency depends on the width of the QW. We found that the resonant frequencies of the $S+$ and $S-$ modes in a 120-Å QW are $\omega_{S+}^r = 371.4$ cm^{-1} and $\omega_{S-}^r = 281.7$ cm^{-1}, respectively.

In order to investigate the importance of the phonon-assisted harmonics, we calculated the strength of the different peaks for the situation of Fig. 6. They are shown in Fig. 7(a) for the first phonon-assisted harmonics $\omega_{1,j} = \omega_j^r + \omega_c^{np}$, and in Fig. 7(b) for the second phonon-assisted harmonics $\omega_{2,j} = \omega_j^r + 2\omega_c^{np}$. Notice that they are
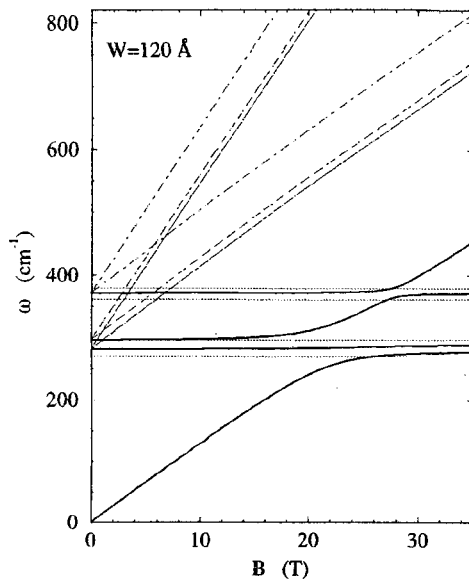
FIG. 6. The positions of the first ten peaks in the magneto-optical-absorption spectrum as a function of the magnetic field in a 120-Å-wide QW. The positions of the harmonics due to the GaAs-like interface mode $(S-)$, slab modes, and AlAs-like interface mode $(S+)$, are indicated by thin-solid, dashed, and dotted curves, respectively. The horizontal dotted lines are the frequencies of the GaAs and AlAs-like phonons.
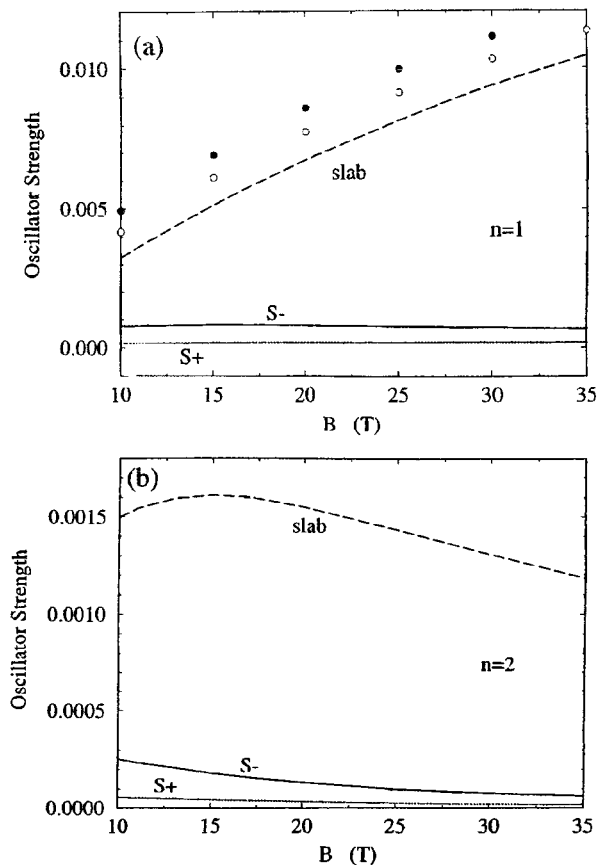

FIG. 7. The oscillator strength of (a) the first $(n=1)$ and (b) the second $(n=2)$ phonon-assisted harmonics in the magneto-optical-absorption spectrum as a function of the magnetic field in a 120-Å-wide QW. The solid dots in (a) are the results using the GaAs bulk-phonon modes, and the open dots are the sum of the oscillator strength of the $S+$, $S-$, and slab peaks.

typically two orders of magnitude smaller than the oscillator strength of the experimentally studied resonances (see Fig. 2). This result agrees with the earlier calculation of Wu, Peeters, and Devreese,[12] who included only interaction with bulk GaAs phonons for a Q2D system of GaAs heterojunction. The results using the 3D phonon modes are shown as solid dots in Fig. 7(a), and are compared with the present results (open dots), where we added the oscillator strength of the $S+$, $S-$, and slab peaks. The present results for the oscillator strength of the first phonon-assisted harmonics are one order of magnitude smaller than the theoretical results of Tanatar and Singh.[14] Our theoretical results are in agreement with recent experimental results[15] which were unable to observe the first phonon-assisted harmonics in a number of different GaAs quantum wells, and where it was estimated that the oscillator strength of this line must be less than 1% of the main CR peak. On the other hand, in a recent experiment,[16] a phonon-assisted *impurity* transition was observed in a donor-doped sample using photoconductivity at high frequencies. These results are not in disagreement with the present results, because here we considered free electrons and calculated the CR absorptions, while the experiment in Ref. 16 is for shallow bound electrons and where photoconductivity was used. Therefore, we expect that it will be extremely hard to see these phonon-assisted harmonics experimentally in GaAs/Al$_{0.3}$Ga$_{0.7}$As quantum wells.

IV. SUMMARY AND CONCLUSIONS

A detailed theoretical analysis of the magneto-optical absorption spectrum of low density electrons in GaAs/Al$_x$Ga$_{1-x}$As quantum wells was presented. From our calculation of the polaron CR spectrum in GaAs/Al$_{0.3}$Ga$_{0.7}$As quantum wells and a comparison with the experimental results of Ref. 5, we demonstrated that, in order to achieve good agreement with the experiments, it is important to include correctly (1) an appropriate electron effective mass for motion in the plane of the QW which is renormalized by the penetration of the electron wave function into the barriers, (2) band nonparabolicity effects, and (3) interface phonon modes in order to explain the magnetopolaron resonance around the AlAs-like optical phonons. The phonon-assisted harmonics exhibit clear signatures of the different interface phonons, and the slab phonons, but their oscillator strengths are two orders of magnitude smaller than the main CR resonances.

ACKNOWLEDGMENTS

[1] G. Q. Hai, F. M. Peeters, and J. T. Devreese, Phys. Rev. B **47**, 10 358 (1993).

[2] G. Q. Hai, F. M. Peeters, and J. T. Devreese, Phys. Rev. B **48**, 4666 (1993).

[3] N. Mori and T. Ando, Phys. Rev. B **40**, 6175 (1989).

[4] S. W. Gu, X. J. Kong, and C. W. Wei, Phys. Rev. B **36**, 7984 (1987); D. L. Lin, R. Chen, and T. F. George, *ibid.* **43**, 9328 (1991).

[5] Y. J. Wang, H. A. Nickel, B. D. McCombe, F. M. Peeters, J. M. Shi, G. Q. Hai, X.-G. Wu, T. J. Eustis, and W. Schaff, Phys. Rev. Lett. **79**, 3226 (1997).

[6] F. M. Peeters, Xiao-Guang Wu, and J. T. Devreese, Phys. Rev. B **33**, 4338 (1986).

[7] R. C. Enck, A. S. Saleh, and H. Y. Fan, Phys. Rev. **182**, 790 (1969); B. D. McCombe, R. J. Wagner, and G. A. Prinz, Solid State Commun. **7**, 1381 (1969); R. Grisar, H. Wachering, G.

[8] Bauer, J. Wlasek, J. Kowalski, and W. Zawadzki, Phys. Rev. B **18**, 4355 (1978).

[8] B. D. McCombe, R. J. Wagner, and G. A. Prinz, Solid State Commun. **8**, 1687 (1970).

[9] T. Ruf and M. Cardona, Phys. Rev. B **41**, 10 747 (1991).

[10] G. Ambrazevičius, M. Cardona, and R. Merlin, Phys. Rev. Lett. **59**, 700 (1987).

[11] W. Zawadzki, C. Chaubet, D. Dur, W. Knap, and A. Raymond, Semicond. Sci. Technol. **9**, 320 (1994); P. Pfeffer and W. Zawadzki, Phys. Rev. B **37**, 2695 (1988).

[12] X.-G. Wu, F. M. Peeters, and J. T. Devreese, Phys. Rev. B **34**, 8800 (1986).

[13] S. Adachi, J. Appl. Phys. **58**, R1 (1985).

[14] B. Tanatar and M. Singh, Phys. Rev. B **42**, 3077 (1990).

[15] S. R. Ryu and B. D. McCombe (unpublished).

[16] S. R. Ryu, T. M. Yeo, B. D. McCombe, and W. Schaff, Bull. Am. Phys. Soc. **42**, 192 (1997); (unpublished).

Resonant Magnetopolaron Effects due to Interface Phonons in GaAs/AlGaAs Multiple Quantum Well Structures

Y. J. Wang

National High Magnetic Field Laboratory at Florida State University, Tallahassee, Florida 32306

H. A. Nickel and B. D. McCombe

Department of Physics, State University of New York at Buffalo, Buffalo, New York 14260

F. M. Peeters and J. M. Shi

Department Natuurkunde, Universiteit Antwerpen (UIA), B-2610 Antwerpen, Belgium

G. Q. Hai

Departamento de Física, Universidade Federal de São Carlos, 13565-905 São Carlos, São Paulo, Brazil

X.-G. Wu

National Laboratory for Superlattices and Microstructures, Institute of Semiconductors, Chinese Academy of Science, Beijing, China

T. J. Eustis and W. Schaff

Department of Electrical Engineering, Cornell University, Ithaca, New York 14853
(Received 18 February 1997)

Polaron cyclotron resonance (CR) has been studied in three modulation-doped GaAs/Al$_{0.3}$Ga$_{0.7}$As multiple quantum well structures in magnetic field up to 30 T. Large avoided-level-crossing splittings of the CR near the GaAs reststrahlen region, and smaller splittings in the region of the AlAs-like optical phonons of th AlGaAs barriers, are observed. Based on a comparison with a detailed theoretical calculation, the high frequency splitting, the magnitude of which increases with decreasing well width, is assigned to resonant polaron interactions with AlAs-like interface phonons. [S0031-9007(97)04404-9]

The interaction of charge carriers with optical phonons in quasi-two-dimensional (Q2D) systems has been of considerable interest both experimentally [1–6] and theoretically [7–12] for several years, since the electronic properties of semiconductors, particularly energy loss mechanisms for hot carriers, are strongly affected by this interaction. For bulk polar materials, the dominant interaction is between the charge carriers and longitudinal optical (LO) phonons [7]. Interface and confined phonons [11,12] and their interaction with charge carriers in quantum wells have received considerable attention recently, and it has been shown theoretically that these modes can play a significant role in narrow wells. However, a number of issues remain unresolved. In particular, a sum rule [13] makes it difficult to deconvolve the relative important of interactions with the various phonon modes of confined systems from measurements which are not phonon-frequency specific [14]. There has also been some controversy about the importance of interface and confined phonon modes in the region of resonant magnetopolaron interaction with GaAs phonons [6,11,12]. Raman scattering studies of short period GaAs/AlAs superlattices [15,16] have provided experimental evidence for both confined and interface modes, but there have been no experimental measurements of the strength of

the interactions in either GaAs/AlAs or GaAs/AlGaAs quantum wells, there has been no experimental work showing the effects of interface phonons in quantum well structures with alloy barriers, and there has been no work demonstrating clearly the importance of this interaction in "normal" well width range (the order of greater than 100 Å) for practical devices (e.g., intersubband detectors).

The resonant magnetopolaron effect, which has been studied for a number of years in bulk [17,18] and Q2D [4–6] systems, provides a means of determining the strength of interactions with specific phonons. When the cyclotron resonance (CR) frequency, $\omega_c = eB/m^*c$, is tuned through the frequency of an appropriate optical phonon, a resonant avoid level crossing occurs. The magnitude of this avoided-level-crossing resonance is a direct measure of the strength of the effective interaction. Although such effects have been studied for some time, much remains unknown or poorly understood. Enhanced [1,19], comparable [20], and reduced [3,5,21] resonant polaron effects (relative to 3D) have been previously reported in Q2D systems. The detailed mechanisms leading to these observations have been obscured in some cases by inadequate theoretical models for the specific structures, and in other cases by incomplete experimental data due to an insufficient magnetic field. Nevertheless, appropriate

experiments spanning the resonant region can reveal the existence of interactions with particular phonon modes, and, when combined with theoretical calculations, can be used to determine the strength of the interaction.

We have carried out an experimental study of electron CR vs magnetic field in three modulation-doped $GaAs/Al_{0.3}Ga_{0.7}As$ multiple-quantum-well samples in magnetic fields up to 30 T. Strong resonant avoided-level-crossing behavior was observed in the region of the GaAs optical phonons with a large splitting of the CR into upper and lower branches. In addition, and of paramount importance, a weaker splitting was observed at higher frequencies in the region of the AlAs-like optical phonons of the barriers. This splitting increases with decreasing well width from 240 to 120 Å, and is attributed to the resonant magnetopolaron interaction of electrons in the GaAs wells with barrier AlAs-like interface phonons. This permits the direct measurement of the importance of the interaction as a function of well width. The magnitude of the splitting is in good agreement with theoretical calculations carried out in the framework of the memory-function formalism [11] including effects of interface optical phonon modes, as well as screening and occupation effects. Our measurements, which are sensitive to specific phonons via the spectral specificity of the technique, demonstrate that, even for barriers containing only 30% Al and relatively wide GaAs wells, the AlAs-like interface phonon modes associated with the barriers interact significantly with electrons in the GaAs wells. A detailed comparison of theory and experiment for the upper and lower branches in the GaAs optical phonon region for two samples with different carrier densities suggests that screening and occupation effects are significant at the higher density and are of nearly equal importance.

The far infrared transmission measurements were carried out with a Bruker 113v Fourier transform interferometric spectrometer in conjunction with a metal light-pipe condensing-cone system and a 4.2 K silicon bolometer detector on samples maintained at 4.2 K in a 30 T resistive magnet. The three $GaAs/Al_{0.3}Ga_{0.7}As$ multiple-quantum-well (240 Å barrier) samples were grown by molecular beam epitaxy with fifteen and ten 240 Å wells, and eight 120 Å wells for samples A, B, and C, respectively. All samples are doped with silicon donors in the barriers, samples A and B over central $\frac{1}{3}$ and sample C in a planar sheet. The measured (from the quantum hall effect) electron densities per well for samples A and B are 1.5×10^{11} and $3.0 \times 10^{11} cm^{-2}$, respectively; the nominal doping for sample C is $1.5 \times 10^{11} cm^{-2}$. The maximum 30 T magnetic field permits CR measurements that span the entire GaAs and AlAs optical phonon regions.

Figure 1 is a plot of the measured CR frequency vs magnetic field for these samples; the solid lines are the calculated unperturbed single particle CR transition frequencies, which include the conduction band nonparabolicity. The data for all samples show clear, large CR splittings in the GaAs reststrahlen region. The fre-
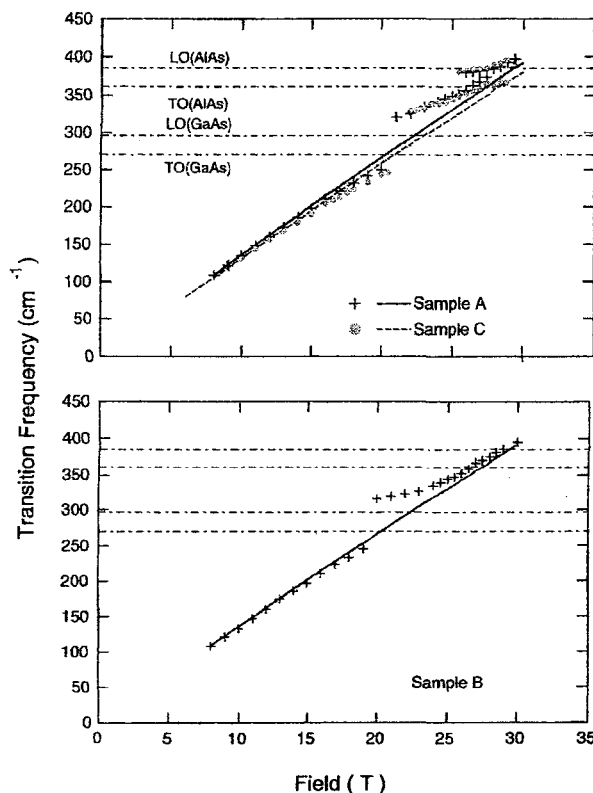

FIG. 1. Experimental data for all three samples. The tilted straight lines in the figures are the calculated CR transitions including nonparabolicity only.

quencies of the lowest energy branch start to deviate from those of the unperturbed CR well below the GaAs-like optical phonon energies, and the intermediate branch approaches the GaAs-like LO phonon frequency from above as the field is decreased. The CR frequencies of samples A and B are indistinguishable at fields below 10 T. Larger differences are observed at higher fields, particularly for the intermediate branch in the region of resonance with the GaAs optical phonons.

At higher frequencies there are smaller splittings observed in the AlAs-like phonon region for samples A and C. Raw magnetotransmission spectra for these samples are shown in Fig. 2, at magnetic fields between 25 and 29 T. For sample A at 25 and 29 T, there is only one observable resonance minimum at 348 and 391 cm^{-1}, respectively. However, when the CR is tuned through the AlAs-like optical phonon region of the barriers ($\sim 26-28$ T), the resonance is clearly split into two branches. The intermediate energy branch loses intensity gradually when the field is increased, while the highest energy branch gains intensity over this same region. Note that the pinning frequency ($\sim 370 cm^{-1}$) lies *between* the AlAs-like LO and transverse optical (TO) frequencies. The minimum separation between the two branches at 27.5 T is approximately 8 cm^{-1}. A much clearer and larger splitting is observed in sample C with a minimum separation of 20 cm^{-1} at 27 T, and pinning frequency
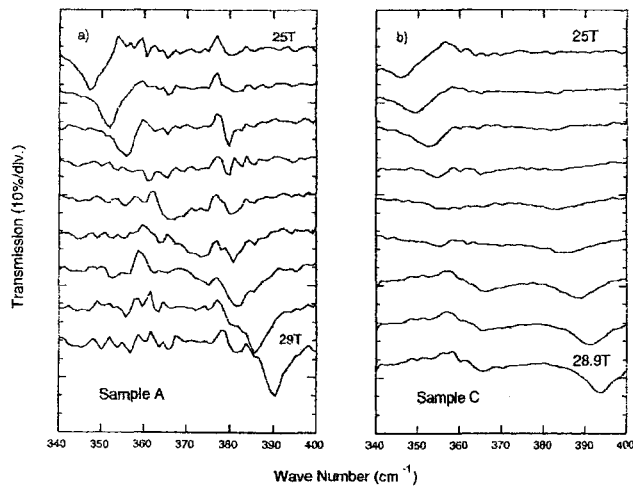
3227

FIG. 2. Transmission spectra at several different fields divided by a zero-field reference spectrum for samples A and C. The traces are spaced every 0.5 T, except the lowest trace in (b). (a) sample A, (b) sample C.

close to 370 cm^{-1}. The interaction which causes the splitting clearly *increases* with decreasing well width.

There are two possible origins for this splitting: (1) electrons localized in the GaAs wells interacting with the AlAs-like slab LO phonons in the barriers due to electron wave-function penetration into the barriers, or (2) electrons in the GaAs wells interacting with AlAs-like *interface* phonons due to the tail of the interface modes in the GaAs wells. To estimate the importance of (1) we have calculated the fraction of the probability density of the ground confinement subband wave function penetrating into the $Al_{0.3}Ga_{0.7}As$ barrier for the structures of samples A and C. For a 240 Å × 240 Å structure this fraction is 3×10^{-4}; for a 120 Å × 240 Å structure it is 2×10^{-3}. Since the splitting of the CR at resonance with the GaAs LO modes is approximately 40 cm^{-1} (see Fig. 1), observed splittings (8 and 20 cm^{-1}) cannot be due to the interaction of the electrons in the wells with the AlAs-like LO phonons in the barriers, which should scale with the fraction of electron probability in the barriers because the Fröhlich electron-phonon coupling constant is approximately the same for GaAs (~0.068) and $Al_{0.3}Ga_{0.7}As$ (~0.073). Another strong argument against possibility (1) is the fact that for both well widths the pinning energies clearly lie *below* the AlAs-like LO phonon frequency for $Al_{0.3}Ga_{0.7}As$ at helium temperature [22].

The interaction between electrons and the symmetric pure AlAs interface optical (IO) phonon modes has been calculated [11]. In order to compare with the present experimental results, the contribution from the pure AlAs IO phonon modes is multiplied by 0.3. The modified theoretical calculation gives splittings of approximately 10 and 16 cm^{-1} near 371 cm^{-1} for the 240 and 120 Å wells, respectively, in reasonable agreement with the measured values. This is taken to be a confirmation of this

assignment. For sample B the splitting into two branches is not resolved. It is likely that screening and Pauli principle effects reduce the effective interaction since the electron density for sample B is twice that of sample A.

Dielectric artifacts can also give rise to apparent splittings [5,23] in the reststrahlen region due to the resonant dielectric function of the material at the TO frequency. A computer simulation of the classical dielectric effects [24] in the reststrahlen region in the multilayer structure of our samples was performed to examine the possible effect of dielectric artifacts. For the present sample parameters, no measurable CR splitting in the GaAs reststrahlen region or in the region of the AlAs-like barrier phonons appears in the simulation.

To test the above conclusion, detailed theoretical calculations for the sample structures are compared with the experimental results in Fig. 3. The *difference* between the measured polaron CR frequency and the unperturbed CR frequency is plotted vs the measured frequency. The electron-phonon interaction Hamiltonian is given by the Fröhlich model, with the phonon modes modified due to confinement and the presence of the interfaces. Three types of optical phonon modes can interact with the electrons in the wells: (1) symmetric interface optical (IO) phonon modes, (2) antisymmetric IO phonon modes, and (3) confined GaAs slab LO phonon modes in the wells. The solid line in Fig. 3 was obtained by considering the effects of symmetric IO phonon and confined slab LO phonon modes in a single electron picture. This calculation agrees well with the experimental results over the entire resonant region. A calculation was also performed for coupling with only bulk GaAs 3D LO phonons (other lines in the figure). The results are nearly the same for the wider well samples (A and B), except near the AlAs-like phonon frequencies. This is to be expected for relatively wide quantum wells. But the agreement for sample C is clearly significantly worse. Confined and interface modes must be accounted for to get good agreement in this case. The GaAs-like interface phonon modes do not play an important role over the range of fields and frequencies for which the polaron CR is observable since their interaction with electrons is smaller than that of the GaAs confined phonon modes, and the experiments do not probe into the reststrahlen region where the resonance occurs. On the other hand, the AlAs-like IO modes do play an important role since there is no strong interaction with any slab modes, and the total AlGaAs thickness is small enough that the reststrahlen effect does not obscure the interaction. The symmetric AlAs-like IO modes are responsible for the splittings near 370 cm^{-1}, and inclusion of this interaction provides good agreement with experiment.

The doping concentrations of the samples lie in an intermediate regime for which both screening and occupation effects must be considered. The dashed lines in Fig. 3 are calculated results for coupling with only bulk GaAs LO phonons, and the dash-dotted lines are
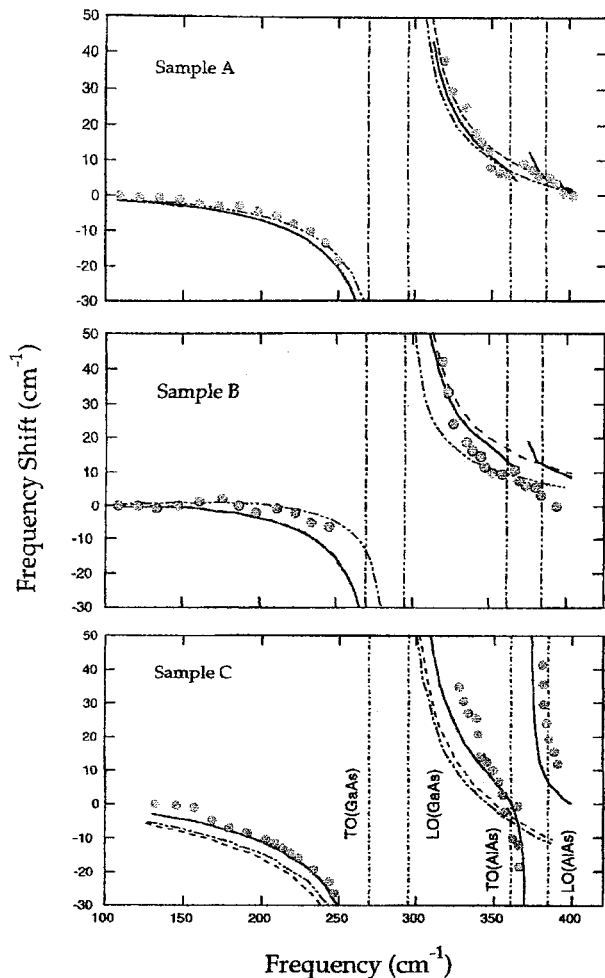
FIG. 3. Plot of frequency shift vs frequency for three samples. The dots are experimental data. The dashed curves are for coupling with only bulk GaAs optical phonons, the dash-dotted curves include screening effects within the RPA in addition to the coupling with the GaAs bulk phonons, and the solid curves consider the effects of IO phonon and slab LO optical phonon modes.

calculated results in which both screening (within the static random-phase approximation [10]) and occupation effects are taken into account in addition to the coupling with bulk GaAs optical phonons. It can be seen that, when occupation and screening effects are included, the agreement between the calculations and the experimental results are further improved in the GaAs region for sample B.

The importance of screening and Landau level occupation can also be seen from the region of AlAs-like phonons. Since the contribution to the interaction from screening and occupation effects are both important [25] in this region, the fact that a splitting in the AlAs-like phonon region is not observed in the higher doped sample B shows these effects play a strong role here.

Experimental work was performed at the National High Magnetic Field Laboratory, which is supported by NSF

[1] M. Horst, U. Merkt, and J.P. Kotthaus, Phys. Rev. Lett. 50, 745 (1983).

[2] W. Seidenbusch, G. Lindemann, R. Lassnig, J. Edlinger, and G. Gornik, Surf. Sci. 142, 375 (1984).

[3] H. Sigg, P. Wyder, and J.A.A.J. Perenboom, Phys. Rev. B 31, 5253 (1985).

[4] Y.-H. Chang, B.D. McCombe, J.-M. Mercy, A.A. Reeder, J. Ralston, and G.A. Wicks, Phys. Rev. Lett. 61, 1408 (1988).

[5] M. Ziesmann, D. Heitmann, and L.L. Chang, Phys. Rev. B 35, 4541 (1987).

[6] J.P. Cheng, B.D. McCombe, and G. Brozak, Phys. Rev. B 43, 9324 (1991).

[7] S. Das Sarma, Phys. Rev. B 27, 2590 (1983).

[8] D.M. Larsen, Phys. Rev. B 30, 4595 (1984).

[9] S. Das Sarma and B.A. Mason, Phys. Rev. B 31, 5536 (1985).

[10] F.M. Peeters, X.-G. Wu, J.T. Devreese, C.J.G.M. Langerak, J. Singleton, D.J. Barnes, and R.J. Nicholas, Phys. Rev. B 45, 4296 (1992).

[11] G.Q. Hai, F.M. Peeters, and J.T. Devreese, Phys. Rev. B 47, 10358 (1993).

[12] R. Chen, D.L. Lin, and T.F. George, Phys. Rev. B 41, 1435 (1990).

[13] N. Mori and T. Ando, Phys. Rev. B 40, 6175 (1989).

[14] According to the sum rule, the sum of all contributions of all phonon modes in confined systems to the form factors is exactly equal to that of the bulk phonon modes if the respective coupling constants are equal.

[15] A.K. Sood, J. Menendez, M. Cardona, and K. Ploog, Phys. Rev. Lett. 54, 2115 (1985).

[16] C. Colvard, T.A. Gant, M.V. Klein, R. Merlin, R. Fischer, H. Morkoc, and A.C. Gossard, Phys. Rev. B 31, 2080 (1985).

[17] D. Larsen, Phys. Rev. 135, A419 (1964).

[18] B.D. McCombe and R. Kaplan, Phys. Rev. Lett. 21, 756 (1968).

[19] J. Singleton, R.J. Nicholas, and F. Nasir, Solid State Commun. 58, 833 (1986).

[20] J. Singleton, R.J. Nicholas, D.C. Rogers, and C.T.B. Foxon, Surf. Sci. 196, 429 (1988).

[21] M.A. Hopkins, R.J. Nicholas, M.A. Brummell, J.J. Harris, and C.T. Foxon, Superlattices Microstruct. 2, 319 (1986).

[22] From extrapolations of room temperature measurements quoted in S. Adachi, GaAs and Related Materials (World Scientific, Singapore, 1994), the helium temperature values are ω_{TO} (AlAs-like) = 361 cm^{-1}; ω_{TO} (AlAs-like) = 385 cm^{-1}.

[23] K. Karrai, S. Huant, G. Martinez, and L.C. Brunel, Solid State Commun. 66, 355 (1988).

[24] J.P. Cheng and B.D. McCombe, Phys. Rev. Lett. 62, 1925 (1989).

[25] X.-G. Wu, F.M. Peeters, and J.D. Devreese, Phys. Rev. B 36, 9760 (1987).

BRUNO-ALFONSO, A.; HAI, GUO-QIANG; PEETERS, F. M.; YEO, T.; RYU, S. R.; MCCOMBE, B. D. High-energy transitions of shallow magnetodonors in a GaAs/Al$_{0.3}$Ga$_{0.7}$As multiple quantum well. **Journal of Physics:** condensed matter, Bristol, v. 13, n.43, p.9761-9772, 2001.

Optically detected magnetophonon resonances in GaAs

G.-Q. Hai

Instituto de Física de São Carlos, Universidade de São Paulo, 13560-970 São Carlos, São Paulo, Brazil

F. M. Peeters

Departement Natuurkunde, Universiteit Antwerpen (UIA), B-2610 Antwerpen, Belgium

(Received 1 June 1999)

Magnetophonon resonances are found for $\omega_c = \omega_{LO}/N$ with $N = 1,2,3\ldots$ in the polaron cyclotron resonance (CR) linewidth and effective mass of bulk polar semiconductors. The CR mass and the linewidth are obtained from the full polaron magneto-optical absorption spectrum which are calculated using the memory function technique. The amplitude of the resonant peak in the linewidth can be described by exponential law at low temperature. [S0163-1829(99)09139-0]

I. INTRODUCTION

Magnetophonon resonance (MPR) occurs when two Landau levels are a phonon energy apart that leads to a resonant scattering due to emission or absorption of phonons. Since the pioneer work by Gurevich and Firsov,[1] this effect has been extensively studied in bulk[2,3] as well as low-dimensional semiconductor systems.[4-9] The resonant character makes it a powerful spectroscopic tool. Magnetophonon resonances have been used to obtain information on band-structure parameters, such as the effective mass and the energy levels, and on the electron-phonon interaction. The vast majority of work on the MPR has been done on the transport properties of semiconductors, usually the magnetoresistance, which inevitably involves a complicated average of scattering processes. The oscillations in the magnetoresistance are the results of a combination of scattering and broadening processes that can lead to a quite complicated dependence of the resonance amplitudes on doping, sample structure, carrier concentration, and temperature. However, the MPR can also be observed directly through a study of the electron cyclotron resonance (CR) linewidth and effective mass, i.e., the so-called optically detected MPR (ODMPR), as was demonstrated in two-dimensional (2D) semiconductor systems of GaAs/Al$_x$Ga$_{1-x}$As heterojunctions by Barnes *et al.*[10] The ODMPR allows one to make quantitative measurements of the scattering strength for specific Landau levels and yields direct information on the nature of the electron-phonon interaction in semiconductors.

In this work, we extend the theory for ODMPR to three-dimensional (3D) systems and present a theoretical study of the magnetophonon resonances in the frequency-dependent conductivity in bulk polar semiconductors. Our calculations show strong oscillations of both the linewidth and the effective mass in a 3D system of GaAs that indicate that the ODMPR should also be observed experimentally in bulk polar semiconductors.

The present paper is organized as follows. In Sec. II, we present our theoretical formulations of the problem. The numerical results and discussions are given in Sec. III, and we summarize our results in Sec. IV.

II. THEORETICAL FRAMEWORK

Magnetophonon resonance is essentially a single-particle effect and, consequently, can be treated as a one-polaron problem. We consider a polar semiconductor in a uniform magnetic field **B** directed along the z axis. The system under consideration can be described by the following Hamiltonian,

$$H = H_e + H_{ph} + H_{int} \tag{1}$$

with

$$H_e = \frac{1}{2m_b}(\vec{p} + e\vec{A})^2 \tag{2}$$

and

$$H_{ph} = \sum_q \hbar\omega_{\vec{q}}\left(a_{\vec{q}}^{\dagger}a_{\vec{q}} + \tfrac{1}{2}\right), \tag{3}$$

where m_b is the bare electron effective mass, the vector potential $\vec{A} = B/2(-y,x,0)$ is chosen in the symmetrical Coulomb gauge, $\vec{q}$ ($\vec{r}$) the momentum (position) operator of the electron, $a_{\vec{q}}^{\dagger}$ ($a_{\vec{q}}$) the creation (annihilation) operator of an optical phonon with wave vector $\vec{q}$ and energy $\hbar\omega_{\vec{q}}$. The electron-phonon interaction Hamiltonian H_{int} is given by the Fröhlich interaction Hamiltonian

$$H_{int} = \sum_q (V_{\vec{q}}a_{\vec{q}}e^{i\vec{q}\cdot\vec{r}} + V_{\vec{q}}^{*}a_{\vec{q}}^{\dagger}e^{-i\vec{q}\cdot\vec{r}}), \tag{4}$$

where

$$V_{\vec{q}} = -i\hbar\omega_{LO}\left(\frac{\hbar}{2m_b\omega_{LO}}\right)^{1/4}\sqrt{\frac{4\pi\alpha}{Vq^2}}, \tag{5}$$

and α is the electron-LO-phonon coupling constant.

First, we calculate the optical-absorption spectrum of the polaron in magnetic fields from which we are able to investigate the polaron CR spectrum and the MPR effects. For convenience we use units such that $\hbar = m_b = \omega_{LO} = 1$. Within

the linear-response theory, the frequency-dependent magneto-optical-absorption spectrum for cyclotron resonance[11-13] is given by

$$A(\omega) = -\frac{1}{2} \frac{\operatorname{Im}\Sigma(z)}{[\omega - \omega_c - \operatorname{Re}\Sigma(z)]^2 + [\operatorname{Im}\Sigma(z)]^2}, \quad (6)$$

where $\omega_c = eB/m_b$ is the unperturbed electron cyclotron frequency, $\Sigma(z)$ is the so-called memory function, and $z = \omega + i\gamma$ and γ is a broadening parameter. Notice that γ is introduced semiempirically to remove the divergence of the Landau-level density of states. We take γ as a constant. For the magneto-optical-absorption spectrum in the Faraday (active-mode) configuration, which corresponds to the cyclotron resonance experiments, the memory function is given by[12]

$$\Sigma(z) = \frac{1}{2m_b} \sum_{\vec{q}} q^2 |V_{\vec{q}}|^2 F_{\vec{q}}(z) \quad (7)$$

with

$$F_{\vec{q}}(z) = -\frac{2}{z} \int_0^\infty dt(1 - e^{izt}) \operatorname{Im}\langle [b_{\vec{q}}(t), b_{\vec{q}}^\dagger(0)] \rangle, \quad (8)$$

where $b_{\vec{q}} = a_{\vec{q}} e^{i\vec{q}\cdot\vec{r}}$, and the correlation function is given by

$$\langle [b_{\vec{q}}(t), b_{\vec{q}}^\dagger(0)] \rangle = [1 + n(\omega_{LO})] e^{-i\omega_{LO}t} S^*(-\vec{q}, t)$$
$$- n(\omega_{LO}) e^{-i\omega_{LO}t} S(\vec{q}, t), \quad (9)$$

where

$$n(\omega_{LO}) = \frac{1}{e^{\beta\omega_{LO}} - 1} \quad (10)$$

is the number of the LO phonons and

$$S(\vec{q}, t) = \langle e^{i\vec{q}\cdot\vec{r}(t)} e^{-i\vec{q}\cdot\vec{r}(0)} \rangle \quad (11)$$

is the space Fourier transform of the electron density-density correlation function. In Eq. (10) $\beta = 1/k_B T$, where k_B is the Boltzmann constant. For a weak electron-LO-phonon coupling system, i.e., $\alpha \ll 1$, the density-density correlation function is calculated for a free electron in a magnetic field which is given by

$$S(\vec{q}, t) = e^{q_z^2 D(t)} e^{-q_\parallel^2 D_H(t)} \quad (12)$$

with

$$D(t) = \frac{1}{2}(-it + t^2/\beta) \quad (13)$$

and

$$D_H(t) = \frac{1}{2\omega_c}[1 - e^{i\omega_c t} + 4n(\omega_c)\sin^2(\omega_c t/2)].$$

From the above equations, we obtain the memory function for $\gamma = 0$. The calculation proceeds along the lines of a similar calculation which was presented in Ref. 12. The results for the memory function are

$$\operatorname{Re}\Sigma(\omega) = \frac{\alpha\sqrt{\beta}}{2\pi\omega} \frac{\omega_c \tanh(\beta\omega_c/2)}{\sinh(\beta/2)} \sum_{n,n'=0}^\infty \frac{[2\cosh(\beta\omega_c/2)]^{-(n+n')}}{n!n'!} \int_0^\infty \frac{dx}{x} E_{n+n'+1}\left(\frac{x^2}{\omega_c\tanh(\beta\omega_c/2)}\right)$$

$$\times \left\{ \exp\left(\frac{\beta\omega_{nn'}}{2}\right)\left[2D\left(\frac{\sqrt{\beta}x}{2} + \frac{\sqrt{\beta}}{2x}\omega_{nn'}\right) - D\left(\frac{\sqrt{\beta}x}{2} + \frac{\sqrt{\beta}}{2x}(\omega_{nn'} + \omega)\right) - D\left(\frac{\sqrt{\beta}x}{2} + \frac{\sqrt{\beta}}{2x}(\omega_{n'n} - \omega)\right)\right] \right.$$

$$+ \exp\left(-\frac{\beta\omega_{n'n}}{2}\right)\left[2D\left(\frac{\sqrt{\beta}x}{2} - \frac{\sqrt{\beta}}{2x}\omega_{n'n}\right)\right.$$

$$\left.\left. - D\left(\frac{\sqrt{\beta}x}{2} - \frac{\sqrt{\beta}}{2x}(\omega_{n'n} - \omega)\right) - D\left(\frac{\sqrt{\beta}x}{2} - \frac{\sqrt{\beta}}{2x}(\omega_{n'n} + \omega)\right)\right] \right\}, \quad (14)$$

and

$$\operatorname{Im}\Sigma(\omega) = -\frac{\alpha\sqrt{\beta}}{4\sqrt{\pi}\omega} \frac{\omega_c \sinh(\beta\omega/2)\tanh(\beta\omega_c/2)}{\sinh(\beta/2)} \sum_{n,n'=0}^\infty \frac{[2\cosh(\beta\omega_c/2)]^{-(n+n')}}{n!n'!}$$

$$\times \int_0^\infty \frac{dx}{x} E_{n+n'+1}\left(\frac{x^2}{\omega_c\tanh(\beta\omega_c/2)}\right)$$

$$\times \left[\exp\left(-\frac{\beta x}{4} - \frac{\beta}{4x}(\omega_{nn'} - \omega)\right) + \exp\left(-\frac{\beta x}{4} + \frac{\beta}{4x}(\omega_{n'n} - \omega)\right)\right], \quad (15)$$

where $\omega_{nn'} = 1 + (n - n')\omega_c$, $D(x)$ is the Dawson's integral function, and

$$E_n = \int_0^\infty dt \frac{t^n e^{-t}}{t+x}. \quad (16)$$

In the case of $\gamma \neq 0$, the calculation is more tedious. We obtain the following results of the memory function,
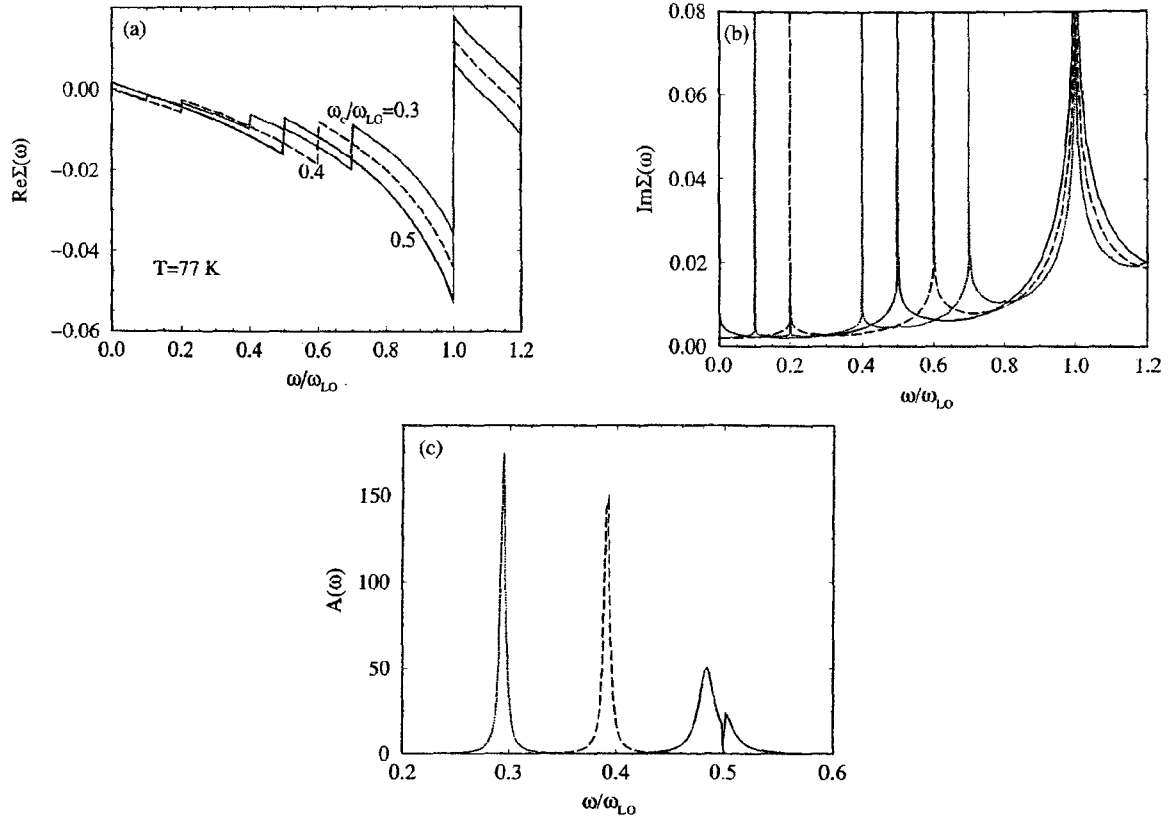
FIG. 1. (a) Re $\Sigma(\omega)$ and (b) Im $\Sigma(\omega)$ as a function of frequency ω in GaAs at different magnetic fields $\omega_c/\omega_{LO}=0.3$ (dotted curves), 0.4 (dashed curves), and 0.5 (solid curves). The corresponding absorption spectra are given in (c). The broadening parameter $\gamma=0$ and temperature $T=77$ K.

$$\mathrm{Re}\,\Sigma(\omega)=-\frac{\alpha}{\sqrt{2}\,\pi(\omega^2+\gamma^2)}[\omega I_1(\omega)+\gamma I_2(\omega)] \tag{17}$$

and

$$\mathrm{Im}\,\Sigma(\omega)=\frac{\alpha}{\sqrt{2}\,\pi(\omega^2+\gamma^2)}[\omega I_2(\omega)+\gamma I_1(\omega)] \tag{18}$$

with

$$I_1(\omega)=-\sqrt{2\beta}\,\frac{\omega_c\tanh(\beta\omega_c/2)}{\sinh(\beta/2)}\sum_{n,n'=0}^{\infty}\frac{[2\cosh(\beta\omega_c/2)]^{-(n+n')}}{n!\,n'!}\int_0^\infty\frac{dx}{x}E_{n+n'+1}\!\left(\frac{x^2}{\omega_c\tanh(\beta\omega_c/2)}\right)$$

$$\times\left(\exp\!\left(\frac{\beta\omega_{nn'}}{2}\right)\left\{D\!\left(\frac{\sqrt{\beta}x}{2}+\frac{\sqrt{\beta}}{2x}\,\omega_{nn'}\right)\right.\right.$$

$$\left.-\frac{\sqrt{\pi}}{4}\left[\mathrm{Im}\,W\!\left(\frac{\sqrt{\beta}x}{2}+\frac{\sqrt{\beta}}{2x}(\omega_{nn'}+\omega+i\gamma)\right)+\mathrm{Im}\,W\!\left(\frac{\sqrt{\beta}x}{2}+\frac{\sqrt{\beta}}{2x}(\omega_{n'n}-\omega+i\gamma)\right)\right]\right\}$$

$$+\exp\!\left(-\frac{\beta\omega_{n'n}}{2}\right)\left\{D\!\left(\frac{\sqrt{\beta}x}{2}-\frac{\sqrt{\beta}}{2x}\,\omega_{n'n}\right)\right.$$

$$\left.\left.-\frac{\sqrt{\pi}}{4}\left[\mathrm{Im}\,W\!\left(\frac{\sqrt{\beta}x}{2}-\frac{\sqrt{\beta}}{2x}(\omega_{n'n}-\omega-i\gamma)\right)+\mathrm{Im}\,W\!\left(\frac{\sqrt{\beta}x}{2}-\frac{\sqrt{\beta}}{2x}(\omega_{n'n}+\omega-i\gamma)\right)\right]\right\}\right), \tag{19}$$

and

$$I_2(\omega) = -\frac{\sqrt{\pi\beta}}{2\sqrt{2}} \frac{\omega_c \tanh(\beta\omega_c/2)}{\sinh(\beta/2)} \sum_{n,n'=0}^{\infty} \frac{[2\cosh(\beta\omega_c/2)]^{-(n+n')}}{n!n'!} \int_0^\infty \frac{dx}{x} E_{n+n'+1}\left(\frac{x^2}{\omega_c \tanh(\beta\omega_c/2)}\right)$$

$$\times \left\{ \exp\left(\frac{\beta\omega_{nn'}}{2}\right)\left[\mathrm{Re}\,W\left(\frac{\sqrt{\beta}x}{2} + \frac{\sqrt{\beta}}{2x}(\omega_{nn'}+\omega+i\gamma)\right) - \mathrm{Re}\,W\left(\frac{\sqrt{\beta}x}{2} + \frac{\sqrt{\beta}}{2x}(\omega_{nn'}-\omega+i\gamma)\right)\right]\right.$$

$$\left. + \exp\left(-\frac{\beta\omega_{n'n}}{2}\right)\left[\mathrm{Re}\,W\left(\frac{\sqrt{\beta}x}{2} - \frac{\sqrt{\beta}}{2x}(\omega_{n'n}-\omega-i\gamma)\right) - \mathrm{Re}\,W\left(\frac{\sqrt{\beta}x}{2} - \frac{\sqrt{\beta}}{2x}(\omega_{n'n}+\omega-i\gamma)\right)\right]\right\}, \quad (20)$$

where $W(z) = e^{-z^2}\mathrm{erfc}(-iz)$ is the complex error function.

III. NUMERICAL RESULTS AND DISCUSSIONS

In this section, we are going to present our numerical results on the magneto-optical-absorption spectra and to study the magnetophonon resonant effects. As an example of weak electron-LO-phonon coupling, we apply our theory to semiconductor GaAs where $\alpha = 0.07$. First, we show some numerical results for temperature $T = 77$ K and level broadening parameter $\gamma = 0$. Due to the importance of the memory function in the absorption spectrum, we plot the real and imaginary parts of the memory function in Figs. 1(a) and 1(b), respectively, as a function of frequency at different magnetic fields. We see that, at $\omega = |\omega_{LO} - n\omega_c|$ ($n = 0,1,2,\ldots$), $\mathrm{Re}\,\Sigma(\omega)$ exhibits a jump while $\mathrm{Im}\,\Sigma(\omega)$ diverges logarithmically. The discontinuity of $\mathrm{Re}\,\Sigma(\omega)$ and the divergency in $\mathrm{Im}\,\Sigma(\omega)$ reflects the resonant coupling between

the state $E_0 + \omega_{LO}$ and Landau level $E_n = (1/2+n)\omega_c$. The stronger this coupling, the larger the discontinuity in $\mathrm{Re}\,\Sigma(\omega)$. Actually, the real part of the memory function $\mathrm{Re}\,\Sigma(\omega)$ is responsible for the shift in the observed CR energy which is due to the electron-phonon interaction, while the imaginary part leads to a broadening of the spectrum which is a result of scattering. When $\mathrm{Im}\,\Sigma(\omega) = 0$ like in a 2D system, the absorption is a δ function, and its position is determined by the equation $\omega_c^* - \omega_c - \mathrm{Re}\,\Sigma(\omega_c^*) = 0$. Figure 1(b) shows that in the present system the $\mathrm{Im}\,\Sigma(\omega)$ is always non-zero, which reflects the 3D character of the electron states. The scattering in the direction parallel to the magnetic field results in a finite $\mathrm{Im}\,\Sigma(\omega)$ and, consequently, a finite linewidth even for $\gamma = 0$. In Fig. 1(c), we show the corresponding magneto-optical-absorption spectra. The position of the absorption peak corresponds to the cyclotron resonant frequency ω_c^* at which the cyclotron resonance occurs. We see an asymmetric double peak structure around $\omega = \omega_{LO}/2$ for $\omega_c = \omega_{LO}/2$ (the solid curve), and the absorption becomes zero at $\omega = \omega_c = \omega_{LO}/2$. The zeros in the absorption spectrum are a consequence of the divergences in $\mathrm{Im}\,\Sigma(\omega)$ and can be traced back to the divergent nature of the density of states. The double peak structure is a consequence of the magnetophonon resonance which leads to an anticross behavior in the CR spectrum. When the unperturbed CR frequency ω_c deviates from ω_{LO}/N, this splitting becomes very weak and difficult to be observed in the absorption spectrum. As we will see below, however, the magnetophonon resonance will strongly affect the linewidth of the magneto-optical absorption and the CR mass. From the dashed and dotted curves,
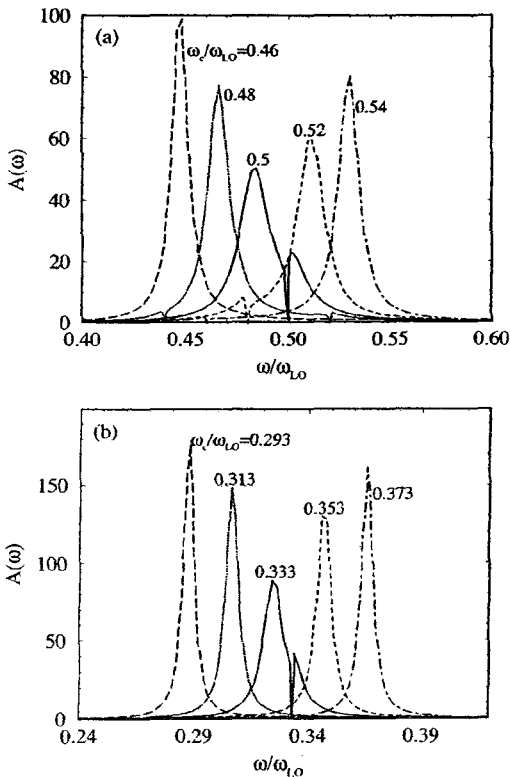

FIG. 2. The magneto-optical-absorption spectrum at around (a) $\omega_c/\omega_{LO} = 1/2$ and (b) $\omega_c/\omega_{LO} = 1/3$. $T = 77$ K and $\gamma = 0$.
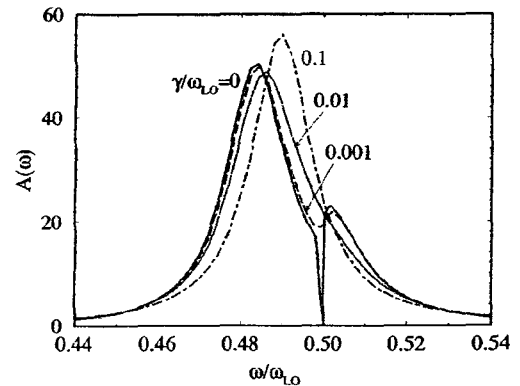

FIG. 3. The magneto-optical-absorption spectra as a function of frequency ω in GaAs for $\gamma/\omega_{LO} = 0$ (solid curve), 0.001 (dashed curve), 0.01 (dotted curve), and 0.1 (dash-dotted curve) at $\omega_c/\omega_{LO} = 0.5$ and $T = 77$ K.
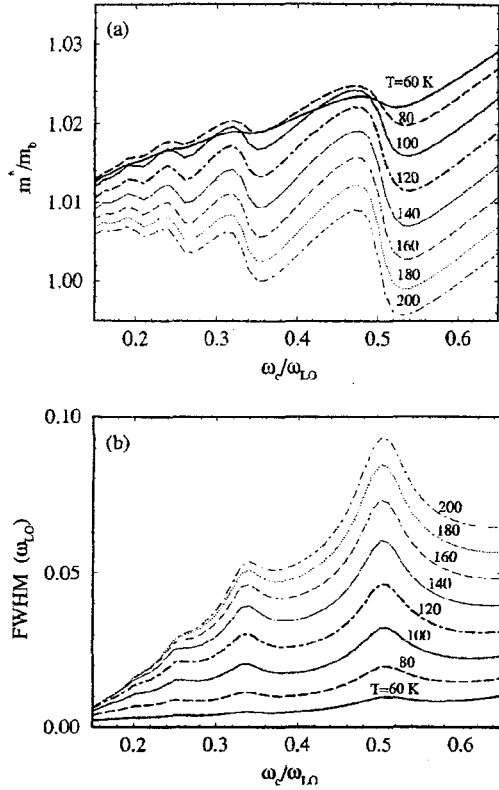
FIG. 4. (a) Polaron CR mass and (b) FWHM as a function of ω_c at different temperatures from 60 K to 200 K with $\gamma/\omega_{LO}=0.05$.

FIG. 6. An activation plot of the amplitude of the resonant peak in the FWHM at $\omega_c/\omega_{LO}=1/2$ (circles) and $\omega_c/\omega_{LO}=1/3$ (triangles) as a function of T^{-1}. The solid line $\propto\exp(-\hbar\omega_{LO}/2k_BT)$ and the dotted line $\propto\exp(-2\hbar\omega_{LO}/3k_BT)$.

we observe that the absorption peak appears at $\omega_c^*<\omega_c$ due to the polaron effect which shifts the cyclotron frequency to lower frequencies. The latter is often interpreted as an increase of the cyclotron mass, i.e., $\omega_c^*=eB/m^*$. In Fig. 2, we show the absorption spectrum around (a) $\omega_c=\omega_{LO}/2$ and (b) $\omega_c=\omega_{LO}/3$. The double peak structure disappears when ω_c deviates from ω_{LO}/N ($N=2,3$). The absorption spectra also demonstrate clearly a nonlinear magnetic-field dependence of the peak position and linewidth around ω_{LO}/N.

Figure 3 demonstrates the effect of the broadening parameter γ on the absorption spectrum. Notice that, with increasing γ. (i) the double peak structure disappears for $\gamma >0.01\omega_{LO}$, (ii) the zero in the absorption spectrum disap-

pears when $\gamma>0$, and (iii) the position of the absorption peak shifts to higher frequency. This indicates that the anticrossing behavior in the CR spectrum will be difficult to be observed experimentally at $\omega_c=\omega_{LO}/2$, due to broadening effects which are a consequence of scattering on e.g., impurities and acoustical phonons.

As soon as the polaron CR frequency ω_c^* is determined from the position of the magneto-optical-absorption peak, the CR mass of the polaron is obtained by

$$m^*/m_b=\omega_c/\omega_c^*. \tag{21}$$

The numerical results of the polaron CR mass and the FWHM (full width at half maximum) for $\gamma=0.05\omega_{LO}$ are plotted as a function of the unperturbed CR frequency at different temperatures in Figs. 4(a) and 4(b), respectively. One observes that the polaron CR mass is an oscillatory function of magnetic field. Figure 4(b) shows that the FWHM of the polaron magneto-optical-absorption spectrum reach a local maximum at $\omega_c=\omega_{LO}/N$ where the polaron mass has an inflection point. This result demonstrates the derivativelike relation between the polaron CR mass and the linewidth which are due to the fact that the real and imaginary part of the memory function are related to each other through a Kramers-Kronig relation. One finds that, for temperature $T<100$ K, the resonance grows rapidly with increasing T. This effect can lead to a direct measure of the optical-phonon scattering rate. We also show an overall increase of the linewidth with temperature but an overall decrease of the effective mass for $T>80$ K. The resonant position is slightly larger than the unperturbed resonant condition $\omega_c=\omega_{LO}/N$ and is almost independent of temperature. A detailed analysis indicates that, at $N=2$ and 3, the peak position both in the FWHM and in the derivative of the CR mass is at about $0.504\omega_{LO}$ and $0.336\omega_{LO}$, respectively. Experimentally, this position determines the so-called fundamental field $B_0=m^*\omega_{LO}/e$, which is an important quantity to study the effective mass, nonparabolicity of the energy band, as well as the LO-phonon frequency. The linewidth is a direct measure of the lifetime of the state. Notice that the conventional MPR occurs in the resistivity, which is given by $\rho_{zz}=-\text{Im}\Sigma(\omega=0)$. But ODMPR is related to both the
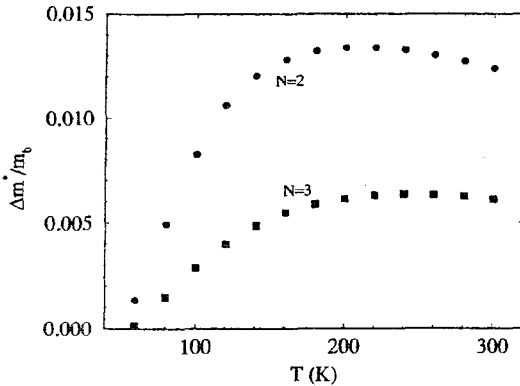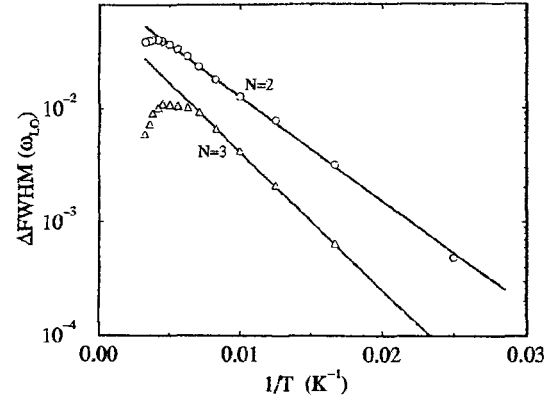

FIG. 5. The CR mass oscillation amplitude as a function of temperature at $\omega_c/\omega_{LO}=1/2$ (dots) and $\omega_c/\omega_{LO}=1/3$ (solid squares) with $\gamma/\omega_{LO}=0.05$.

real and imaginary part of the memory function which occurs for $\omega \neq 0$ and is a dynamical MPR.

Figure 5 shows the CR mass oscillation amplitude at $\omega_c/\omega_{LO} = 1/2$ and $1/3$ as a function of temperature. With increasing temperature, the number of phonons increases and, consequently, the oscillation amplitude increases. On the other hand, the background electron-phonon scattering (coupling) increases, which results in a suppression of the oscillation amplitude. Figure 6 shows an activation plot of the amplitude of the resonant peak in the FWHM at $\omega_c/\omega_{LO} = 1/2$ and $1/3$ as a function of T^{-1}. We find that, for the resonance around $N=2$, the linewidth can be described rather well by the exponential law $\exp(-\hbar\omega_{LO}/2kT)$ for $T < 240$ K, while that around $N=3$ can be described by $\exp(-2\hbar\omega_{LO}/3kT)$ for $T < 140$ K. This exponential behavior can be understood as follows. MPR is proportional to the number of LO phonons which are present and therefore should increase as $n(\omega_{LO})$. On the other hand, thermal broadening of the Landau levels, which is proportional to $n(\omega_c)$, will diminish the resonant structure in ΔFWHM. Thus, this contribution decreases the resonant character, and consequently we expect that ΔFWHM $\sim n(\omega_{LO})/n(\omega_c) \approx \exp[-\hbar(\omega_{LO}-\omega_c)/k_B T]$ which agrees with the exponential laws found for $N=2$ and $N=3$.

IV. SUMMARY

We have extended the theory for ODMPR to three-dimensional (3D) systems and present the first detailed theoretical study of the magnetophonon resonance in the magneto-optical-absorption spectrum in bulk GaAs. In comparison to the corresponding 2D systems, the theoretically obtained amplitudes for the oscillations of both the linewidth and the effective mass in a 3D system are for GaAs predicted to be about half of those in 2D. Therefore, we believe that ODMPR can also be observed experimentally in bulk polar semiconductors. Our numerical results indicate that the amplitude of the resonant peak in the FWHM can be described by exponential law at low temperature.

ACKNOWLEDGMENTS

[1] J. R. Barker, J. Phys. C 5, 1657 (1972).

[2] R. J. Nicholas, Prog. Quantum Electron. 10, 1 (1985); R. V. Parfen'ev, G. I. Kharus, I. M. Tsidil'kovskii, and S. S. Shalyt, Usp. Fiz. Nauk. 112, 3 (1974) [Sov. Phys. Usp. 17, 1 (1974)]; J. Van Royen, J. De Sitter, L. F. Lemmens, and J. T. Devreese, Physica B 89, 101 (1977); J. Van Royen, J. De Sitter, and J. T. Devreese, Phys. Rev. B 30, 7154 (1984); J. P. Vigneron, R. Evrard, and E. Kartheuser, ibid. 18, 6930 (1978).

[3] D. Schneider, C. Brink, G. Irmer, and P. Verma, Physica B 256-258, 625 (1998); D. Schneider, K. Fricke, J. Schulz, G. Irmer, and M. Wenzel, in Proceedings of the 23rd International Conference on the Physics of Semiconductors, edited by M. Scheffler and R. Zimmermann (World Scientific, Singapore, 1996), p. 221.

[4] P. Warmenbol, F. M. Peeters, and J. T. Devreese, Solid-State Electron. 31, 771 (1988); 32, 1545 (1989); Phys. Rev. B 37, 4694 (1988).

[5] W. Xu, F. M. Peeters, J. T. Devreese, D. R. Leadley, and R. J. Nicholas, Int. J. Mod. Phys. B 10, 169 (1996); D. R. Leadley, R. J. Nicholas, J. Singleton, W. Xu, F. M. Peeters, J. T. Devreese, J. A. A. J. Perenboom, L. Van Bockstal, F. Herlach, J. J. Harris, and C. T. Foxon, Phys. Rev. Lett. 73, 589 (1994).

[6] R. J. Nicholas, in Landau Level Spectroscopy, edited by G. Landwehr and E. I. Rashba (North-Holland, Amsterdam, 1990).

[7] X.-G. Wu and F. M. Peeters, Phys. Rev. B 55, 9333 (1997); 34, 8800 (1986).

[8] P. Vasilopoulos, P. Warmenbol, F. M. Peeters, and J. T. Devreese, Phys. Rev. B 40, 1810 (1989).

[9] G. Ploner, J. Smoliner, G. Strasser, M. Hauser, and E. Gornik, Phys. Rev. B 57, 3966 (1998).

[10] D. J. Barnes, R. J. Nicholas, F. M. Peeters, X. G. Wu, J. T. Devreese, J. Singleton, C. J. G. M. Langerak, J. J. Harris, and Foxon, Phys. Rev. Lett. 66, 794 (1991).

[11] F. M. Peeters and J. T. Devreese, Phys. Rev. B 28, 6051 (1983).

[12] F. M. Peeters and J. T. Devreese, Phys. Rev. B 34, 7246 (1986).

[13] G. Q. Hai, F. M. Peeters, and J. T. Devreese, Phys. Rev. B 47, 10 358 (1993).

Capítulo 6

Sumário

Concluímos aqui a síntese de minhas atividades de pesquisa realizadas ao longo dos últimos anos. Este texto é composto basicamente por três assuntos principais.

Primeiro, mostramos teoricamente, em um sistema de dois fios quânticos acoplados, um efeito oriundo da ressonância entre os plasmons acústicos e as excitações de partícula independente. O campo magnético extra pode aumentar esta ressonância. Estendemos a aproximação GW para calcular o tempo de relaxação de elétrons devido a interação elétron-elétron em sistemas de multisubbandas. Estudamos os processos de relaxamento nos poços e fios quânticos acoplados. Relacionado com este assunto, estamos estudando: (i) a dispersão de plasmons e efeito de correlação em sistemas de elétrons com duas camadas acopladas; (ii) efeito de desordem nas propriedades físicas das fases sólido-fluido do gás de elétrons 2D presentes em heterojunções semicondutoras; e (iii) plasmons em sistemas de multisubbandas a temperatura finita, como gás de elétrons Q1D na superfície de hélio líquido.

Segundo, nosso trabalho mostrou que a teoria de RPA pode descrever corretamente a blindagem de gás de elétrons no espalhamento de impureza ionizadas no sistema de multisubbandas. Pela primeira vez conseguimos uma explicação teórica das mobilidades de sistemas de multisubbandas, onde destacamos a importância de mecanismos de acoplamento intersubbandas no transporte eletrônico. (i) Embora nossos resultados apresentem concordância quantitativa com as mobilidades quânticas experimentais, as mobilidades de

transporte calculadas são quase duas vezes maiores que as experimentais. Recentemente, descobrimos que tal diferença pode ser corrigida através do cálculo da amplitude de espalhamento além da aproximação de Born. Obtivemos então a taxa de espalhamento através a solução exata da equação Lippmann-Schwinger. (ii) Por outro lado, estamos estendendo nossos cálculos de mobilidade a sistemas com spin polarizado.

Terceiro, explicamos a primeira observação experimental de ressonância de *magneto-polaron* devida a fônons interfaciais em poços quânticos de GaAs-$Al_{0.3}Ga_{0.7}As$. Confirmamos também a observação experimental de harmônicos assistidos por fônons em sistemas dopados de super-rede devido aos estados ligados de impurezas rasas. Como uma continuidade deste assunto, estamos ainda estudando acoplamento elétron-fônon em pontos quânticos. Conseguimos a densidade de estado e autoenergia devidos interação elétron-fonon em pontos quânticos. Estamos trabalhando também para obter os espectros de absorção de ponto quântico (estados ligados em geral) no campo magnético usando a formula de Kubo.